7-2-2011

Swirling jets for the mitigation of hot spots and thermal Sstratification in the VHTR lower plenum

salvador rodriguez

Follow this and additional works at: https://digitalrepository.unm.edu/ne_etds
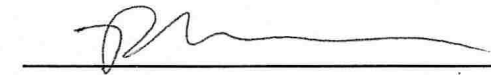
Salvador B. Rodríguez
Candidate

Chemical and Nuclear Engineering
Department

This dissertation is approved, and it is acceptable in quality
and form for publication:

Approved by the Dissertation Committee:

(signature) , Chairperson

(signature)

(signature) Stanly Steenberg.

(signature) D Petsu

(signature)

Swirling Jets for the Mitigation of Hot Spots and Thermal Stratification in the VHTR Lower Plenum

By

Salvador B. Rodríguez

B.S. Nuclear Engineering, University of California at Santa Barbara, 1985

M.S. Mechanical Engineering, University of Idaho, 1993

M.S. Applied Mathematics, University of New Mexico, 2004

Ph.D. Philosophy and Apologetics,
Trinity Theological College and Seminary, 2005

Ph.D. Nuclear Engineering, University of New Mexico, 2011

DISSERTATION

Submitted in Partial Fulfillment of the
Requirements for the Degree of

Doctor of Philosophy

Engineering

The University of New Mexico
Albuquerque, New Mexico

May 2011

DEDICATION

I would like to dedicate this work to my immediate family:

Matilde Zapata, father-in-law

Salvador J. Rodríguez, father

Soledad Zapata, mother-in-law

Juana Rodríguez, mother

Enrique Rodríguez, brother

Elena Rodríguez, wife

Griselda Rodríguez, sister-in-law

Yoli Rodríguez, sister

Vanessa Rodríguez, niece

Iesha Rodríguez, niece

Enrique Rodríguez, Jr., nephew

Sarai Rodríguez, daughter

Salvador Emiliano Zapata Rodríguez, the 3rd, son and

Emily Esther Zapata Rodríguez, daughter.

As far as I can tell, I have family members in New Mexico, California, Arizona, Texas, Utah, Washington, Idaho, Baja California Norte, Baja California Sur, Guanajuato, Distrito Federal, Chihuahua, Zacatecas, Michoacán, Jalisco, Sonora…I greet you all and thank you for your support.

Most importantly, I make a special dedication to my loving wife and three children: when you look upon the stars, know that I will always be with you, both in spirit and mind. May the stars above the skies always be a symbol of my love for you,

and may we someday share this love forever in God's Heaven, where our glory will be like that of the stars (Daniel 12:3). I realize that this degree has probably required thousands of hours, hours that I could have spent with you. These are hours that can never be recuperated. On the other hand, I hope that I am now a better husband and father. In addition, I hope that you will be blessed when you read this work and the associated research papers, and that therefore such time was well spent. These works are part of your inheritance, and one that I hope will most certainly yield many rewards for you. I also hope that by obtaining this doctorate, I will be a better role model for you. I anticipate that when the time is right, you, too, will follow; if I can do it, you certainly can!

ACKNOWLEDGMENTS

Jocelyn White, the UNM Program Advisement Coordinator for her excellent round-up of all the paperwork required for the graduation process.

I am very indebted to you all. Many thanks! ¡Muchas gracias! Merci beaucoup! Bolshoi spasibo!

Swirling Jets for the Mitigation of Hot Spots and Thermal Stratification in the VHTR Lower Plenum

By

Salvador B. Rodríguez

ABSTRACT OF DISSERTATION

Submitted in Partial Fulfillment of the
Requirements for the Degree of

Doctor of Philosophy

Engineering

The University of New Mexico
Albuquerque, New Mexico

May 2011

Swirling Jets for the Mitigation of Hot Spots and Thermal Stratification in the VHTR Lower Plenum

By

Salvador B. Rodríguez

B.S. Nuclear Engineering, University of California at Santa Barbara, 1985

M.S. Mechanical Engineering, University of Idaho, 1993

M.S. Applied Mathematics, University of New Mexico, 2004

Ph.D. Philosophy and Apologetics, Trinity Theological College and Seminary, 2005

Ph.D. Nuclear Engineering, University of New Mexico, 2011

ABSTRACT

The literature indicates that a prismatic-core very high temperature reactor can experience thermal stratification and hot spot issues in the lower plenum (LP). This research hypothesizes that the complex thermalhydraulic phenomena in the LP requires a sophisticated computational fluid dynamics (CFD) code with state-of-the-art turbulence models and advanced swirling jet technology to mitigate the two issues.

The primary research goals were to increase the heat transfer and mixing capacity of swirling jets, extend swirling jet theory, and to apply those advancements for the mitigation of the thermalhydraulic issues.

First, it was demonstrated that the Fuego CFD code successfully modeled a set of key LP thermalhydraulic phenomena. Thereafter, a helicoid vortex swirl model was developed to investigate the impact of the swirl number (S) on mixing and heat transfer. The development of azimuthal and axial velocities that are purely functions of S permitted the analysis of the central recirculation zone's (CRZ) impact on the LP flow field.

At this point, several characteristics were found in common between the helicoid vortex and other axisymmetric, Newtonian, incompressible vortices found in the literature. This observation resulted in a more fundamental understanding of how vortices behave, and which traits can be exploited for the purpose of maximizing heat transfer and mixing. Because the CRZ is a strong function of the azimuthal and axial velocities, shaping those velocity profiles had a substantial impact on the flow field. Eventually, this led to the discovery that vortices may be expressed as alternating series that expand geometrically with odd exponents. This helped corroborate that the 15 axisymmetric vortices discussed in this research are part of a vortex family with seven common traits. This also led to the development of new vortices that are based on one or two series terms that satisfy the Navier-Stokes equations and conservation of mass. In addition, the impact of Reynolds number and swirl decay were explored in order to further quantify their impact on mixing and heat transfer.

Finally, the above theories and modeling insights were applied towards a comprehensive set of LP calculations that showed that the swirling jets mitigated the entrainment and hot spot issues, while resulting in a reasonable pressure drop.

CONTENTS

FIGURES

xxi

TABLES

NOMENCLATURE

A	Coefficient in St formulation
a	Jet core radius (m)
A_n	Coefficient in AVE vortex, n=1, 2, …
ASC	Advanced Simulation and Computing
AVE	Aboelkassem, Vatistas, and Esmail
B	Coefficient in St formulation
b	Jet width (m)
b(z)	Jet width as a function of z (m)
BC	Boundary condition
B_n	Arbitrary constant, n=0, 1, 2,…
$B_n(z)$	Arbitrary function of z, n=0, 1, 2,…
C	Curve C
C	Coefficient in St formulation
CCW	Counter-clockwise
C_{DS}	Dynamic Smagorinsky parameter
CFD	Computational fluid dynamics
CFL	Courant-Friedrichs-Lewy condition
CHT	Conjugate heat transfer
C_n	Coefficients used mainly in vortex expansions, n=-1, 0, 1, 2,…
CRZ	Central recirculation zone
C_S	Standard Smagorinsky parameter

CVP	Counter-rotating vortex pair
CW	Clockwise
c_1	Crossflow jet coefficient
C_3	Coefficient in conventional jet axial velocity
C_μ	Coefficient in k-ε turbulence model = 0.09
D	Diameter of coolant jets or cylinder diameter (m)
DNS	Direct numerical simulation
DOE	Department of Energy
EDC	Magnussen's eddy dissipation concept model
f	Vortex shedding frequency (1/s)
G	Gas mass flux, ρV (kg/m^{2}s)
G	Scalar flux
g	Gravitational constant (m/s^2)
GA	General Atomics
GT-MHR	General Atomics gas turbine modular helium reactor
H	LP height (m)
h	Heat transfer coefficient (W/m^2-K)
h	Vertical jet spacing (m)
HSVM	Helicoid swirl vortex model
HTTR	High Temperature Test Reactor
i	Imaginary number used solely in Equation 80 ($\sqrt{-1}$)
INL	Idaho National Laboratory
I_t	Turbulence intensity (-)

J_1	Bessel function of order 1
k	Thermal conductivity (W/m-K)
k	Turbulent kinetic energy (m^2/s^2, i.e. per unit mass)
k	Coefficient in Chepura and Modified Chepura vortices
K_e	Entrainment constant
KSGS	Kinetic Subgrid-scale (turbulence model)
L	Distance from jet exit to LP plate normal to z (m)
L'	Length of one complete helicoid revolution (m)
LES	Large eddy simulation
LHS	Left hand side
l_o	Turbulence length scale (m)
LP	Lower plenum
Ma	Mach number, v/v_s
N	Number of computational time steps
n	Exponential coefficient
n	Normal
NGNP	Next Generation Nuclear Plant
NRC	Nuclear Regulatory Commission
NS	Navier-Stokes
Nu	Nusselt number, hx/k
Nu_o	Nusselt number at stagnation point
ODE	Ordinary differential equation
ORNL	Oak Ridge National Laboratory

P	Pressure (Pa)
P	Rod pitch (m)
p	Helicoid pitch, $L'/(2\pi)$ (m)
PDE	Partial differential equation
PIRT	Phenomena identification and ranking table
PIV	Particle image velocimetry
PMR	Participating media radiation
PWR	Pressurized water reactor
q	Alternate S definition, $\Gamma/(2a\pi W)$
q	Substitutionary integration variable
q	Coefficient in Martynenko's equations
q	Heat flux (W/m^2)
r	Radial distance from the stagnation point (m)
r	Radial coordinate for cylindrical system
r'	Radial distance from the symmetry axis (i.e., z) (m)
$\vec{r}$	Position vector (m)
RANS	Reynolds-averaged Navier-Stokes
Re	Reynolds number, GD/ρ
Re$_\Gamma$	Reynolds number based on circulation, Γ/v
RHS	Right hand side
RNG	Renormalization group (turbulence model)
RSM	Reynolds Stress Model (turbulence model)
S	Geometric swirl number, $\frac{2}{3}\tan(\theta)$

s	Space grid filter for LES method
s	Length of helical ribbon as it twists about the z-axis (m)
SI	Sulfur-Iodine
s_i	i^{th} ordinate direction
S_{ij}	Strain rate tensor (1/s)
SNL	Sandia National Laboratories
SST	Shear stress transport (turbulence model)
St	Strouhal number, $\dfrac{fD}{U_a}$
T	Temperature (K)
T	Period (s)
T	Time (s)
t	Parametric variable
t	Test filter for LES method
t_n	Time interval at fixed time n=1, 2, 3,… (s)
t_n	Parametric space at fixed interval n=1, 2, 3,…
t_O	Temporal interval taken at fixed time (s)
TRISO	Tristructural-isotropic nuclear fuel
U_a	Approach velocity (m/s)
u	Velocity in the r direction (m/s)
u_1	Crossflow velocity (m/s)
UNM	University of New Mexico
URANS	Unsteady Reynolds-averaged Navier-Stokes
U_∞	Velocity far away from the cylinder (m/s)

$\vec{V}$	Velocity vector consisting of (v_x, v_y, v_z) components in Cartesian coordinates (m/s)
$\vec{V}$	Velocity vector consisting of (u, v, w) components in cylindrical coordinates (m/s)
$\tilde{V}$	Volume (m^3)
v	Velocity in the θ direction (azimuthal velocity) (m/s)
VHTR	Very high temperature reactor
V&V	Validation and verification
v_x	Velocity in the x direction (m/s)
v_y	Velocity in the y direction (m/s)
v_z	Velocity in the z direction (m/s)
v_θ	Azimuthal velocity (m/s)
$v_{\theta,C}$	Characteristic azimuthal velocity, $\Gamma/(2\pi a)$ (m/s)
W	Centerline axial velocity (m/s)
w	Velocity in the axial direction (m/s)
x	Cartesian coordinate
y	Cartesian coordinate
z	Cartesian coordinate (direction of jet flow for S = 0)
z	Axial coordinate for cylindrical system (direction of jet flow for S = 0)
z_O	Planar slice taken at fixed point along z axis (m)
1D	One-dimensional
2D	Two-dimensional
3D	Three-dimensional

Greek Symbols

α	Coefficient in Loitsyanskiy's equations
α	Coefficient in Martynenko's equations
β	Coefficient in Loitsyanskiy's equations
β	Coefficient in AVE vortex
Γ	Circulation, $\int_{0}^{2\pi} v(r)rd\theta$ (m^2/s)
γ	Coefficient in Loitsyanskiy's equations
γ	Coefficient in Martynenko's equations
Γ_C	Characteristic circulation, $2\pi r u_{\theta,C}$ (m^2/s)
Γ_{max}	Maximum circulation, $2\pi r u_{\theta,max}$ (m^2/s)
Δ	Turbulence filter length $= \tilde{V}^{1/3}$ (m)
η	Coefficient in Loitsyanskiy's equations
η	Coefficient in Martynenko's equations
ε	Turbulent dissipation rate (m^2/s^3)
ε	Emissivity (-)
θ	Swirl angle of helicoid surface (^{o})
θ	Azimuthal coordinate for cylindrical system
λ	Coefficient in AVE vortex
μ	Dynamic viscosity (Pa-s, kg/m-s)
μ_a	Absorption coefficient
ν	Kinematic viscosity (m^2/s)
ρ	Gas density (kg/m^3)

ρ	Reflectivity (-)	
σ	Stefan-Boltzmann constant (5.67×10^{-8} W/m^2-K^4)	
τ	Turbulent time scale (s)	
τ	Turbulent shear (kg/m-s^2)	
T	Transmissivity (-)	
ζ	Coefficient in Martynenko's equations	
Ω	Coefficient in Rankine vortex (1/s)	
ω	Angular frequency (1/s)	
ω	Specific dissipation rate (m^2/s^3)	
ω	Coefficient in Martynenko's equations	
$\bar{\omega}$	Vorticity (1/s)	

Subscripts

bin	Discrete partitioning
CCW	Counter-clockwise
conv	Conventional jet (θ=0º, S=0)
CW	Clockwise
j	Jet
max	Maximum
min	Minimum
o	Constant parameter for S=0 at jet outlet
rot	Rotation
S	Static

s	Sound
T	Turbulent
w	Wall
∞	Property taken far away from the jet

Superscripts

c	Conduction
F	Fluid
r	Radiative
S	Solid
t	Turbulent
v	Viscous
$\cdot$	Time derivative
'	Temporal instantaneous fluctuation
$^-$	Average
→	Vector
*	Nondimensionalized

I. INTRODUCTION

1.1   Research Needs

The Department of Energy (DOE) has a special interest in the development of

Generation IV next generation nuclear plants (NGNPs) in the form of very high (gas-

cooled) temperature reactors (VHTRs) for the production of electricity, hydrogen, and

process heat. As of 2010, the prismatic and pebble bed reactors are the top VHTR

candidates [ORNL, 2010; Wikipedia, 2010a; World Nuclear News, 2010; Kinsey, 2010].

However, for reasons elucidated in Section 2, this research will concentrate on the

prismatic core VHTR.

As currently conceived in the prismatic VHTR design, helium gas removes the

reactor core heat, causing the gas to heat up, and upon exiting the core, the hot helium

reaches temperatures (T) ranging from 1,123 – 1,273 K [MacDonald *et al*., 2003;

Southworth *et al*., 2004; Schultz *et al*., 2004; MacDonald, 2004; INL, 2007]. The

effluent then enters the lower plenum (LP), where the flow from the multiple channels

mixes. The LP acts as a location where the multiple channels mix, mostly under

turbulent conditions and with crossflows and flow obstructions such as support posts.

However, the flow may also approach stagnant conditions near the outermost periphery

wall [Goldstein, 1982; McEligot and McCreery, 2004; McCreery and Condie, 2004].

Under some instances, due to core geometry and fuel loading, some coolant channels

experience an exit temperature that may be on the order of 300 K hotter than the average

exit temperature [McEligot and McCreery, 2004]. This causes what is known as "hot

spots" (a.k.a. "hot streaking"). Basically, the hot channels that exit near the LP center mix

with the cooler effluent from the other channels, and thus pose no further problem. On

the other hand, if the resulting hot spot occurs near the LP exit, or near the stagnation

zone near the LP outer periphery (opposite end of the LP exit), then there is a possibility

that the hot effluent will not mix adequately, causing the LP to unnecessarily heat up,

potentially fomenting its premature failure [McEligot and McCreery; 2004; Nishino *et*

al., 1996]. The poor mixing (thermal stratification), can be aggravated under some

circumstances by the obstruction of the graphite support posts [Johnson and Schultz,

2009]. Basically, there is approximately a factor of eight drop in both the experimental

data and calculated velocity as the approaching gas flows around the first support post on

the left hand side of an experiment conducted at the Idaho National Laboratory (INL)

[Johnson and Schultz, 2009].

Figure 1 shows the LP region where hot spots and stratification can occur, while

Figure 2 shows a half-symmetry, side view of the LP with its myriad of support posts.

The location of the LP, fuel, and lower reactor internals is shown in Figure 3. Key flow

phenomena expected to occur in the LP include multiple jet flow field interaction and

mixing, crossflow entrainment and mixing, flow around the cylindrical graphite support

posts, vortex shedding, impinging, and the Coanda effect [McEligot and McCreery, 2004;

McEligot, D. M. *et al*, 2005]. Additionally, there would be regions of high Reynolds

number (Re), flow transition, and recirculation, vortex interaction and instability, and

mixing enhancement/suppression as well as stagnation zones; this is shown schematically

in Figure 4. Indeed, it is expected that jet Re approaches 90,000, while the plenum Re

ranges from 24,000 to 3×10^6, depending on location within the plenum [McEligot and

McCreery, 2004]. The lower Re is near the outer periphery of the LP, while the highest

Re is near the exit. The Mach number (Ma) is on the order of 0.01, so the flow is incompressible. Not only is the flow highly turbulent, but due to the number of obstructions and jet-to-jet interaction, the flow is anisotropic. In summary, it is believed that the LP is a region where complex heat, mass, and momentum transfer will occur, resulting in an intricate, phenomena-rich domain that requires advanced, multiphysics simulation tools.

Fuego has recently undergone key validation and verification (V&V) studies that include:

1. Conventional jet

2. Swirling jet

3. Conventional jet in crossflow

4. Swirling jet in crossflow

5. Flow around a vertical cylinder

6. Central recirculation zone (CRZ) formation, and

7. Staggered tubes in crossflow (*see* Section 5.2   Fuego Validation and Verification (V&V)).

The motivation for this work is to reduce the likelihood of forming hot spots and stratification in LP. This is approached by using swirling jets whose principal purpose is to enhance mixing and minimize the impingement of the hot helium exiting the coolant channels in the reactor core on the bottom LP plate.

The mixing and heat transfer properties of conventional impinging jets are well-known [Celik and Eren, 2007]. An excellent review of heat transfer for conventional impinging jets was compiled recently [Jambunathan *et al*., 1992]). By adding swirl to the

jets, additional mixing and heat transfer has been noted [Huang and El-Genk, 1994; Huang and El-Genk, 1998; El-Genk and Huang, 1999; Cziesla *et al*., 2001; Merci and Dick, 2003; Bilen *et al*., 2002; Nozaki, Igarashi, and Hishida, 2003; Larocque, 2004; Wang and Bai, 2004; Wen, 2004]. These results are realized through reducing the axial momentum, while increasing the angular momentum of the exiting helium jets [Rodriguez and El-Genk, 2008a, b, c, and d; Rodriguez, Domino, and El-Genk, 2010; Rodriguez and El-Genk, 2010a and b; Rodriguez and El-Genk, 2011a and b]. The acquired azimuthal velocity of the swirling jets increases the entrainment of the surrounding helium, causing the velocity field to spread radially as the jet travels away from its origin.
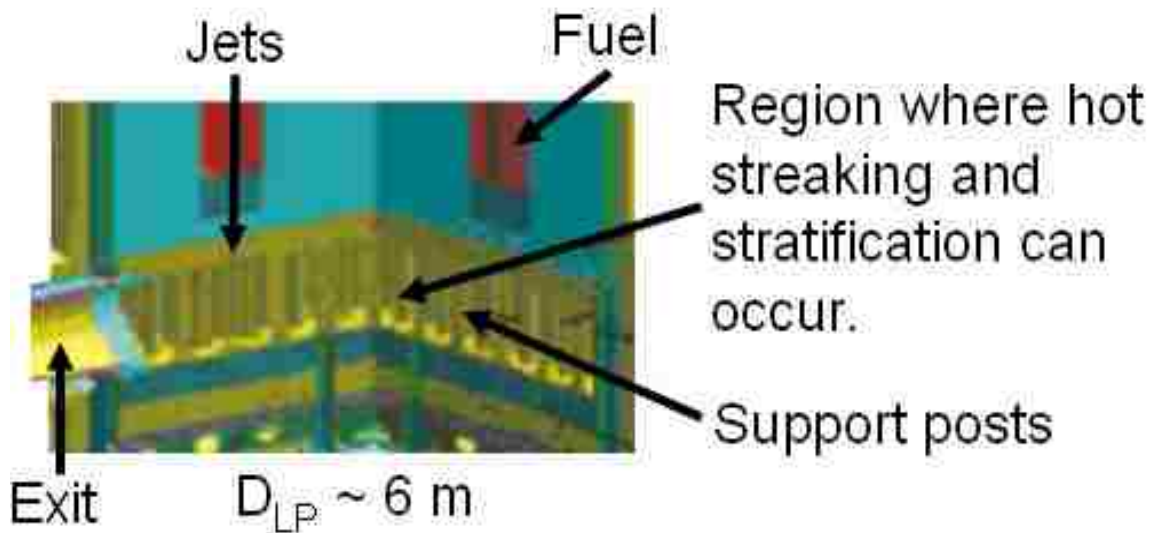
Figure 1. Cut-Away View of the LP in a Prismatic Core VHTR [Johnson, 2008; McEligot and McCreery, 2004].
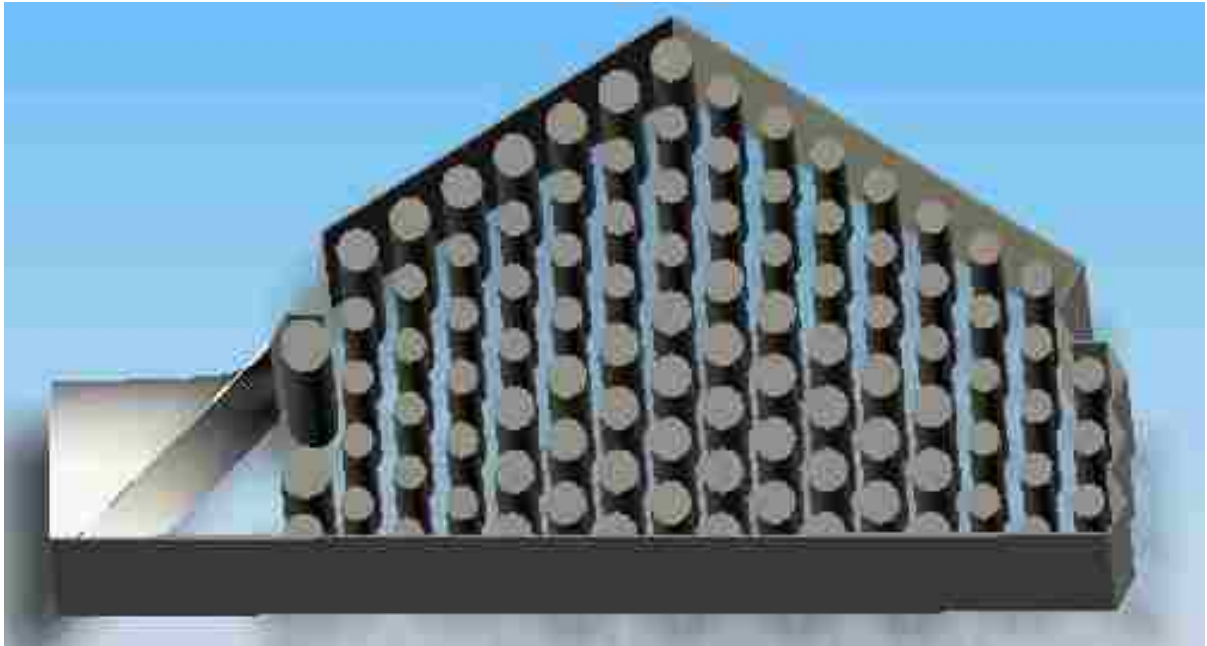
Figure 2. Half-Symmetry, Top View of the LP with Support Posts.
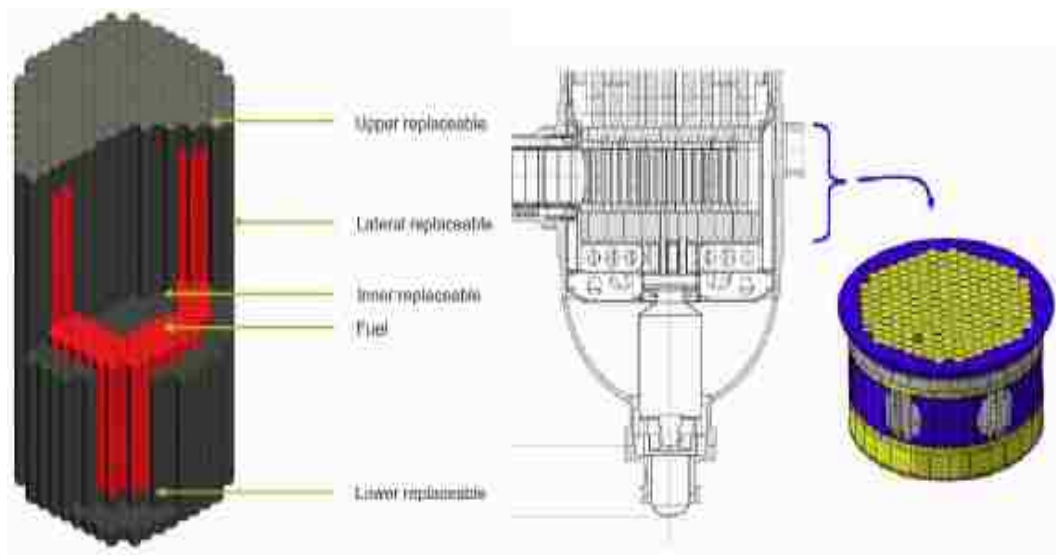
Figure 3. Graphite Stacks (LHS), Core Meridian Cross-Section (Middle), and LP (RHS) [INL, 2007].

The acquired azimuthal momentum also weakens the impingent of the hot helium jets onto the bottom plate in the VHTR LP, thus reducing the likelihood of hot spots. These

improvements in performance and operation of VHTRs are possible by altering the nature of the hot helium flow exiting the coolant channels; basically, the VHTR core coolant channel exits are modified from conventional to swirling jet.

Recent theoretical studies and experiments have been reported which investigated free conventional [Celik and Eren, 2007] and swirling jets for mass and heat transfer applications [Huang and El-Genk, 1994; Huang and El-Genk, 1998; El-Genk and Huang, 1999; Cziesla *et al*., 2001; Bilen *et al*., 2002; Merci and Dick, 2003; Nozaki, Igarashi, and Hishida, 2003; Larocque, 2004; Wang and Bai, 2004; Wen, 2004; Rodriguez and El-Genk, 2008a, b, c, and d; Rodriguez, Domino, and El-Genk, 2010; Rodriguez and El-Genk, 2010a and b; Rodriguez and El-Genk, 2011a and b]. However, investigations of the flow fields of single and multiple swirling hot gas jets at the temperatures of interest in VHTRs are limited [Kim, Lim, and Lee, 2007; Lavante and Laurien, 2007; Rodriguez and El-Genk, 2008a, b, c, and d; Laurien, Lavante, and Wang, 2010; Rodriguez, Domino, and El-Genk, 2010; Rodriguez and El-Genk, 2010a and b; Rodriguez and El-Genk, 2011a and b]. Unlike liquids, the dynamic viscosity of gases increases with temperature, while stabilizing the flow field. Viscosity also affects the flow mixing and the entrainment of surrounding gas into the flow field of a swirling jet. The flow field involving multiple swirling jets is therefore very complex.

Of particular interest to VHTR operation and safety is to quantify the effects of crossflow and obstructions by the support posts on the flow field (Figure 4). Independent investigations of the LP flow field are sparse as of 2010 [McIlroy, H. M. *et al*., 2006a; Guillen and McIlroy, 2007; McIlroy, McEligot, and Pink, 2007; McIlroy, McEligot, and

6

Pink, 2008a and b; Johnson, 2009a and b; Johnson and Schultz, 2009; McIlroy, McEligot, and Pink, 2010a and b; Rodriguez and El-Genk, 2010a].
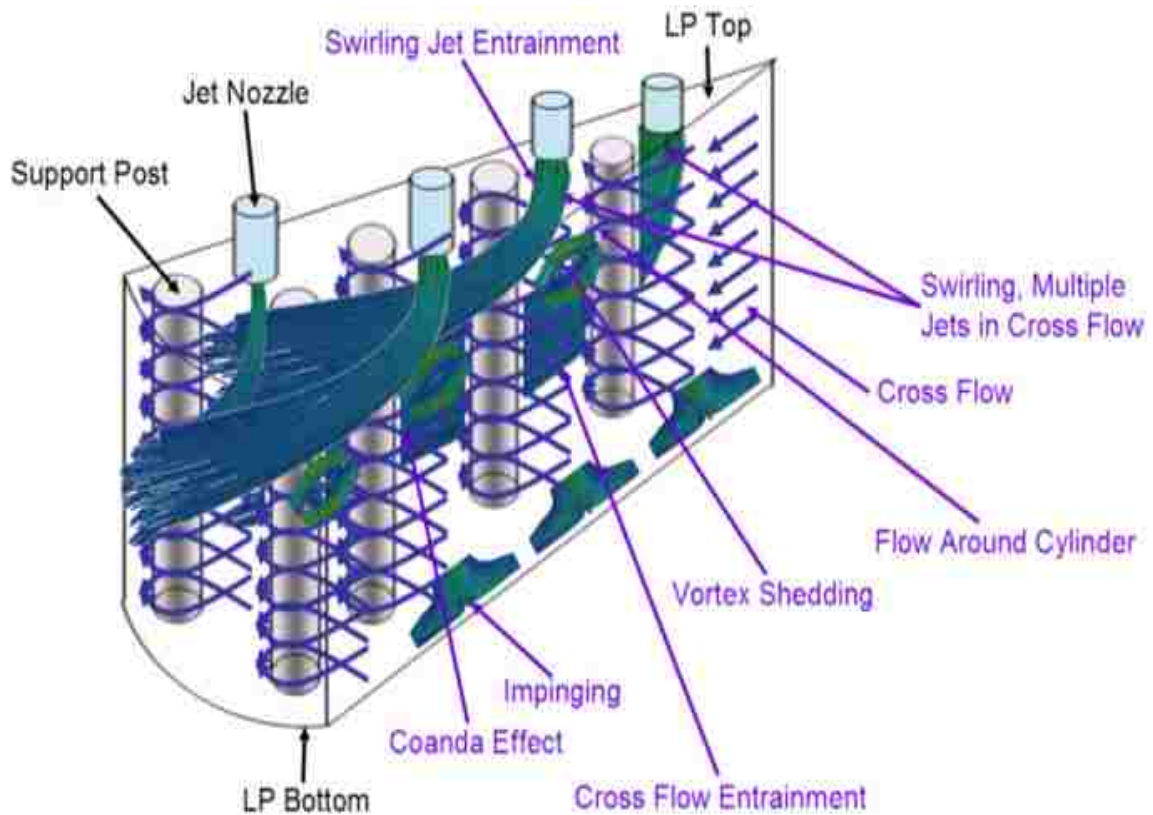
Figure 4. Key Flow Regimes in the LP of a Prismatic Core VHTR.

1.2 Objectives

The objectives of the work presented herein is to investigate the potential of using swirling jets at the exit of the coolant channels in a prismatic core VHTR to minimize the formation of hot spots in the bottom plate and to enhance flow mixing in the LP chamber. The effects of changing the swirl number (S), central recirculation zone formation (CRZ), swirl decay, and the rotation direction of the swirling jets will also be investigated.

The premise of this research is that the adverse effects from the LP hot spots and thermal stratification can be mitigated significantly by more effectively distributing the

heat and enhancing the mixing of the helium gas. In particular, it is postulated that the hot spots and thermal stratification can be significantly mitigated by replacing the conventional jets with static, swirling jets.

Increased turbulence is associated with higher heat transfer for impinging jets [Gardon and Akfirat, 1965]. Researchers have recently shown that increasing S increased the turbulent viscosity, the turbulent kinetic energy, the length scales, and the degree of anisotropy [Abujelala, Jackson, and Lilley, 1984]. In some cases, turbulent viscosity nearly doubled [Abujelala, Jackson, and Lilley, 1984]. Comparison of experiments for a weakly swirling jet (S~0.23) and a conventional jet showed that all the Re stresses and turbulent kinetic energy balances for the swirling jets were 30 to 100% larger the conventional jets [Toutiaei, Semaan, and Naughton, 2010]. Their research also showed that swirling jets had larger production, mean convection, and turbulence transport than the conventional jet. Finally, the swirl field has been noted to increase turbulence and entrainment of the adjacent, colder fluid [Blevins, 1992; El-Genk and Huang, 1995, 1999; Ligrani and Oliveira, 2003; Senda *et al*., 2005].

It is therefore hypothesized that the swirling motion enhancements will translate to net gains in mixing and heat transfer in the complex LP flow field, while at the same time result in manageable pressure losses for well-designed swirl generators. The optimized swirl generators ought to produce a spinning gas vortex that extends onto regions that are relatively colder. As the gas is entrained at the periphery of the vortex, it ought to experience a higher degree of turbulence from the swirling motion, as opposed to just having an axial and radial motion [Larocque, 2004]. Furthermore, Larocque showed that there was a recirculation zone between the jet plume adjacent to the wall, where a

recirculation pattern formed and broke the thermal boundary layer near the wall, thus increasing the heat transfer.

Because of the complex geometry and thermalhydraulic conditions of the proposed LP design, there currently exists no integral, full-scale experiment data set. To build a full-scale experiment at prototypic thermalhydraulic conditions would require multiple millions of dollars. However, there are numerous, single-effect experiments of key phenomena found in the LP. Thus, the validity of this research's premise can be demonstrated through a set of carefully-chosen validation and verification (V&V) computational fluid dynamics (CFD) simulations of key, single-effect LP phenomena [McEligot, D. M. *et al*, 2005; Johnson, 2009a]. Details of the key V&V single-effect thermalhydraulic phenomena are found in Table 6 of Section 5.2.

In brief, the proposed research aims to extend the current level of knowledge of heat transfer and mixing enhancement via swirling jets, to extend swirling jet theory (including CRZ formation), and to apply that knowledge to enhance the safety and design of the LP. In particular, it is the goal of this research to better understand and interrelate how mixing and heat transfer of swirling jets depends on S, Re, the CRZ, and swirl decay—and ultimately how this knowledge can increase nuclear reactor safety and design.

2. BACKGROUND

2.1 Very-High Temperature Reactors

There is currently much interest in the development of advanced reactors known as NGNPs. The NGNP is a Generation IV reactor that is being researched by the DOE, universities, national laboratories, commercial enterprises, as well as international corporations and entities [Wikipedia, 2010a; World Nuclear News, 2010]. NGNPs are currently envisioned as VHTRs whose purpose includes the production of hydrogen, generation of electricity at competitive rates, and the supply of process heat [MacDonald *et al.*, 2003; Allen, 2004; Burchell, Bratton, Windes, 2007; DOE, 2008; Petti, 2008; NRC, 2008; INL, 2009; Kinsey, 2010; ORNL, 2010; Wikipedia, 2010a; World Nuclear News, 2010]. Leading reactor designs include the prismatic core reactor (Figure 5) and the pebble bed reactor (Figure 6) [DOE, 2008; Petti, 2008; Johnson, 2008; NRC, 2008; INL, 2009]. As of the February 2011, both designs are still being pursued, with the pebble bed design being led by Westinghouse and the prismatic core being led by General Atomics [World Nuclear News, 2010].
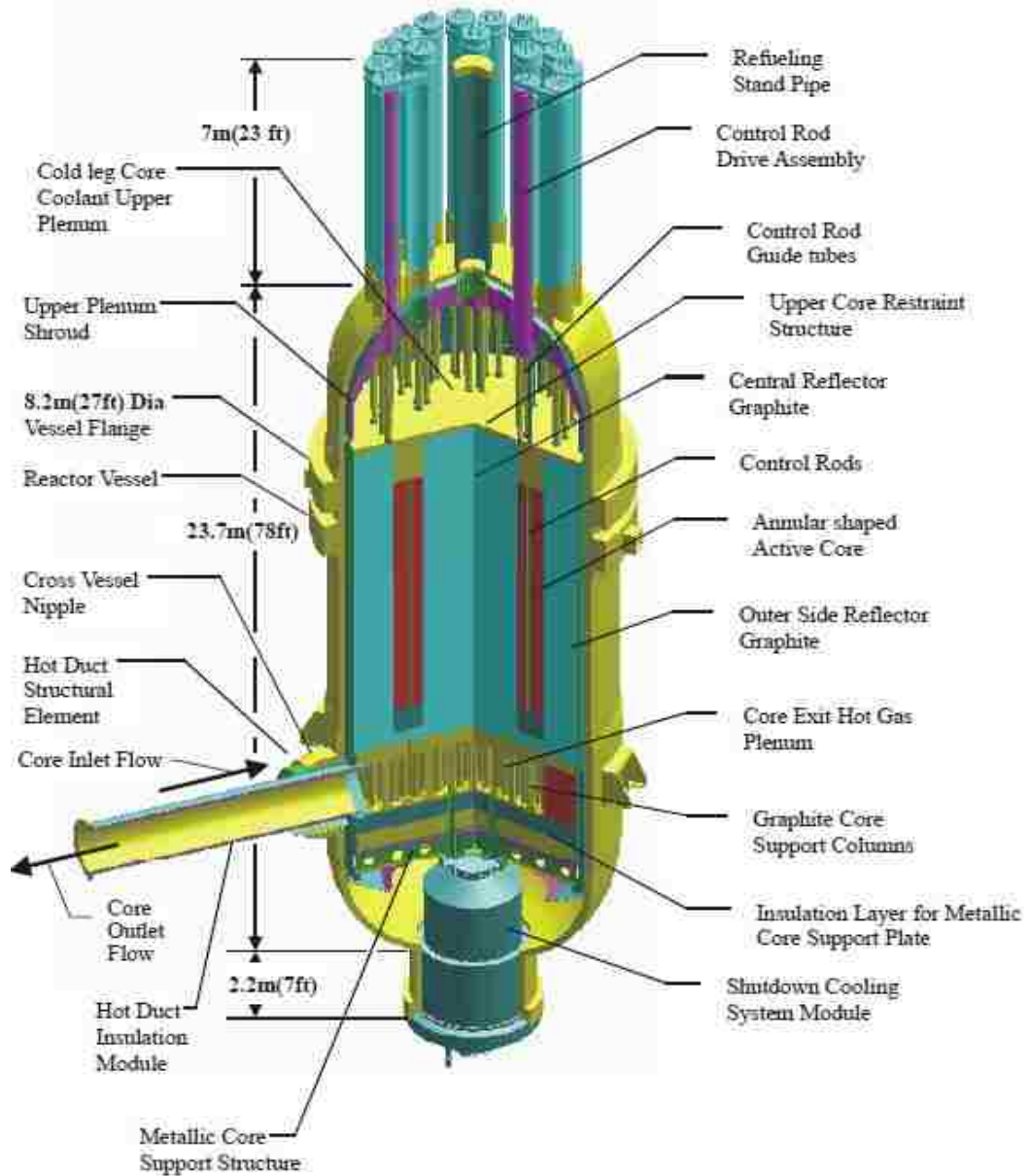
Figure 5. Prismatic Core GT-MHR [MacDonald *et al.*, 2003].
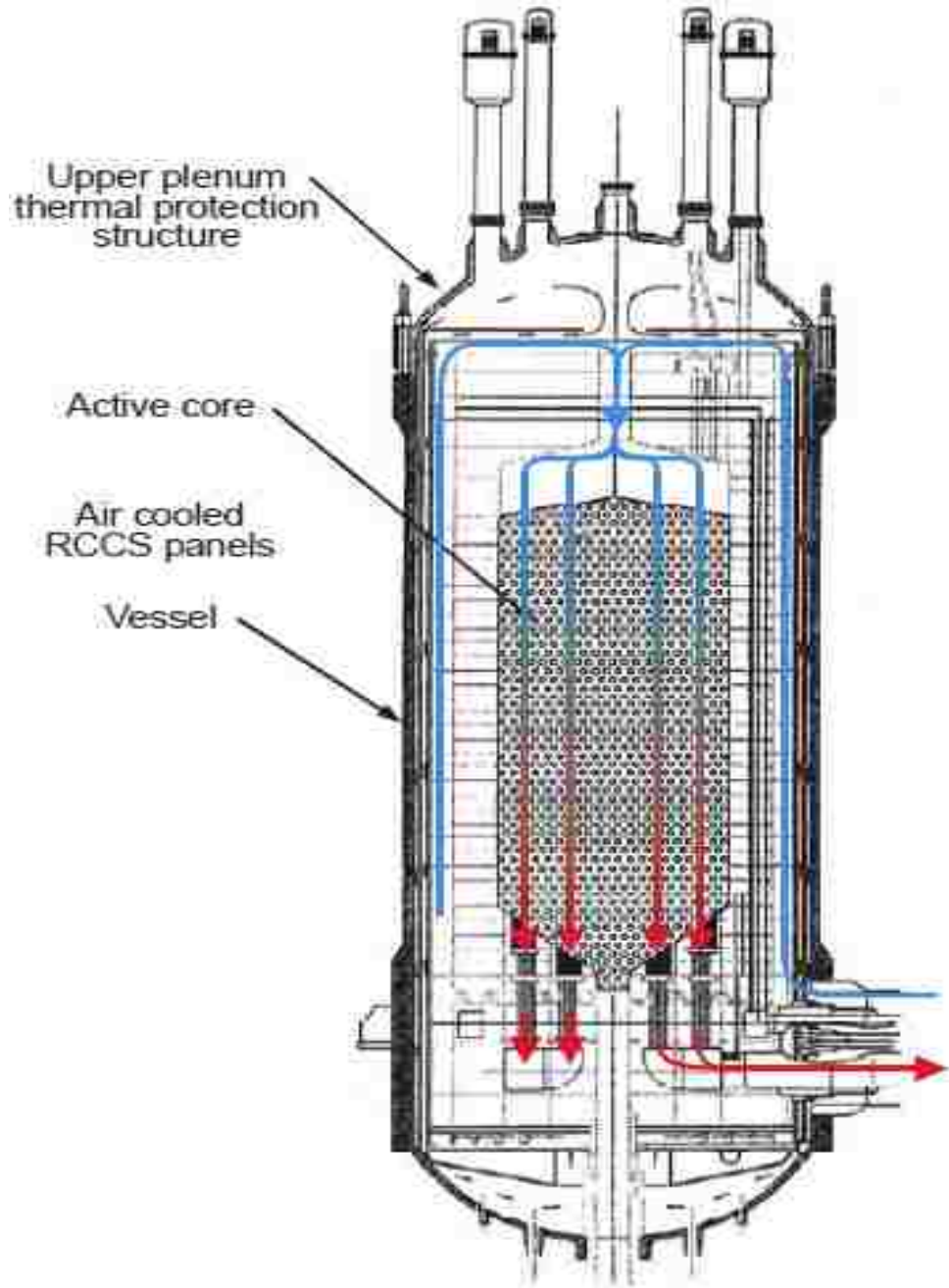
Figure 6. Pebble Bed Core [Schultz *et al.*, 2004].

Both proposed VHTR designs use enriched uranium dioxide spherical kernels that are approximately 0.5 mm in diameter. The fuel kernels are coated and sealed with pyrolytic carbon, silicon carbide, and porous carbon (Figure 7) [Matzner, 2004]. The coated fuel kernels are known as tristructural-isotropic (TRISO) particles, and have a diameter of

approximately 0.92 mm. For the prismatic core, the TRISO particles are agglomerated

into cylindrical fuel compacts, which are then placed into 1,020 hexagonal graphite

blocks that are assembled side by side to form the core [INL, 2007] (Figure 8). For the

pebble bed core, the TRISO particles are agglomerated into 60 mm fuel spheres (also

known as pebbles). Thus, a 300 MWth pebble bed core consists of approximately

462,000 pebbles that are stacked to form the core, as shown conceptually in Figure 9.

The average packing fraction for the pebble bed core is estimated at 61 to 64 [Schultz *et

al.*, 2004]. Both cores consist of an annular fuel region that is surrounded and moderated

by graphite and cooled by downward-flowing helium.
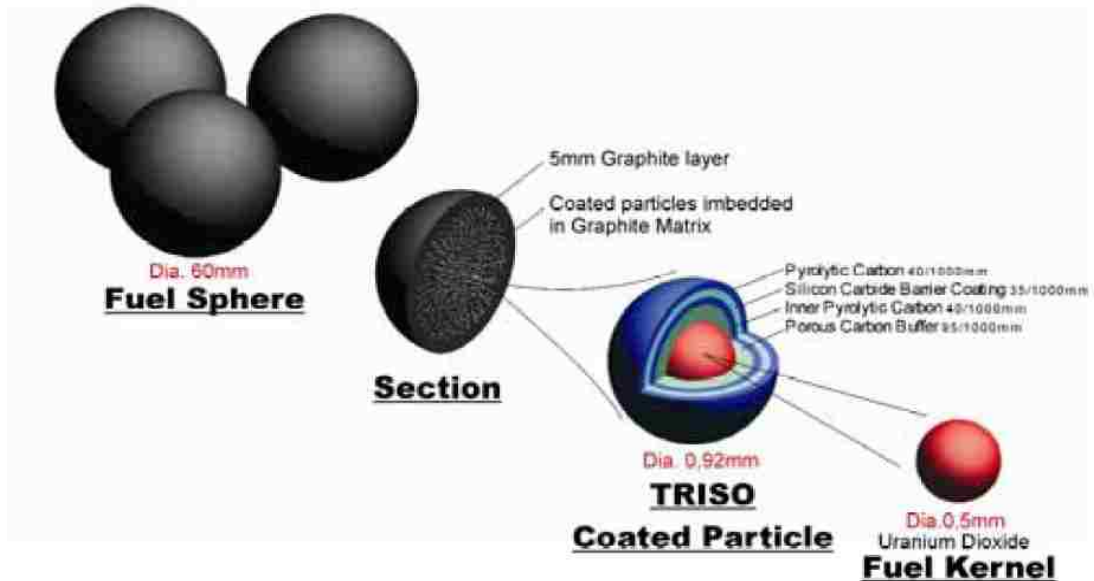
Figure 7. TRISO Particles and Fuel Spheres [Matzner, 2004].
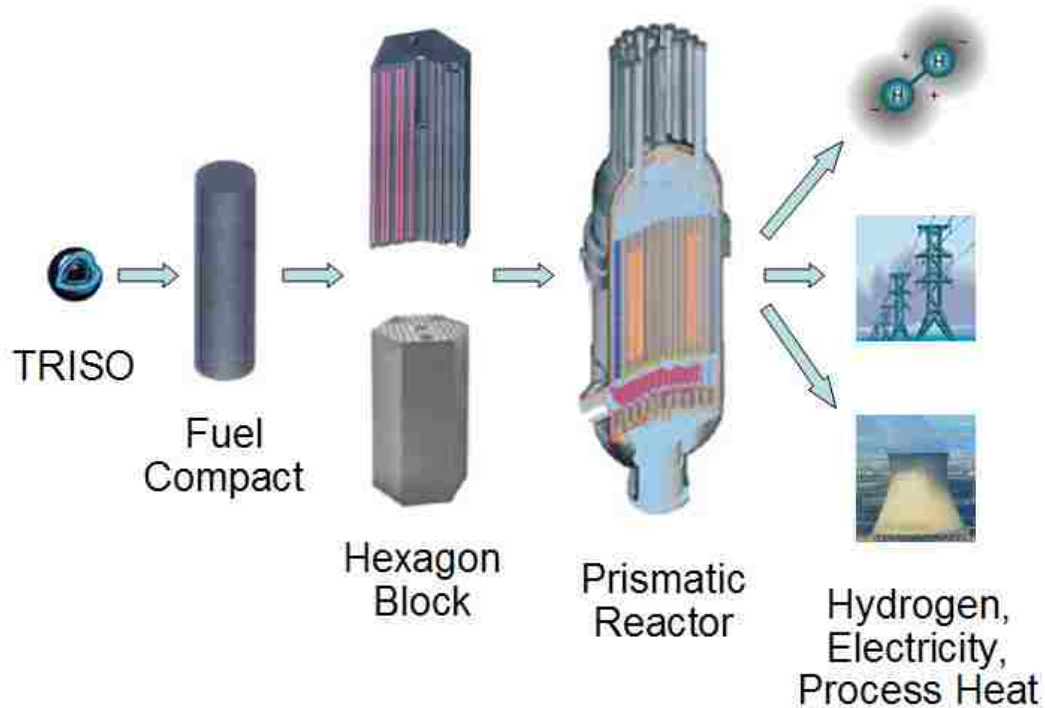
Figure 8. Conceptual Scheme for the Prismatic Core Reactor.
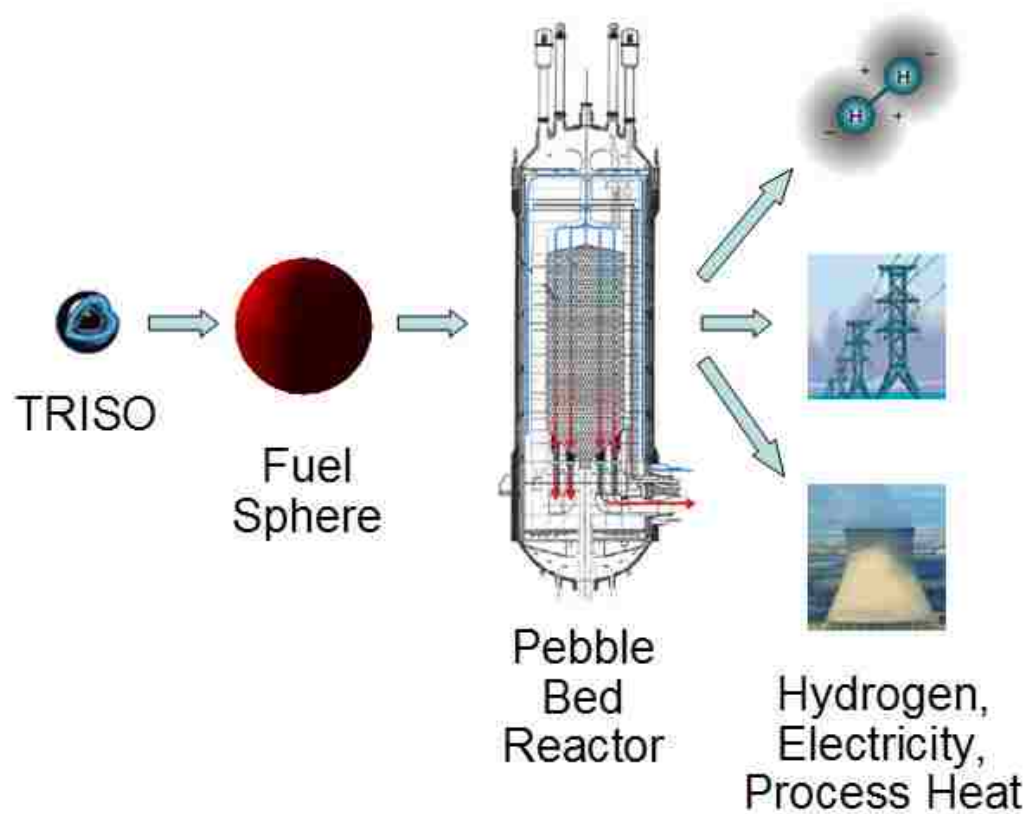
Figure 9. Conceptual Scheme for the Pebble Bed Reactor.

A schematic of a typical plant layout for the cogeneration of electricity and hydrogen using a thermo-chemical sulfur-iodine (SI) process is shown in Figure 10, which includes the nuclear reactor and the primary helium loop, a secondary loop for the production of electricity, and for providing thermal energy for the production of hydrogen [Rodriguez *et al*., 2009].

The plant may employ either a pebble bed or a prismatic core. However, due to the pebble bed reactor's tendency to form graphite dust [INL, 2007], the possibility of adverse reactivity insertions as a result of adverse pebble stacking [Schultz *et al*., 2004], and other safety issues, it appears likely that the prismatic core will be chosen for production by the DOE. For example, a net sudden change of just 3% in the packing fraction may result in "significant reactivity transients" [Schultz *et al*., 2004]. Furthermore, the US has experience primarily for the prismatic core, e.g. the Fort St. Vrain gas-cooled reactor and GA's GT-MHR model design [MacDonald *et al*., 2003]. *Consequently, this research will hereafter focus solely on the prismatic core VHTR.*
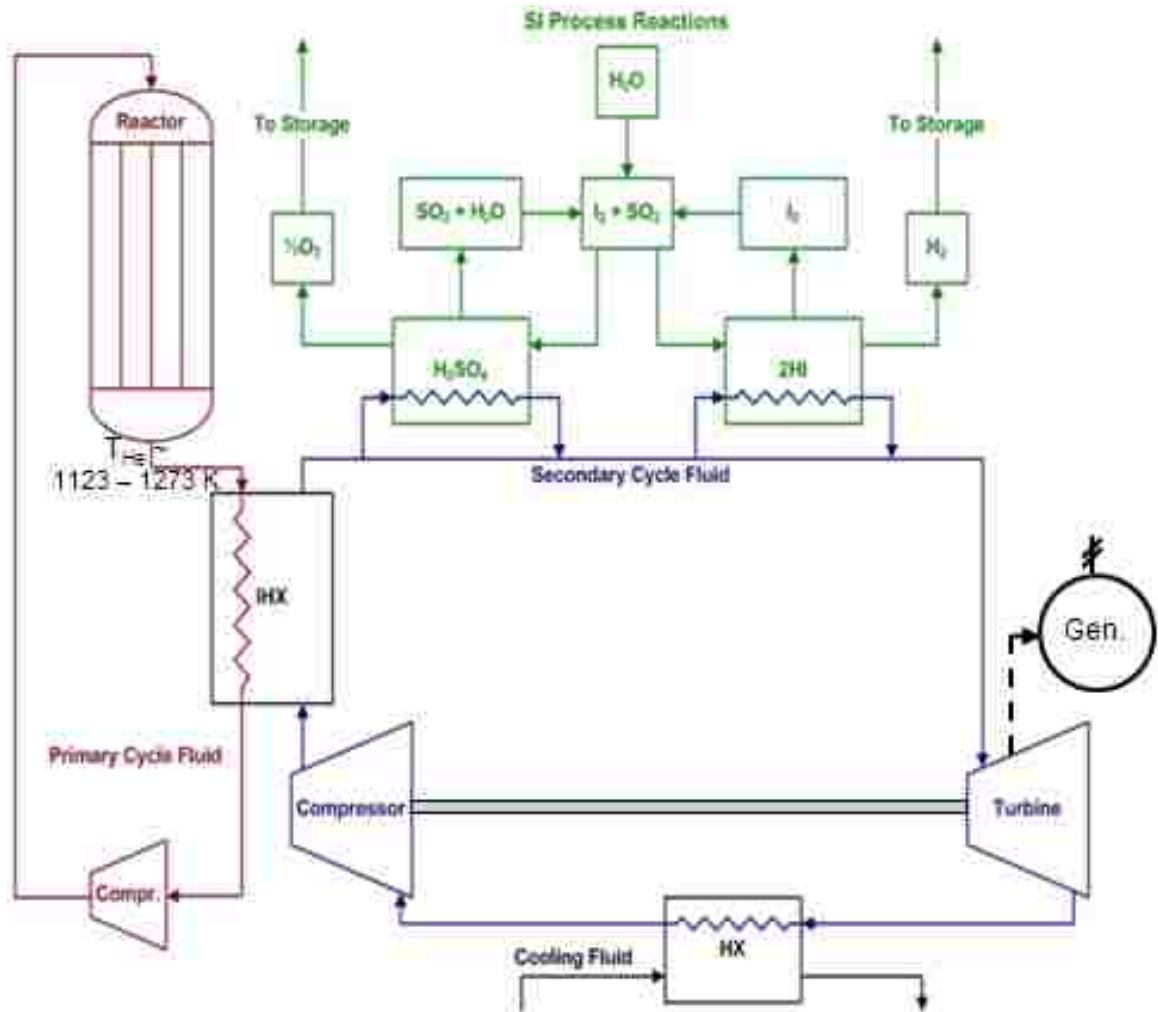
Figure 10. Fully-Coupled VHTR System with Primary, Secondary, and Chemistry Loops.

The prismatic core design is based on research from the General Atomics gas turbine

modular helium reactor (GT-MHR) [McEligot and McCreery, 2004; Rodriguez *et al.*,

2009; INL, 2009]. About 2/3 of the graphite blocks function as the inner and outer

reflectors, while the rest form the annular fuel core (Figure 11) [MacDonald *et al.*, 2003].

The blocks have a total of 108 flow channels per hexagonal block for cooling of the core

(the small, white circles shown in Figure 12) [MacDonald *et al.*, 2003]. Figure 13 shows

a High-Temperature Test Reactor (HTTR) hexagonal fuel block as it is being machined.

16

The prismatic core fuel and graphite are cooled by helium flowing in the downward direction at a mass flow rate of 226 kg/s for the 600 MWth design. Note that as the helium flow channels exit the core and reach the LP, the gas behaves as a conventional jet. The hexagonal blocks are stacked up to 10 blocks high, with studies showing that there is xenon stability in the radial, axial, and azimuthal directions for a 600 MWth core [MacDonald *et al*., 2003]. The fuel kernels are enriched to 10.4wt% U^{235} for the fresh core, and to as much as 12 to 15% during refueling [MacDonald *et al*., 2003]. The design uses B_4C burnable poison rods distributed throughout the core [MacDonald *et al*., 2003]. The power density is about 6.5 W/cm^3. The reactor has a power level on the order of 600 to 800 MWth, with an inlet temperature of 763 K, and a mean outlet temperature of 1,273 K [MacDonald *et al*., 2003].

The VHTR prismatic design has many desirable safety features. For example, helium is a single-phase, inert gas. Further, the TRISO fuel can withstand high temperatures (1,873 K during emergency conditions), and have low fission product release, while the graphite moderator is also a high-temperature material with a long thermal response time [MacDonald *et al*., 2003; MacDonald, 2004; Buckthorpe, 2009]. The core has both negative Doppler and isothermal thermal temperature coefficients [MacDonald *et al*., 2003; MacDonald, 2004; Southworth *et al*., 2004]. Furthermore, the prismatic core has a relatively low power density compared to pressurized water reactors (PWRs) [MacDonald *et al*., 2003]. The VHTR also includes passive decay heat removal [MacDonald, 2004].
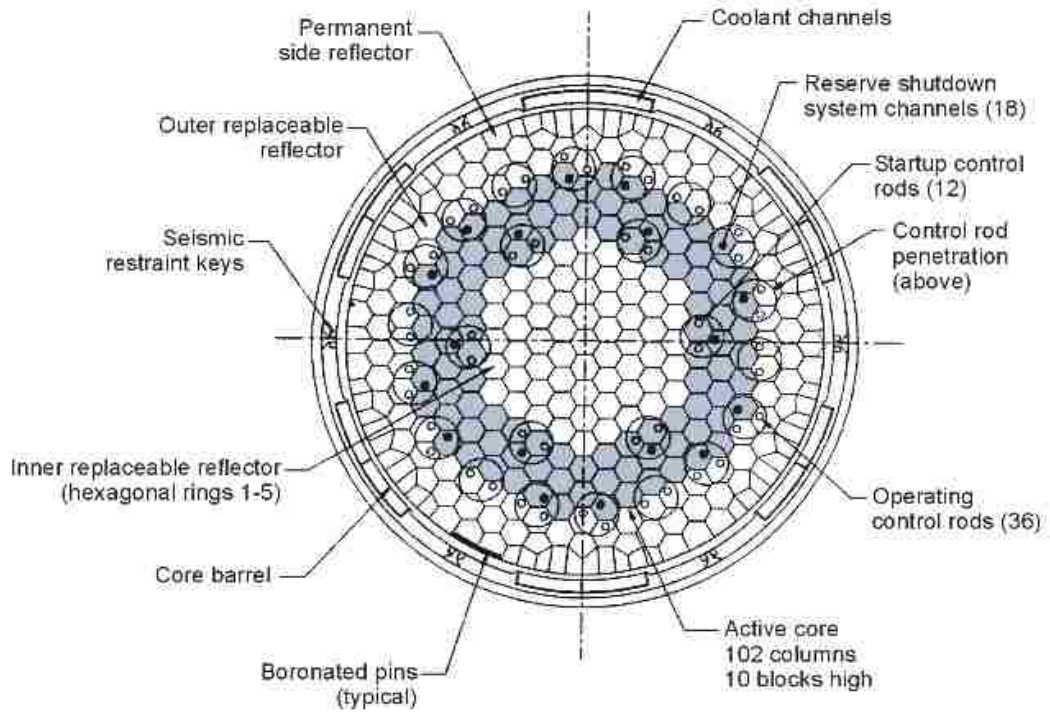
Figure 11. Prismatic Core Cross-Section [MacDonald, 2004].

Figure 12. Hexagon Block Cross-Section [INL, 2007].

18

Figure 13. Hexagon Block Being Machined [Burchell, Bratton, Windes, 2007].

Table 1summarizes key prismatic core VHTR attributes. The low and high best-estimate cost for the NGNP is expected to be on the range of 3.8 to 4.3 billion dollars, with start-up and testing occurring between 2016 and 2018 (Table 2); of course, the period of performance estimates were made a few years ago, and are highly unlikely as of 2011.

Table 1. Summary of Key VHTR Prismatic Core Attributes [MacDonald *et al.*, 2003; MacDonald, 2004; Southworth *et al.*, 2004; Schultz *et al.*, 2004; INL, 2007].

Parameter / Attribute	Value / Description
Power	600 – 800 MWth
Power density, ave.	6.5 W/cm^3 (vs. 105 for a PWR [Todreas and Kazimi, 1990])
Thermal efficiency	48% (Direct cycle) (~33.5 for a PWR [Todreas and Kazimi, 1990])
Core design	Hexagonal graphite blocks, stacked to about 10 blocks high; annular configuration
Coolant mass flow rate	226 kg/s for 600 MWth; 448 kg/s for 840 MWth
Bypass flow fraction	10 to 25%
Coolant pressure	7.12 MPa
Core pressure drop	0.0476 MPa
Core inlet temperature	673 K
Core outlet temperature	1,123 – 1,273 K
Reactor design lifetime	60 years
Fuel	U^{235} enriched between 10.4 and 15 wt%; PyC or SiC. (~2.6 for a PWR [Todreas and Kazimi, 1990])
Fuel maximum normal operating temperature	1,523 K for SiC coated; 1,673 K for ZrC coated
Fuel burnup	110,000 MWd/ton
Number of loops	2
Primary coolant	Helium
Moderator	Graphite
Control rods	B$_4$C
Upper plenum	Carbon-carbon composite
Lower plenum	Similar to GT-MHR design, but with more insulation.
Intermediate heat exchanger	Printed circuit heat exchanger,

Parameter / Attribute	Value / Description
	In617
Secondary coolant	Helium
Power conversion	Direct (Brayton cycle gas turbine); Direct/indirect (combined cycle)
Hydrogen production	60 MWth, SI cycle; 5 MWth, high-temperature electrolysis
Production cost of hydrogen	$2.5/kg
Electricity production cost	$60/MWh

Table 2. Best-Estimate Cost and Schedule for Building the NGNP [INL, 2007].

Task	Best-Estimate Cost, in Millions of Dollars		Period of Performance (FY)
	Low	**High**	
Conceptual Design	169	191	08 – 09
Preliminary Design	270	305	10 – 11
Final Design	468	530	11 – 13
Licensing	129	146	8 – 18
R&D	479	542	7 – 18
Construction	1,772	2,005	13 – 16
Start-up and Testing	205	232	16 – 18
Project Support	308	349	8 – 18
Total	**3,800**	**4,300**	**Range 07 – 18**

Despite its great potential, the high operation temperature of presents structural, operational, and safety challenges [Johnson, 2008]. Of particular concern in the prismatic core VHTR are the "hot spots" in the bottom plate and thermal stratification of the helium coolant in the LP. The hot spots are caused by the impingement of the hot helium jets exiting the reactor core at > 60 m/s onto the bottom plate. The thermal stratification, however, is caused by the poor mixing of the helium coolant in the LP, and can be aggravated under some circumstances by the obstruction of the graphite support posts (Figure 4). The issues were corroborated in this study, as well as independent studies (e.g., *see* [Johnson and Schultz, 2009] where Figure S-4 of the cited report shows approximately a factor of eight decrease in both the experimental and calculated velocity as the approaching gas flows around the first support post on the left hand side).

2.2   Axisymmetric Swirling (Vortex) Jets

The concept of enhancing heat transfer and mixing via swirling jets has been known for nearly seven decades, and many practical applications are currently being made. Among these are

- Combustion [Syred and Beer, 1974; Khalil, Spalding, and Whitelaw, 1975; Lilley, 1977; Huang, 1996; Qi, Gupta, and Lewis, 1997; Paschereit, Gutmark, and Weisenstein, 1999; Schluter, 2001; Li, 2004; Vanoverberghe, 2004; Duwig *et al.*, 2005; Li and Gutmark, 2006; Paschereit, Flohr, and Gutmark, 2006; Nirmolo, 2007; Yongqiang, 2008; Valera-Medina, 2009; Stein, 2009],

- Medical applications [Atvars, Thompson, and Hourigan, 2009],

- Electrochemical mass transfer [Arzutug and Yapici, 2009],

- Metallurgy [Bilen *et al*., 2002; Chung, Luo, and Sandham, 2002; Tong, 2003; Vanoverberghe, 2004],

- Fire modeling [Chuah and Kushida, 2007],

- Propulsion nozzles [Knowles and Carpenter, 1988; Knowles and Carpenter, 1990],

- Aircraft design and safety [Batchelor, 1964; Kavsaoglu and Schetz, 1989; Rusak and Lamb, 1999; Pandya, Murman, and Sankaran, 2003; Nelson, 2004; Whitehead, 2009],

- Quieter air transport [Shah, Mobed, and Spakovszky, 2007],

- Helicopter blades [Scully, 1975; Zioutis *et al*., 2010],

- Rocket engines [Fu, Yang, and Wang, 2010],

- Propeller design [Chattot, 2000],

- Heavy particle motion [Marcu, Meiburg, and Newton, 1994],

- Cooling of high-power electronics and computer chips [King, c. 2005],

- Diesel engines and compressed natural gas engines [Mardani, 2004; Jagus *et al*., 2008],

- Turbines and combustors (e.g., three air passages, each with its own swirler device) [Chattot, 2006; Li and Gutmark, 2006],

- Various types of turbines [Eldrainy, Ahmad, and Jaafar, 2009],

- Vortex whistle in gas turbines [Kurosaka, 1981],

- Nuclear reactor applications [Kim, Lim, and Lee, 2007; Lavante and Laurien, 2007; Nematollahi and Nazifi, 2007; Johnson, 2008; Rodriguez and El-Genk, 2008a, b, c, and d; Rodriguez, Domino, and El-Genk, 2010; Rodriguez and El-

Genk, 2010a and b; Rodriguez and El-Genk, 2011a and b; Laurien, Lavante, and Wang, 2010],

- Wind tunnels [Wigeland, Ahmed, and Nagib, 1978],

- Atomizers, fluidized beds [Chang, Wan, and Chen, 1997],

- Droplets, sprays, cyclone dust separators [Taylor, 1950; Aggarwal and Park, 1999; O'Doherty *et al.,* 1999; Sivakumar and Raghunandan, 2002; Salewski and Fuchs, 2005; Moon, Abo-Serie, and Bae, 2007; Fuchimoto *et al*., 2009; Kenny *et al*., 2009],

- Weather modeling (including tornadoes, dust devils, whirl pools, and hurricanes) [Richardson, 1922; Hall, c. 1966; Al'tshul' and Margolin, 1970; Shteirn and Drazin, 2000; Batterson, Maicke, and Majdalani, 2007Aboelkassem and Vatistas, 2007],

- Hair blowers [Kullen, 1987],

- Improved pizza ovens [Ovadia, 2001], and

- A swirling oscillation coffee maker [Richter, 1999].

There is also a patent for a swirl generator with axial vanes that are described mathematically with sinusoids, and whose purpose is to gradually generate swirling flow such that pressure drop and turbulence intensity is minimized [Yang and Chen, 1993]. Evidently, the applications are indeed quite numerous, and only limited by imagination (*see* Figure 14)!
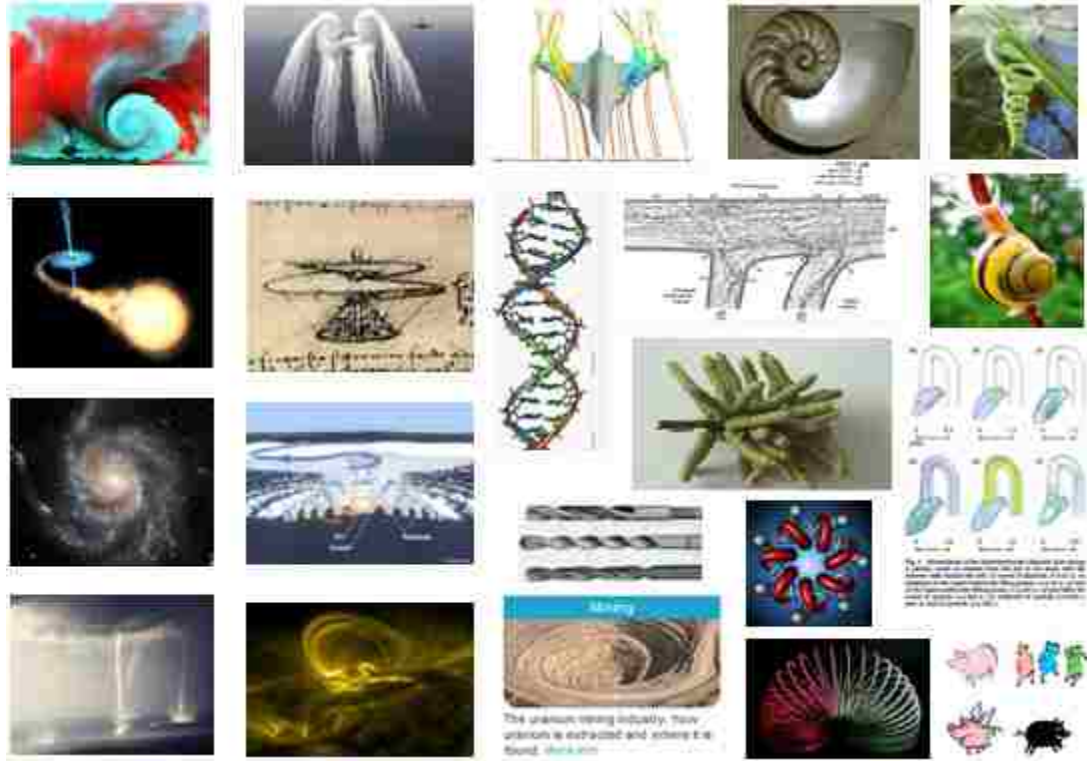
Figure 14. The Wide Variety of Vortices in Nature and Man-Made Applications.

Perhaps the largest degree of swirl research, as attributed by volume of papers found in the literature, is in the area of combustion. Lilley did an excellent job summarizing early combustion research [Lilley, 1977].

Recent theoretical studies and experiments have been reported which investigate conventional and swirling jets for mass and heat transfer applications [Huang and El-Genk, 1994, Huang, 1996; 1998; El-Genk and Huang, 1999; Cziesla *et al*., 2001; Merci and Dick, 2003; Larocque, 2004; Wang and Bai, 2004; King, c. 2005; Rodriguez and El-Genk, 2008a, b, c, and d; Rodriguez, Domino, and El-Genk, 2010; Rodriguez and El-Genk, 2010a and b; Rodriguez and El-Genk, 2011a and b]. However, investigations of the flow fields for multiple conventional and swirling hot gas jets at the temperatures of interest in VHTRs are limited [McEligot and McCreery, 2004; Lavante and Laurien,

2007; Rodriguez and El-Genk, 2008a, b, c, and d; Rodriguez, Domino, and El-Genk, 2010; Rodriguez and El-Genk, 2010a and b; Rodriguez and El-Genk, 2011a and b; Laurien, Lavante, and Wang, 2010]. Unlike liquids, the dynamic viscosity of gases increases with temperature, while stabilizing the flow field. Viscosity also affects the flow mixing and the entrainment of surrounding gas into the flow field of a swirling jet. The kinematic viscosity for air and helium are, respectively,

$$\nu_{air} = 1.37 \text{x} 10^{-9} T^{1.645} \tag{1}$$

and

$$\nu_{He} = 1.06 \text{x} 10^{-8} T^{1.645} \tag{2}$$

Figure 15 shows that there is a significant effect of temperature on gas viscosity, especially for helium.
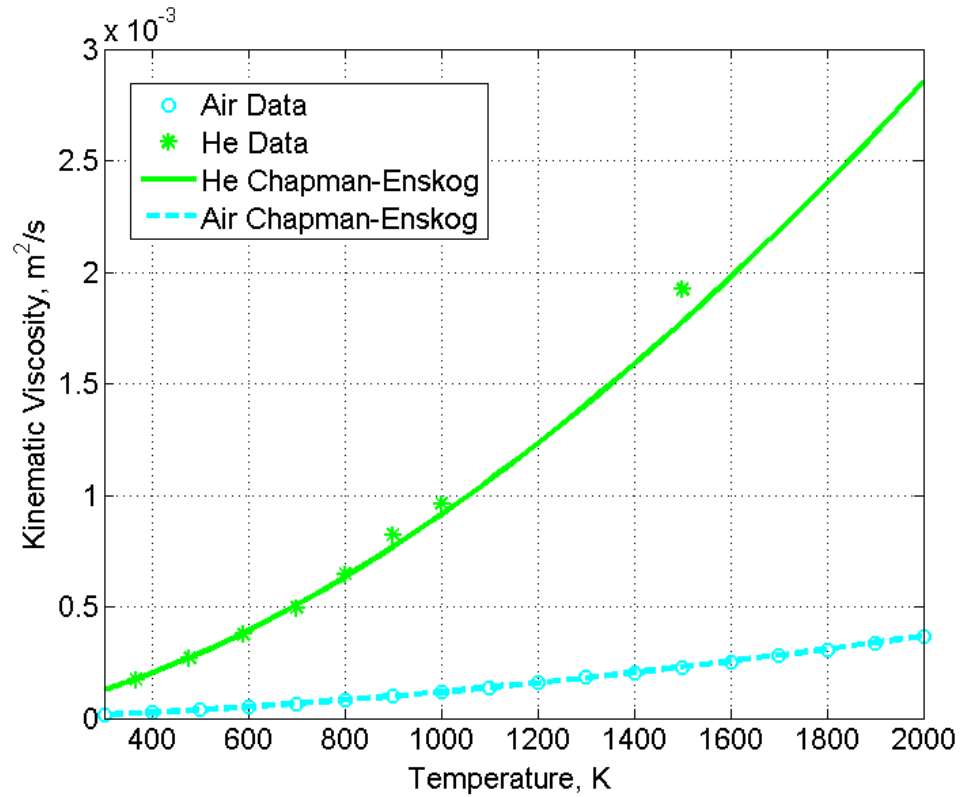
Figure 15. Kinematic Viscosity of Helium and Air as a Function of Temperature.

Modern research of swirling flow began with a simplified, 1D, axisymmetric steady-state flow that was investigated a little over 150 years ago [Rankine, 1858]. The first theoretical, axisymmetric, transient swirling flow in 1D was investigated 74 years later [Lamb, 1932]. The first published experimental work for swirling jets was conducted a few years later [Watson and Clarke, 1947]. It was not until 1948 that the first steady state, three velocity field of a 2D swirling jet was first investigated [Burgers, 1948]. Then, the theory of axisymmetric jets was significantly enhanced in the 1950s through a rigorous mathematical development [Loitsyanskiy, 1953; Blevins, 1992]. Thereafter, the investigation of swirling jets literally expanded exponentially. Among these are the classical experimental works that confirmed the theory laid out by Loitsyanskiy [Chigier and Chervinsky, 1967; Mathur and MacCallum, 1967], as well as theoretical derivation

27

for laminar swirling jets with free convection [Martynenko, Korovkin, and Sokovishin, 1985] and swirling jets with and without buoyant terms [Martynenko, Korovkin, and Sokovishin, 1989]. There are excellent recent reviews of vortices [Rossi, 2006].

In any case, the first laminar and turbulent theoretical solutions for 2D axisymmetric jets were derived by assuming small swirl perturbations and incompressible flow [Loitsyanskiy, 1953]. Loitsyanskiy obtained the following expressions for the radial, azimuthal, and axial velocity components,

$$u(\eta) = \frac{\alpha\sqrt{\nu}}{z} \frac{\alpha\eta\left(1 - \frac{\alpha^2\eta^2}{4}\right)}{\left(1 + \frac{\alpha^2\eta^2}{4}\right)^2},$$

(3)

where $\eta = \frac{1}{\sqrt{\nu}} \frac{r}{z}$.

$$v(\eta) = \frac{1}{z^2} \frac{\alpha\gamma\eta}{\left(1 + \frac{\alpha^2\eta^2}{4}\right)^2}$$

(4)

and

$$w(\eta) = \frac{2\alpha^2}{z} \frac{1}{\left(1 + \frac{\alpha^2\eta^2}{4}\right)^2}.$$

(5)

He also obtained the pressure as

$$p(\eta) = -\frac{2\gamma^2}{3} \frac{1}{\left(1 + \frac{\alpha^2\eta^2}{4}\right)^3} \frac{1}{z^4}.$$

(6)

Note that swirl is categorized as weak, moderate, and strong in the literature [Gupta, Lilley, and Syred, 1984; Bilen *et al.*, 2002]:

$$S < 0.2: \qquad \text{weak}$$
$$0.2 \ \leq \ S \ \leq \ 0.6: \ \text{moderate} \qquad\qquad\qquad\qquad\qquad\qquad\qquad (7)$$
$$S > 0.6: \qquad \text{strong}$$

Loitsyanskiy's equations were obtained by using the weak swirl approximation; a similar strategy was adopted a year later by Gortler [Gortler, 1954]. Some time later, concerns were issued regarding how Loitsyanskiy derived the swirling coefficients for his solutions [Lee, 1965]. However, a review of both Loitsyanskiy's and Lee's papers shows that the original development is reasonable, emulated by others [Gortler, 1954; Blevins, 1992], and conforms with experimental data [Chigier and Chervinsky, 1967; Mathur and MacCallum, 1967]. In any case, though Loitsyanskiy's solutions apply relatively well for weak to moderate swirl, he warned that the equations are most certainly not appropriate for strong swirl where the CRZ has formed [Loitsyanskiy, 1953]. Basically, strong swirl means that a CRZ has formed, and therefore there exists one or more regions within the jet core with backflow or some form of vortex breakdown that is not described by Equations 3 through 6.

The impact of heat transfer and mixing via swirling jets has been researched for nearly seven decades, starting with the first published paper in 1947 [Watson and Clarke 1947]. Since then, much knowledge has been accumulated regarding swirling jets. Blevins includes a great starting point for swirling advances up to the 1980s [Blevins, 1992]. Recently, researchers have shown that there is a significant increase in Nusselt number (Nu) when using a swirling jet as opposed to a conventional jet under the same operating conditions [Huang and El-Genk, 1998]. The researchers also developed a schematic description of a swirling, impinging jet, shown in Figure 16. Additionally,

better radial uniformity in heat distribution can be achieved with swirling jets when compared with conventional jets [Huang and El-Genk, 1998; King, c. 2005].
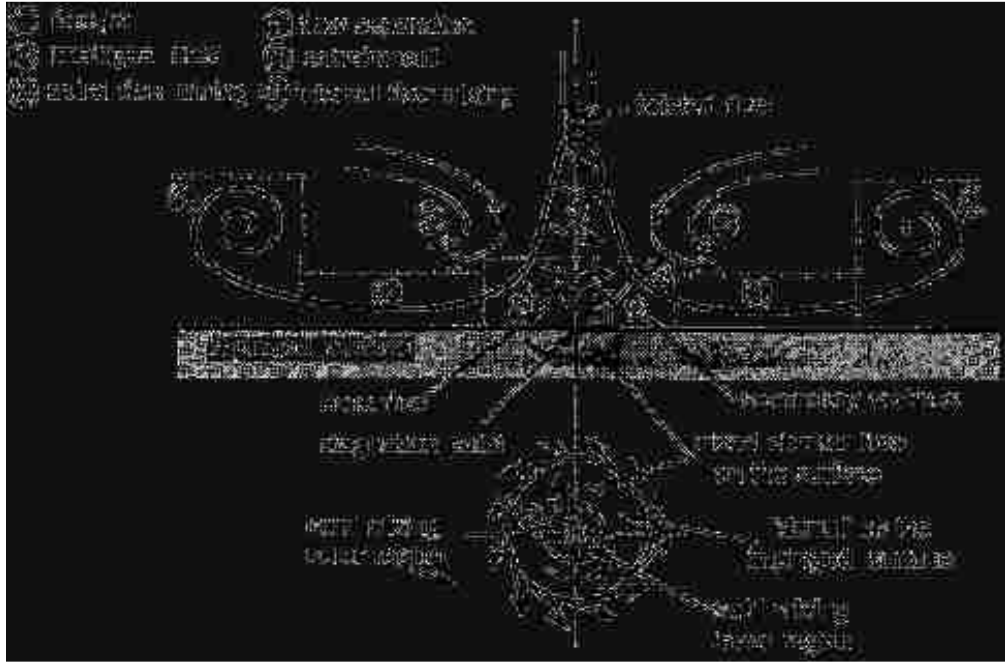
Figure 16. Schematic of a Swirling, Impinging Jet [Huang and El-Genk, 1998].

Recently, CFD codes have been applied in the NGNP nuclear industry by some researchers [Guillen and McIlroy, 2007; McIlroy, McEligot, and Pink, 2007; McIlroy, McEligot, and Pink, 2008 a and b; Johnson, 2009a and b; Johnson and Schultz, 2009; McIlroy, McEligot, and Pink, 2010a and b; Rodriguez and El-Genk, 2010a].

The swirling jet subject matter is quite rich, and there are thousands of swirling jet papers in the literature as of 2011. The bulk of the reported work over the past two decades involves experiments, theoretical research, and CFD analysis. The CFD analysis typically uses LES (*see* Section 4.3.1). Primarily during the two decades, CFD LES research has contributed much to the knowledge of swirling jet behavior [Won-Wook and

Menon, 1999; Cziesla *et al*., 2001; Schluter, 2001; Garcia-Villalba, Frohlich, and Rodi, 2004; Wang and Bai, 2004; Duwig *et al*, 2005; Fujimoto, Inokuchi, and Yamasaki, 2005; Garcia-Villalba, Frohlich, and Rodi, 2005; Garcia-Villalba, 2006; Afgan, 2007; Muller and Kleiser, 2007; Stein, 2009; Zemtsop *et al*., 2009].

When conventional jets (S=0) are replaced with swirling jets (S>0), more uniform spatial distributions of the heat transfer coefficient and the surface temperature have been reported [Huang and El-Genk, 1998]. Inevitably, the primary objectives for recent CFD swirling jet research gravitate along the lines of increasing understanding of the enhanced mixing, heat, and mass transfer that can be achieved for swirling jets compared to conventional jets. However, the impact of the many dozens of turbulence models for usage in the calculations is not fully understood. In general, LES methods yield results that are closer to experimental data than the Reynolds averaged Navier-Stokes (RANS) methods, as is shown in Section 4.3.1.

A search of the literature indicates that there are no definite guidelines regarding the impact of S, T, Re, and the CRZ on mixing and heat transfer of swirling jets [Rose, 1962; Chigier and Chervinsky, 1967; Lilley, 1973; Escudier and Keller, 1985; Darmofal, 1993; Shee, Chen, and Jeng, 1996; Billant *et al*., 1998; Bilen *et al*., 2002; Garcia-Villalba, Frohlich, and Rodi, 2005; Gilchrist and Naughton, 2005; Shiri, George, and Toutiaei, 2007; Shiri, George, and Naughton, 2008; Semaan, Naughton, and Ewing, 2009]. Various mechanisms for the formation of the CRZ have been proposed in the literature, but there currently exists no specific guidance as to when it specifically ought to occur in general, and whether its formation is gradual or appears only under unique, specific conditions [Lucca-Negro and O'Doherty, 2001; Li, 2004; Li and Gutmark, 2006;

Giannadakis *et al*., 2007; Vanierschot and Bulck, 2008; Valera-Medina *et al*., 2008, 2009].

Therefore, of key importance for this research is the extension of knowledge regarding how swirling jets can enhance nuclear reactor safety and design. This will in turn necessitate a deeper understanding of how to more effectively model swirl boundary conditions (BCs), as well as yield a better understanding of the overall impact of a high-temperature swirling-jet gas's mixing and heat transfer as functions of Re, S, the CRZ, and swirl decay.

2.3 Turbulence Modeling

Vortex flows have intrigued researchers for many centuries, as evidenced by the 1507 turbulence drawing of Leonardo da Vinci, in an attempt to understand turbulence's aesthetic and physical attributes (Figure 17). Five centuries later, much progress has been made, as evidenced by the thousands of papers and books written on the subject matter. Part of the difficulty of pinning down turbulence is its stochastic nature. Before sinking deeper into the serious nature of turbulence, some of the most famous, lighthearted (and frustrated!) descriptions of turbulence are noted, as follows.

According to Leonardo da Vinci [Hall, c. 1966],

"Of the eddies one is slower at the centre than on the sides, another is

swifter at the centre than on the sides; others there are which turn back in

the opposite direction to their first movement."

The seemingly never-ending turbulence scale was described nearly two centuries ago by Richardson as [Richardson, 1922; Ecke, 2005],

"Big whorls have little whorls that feed on their velocity, and little whorls

have lesser whorls and so on to viscosity."

The poetic fashion of describing turbulence was based on a word play of a poem

about fleas [Wikipedia, 2011a]:

"So, the naturalists observe, the flea hath smaller fleas that on him prey;

And these have smaller still to bite 'em."

Another illustrious researcher, Sir Horace Lamb, remarked,

"I am an old man now, and when I die and go to heaven there are two

matters on which I hope for enlightenment. One is quantum

electrodynamics, and the other is the turbulent motion of fluids. And

about the former I am rather optimistic."

These ubiquitous eddies in turbulent flow, that have so frustrated many prominent

researchers, form vortices, twisted jets, hydraulic cyclones, vortex chambers, and

atmospheric vortices that have a common central region with rigid ("solid body") vortex

rotation that is subsequently followed by a "free" region where the vortex decays

[Al'tshul' and Margolin, 1970]. This is basically a description of the Rankine vortex

[Rankine, 1858], which will be studied in subsequent sections of this research, including

Sections 5.1.6, 5.1.7, and 5.1.10.

Because there are many modern turbulence modeling approaches, three mayor

categories were considered for this research in order to select the most appropriate

method for modeling multiple impinging swirling jets in crossflow:

1. Direct numerical simulation (DNS),

2. RANS, and

3.   LES.

These approaches will be discussed in the subsections that follow. However, due to turbulence's large scope, only a brief survey can be included; to not do so would result in thousands of pages worth of summary. The interested reader is referred to summaries of turbulence models found elsewhere [Nirmolo, 1970; Hinze, 1975; Rogallo and Moin, 1984; Lesieur, 1997; Davidson, 2003; Bakker, 2005; Ecke, 2005; Afgan, 2007; Sodja, 2007; Fuego, 2008; Alfonsi, 2009].

Figure 17. Leonardo da Vinci's Turbulence Drawing [The Royal Collection, 2004].

2.3.1   Direct Numerical Simulation (DNS) Methods

For DNS calculations, no turbulence models are employed. Instead, the Navier-Stokes (NS) equations are solved by resolving the entire range of temporal and spatial scales. That is, the mesh has to be sufficiently discretized in order for it to capture the scales of motion, from the largest macroscopic structures up to the finest Kolmogorov scales [Afgan, 2007], and the time step must be sufficient small. The DNS approach calculates both the averaged and instantaneous fields.

When high-order numerical methods are used, along with a well-resolved spatial and temporal scales, the calculations compare quite favorably with experimental data, to the point that many authors go as far as considering the output as good as experimental data [Moet *et al.*, 2004; Freitag and Klein, 2005; Duraisamy and Lele, 2006; Afgan, 2007; Bonaldo, 2007; Busch, Ryan, and Sheard, 2007; Walther *et al.*, 2007; Taub *et al.*, 2010]. Though the DNS approach was recently restricted to low to moderate Re [Stein, 2009], computational advances using supercomputers keep extending the magnitude of Re. For example, excellent results for swirling jets at Re=5,000 and S=0.79 [Freitag and Klein, 2005], as well as $12,000 \leq Re \leq 33,500$ and $S \leq 0.5$ [Facciolo, 2006] were reported recently for turbulent swirling jets.

2.3.2   Reynolds-Averaged Navier-Stokes (RANS) Methods

In the RANS zero-, one-, and two-equation models, an isotropic turbulence viscosity is introduced to provide closure for the Reynolds stress terms. This approach involves the modified Boussinesq turbulent viscosity approximation. The stress-equation RANS models are also known as Reynolds Stress Models (RSMs). For 3D applications, they require six partial differential equations to solve each of the six independent components

in the stress tensor [Alfonsi, 2009; Bakker, 2009]. Stress closure can be handled by a variety of modeling techniques, as will be shown in the following subsections, which include a discussion of the RANS time-filtering and LES space-filtering techniques.

2.3.2.1   Time Filtering

The RANS time filtering methodology is described as follows. Suppose a fluid transitions from laminar to turbulent flow. Then, the Newtonian shear relationship

$$\tau = -\mu \frac{dv}{dy} \tag{8}$$

no longer adequately describes the fluid shear. Instead, the relationship must additionally include the impact of the turbulence-generated shear terms that are collectively known as the Reynolds stresses. These will be derived next.

First, consider that a turbulent fluid undergoes random fluctuations of a given primitive variable, say the velocity v_z in the axial direction. Then, the temporal behavior of $v_z(t)$ can be considered as comprised of two terms, the average velocity $\overline{v}_z$ and the instantaneous velocity fluctuations that occur due to turbulence, v_z', as shown in Figure 18. This approximation is referred as "Reynolds decomposition" [Bird, Stewart, and Lightfoot, 2007]. Therefore,

$$v_z(t) = \overline{v}_z + v_z'. \tag{9}$$

In likewise fashion, the pressure can be decomposed as

$$p(t) = \overline{p} + p'. \tag{10}$$

The relationship between the barred and primed velocity is shown in Figures 18 and 19, where steady and unsteady turbulent flows are considered, respectfully. In Figure 18, $\overline{v}_z$ is time independent, whereas in Figure 19, $\overline{v}_z$ is time dependent.
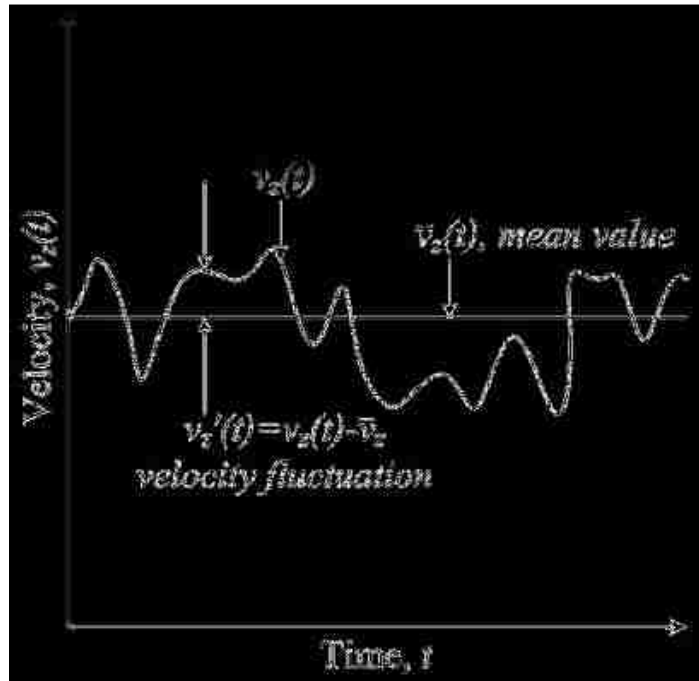
Figure 18. Turbulent Velocity History for a Steady Flow [Bird, Steward, and Lightfoot, 2007].
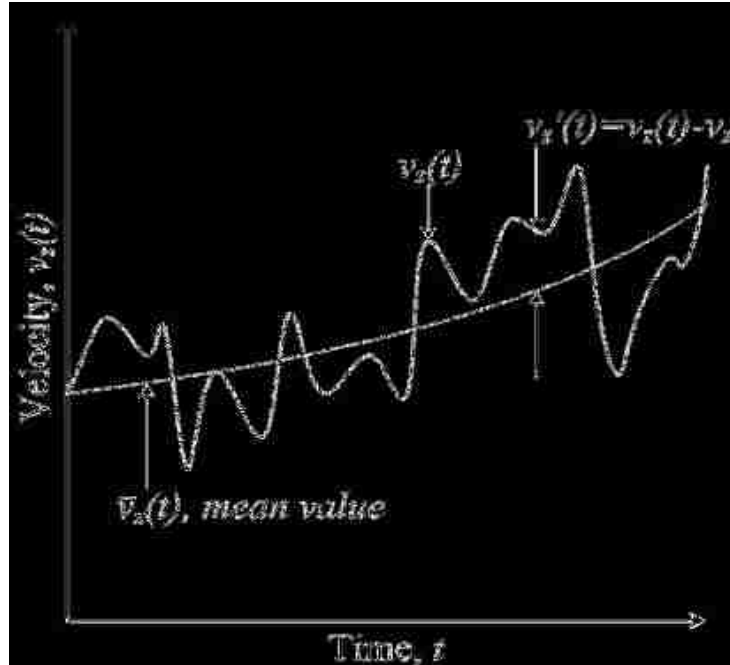
Figure 19. Turbulent Velocity History for Unsteady Flow [Bird, Steward, and Lightfoot, 2007].

Now, $\overline{v}_z$ can be calculated if integration over sufficient time t_o is allowed; that is, the integral time interval of consideration is sufficiently large such that it incorporates a sufficient number of velocity fluctuations, thus allowing for smoothed, averaged computation,

$$\overline{v}_z = \frac{1}{t_0}\int_{t-\frac{1}{2}t_0}^{t+\frac{1}{2}t_0} v_z(q)\,dq, \tag{11}$$

with q being a dummy variable of integration. Other primitive variables such as v_x, v_y, p, and T may be averaged in likewise fashion. From the definition of $\overline{v}_z$, the following properties can be observed:

$$\overline{v_z'} = 0, \quad \overline{\overline{v}_z v_z} = \overline{v}_z,$$

$$\overline{\overline{v}_z v_z'} = 0, \quad \overline{\frac{\partial}{\partial x} v_z} = \frac{\partial}{\partial x}\overline{v}_z,$$

$$\overline{\frac{\partial}{\partial t} v_z} = \frac{\partial}{\partial t}\overline{v}_z, \quad \overline{v_x' v_y'} \neq 0,$$

$$\text{and} \quad \overline{v_z'^2} \neq 0 \tag{12}$$

The above properties are very useful in deriving and simplifying the turbulent forms of the conservation of mass and NS equations. Note that the last relationship, in general, is not equal to zero. In fact, it forms part of what is referred to as "turbulence intensity", I_t, which is a good measure of the magnitude of the turbulent fluctuations,

$$I_t = \frac{\sqrt{\overline{v_z'^2}}}{\langle \overline{v}_z \rangle}. \tag{13}$$

Notice that the turbulence intensity typically varies between 1 to 10% within the turbulent core, and by 25% or more near the wall [Bird, Stewart, and Lightfoot, 2007].

Substitution of Equation 12 into the Cartesian conservation of mass and momentum equations yields, respectively, for x-momentum,

$$\frac{\partial}{\partial x}\left(\overline{v}_x + v_x'\right) + \frac{\partial}{\partial y}\left(\overline{v}_y + v_y'\right) + \frac{\partial}{\partial z}\left(\overline{v}_z + v_z'\right) = 0 \tag{14}$$

and

$$\frac{\partial}{\partial t}\rho\left(\overline{v}_x + v_x'\right) = -\frac{\partial}{\partial x}\left(\overline{p} + p'\right)$$

$$-\left[\frac{\partial}{\partial x}\rho\left(\overline{v}_x + v_x'\right)\left(\overline{v}_x + v_x'\right) + \frac{\partial}{\partial y}\rho\left(\overline{v}_y + v_y'\right)\left(\overline{v}_x + v_x'\right) + \frac{\partial}{\partial z}\rho\left(\overline{v}_z + v_z'\right)\left(\overline{v}_x + v_x'\right)\right] \tag{15}$$

$$+\mu\nabla^2\left(\overline{v}_x + v_x'\right) + \rho g_x$$

Note that similar expressions can be developed for the y and z momentum equations; however, their explicit derivation is not required. Rather, it is possible to extend the

turbulent form of the mass and momentum equations into invariant forms. Therefore, the derivational process employed here proceeds by time-smoothing the above two equations; that is, by taking their over-bar. Then, use is made of the properties in Equation 12 to simplify the resulting equations,

$$\frac{\partial}{\partial x}\overline{v}_x + \frac{\partial}{\partial y}\overline{v}_y + \frac{\partial}{\partial z}\overline{v}_z = 0 \tag{16}$$

and

$$\frac{\partial}{\partial t}\rho\overline{v}_x = -\frac{\partial}{\partial x}\overline{p}$$

$$-\left(\frac{\partial}{\partial x}\rho\overline{v}_x\overline{v}_x + \frac{\partial}{\partial y}\rho\overline{v}_y\overline{v}_x + \frac{\partial}{\partial z}\rho\overline{v}_z\overline{v}_x\right) - \left(\frac{\partial}{\partial x}\rho\overline{v_x'v_x'} + \frac{\partial}{\partial y}\rho\overline{v_y'v_x'} + \frac{\partial}{\partial z}\rho\overline{v_z'v_x'}\right) \tag{17}$$

$$+\mu\nabla^2\overline{v}_x + \rho g_x$$

By observing the expression of the above two turbulent equations, their invariant form is inferred as follows,

$$\vec{\nabla}\cdot\vec{\overline{v}} = \vec{0} \tag{18}$$

and

$$\frac{D\rho\vec{\overline{v}}}{Dt} = \frac{\partial}{\partial t}\rho\vec{\overline{v}} + \vec{\nabla}\cdot\rho\vec{\overline{v}}\vec{\overline{v}} = -\vec{\nabla}\overline{p} - \vec{\nabla}\cdot\left(\vec{\overline{\tau}}^{(v)} + \vec{\overline{\tau}}^{(t)}\right) + \rho\vec{g}, \tag{19}$$

where the superscripts v and t in the shear stress terms refers to "viscous" and "turbulent", respectively. The two shear terms will be described shortly. The operator $\dfrac{D}{Dt}$ is the material derivative.

Now, in order to obtain some useful insights into the nature of turbulence, consider the laminar mass and momentum conservation equations shown immediately below, and compare them with the respective turbulent forms Equations 16 and 17:

$$\frac{\partial}{\partial x} \mathrm{v}_x + \frac{\partial}{\partial y} \mathrm{v}_y + \frac{\partial}{\partial z} \mathrm{v}_z = 0 \tag{20}$$

and

$$\frac{\partial}{\partial t} \rho \mathrm{v}_x = -\frac{\partial \mathrm{p}}{\partial x} - \left(\frac{\partial}{\partial x} \rho \mathrm{v}_x \mathrm{v}_x + \frac{\partial}{\partial y} \rho \mathrm{v}_y \mathrm{v}_x + \frac{\partial}{\partial z} \rho \mathrm{v}_z \mathrm{v}_x \right) + \mu \nabla^2 \mathrm{v}_x + \rho g_x. \tag{21}$$

Then, it is readily evident that the conservation of mass equations are identical, except that the turbulent equation uses a bar, and the laminar form does not. As for the equation of motion, the same variable bar situation occurs, with one major exception. Notice that the primed terms in the turbulent momentum equation do not disappear. These extra terms are at the crux of turbulence modeling. They are responsible for the fundamental differences between laminar and turbulent flow. These terms are the so-called "Reynolds stresses" [Bird, Stewart, and Lightfoot, 2007], and are complex functions of position and turbulence intensity. *Because the primed v terms are not related to averaged velocity gradients in obvious ways, a consequence is that more unknown variables than independent equations appear, thereby negating the possibility of obtaining a complete set of state equations that can solve all the unknowns.* Therefore, the Reynolds stresses must be obtained experimentally, empirically, through approximations, or numerically (e.g., DNS).

For a Newtonian incompressible fluid ($\vec{\nabla} \cdot \vec{\mathrm{v}} = \vec{0}$), the viscous shear stresses for the x-momentum are

$$\bar{\tau}_{xx}^{(v)} = -2\mu \frac{\partial \bar{\mathrm{v}}_x}{\partial x}, \tag{22}$$

$$\bar{\tau}_{xy}^{(v)} = -\mu \left(\frac{\partial \bar{\mathrm{v}}_y}{\partial x} + \frac{\partial \bar{\mathrm{v}}_x}{\partial y} \right), \tag{23}$$

and

$$\overline{\tau}_{xz}^{(v)} = -\mu\left(\frac{\partial\overline{v}_x}{\partial z} + \frac{\partial\overline{v}_z}{\partial x}\right). \tag{24}$$

Represented mathematically, the turbulence momentum terms (the Reynolds stresses), are explicit functions of the velocity fluctuations that arise from the turbulent motion,

$$\overline{\tau}_{xx}^{(t)} = -\rho\overline{v_x' v_x'}, \tag{25}$$

$$\overline{\tau}_{xy}^{(t)} = -\rho\overline{v_x' v_y'}, \tag{26}$$

and

$$\overline{\tau}_{xz}^{(t)} = -\rho\overline{v_x' v_z'}. \tag{27}$$

2.3.2.2   Overview of RANS Methods

As noted in the previous section, the Reynolds stresses cannot be determined directly, but must instead be obtained experimentally, empirically, through approximations, or numerically. The RANS models attempt to do so numerically by assuming certain spatial and temporal simplifications concerning eddies. These simplifications will be discussed next.

2.3.2.2.1   Zero-Equation Models

The simplest RANS type is the zero-equation model. These models were the first attempts to model turbulent flows, dating less than 100 years ago [Prandtl, 1925, 1942]. Because of their mathematical simplicity, these models are still used to obtain analytical

solutions for the NS equations. However, their applicability and modeling capacity are very limited.

Zero-equation models attempt to provide a single turbulence time, τ_O, and length scale, l_O [Alfonsi, 2009]:

$$\nu_T \propto \frac{l_O^2}{\tau_O}. \tag{28}$$

The zero-equation model's simplicity provides useful and insightful results, but also many over-simplified results [Alfonsi, 2009]. This is the case because experimental data show very large variations across both space and time [Alfonsi, 2009].

Prandtl successfully modeled circular jet behavior by considering that turbulent viscosity is analogous to viscous shear. By analogy with the Newtonian viscous law, he assumed that

$$\overline{\tau}_{yx}^{(t)} = -\mu^{(t)} \frac{d\overline{\mathbf{v}}_x}{dy}. \tag{29}$$

Thus, instead of considering the instantaneous velocity fluctuations $\mathbf{v}'$, which are unknown, the gradient of the averaged velocity $\overline{\mathbf{v}}$ is taken. In addition, the fluid viscosity is replaced with the turbulent viscosity (also known as the eddy viscosity), $\mu^{(t)}$. After making these assumptions, then it is a matter of formulating an empirical relationship for the turbulent viscosity. Prandtl found that the following relationship quite adequately reproduced circular jet data [Prandtl, 1925, 1942; Bird, Stewart, and Lightfoot, 2007]:

$$\mu^{(t)} = \rho \kappa b \left(\overline{\mathbf{v}}_{z,\max} - \overline{\mathbf{v}}_{z,\min} \right). \tag{30}$$

In the above empirical equation, κ is a unitless constant derived from experimental data, ρ is the fluid density, while b is the diameter of the jet at location z. Therefore,

$$\overline{\tau}_{yx}^{(t)} = \overline{\tau}_{yx,j}^{(t)} = -\rho\kappa b\left(\overline{v}_{z,max} - \overline{v}_{z,min}\right)\frac{d\overline{v}_x}{dy},$$ (31)

where j refers to jet.

In an alternative expression for turbulent shear, Prandtl suggested the following form, which was derived by assuming that eddies behave akin to the motion of molecules within a low density gas,

$$\overline{\tau}_{yx}^{(t)} = -\rho l^2 \left|\frac{d\overline{v}_x}{dy}\right|\frac{d\overline{v}_x}{dy},$$ (32)

where l is the eddy mean free path. For a jet, Prandtl calculated l as $l = \kappa_1 b$, where κ_1 is a unitless constant that can be found experimentally. Therefore,

$$\overline{\tau}_{yx}^{(t)} = -\rho\kappa_1^2 b^2 \left|\frac{d\overline{v}_x}{dy}\right|\frac{d\overline{v}_x}{dy}.$$ (33)

Similarly to Prandtl's analogy, the turbulent shear for a swirling jet can be approximated by assuming that the shear is a separable product function of the circular jet turbulence and some function f of the swirl angle, θ, that is valid for $0 \leq \theta < 90°$. Thus,

$$\overline{\tau}_{yx,sj}^{(t)} = \overline{\tau}_{yx,j}^{(t)} f\left(\theta\right).$$ (34)

The behavior of f is such that when θ is zero, $f\left(\theta{=}0\right)=1$, thereby collapsing the swirling jet turbulent shear to that of a conventional jet. On the other hand, as θ approaches 45°, the function should reach a maximum; this reflects the notion that the product of the body forces times their sines and cosines reach maximum at this point. Finally, as θ approaches 90°, $f\left(\theta\to 90°\right)\to 1$. These constraints are readily satisfied by

$$f(\theta) = 1 + \sin(2\theta).\tag{35}$$

Therefore,

$$\overline{\tau}_{yx,sj}^{(t)} = -\rho\kappa_0 b\left(\overline{v}_{z,\max} - \overline{v}_{z,\min}\right)\left[1 + \sin(2\theta)\right]\frac{d\overline{v}_x}{dy}.\tag{36}$$

2.3.2.2.2   One-Equation Models

One-equation RANS models typically solve the turbulent kinetic energy (k) [Alfonsi, 2009]. These models are not used much in the modern literature, say from 2000 and on. In one example of a recent application of one-equation models, the Spalart-Allmaras turbulence model was used to model an impinging jet with crossflow [Pandya, Murman, and Sankaran, 2003]. The model was able to reproduce some of the classical vortices, but the authors noted that it tended to produce an unphysical eddy viscosity that was about an order of magnitude higher than the eddy viscosity near the wall.

2.3.2.2.3   Two-Equation Models

Two-equation RANS attempt to solve both k and the turbulent dissipation rate, ε. The first attempt yielded the standard k-ε model [Launder and Spalding, 1974], which remains very popular, despite its inability to model anisotropic turbulent flows, such as swirling flows.

For the standard k-ε turbulence model, the transport equations for k and ε are solved, and are assumed to be related to l_O and τ_O, as follows [Alfonsi, 2009]:

$$l_O \propto \frac{k^{3/2}}{\varepsilon}\tag{37}$$

and

$$\tau_O \ \propto \ \frac{k}{\varepsilon} . \tag{38}$$

With those length and time scales, then the turbulent viscosity is [Alfonsi, 2009]

$$\nu_T = C_\mu \frac{k^2}{\varepsilon} . \tag{39}$$

C_μ is calculated from experiments as 0.09 [Alfonsi, 2009].

The standard k-ε and various modifications have had various degrees of successes and failures [Leschziner and Rodi, 1984; Abujelala and Lilley, 1985; Kilik and Finstad, 1985; Ahuja, Deshpande, and Merle, 1997; Meyyapan, Schwarz, and Perry, 1997; Larocque, 2004; Li, 2004; Mardani, 2004; Taglia *et al.*, 2004; Guillen and McIlroy, 2007; Nematollahi and Nazifi, 2007; El-Behery and Hamed, 2009; Eldrainy, Ahmad, and Jaafar, 2009; Laurien, Lavante, and Wang, 2010]. As a result of various shortcomings, many RANS models attempt to improve the standard k-ε, again, with various degrees of successes and failures. Some of these approaches are considered next.

The renormalization group (RNG) k-ε, was derived from statistical decomposition of the velocity field, and may be suitable for swirling flow [Fuego, 2008]. It is similar to the standard k-ε, except that it also includes an additional dissipation source term.

The v^2-f model is somewhat similar to the standard k-ε, but includes formulation for modeling the wall region without using wall or damping functions. The turbulent kinetic energy is the same as the standard k-ε, while the dissipation is notably different.

The literature results for the v^2-f model are mixed [Larocque, 2004]. Good comparisons with data occurred when a large impingement distance was used (the swirling jet far field), as well as when S=0.89. For S ≤0.3, the results were poor. The impact of the v^2-f model on turbulent jet impingement was investigated recently, and

found to yield excellent results [Merci and Dick, 2003]. Most recently, the model was found to calculate quite well for planar, asymmetric diffuser [El-Behery and Hamed, 2009]. The Fuego model is notoriously "finicky", requiring much finessing in order to avoid code aborts.

The shear stress transport (SST) model uses the standard k-ε away from the wall and k-ω near the wall, in a unique blend that tries to overcome the shortcomings of either model when used individually. Its turbulent kinetic energy is nearly the same as the standard k-ε, while the dissipation includes a cross-diffusion term. Good swirling jet comparisons were obtained for high Re (20,000 to 40,000) and weak to intermediate S (0 to 0.3). The SST did not perform as well for strong S (0.89) [Larocque, 2004]. Good results were obtained for asymmetric diffuser flows [El-Behery and Hamed, 2009].

The k-ω model is similar to the standard k-ε. The dissipation is the same, and the kinetic energy includes the so-called turbulent frequency, which is the reciprocal of the turbulent time scale. For the k-ω model, the turbulence viscosity is expressed by the relationship [Wilcox, 1998]:

$$\mu_t = \rho \frac{k}{\omega} \tag{40}$$

In the above equation, ρ is the fluid density, while ω is the specific dissipation rate. Details of the k-ω model are presented elsewhere [Wilcox, 1998]. The k-ω turbulence model has also been considered for swirling and asymmetric flows [El-Behery and Hamed, 2009; DeChant, 2010; Valera-Medina *et al*., 2010], and has generally reported good results. Notwithstanding the successes, the literature is very limited in terms of this model's usage for swirling jets. It is not clear at what Re and S this model can successfully model swirling jets.

2.3.2.2.4   Six-Equation RSM Models

The RANS RSMs provide second order closure [Launder, Reece, and Rodi, 1975; Bakker, 2009; Alfonsi, 2009]. Contrary to zero-, one-, and two-equation RANS and LES turbulence models, the turbulent isotropic eddy viscosity is not computed; instead, the Reynolds stresses are calculated directly [Launder, Reece, and Rodi, 1975; Alfonsi, 2009; Bakker, 2009].

The algebraic stress RANS models (e.g., simplified RSM [Abujelala and Lilley, 1985]) have been used with some degree of success for modeling swirling jets [Kim and Chung, 1987], as have other RSM models (e.g., pressure-strain-rate) with various degrees of success [Gibson and Younis, 1986; Hogg and Leschziner, 1989; Lai, 1995; Larocque, 2004; Krishna and Ganesan, 2005; Johnson, 2006; El-Behery and Hamed, 2009]. The literature also reports that not all RSMs have successfully modeled swirling flows [Laurien, Lavante, and Wang, 2010; Valera-Medina *et al*., 2010].

RANS/URANS methods are very effective but require higher spatial discretizations than LES methods [Taglia *et al*., 2004; Bonaldo, 2007; Umeh *et al*., 2009]. They have also been proposed by INL for modeling the VHTR LP [Johnson, 2007].

2.3.3   Large Eddy Simulation (LES) Turbulence Models

The LES methodology uses spatial filtering. The methodology is also known as dynamic subgrid-scale. Fuego LES turbulence models include the kinetic subgrid-scale (KSGS), Smagorinsky, and dynamic Smagorinsky [Fuego, 2008]. The Smagorinsky model assumes that the Smagorinsky parameter, C_S, is constant. On the other hand, in the dynamic Smagorinsky model, the parameter C_{DS} varies in space and time. Its value is

calculated via a space grid (s) and a test (t) filter. The spatial filter, Δ, is based on the grid cell volume, $\tilde{V}$ [Fuego, 2009]:

$$\Delta = \tilde{V}^{1/3}.$$ (41)

2.3.3.1   KSGS Model

The Fuego KSGS model is compatible with the turbulent combustion model known as the Magnussen's eddy dissipation concept (EDC) model [Magnussen *et al*., 1979] and post-processes the dissipation rate. It uses wall functions for energy and momentum transport, is based on a one-equation model for the resolved turbulent kinetic energy, and uses a spatial filter. It therefore closely mimics a LES-type turbulence model. The KSGS spatial filter Δ is based on the grid cell volume, $\tilde{V}$ [Fuego, 2009]. The turbulent viscosity is defined as

$$\mu_T = C_{KSGS} k_{KSGS}^{1/2} \Delta$$ (42)

where $C_{KSGS} = 0.0856$ and k_{KSGS} is the KSGS turbulent kinetic energy.

2.3.3.2   Smagorinsky Model

The standard Smagorinsky model, also referred as the Smagorinsky model, calculates the subgrid turbulent eddy viscosity via a mixing length approximation that includes a fixed leading coefficient, element length, and the strain rate tensor (S_{ij}) magnitude. However, it tends to be overly dissipative, and Fuego users are cautioned to inspect the results carefully [Smagorinsky, 1963; Fuego, 2008].

The turbulent viscosity for the standard Smagorinsky turbulence model is expressed by the following relationship [Fuego, 2009]:

$$\mu_T = \rho \left(C_s \Delta \right)^2 | \sqrt{2 S_{ij} S_{ij}} |.$$ (43)

C_S is typically in the range of 0.1 to 0.24, with Fuego coding set to 0.17 [Fuego, 2009].

2.3.3.3 Dynamic Smagorinsky Model

The subgrid turbulent eddy viscosity is calculated similarly as the standard Smagorinsky model, except that the leading coefficient is now dynamically calculated at every timestep based on the least squares of various stress tensors [Fuego, 2008]. In effect, this process can be considered as *a test filtering of a space filtering.*

Based on space filtering,

$$\tau_{ij} = \left(u_i u_j \right)^s - u_i^s u_j^s . \tag{44}$$

If the above equation is additionally filtered based on t as well,

$$T_{ij} = \left(u_i u_j \right)^{st} - u_i^{st} u_j^{st} . \tag{45}$$

The Germano identity relates the two stresses as follows,

$$L_{ij} \equiv T_{ij} - \tau_{ij}^t \tag{46}$$

Therefore, the resolved turbulent stress simplifies to

$$L_{ij} = \left(u_i^s u_j^s \right)^t - u_i^{st} u_j^{st} \tag{47}$$

The anisotropic components for L_{ij} are

$$L_{ij,ani} = L_{ij} - \frac{\delta_{ij}}{3} L_{kk} = -2C_{DS} M_{ij} \tag{48}$$

where

$$M_{ij} \equiv \left(\Delta^t \right)^2 \left| S_{ij}^{st} \right| S_{ij}^{st} - \left(\Delta^g \right)^2 \left(\left| S_{ij}^s \right| S_{ij}^s \right)^t \tag{49}$$

and S_{ij} is defined as

$$S_{ij} \equiv \frac{1}{2} \left(\frac{\partial u_i}{\partial x_j} + \frac{\partial u_j}{\partial x_i} \right) \tag{50}$$

Finally, the dynamic parameter is evaluated as [Lilly, 1991]

$$C_{DS} = \frac{L_{kl}M_{kl}}{2M_{mn}M_{mn}},$$ (51)

while some researchers also use

$$C_{DS} = \frac{L_{kl}S_{kl}^{s}}{2M_{mn}S_{mn}^{s}}.$$

The Fuego developers prefer the following format:

$$C_{DS} = \frac{\left(L_{kl}M_{kl}\right)^{S}}{2\left(M_{kl}M_{kl}\right)^{S}}$$ (52)

Finally, the dynamic Smagorinsky turbulent viscosity is expressed by the following

relationship [Fuego, 2009]:

$$\mu_{T} = \rho C_{DS}\Delta^{2} \mid \sqrt{2S_{ij}S_{ij}} \mid$$ (53)

In short, the coefficient C_{DS} is given by a dynamic filtering process based on the

local turbulence field.

For complex, anisotropic flows with adverse pressure gradients, as is the case in the

VHTR LP, the standard and dynamic Smagorinsky calculations have obtained excellent

results when compared with experimental data [Kim and Menon, 1999; Kravchenko and

Moin, 2000; Cziesla *et al*., 2001; Schluter, 2001; Apte *et al*., 2003; Garcia-Villalba,

Frohlich, and Rodi, 2004; Moet *et al*., 2004; Duwig *et al*., 2005; Garcia-Villalba,

Frohlich, and Rodi, 2005; Lu *et al*., 2005; Fujimoto and Yamasaki, 2006; Garcia-Villalba

and Frohlich, 2006; Gyllenram, Nilsson, and Davidson, 2006; Afgan, 2007; Bonaldo,

2007; Jagus *et al*., 2008; Muller and Kleiser, 2008; Rodriguez and El-Genk, 2008a, b, c,

and d; Denev, Frohlich, and Bockhorn, 2009; Dinesh and Kirkpatrick, 2009; El-Behery

and Hamed, 2009; Iaccarino and Constantine, 2009; Naughton *et al.*, 2009; Stein, 2009; Uddin *et al.*, 2009; Zemtsop *et al.*, 2009; Doolan, 2010; Rodriguez, Domino, and El-Genk, 2010; Rodriguez and El-Genk, 2010a and b; Rodriguez and El-Genk, 2011a and b].

Nevertheless, some issues have been reported in the literature. For example, there are grid-dependency issues that have yet to be satisfactorily resolved as of 2011 [Bose, Moin, and You, 2011], and one paper was found wherein the LES output did not "conform" to experimental data [Valera-Medina *et al.*, 2010]. On the other hand, no explanation was included in their research, even though the authors confirmed that other researchers had successfully used the LES method.

Note that tensorial eddy viscosity has been recently proposed, but is not extensively tested. The tensor accounts for non-alignment between the resolved strain-rate and turbulent stress [Gallerano and Napoli, 1999]. Other modifications include that of using least squares in order to minimize the resolved stresses with the closure assumption [Lilly, 1991]. A generalized subgrid scale methodology for variable density flow is discussed in the literature, and shown to have excellent agreement with DNS [Moin, 1991]. Hybrid RANS/LES approaches have recently shown promising results [Stoellinger and Zemtsop, 2007; Chenoweth *et al.*, 2008; Kannepalli *et al.*, 2008; Gopalan *et al.,* 2010].

For all the Fuego calculations presented herein, the dynamic Smagorinsky closure model was employed [Smagorinsky, 1963; Germano *et al.*, 1991; Germano, 1992; Ghosal *et al.*, 1995], which is based on a scalar eddy viscosity coefficient (Equation 53).

3. PROBLEM STATEMENT

The problem to be solved consists of reducing the likelihood of hot spot formation and increasing mixing in order to minimize thermal stratification in the LP. The approach taken by this research is to add static swirl devices at the jet exits of the coolant channels. This effectively converts the conventional jets into swirling jets. It is hypothesized that the swirling jets will stimulate more mixing in the LP and minimize the impingement of the hot helium exiting the coolant channels in the reactor core on the bottom plate. The hypothesis is based on the tendency of swirling jets to reduce the axial momentum at the expense of increasing the angular momentum of the jets.

The primary thrust of the proposed research seeks to extend the current level of knowledge of heat transfer and mixing enhancement of turbulent swirling jets and to apply such knowledge to enhance VHTR safety and design.

The key original contributions from this research can be summarized as follows:

1. Advance swirling jet methodology and theory (series expansion of axisymmetric vortices, new NS solutions, vortex rotation direction, and dynamic S).

2. Extend the applicability of a CFD code in the simulation of complex flows by simulating key, stand-alone phenomena.

3. Advance the swirling jet application field by extending the degree of knowledge of the mechanisms that result in the enhancement of mixing and heat transfer via swirling jets, including the impact of Re, S, T, the CRZ, and swirl decay.

4. Develop new vortex swirl models that are based on the superposition of the azimuthal and axial velocities.

5. Investigate the formation of the CRZ, formulate a theory for its formation point, and predict its formation via the Fuego CFD code.

6. Investigate the thermalhydraulic behavior in the LP for multiple swirling jets at elevated temperature (1,200 to 1,400 K) interacting with crossflows, staggered rod bundles, and plate impingement.

7. Apply the methodology and theory discussed in Items 1 through 6 to develop CFD calculations for a safer and better designed LP.

Due to the complex nature of the VHTR LP (e.g., myriad of support posts and high temperature helium), no integral, full-scale LP experimental facility currently exists. Based on the estimates found in Table 2, a full-scale experiment at prototypic thermalhydraulic conditions would easily cost multiple millions of dollars. Therefore, the Fuego code will be used to model a set of key V&V single-effect, stand-alone phenomena found in the LP. If Fuego is shown to be suitable for the modeling of the key phenomena, then confidence is gained that it can be used to model the complex LP geometry with conventional as well as swirling jets. Details of the key V&V stand-alone thermalhydraulic phenomena are found in Table 7 of Section 5.2. Thereafter, a full-scale, half-symmetry finite element model of the LP will be developed.

Because swirling jets will be included in the LP model, it is important to develop a methodology to allow Fuego to numerically compute the correct azimuthal and axial velocity components. This methodology should allow the user to explicitly formulate the velocity components that represent a given swirl field based on the geometric S. Numerous types of swirling vortex flows have been developed over the years, such as the

54

- Loitsyanskiy vortex [Loitsyanskiy, 1953],

- Gortler vortex [Gortler, 1954; Khorrami, 1995],

- Sullivan vortex [Sullivan, 1959; Huang *et al.*, 2008],

- Newman vortex [Newman, 1959],

- Lamb (or Lamb-Oseen) vortex [Lamb, 1932; Mayer and Powell, 1992; Sipp, Coppens, and Jacquin, 1999; Olendraru and Sellier, 1999; Chadwick, 2006; Facciolo, 2006; Takahashi and Miyazaki, 2006; Busch, Ryan, and Sheard, 2007; Sereno, Pereira, and Pereira, 2009; Mao and Sherwin, 2009],

- Batchelor vortex (also known as the "q" vortex) [Batchelor, 1964; Tam, 1971; Duck and Foster, 1980; Mayer and Powell, 1992; Sipp, Coppens, and Jacquin, 1999; Olendraru and Sellier, 1999; Delbende, 2002; Facciolo, 2006; Mao and Sherwin, 2009],

- Squire vortex [Squire, 1965],

- Burgers vortex [Burgers, 1948; Rott, 1958; Rott, 1959; Maxworthy, Hopfinger, and Redekopp, 1985; Bazant and Moffatt, 2005], and

- Rankine vortex (also known as the "solid body" vortex) [Rankine, 1858; Loiseleux, Chomaz, and Huerre, 1998; Billant, Chomaz, and Huerre, 1998; Facciolo, 2006; Rossi, 2006; Ortega-Casanova and Fernandez-Feria, 2009; Sereno, Pereira, and Pereira, 2009].

There are many other vortices, such as vortices whose tangential velocity is only in the shear layer [Lu and Lele, 1997; Cooper and Peake, 2002] and the Scully vortex [Scully, 1975; Zioutis *et al.*, 2010].

Despite the enormous wealth of vortices already found in the literature, this research will develop a new mathematical formulation for a helicoid vortex swirl model that will be used exclusively to replace geometric swirl devices. The primary reasons for this are that:

1. There does not appear to be any one vortex that the literature justifies as the "most" appropriate for swirling flow research,

2. At this point in this research, it is postulated that the azimuthal velocity can be expressed as a simplified sinusoidal distribution that can forms a superposition with a constant axial velocity. This formulation will conveniently allow the vortex flow field to be expressed solely as functions of S (a key feature that was not found in the literature for any of the vortices discussed herein), and

3. If Point 2 above is developed to its full extent (as will be shown in Section 5.1.1), then many important insights regarding swirling flows can be obtained (*see* Sections 5.1.2 through 5.1.12), and in turn, those insights can be used to further extend the ability of swirling jets to enhance mixing and heat transfer in the VHTR LP (*see* Section 5.3).

A detailed helicoid vortex swirl model derivation is found in Section 5.1. A detailed description of the proposed methodology to solve the problem statement is presented in Section 4.

4. METHODOLOGY

The proposed methodology to solve the research problem consists of a three-pronged approach:

1. Develop advanced modeling methodology for swirling jets,

2. Perform V&V of the Fuego CFD code for key LP thermalhydraulic phenomena, and

3. Apply the above insights towards the full-scale modeling of the LP.

As will be shown later, the application of optimized helicoid vortex swirl devices will significantly enhance turbulence and heat transfer. In effect, by developing a unique mathematical model, it will be possible to investigate swirl on a more fundamental basis to assess its adequacy and to improve its thermalhydraulic characteristics. Of course, before the vortex technology can be used with confidence, it is crucial to show that the CFD tool can reliably calculate the complex phenomena in the LP. For that reason, a key set of V&V studies will be conducted and compared with experimental data, theory, and other codes.

Hot-wire anemometers [Jorgensen, 2002; Naughton *et al.,* 2007] and luminescent visualization techniques [Bates, 2007] have been used successfully to measure turbulence. Recently, more modern laser-based flow visualization techniques have been used to visualize turbulent flow patterns and swirling flow [Kihm, Chigier, and Sun, 1990; Danitz, 1995; Munekata, Ohba, and Matsuzaki, 2001; Crimaldi and Knight, 2005; Bonaldo, 2007; Naughton *et al.,* 2007; Felli, Falchi, and Fornari, 2008; Semaan and Naughton, 2009; Toh, Honnery, and Soria, 2010]. Particle image velocimetry (PIV) has

also been used successfully [McIlroy *et al.*, 2006b]. For the computational work presented herein, the Fuego CFD output was analyzed with the visualization software, Paraview [Paraview, 2010], and where appropriate, displayed with Matlab [Matlab, 1999] and Maple [Maple, 2001]. For some of the larger calculations, the Paraview software was used in parallel, with some sessions requiring as many as 64 processors to compute as many as 50,000 velocity streamlines. Other features of Paraview that will be used include volume rendering, thresholds, and the statistical package.

That swirling jets offer enhanced mixing and heat transfer under certain conditions can be readily shown by comparing the flow fields for conventional and swirling gas jets for the stand-alone models, as shown in Figure 20. Note that both jets have the same diameter and expand into an open domain. While the conventional jet had no azimuthal rotation, the swirling jet had S=0.67 (θ=45º). Notice that the swirling jet had a wider jet core diameter, a higher degree of entrainment, and that the azimuthal rotation caused more fluid mixing than the conventional jet. For the swirling jet, part of the axial momentum was converted to azimuthal momentum, so the axial velocity component decayed much faster than the conventional jet, as shown in the figure. For jets in the LP, the research presented herein showed that the jets with S=0.67 were ~ 70% wider than the conventional jets (*see* Section 5.3.3) [Rodriguez and El-Genk, 2010c].
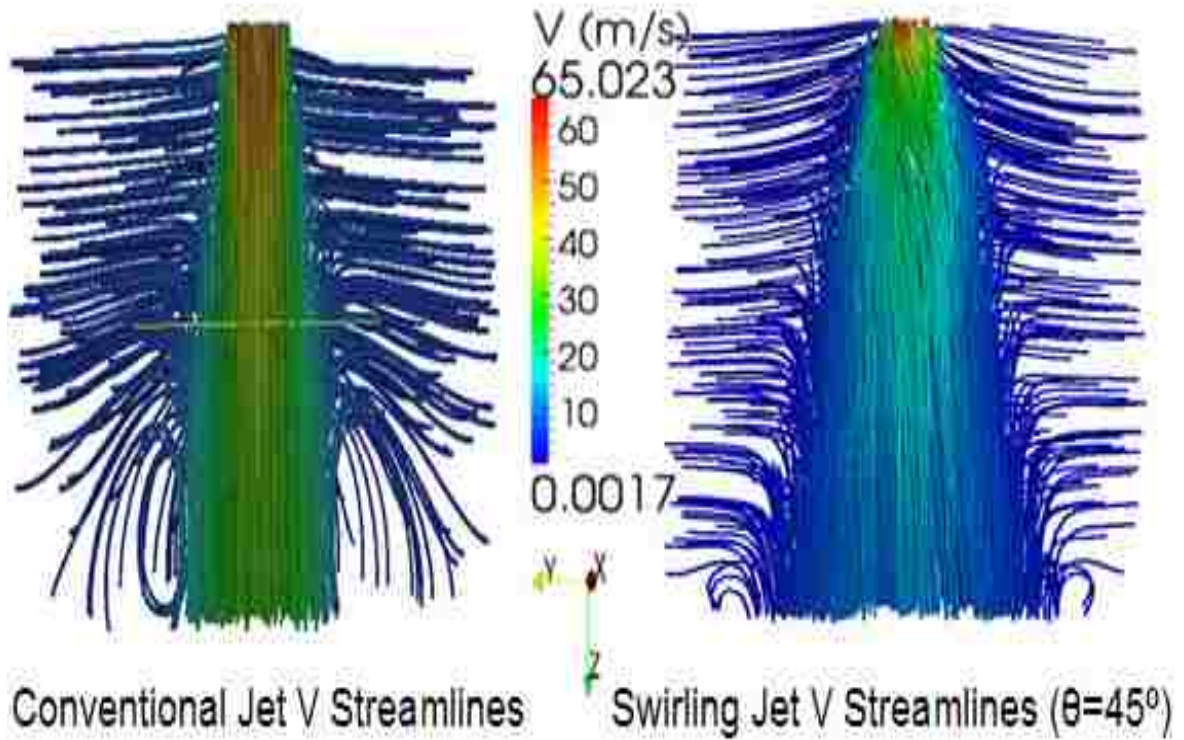
Figure 20. Comparison of Conventional vs. Swirling Jet Velocity Streamlines for the Standalone Models.

4.1 Vortex Modeling

As a starting point for this research, the wide field of turbulent vortex flows can be narrowed down to those that are axisymmetric, incompressible, Newtonian swirling jets with at most a single-cell, as defined in Section 5.1.6. These vortices have been studied in many types of coordinates. A rather "unnatural" selection is Cartesian coordinates, as the flow field rotates about the axisymmetric axis, which is generally selected as the z coordinate. Therefore, the axisymmetric vortex flow is symmetric about the z axis as the flow rotates in the azimuthal direction, and continues to expand in the z direction. Vortex research in Cartesian coordinates includes the Green-Taylor vortex [Taylor and Green, 1937] and the helicoid vortex developed in Section 5.1.1 [Rodriguez and El-Genk, 2008a,

2010d]. Various researchers selected spherical coordinates [Tsukker, 1955; Gol'Dshtik and Yavorskii, 1986; Hwang and Chwang, 1992], but the vast majority of the research found in the literature is in cylindrical coordinates [Rankine, 1858; Lamb, 1932; Burgers, 1948; Loitsyanskiy, 1953; Gortler, 1954; Newman, 1959; Sullivan, 1959; Batchelor, 1964; Squire, 1965; Chepura, 1969; Martynenko, 1989; Aboelkassem, Vatistas, and Esmail, 2005; Rodriguez and El-Genk, 2008a, 2010d]. Cylindrical coordinates are chosen primarily due to its geometric simplicity and excellent mapping of the vortex behavior onto a coordinate system—in particular, as a 3D vortex spins azimuthally as it stretches about the z axis, the vortex velocity field shape fills up a cylindrical geometry. Certainly, conical coordinates could be used, but they are not as convenient to manipulate mathematically, and besides, as the vortex expands, it forms a 3D cone; care needs to be taken such that the swirl angle of the vortex is not so large that it generates a swirl field with an angle that is larger than the conical coordinate system!

Consider a cylindrical coordinate system with r, θ, and z as the radial, azimuthal, and axial components, as defined in Figure 21. The 3D NS equations and conservation of mass are described next.
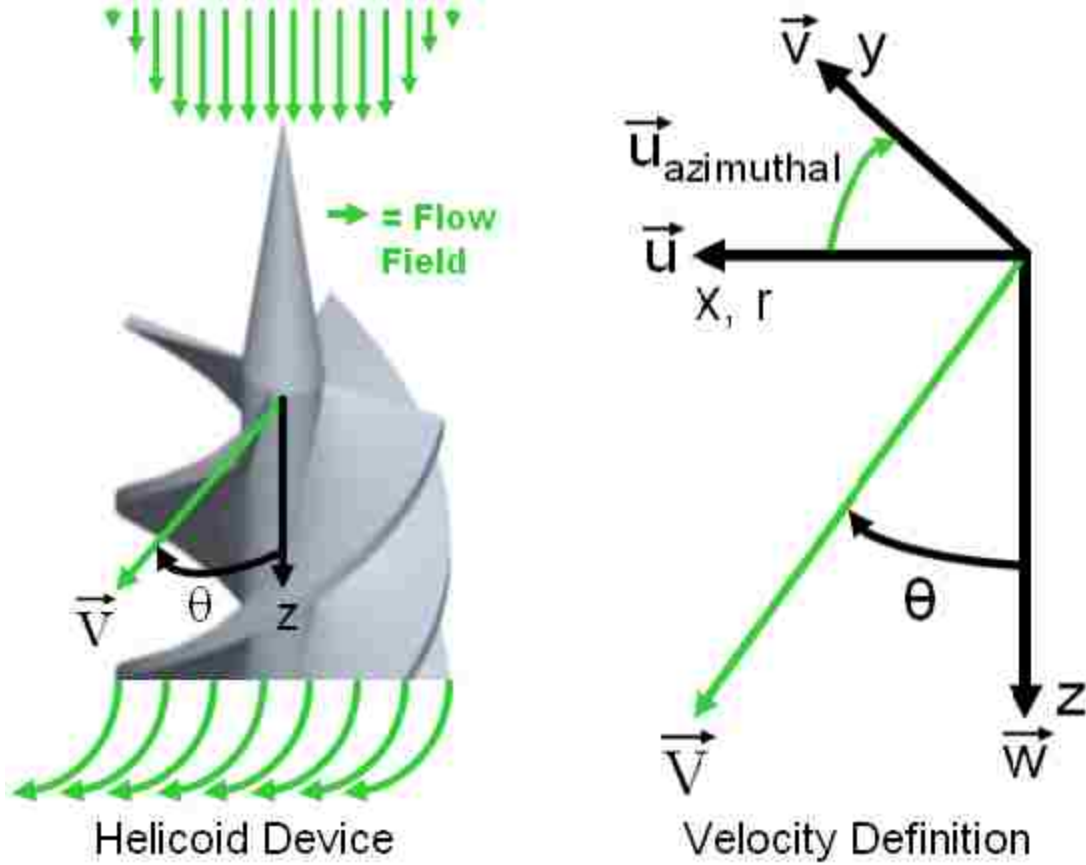
Figure 21. Helicoid Swirl Device and Associated Velocity Distribution.

For conservation of momentum in the r direction:

$$
\begin{aligned}
&\frac{\partial u}{\partial t} + u\frac{\partial u}{\partial r} + \frac{v}{r}\frac{\partial u}{\partial \theta} - \frac{v^2}{r} + w\frac{\partial u}{\partial z} \\
&= -\frac{1}{\rho}\frac{\partial p}{\partial r} + \nu\left(\nabla^2 u - \frac{u}{r^2}\right) + g_r \\
&= -\frac{1}{\rho}\frac{\partial p}{\partial r} + \nu\left\{\frac{\partial}{\partial r}\left[\frac{1}{r}\frac{\partial}{\partial r}(ru)\right] + \frac{1}{r^2}\frac{\partial^2 u}{\partial \theta^2} - \frac{2}{r^2}\frac{\partial v}{\partial \theta} + \frac{\partial^2 u}{\partial z^2}\right\} + g_r \\
&= -\frac{1}{\rho}\frac{\partial p}{\partial r} + \nu\left(\frac{\partial^2 u}{\partial r^2} + \frac{1}{r}\frac{\partial u}{\partial r} - \frac{u}{r^2} + \frac{1}{r^2}\frac{\partial^2 u}{\partial \theta^2} - \frac{2}{r^2}\frac{\partial v}{\partial \theta} + \frac{\partial^2 u}{\partial z^2}\right) + g_r
\end{aligned}
\tag{54}
$$

Conservation of momentum in θ:

$$\frac{\partial v}{\partial t} + u\frac{\partial v}{\partial r} + \frac{v}{r}\frac{\partial v}{\partial \theta} + \frac{vu}{r} + w\frac{\partial v}{\partial z}$$

$$= -\frac{1}{\rho r}\frac{\partial p}{\partial \theta} + \nu\left(\nabla^2 v - \frac{v}{r^2}\right) + g_\theta$$

$$= -\frac{1}{\rho r}\frac{\partial p}{\partial \theta} + \nu\left\{\frac{\partial}{\partial r}\left[\frac{1}{r}\frac{\partial}{\partial r}(rv)\right] + \frac{1}{r^2}\frac{\partial^2 v}{\partial \theta^2} + \frac{2}{r^2}\frac{\partial u}{\partial \theta} + \frac{\partial^2 v}{\partial z^2}\right\} + g_\theta$$

$$= -\frac{1}{\rho r}\frac{\partial p}{\partial \theta} + \nu\left(\frac{\partial^2 v}{\partial r^2} + \frac{1}{r}\frac{\partial v}{\partial r} - \frac{v}{r^2} + \frac{1}{r^2}\frac{\partial^2 v}{\partial \theta^2} + \frac{2}{r^2}\frac{\partial u}{\partial \theta} + \frac{\partial^2 v}{\partial z^2}\right) + g_\theta$$

(55)

Conservation of momentum in z:

$$\frac{\partial w}{\partial t} + u\frac{\partial w}{\partial r} + \frac{v}{r}\frac{\partial w}{\partial \theta} + w\frac{\partial w}{\partial z}$$

$$= -\frac{1}{\rho}\frac{\partial p}{\partial z} + \nu\nabla^2 w + g_z$$

$$= -\frac{1}{\rho}\frac{\partial p}{\partial z} + \nu\left[\frac{1}{r}\frac{\partial}{\partial r}\left(r\frac{\partial w}{\partial r}\right) + \frac{1}{r^2}\frac{\partial^2 w}{\partial \theta^2} + \frac{\partial^2 w}{\partial z^2}\right] + g_z$$

$$= -\frac{1}{\rho}\frac{\partial p}{\partial z} + \nu\left(\frac{\partial^2 w}{\partial r^2} + \frac{1}{r}\frac{\partial w}{\partial r} + \frac{1}{r^2}\frac{\partial^2 w}{\partial \theta^2} + \frac{\partial^2 w}{\partial z^2}\right) + g_z$$

(56)

Conservation of mass:

$$\frac{\partial \rho}{\partial t} + \frac{1}{r}\frac{\partial(\rho ru)}{\partial r} + \frac{1}{r}\frac{\partial(\rho v)}{\partial \theta} + \frac{\partial(\rho w)}{\partial z} = \frac{\partial \rho}{\partial t} + \rho\frac{\partial u}{\partial r} + \frac{\rho u}{r} + \frac{\rho}{r}\frac{\partial v}{\partial \theta} + \frac{\rho\partial w}{\partial z} = 0$$

(57)

where

$$\nabla = \frac{\partial}{\partial r} + \frac{1}{r}\frac{\partial}{\partial \theta} + \frac{\partial}{\partial z}$$

(58)

and

$$\nabla^2 = \frac{1}{r}\frac{\partial}{\partial r}\left(r\frac{\partial}{\partial r}\right) + \frac{1}{r^2}\frac{\partial^2}{\partial \theta^2} + \frac{\partial^2}{\partial z^2} = \frac{\partial^2}{\partial r^2} + \frac{1}{r}\frac{\partial}{\partial r} + \frac{1}{r^2}\frac{\partial^2}{\partial \theta^2} + \frac{\partial^2}{\partial z^2}$$

(59)

For steady state, incompressible, negligible gravitational term, Newtonian, and symmetry about the z axis (axisymmetry), NS and the conservation of mass equations simplify to the following terms:

62

$$u\frac{\partial u_r}{\partial r} - \frac{v^2}{r} + w\frac{\partial u}{\partial z} = -\frac{1}{\rho}\frac{\partial p}{\partial r} + \nu\left(\frac{\partial^2 u}{\partial r^2} + \frac{1}{r}\frac{\partial u}{\partial r} - \frac{u}{r^2} + \frac{\partial^2 u}{\partial z^2}\right) \tag{60}$$

$$u\frac{\partial v}{\partial r} + \frac{vu}{r} + w\frac{\partial v}{\partial z} = \nu\left(\frac{\partial^2 v}{\partial r^2} + \frac{1}{r}\frac{\partial v}{\partial r} - \frac{v}{r^2} + \frac{\partial^2 v}{\partial z^2}\right) \tag{61}$$

$$u\frac{\partial w}{\partial r} + w\frac{\partial w}{\partial z} = -\frac{1}{\rho}\frac{\partial p}{\partial z} + \nu\left(\frac{\partial^2 w}{\partial r^2} + \frac{1}{r}\frac{\partial w}{\partial r} + \frac{\partial^2 w}{\partial z^2}\right) \tag{62}$$

$$\frac{\partial u}{\partial r} + \frac{u}{r} + \frac{\partial w}{\partial z} = 0 \tag{63}$$

with

$$\nabla = \frac{\partial}{\partial r} + \frac{\partial}{\partial z} \tag{64}$$

$$\nabla^2 = \frac{\partial^2}{\partial r^2} + \frac{1}{r}\frac{\partial}{\partial r} + \frac{\partial^2}{\partial z^2} \tag{65}$$

An inspection of the literature over the past 150 years shows that the above equations are generally the departure point for generating analytic solutions for axisymmetric swirling flows (vortices) [Rankine, 1858; Lamb, 1932; Burgers, 1948; Loitsyanskiy, 1953; Gortler, 1954; Newman, 1959; Sullivan, 1959; Batchelor, 1964; Squire, 1965; Chepura, 1969; Martynenko, 1989; Aboelkassem, Vatistas, and Esmail, 2005; Rodriguez and El-Genk, 2008a, 2010d].

4.2   Helicoid Swirl Modeling

Helicoids for the generation of numerical swirling-flow fields may be produced by various approaches. One method is via a geometrical specification of a static, swirling device that consists of helicoidal surfaces, and another is a mathematical description of a swirling BC that reproduces the flow field. It has been reported in the literature and

confirmed by this research that if a CFD code does not have a swirl boundary option, it is customary to develop the geometry for a swirl device and then mesh it [Duwig *et al.* 2005; Fujimoto, Inokuchi, and Yamasaki, 2005; Garcia-Villalba, Frohlich, and Rodi, 2005; Rodriguez and El-Genk, 2008a, b, c, and d; Rodriguez, Domino, and El-Genk, 2010; Rodriguez and El-Genk, 2010a and b; Rodriguez and El-Genk, 2011a and b]. Several static swirl devices are shown in Figures 22 and 23. The swirl device used in this research consisted of a sharp cone that surrounded four helical surfaces that were off-set by 90° and that spiraled symmetrically around the cylinder (Figure 21, LHS). Because the swirling device is static, the helium gas flows around the helicoid surfaces, producing a swirling motion as the gas travels around the surfaces. Then, due to inertia, the swirling motion continues as the helium exits the jet nozzle outlet and into the LP chamber.
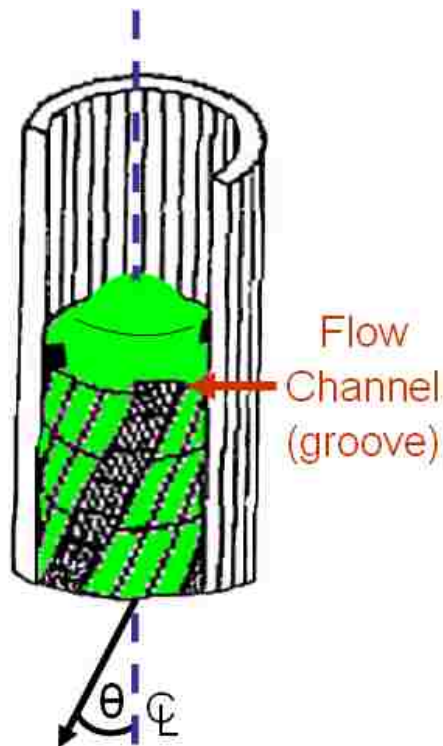
Figure 22. Swirling Device with Geometry Suitable for VHTRs.

64
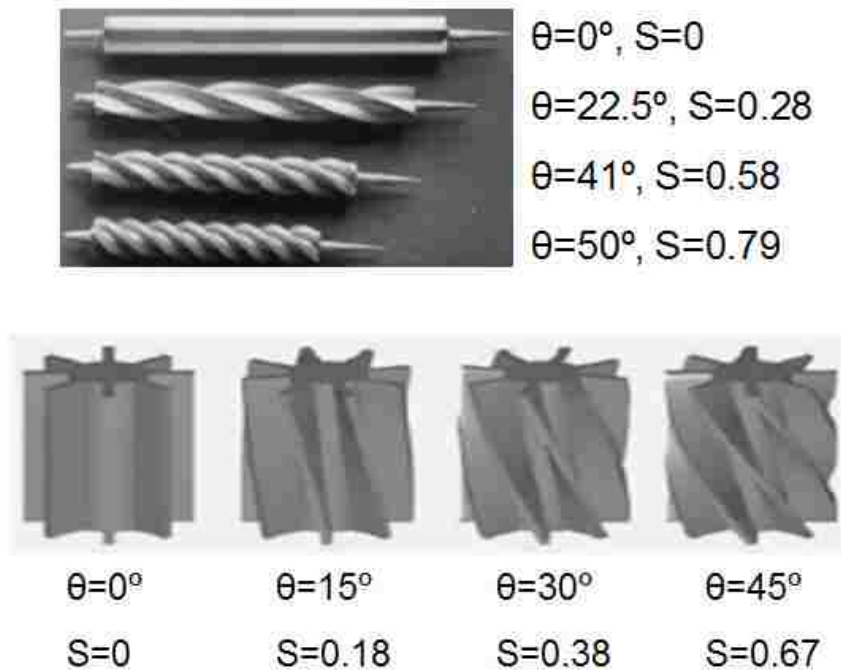
Figure 23. Various Swirl Devices Found in the Literature [Huang, 1996; Huang and El-Genk, 1998; Larocque, 2004].

However, deciding on a particular swirl angle *a priori* for the swirling device, and then meshing its geometry, is computationally-intensive and time consuming, not to mention that it is a tedious, error-prone, and expensive process. Furthermore, it is a challenge to investigate many swirl angles and keep track of all the meshes, which is the case for this research. Finally, as will be shown *a posteriori*, having a closed form mathematical formulation for the swirling field will yield significant insights concerning the behavior of the velocity fields and their impact on heat transfer, as evidenced in Sections 5.1.1 through 5.1.5.

Now, once a mathematical swirl formulation is derived, it is a straightforward matter to apportion the jet velocity fields such that any given swirl angle is uniquely specified. As a result, a mathematically-generated velocity field with no helicoid surfaces (i.e. just swirl BCs) can very closely approximate the swirl field of the geometric helicoid device

shown in Figure 21. To demonstrate this, two meshes were developed: one had a

geometric swirl device and the other used only BCs (*see* Figure 24). The CFD

computation for both meshes had the same S (S is defined in Section 5.1.1).
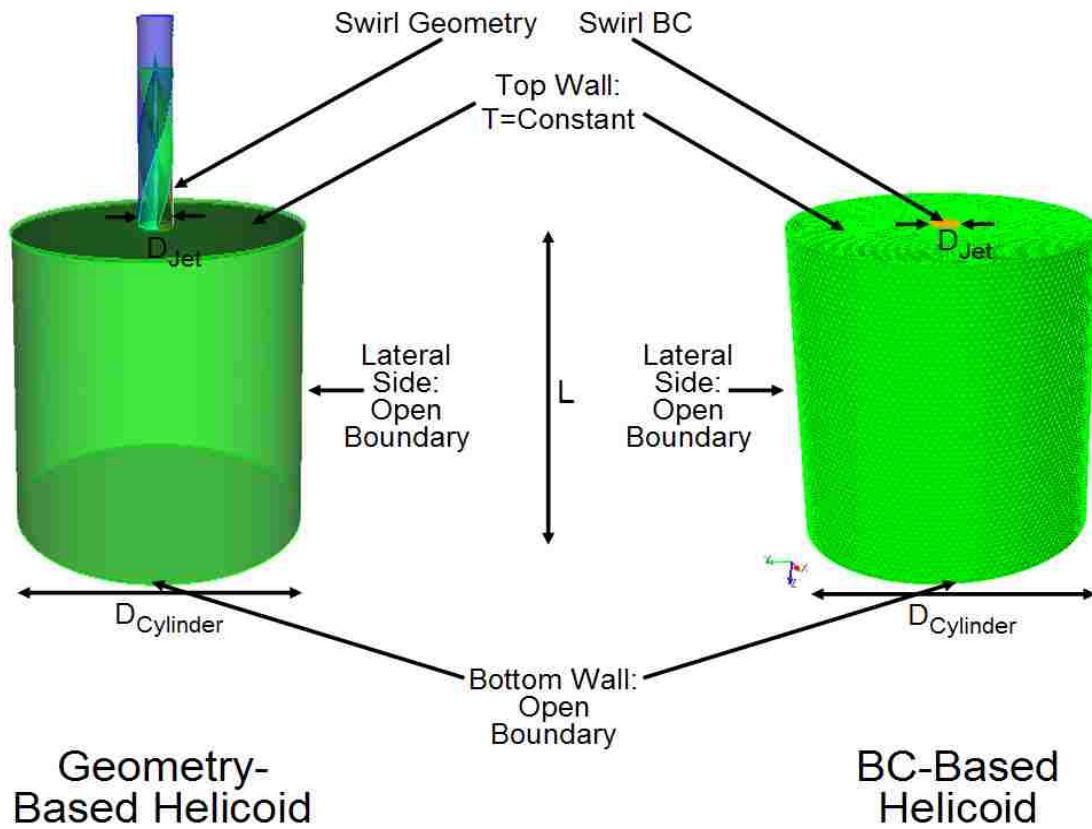
Figure 24. Comparison of Geometric and BC Swirl Models.

A comparison of the output for both models showed that the total velocity vector

streamlines were essentially indistinguishable, as shown in Figure 25. The azimuthal

velocity is compared in Figure 26, again showing that the velocity streamlines were fairly

identical. Finally, Figure 27 compares the u, v, w, and u + v velocity fields at the swirl

boundary (where the swirl circle boundary is coincident with the large cylinder). Recall

that the geometry-based helicoids are formed by four helicoidal surfaces, with a thin

cylinder at the center that holds the surfaces. A consequence of these additional, discontinuous surfaces is that the flow at their walls is zero (the surfaces are not moving). On the other hand, the swirl BCs are based solely on a mathematical model, and therefore the swirl velocity field is represented as a continuous circular surface. Thus, for any cross-section of the helicoids, a cruciform is described by the walls, with the fluid velocity at the walls being zero. In addition, the central hole where the thin cylinder crosses will also have zero velocity. Of course, that is not the case for the BC swirl field, as they neither have the cruciform nor the central hole surface. Accordingly, Figure 27 has blue and red velocity fields for the u and v velocity components in the form of sinusoidal velocity distributions that are quite similar for both models. However, the figure also shows that the main difference in velocity distribution was a consequence of walls with zero velocity. The cruciform and hole surfaces also resulted in differences for the w velocity field distribution, as well as the u + v velocity fields; however, as shown in Figures 25 and 26, the differences are small. So, in the limit as the thin cylinder and the cruciform walls become vanishingly small, the geometrical model approaches the BC model. Therefore, the "perfect" helicoid model can be expressed mathematically rather than geometrically because the helicoid blade thickness could never reach zero thickness in practical applications.

In any case, the emergent velocity fields were sufficiently identical between both models, and this research will therefore employ the mathematical model as often as possible. This will result in significant savings in the meshing and computational effort, especially because the helicoid geometry requires finite elements that are about four times smaller than the rest of the model, and further, the time step is dominated by the

smallest finite element. The development of the helicoid vortex swirl model (swirl BCs) is discussed in full detail in Section 5, and is used in the present investigations with single and multiple swirling jets for numerous S.

In short, Figure 24 shows a "geometry-based" helicoid on the LHS, which is a static insert that induces the swirling flow. The RHS shows a "BC-based" helicoid, which adequately approximates the helicoid geometry flow, as shown by comparing Figures 25 through 27. For the reasons stated above, the BC helicoid method will be used the majority of the time for this research.
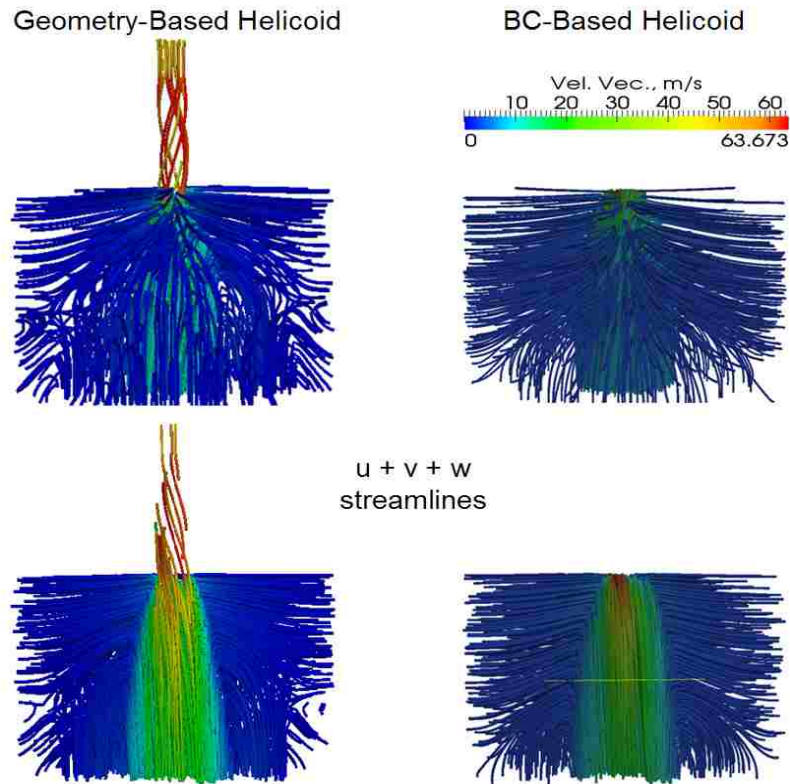
Figure 25. Comparison of the Geometric and BC Swirl Models: U + V + W Streamlines.
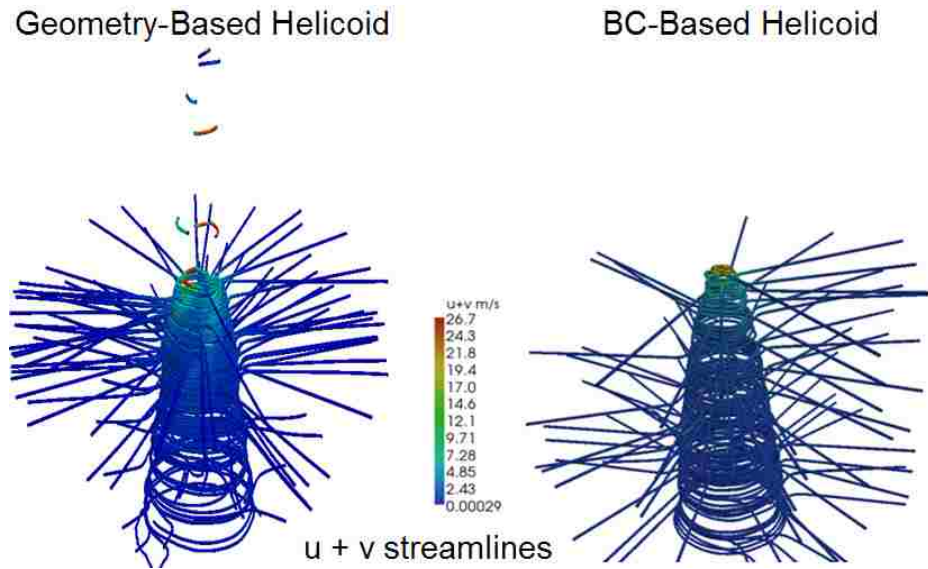
Figure 26. Comparison of the Geometric and BC Swirl Models: Azimuthal Velocity Streamlines.
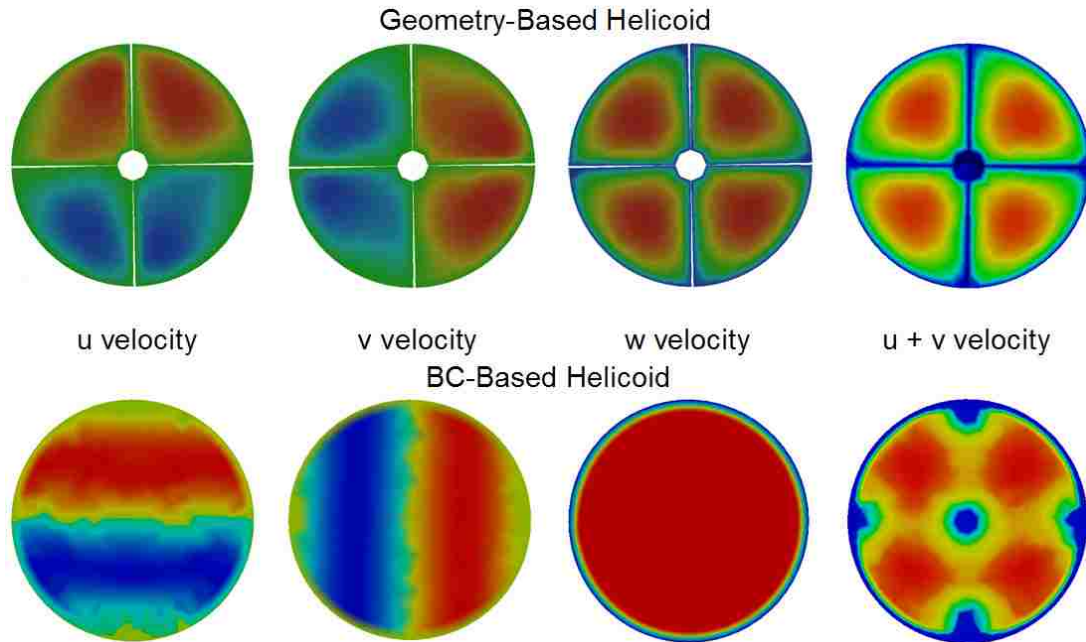
Figure 27. Comparison of the Geometric and BC Swirl Models: U, V, W, and U + V Velocity Fields at the Swirl Boundary.

4.3   Fuego Code and Models

Fuego is a 3D, incompressible, reactive flow, massively parallel, generalized unstructured CFD code with state-of-the-art turbulence models as well as laminar and buoyant flows [Laskowski *et al*., 2006]. It includes RANS and LES models [Domino, 2006; Domino and Gianoulakis, 2007; Fuego, 2008; Fuego, 2009]. The RANS models include v2-f, low Re k-ε, standard k-ε, as well as many others. Among Fuego's more sophisticated LES models are the KSGS, Smagorinsky, and dynamic Smagorinsky. The code has a wide variety of flux limiters, combustion models, participating media radiation (PMR), and conjugate heat transfer (CHT) [Fuego, 2009].

The Fuego CFD code is employed to investigate complex and multidimensional flow fields. The code is currently being developed at Sandia National Laboratories (SNL). Fuego is one of a set of strategic, comprehensive codes currently being developed through the Advanced Simulation and Computing (ASC) program at SNL.

Through user input, Fuego can be coupled to heat conduction and enclosure radiation models, as well as other ASC tools for additional physics calculations.

For the anisotropic turbulent flow fields and complex mixing expected in the VHTR LP, the dynamic Smagorinsky turbulence model is the most appropriate, as shown in Section 4.3.1. Fuego also includes Lagrangian [Price, 2006] transport capabilities appropriate for modeling particles and drops, some deposition modeling physics, and basic chemistry models [Fuego, 2009].

Fuego has recently undergone key V&V that include: conventional jet, swirling jet, conventional jet in crossflow, swirling jet in crossflow, flow around a vertical cylinder,

and staggered tubes in crossflow [Rodriguez and El-Genk, 2010a and b; Rodriguez, Domino, and El-Genk, 2010].

4.3.1   Turbulence Model Selection

Turbulent flow encountered in the VHTR LP involves wide ranges of length and time scales, requiring massive computational resources to directly resolve the physical processes, even for simplified high-Re problems. Modeling approximations must be made to solve complex problems of interest within a reasonable amount of computational time. A CFD user must decide which turbulence model is best suited for a given problem. Fuego has a wide variety of RANS models, which include the v2-f, standard k-ε, low Re k-ε, k-ω, SST, as well as many others, including the LES models [Fuego, 2008].

The commercial CFD code FLUENT has been used by INL to model the flow turbulence and mixing in the LP using conventional jets [McEligot and McCreery, 2004]. INL researchers have recently employed the k-ε, k-ω, and AKN k-ε turbulence models for the simulation of a simplified LP experiment. However, the experiment used mineral oil as the coolant, not high temperature helium. Also, the experiment operated at a relatively low Re (~12,000 vs. 24,000 to 3×10^6 expected in the actual NGNP) [Guillen and McIlroy, 2007; McIlroy, McEligot, and Pink, 2007; McIlroy, McEligot, and Pink, 2008a and b; Johnson, 2009a and b; Johnson and Schultz, 2009; McIlroy, McEligot, and Pink, 2010a and b]. Not quite unexpectedly, the INL research indicated that the k-ε methods did not provide satisfactory results. And interestingly, they noted a desire to employ LES or DNS turbulence methods instead [Schultz *et al*., 2004]!

As a result of the literature search conducted herein (Section 2.3), three mayor types

of turbulence models commonly employed in engineering processes and applications were investigated. *So, which turbulence model is best suited for modeling the LP?* Based on the findings in Section 2.3 and further deliberation found in the following paragraphs of this section, the LES dynamic Smagorinsky turbulence model was chosen as the clear-cut winner. A summary of the reasoning for the choice is presented next.

Although the DNS output compares excellently with experimental data [Moet *et al*., 2004; Freitag and Klein, 2005; Duraisamy and Lele, 2006; Facciolo, 2006; Afgan, 2007; Bonaldo, 2007; Busch, Ryan, and Sheard, 2007; Walther *et al*., 2007; Taub *et al*., 2010], it was not selected because it is computationally expensive. For example, it requires that the number of computational operations is on the order of Re^3 [Wikipedia, 2011b]. Further, for a 3D domain, the number of required cells is $Re^{9/4}$ [Afgan, 2007; Sodja, 2007; Stein, 2009] to as high as $Re^{11/4}$ [Taub *et al*., 2010]. By comparison, the number of computational time steps, N, for LES vs. DNS [Sodja, 2007] shows that

$$N_{LES} \approx \left(\frac{0.4}{Re_T^{1/4}} \right) N_{DNS} \qquad (66)$$

Equation 66 shows the significant savings when using LES over DNS, savings that grow substantially as Re increases.

Of the RANS time-averaged methods [Leschziner and Rodi, 1984; Abujelala and Lilley, 1985; Kilik and Finstad, 1985; Ahuja, Deshpande, and Merle, 1997; Meyyapan, Schwarz, and Perry, 1997; Larocque, 2004; Li, 2004; Mardani, 2004; Taglia *et al*., 2004; Guillen and McIlroy, 2007; Nematollahi and Nazifi, 2007; El-Behery and Hamed, 2009; Eldrainy, Ahmad, and Jaafar, 2009; Laurien, Lavante, and Wang, 2010], the review showed that the k-ω model was the most promising [El-Behery and Hamed, 2009; DeChant, 2010; Valera-Medina *et al*., 2010], but literature successes for the k-ω model in

the area of swirling flows is indeed limited. A substantial advantage of the RANS

methods is that they can require about 5% of the computing time required by LES

methods [Sodja, 2007]. *If so, this would strongly compel future investigation of the k-ω*

model for swirling flows.

Because turbulent jet flow in the LP is anisotropic, the k-ε model is not appropriate,

as clearly shown when the calculational results are compared with experimental data

[Leschziner and Rodi, 1984; Kilik and Finstad, 1985; Abujelala and Lilley, 1985; Ahuja,

Deshpande, and Merle, 1997; Meyyapan, Schwarz, and Perry, 1997; Larocque, 2004; Li,

2004; Mardani, 2004; Taglia *et al*., 2004; Guillen and McIlroy, 2007; Nematollahi and

Nazifi, 2007; El-Behery and Hamed, 2009; Eldrainy, Ahmad, and Jaafar, 2009; Laurien,

Lavante, and Wang, 2010].

Whereas the RANS RSMs are designed to include non-isotropic effects, they had

mixed results in the literature [Gibson and Younis, 1986; Hogg and Leschziner, 1989;

Lai, 1995; Larocque, 2004; Krishna and Ganesan, 2005; Johnson, 2006; El-Behery and

Hamed, 2009; Laurien, Lavante, and Wang, 2010; Valera-Medina *et al*., 2010]. Perhaps

not surprisingly, the literature includes warnings that whereas RSMs are theoretically

suited to tackle swirl flows, "the RSM might not always yield results that are clearly

superior to the simpler models in all classes of flows…" [FLUENT, 2011]. The source

notes that RSMs have a great potential to calculate complex flows, but also points out

that the model's predictive capabilities are only as good as the closure assumptions that

were employed.

By contrast, the literature contains an abundance of applications where the

researchers used the LES spatial-filtering calculations for swirling jets at high Re and

weak to strong S, with favorable comparisons to experimental data [Kim and Menon, 1999; Kravchenko and Moin, 2000; Cziesla *et al*., 2001; Schluter, 2001; Apte *et al*., 2003; Garcia-Villalba, Frohlich, and Rodi, 2004; Wang and Bai, 2004; Moet *et al*., 2004; Duwig *et al*., 2005; Garcia-Villalba, Frohlich, and Rodi, 2005; Lu *et al*., 2005; Fujimoto and Yamasaki, 2006; Garcia-Villalba and Frohlich, 2006; Gyllenram, Nilsson, and Davidson, 2006; Afgan, 2007; Bonaldo, 2007; Jagus *et al*., 2008; Muller and Kleiser, 2008; Rodriguez and El-Genk, 2008a, b, c, and d; Denev, Frohlich, and Bockhorn, 2009; Dinesh and Kirkpatrick, 2009; El-Behery and Hamed, 2009; Iaccarino and Constantine, 2009; Naughton *et al*., 2009; Stein, 2009; Uddin *et al*., 2009; Zemtsop *et al*., 2009; Doolan, 2010; Rodriguez, Domino, and El-Genk, 2010; Rodriguez and El-Genk, 2010a and b; Rodriguez and El-Genk, 2011a and b].

It is noteworthy that a swirling jet in crossflow was recently simulated with the LES Smagorinsky model for $0 \leq S \leq 0.6$ with excellent results [Denev, Frohlich, and Bockhorn, 2009]. In addition, other researchers used LES successfully to model the flow and heat transfer characteristics for an impinging, conventional jet [Cziesla *et al*., 2001; Voke and Gao, 1997].

Furthermore, researchers have noted that LES turbulence models are able to successfully model recirculation zones and vortex breakdown, and are thus suitable for investigating swirling jet instabilities [Dinesh and Kirkpatrick, 2009]. Swirling jet LES calculations with and without a CRZ have been successfully investigated, and have shown that formation of the CRZ impacts the heat transfer [Uddin *et al*., 2009]. A staggered grid of tubes with crossflow at Re=8,600 and with triangular pitch was calculated using LES, and had good agreement with experimental measurements [Liang

and Papadakis, 2007]. Other researchers used LES to model axial flow for a square array of tubes at Re=85,000 and P/D=1.08, with excellent comparison with experimental data [Abbasian, Yu, and Cao, 2010].

On the other hand, only one apparent failure was found in the literature, which even the authors apparently found suspicious [Valera-Medina *et al.*, 2010]. Another issue with LES is that they are notoriously grid-dependent, with issues that have yet to be satisfactorily resolved as of February 2011 [Bose, Moin, and You, 2011].

Therefore, given the LES model's wide application database, its success modeling experimental data for relevant phenomena that includes high Re, jet flows, weak to strong swirl, and staggered tubes in crossflow, as well as its calculational speed compared with DNS, the LES is clearly the best turbulence model for this research. The grid-dependency issue is considered insignificant if care is taken when performing the CFD calculations. Therefore, the Fuego LES dynamic Smagorinsky turbulence model will be used for all the calculations presented herein.

4.3.2   Participating Media Radiation

The spatial variation of the radiative intensity corresponding to a given direction and at a given wavelength within a radiatively participating material, I(s), is governed by the Boltzmann transport equation. In general, the Boltzmann equation represents a point balance between absorption, emission, out-scattering, and in-scattering of radiation. For most engineering applications, however, the steady form of the Boltzmann equation is appropriate since the transient term only becomes important on nanosecond time scales, which are orders of magnitude shorter than the fastest chemical reaction. Under the assumptions of a non-scattering, gray media, with the turbulent fluctuation effects

ignored, the Boltzmann equation for the lth ordinate direction is given by:

$$s_i^l \frac{\partial}{\partial x_i} I^l(s) + \mu_a I^l(s) = \mu_a \frac{\sigma T^4}{\pi} \tag{67}$$

where s_i^l is the lth ordinate direction, μ_a is the absorption coefficient, and I^l is the intensity along the lth ordinate direction. Note that as a first-order approximation, the turbulent fluctuations for non-reacting flow are not included in the Boltzmann equation, as their impact on radiation is small compared to those of the terms that were retained. On the other hand, the turbulent fluctuations are appropriately addressed in the gas phase transport equations. When chemistry is active, the subgrid fluctuations in the radiative source term and mean absorption coefficient are included based on a presumed probability density function approach (correlations between absorption and intensity are always neglected). As noted, scattering effects are also ignored, although an isotropic scattering code capability can be activated, as warranted.

The radiation intensity boundary condition, assuming a diffuse surface, is given by:

$$I(s) = \frac{1}{\pi} \left[\tau \sigma T_\infty^4 + \varepsilon \sigma T_w^4 + (1 - \varepsilon - \tau) q_j^{inc} n_j \right] \tag{68}$$

In this expression, τ is the transmissivity, ε is the emissivity, T_∞ is the environmental temperature, and T_w is the wall temperature. Note that Kirchhoff's law employed in the above equation is used to relate emissivity, transmissivity, and reflectivity, ρ as:

$$\rho + \tau + \varepsilon = 1. \tag{69}$$

This assumes that absorptivity equals the emissivity. A quadrature set is provided to assemble the individual intensity and solve for quantities such as the scalar flux:

$$G = \sum_L w_L I^L, \tag{70}$$

and the radiative flux:

$$q_j^r = \sum_L w_L I^L s^L .$$

(71)

The Sierra mechanics module responsible for the solution of the radiative transport equation is Syrinx. The underlying discretization employs a streamwise upwind Petrov-Galerkin finite element method discretization for the method of discrete ordinates [Burns, 1997]. The degree of local stabilization is controlled by a comparison between the cell size and optical thickness. When the optical thickness increases, the full operator is used, while in thin regions, the Fuego code reverts to an up-winded operator.

The coupling between the fluids and PMR regions is accomplished through the flux divergence source term:

$$\frac{\partial q_i^r}{\partial x_i} = \mu_a \left(4\sigma T^4 - G \right) .$$

(72)

This source term is linearized via a Taylor series to provide a left hand side (LHS) matrix contribution to the static enthalpy degree of freedom equation. The coupling between the PMR and fluids region is provided through the absorption coefficient and the emissive power.

4.3.3 Conjugate Heat Transfer

A CHT problem is one in which the conductive heat transfer in a solid region is coupled to the convective heat transfer in a neighboring fluid flow. In its most general form, the coupling at the boundary between these two regions is governed by the continuity of the heat flux at the interface, as:

$$q_j^F n_j = q_j^S n_j .$$

(73)

In Equation 73, q_j^F and q_j^S are the heat flux in the fluid and solid, respectively, and the normal n_j is directed into the solid and out of the fluid.

In the generalized CHT coupling, a fluids mechanics region solving for the static enthalpy is coupled at the surface to a heat conduction equation solving for temperature [Domino *et al.*, 2007]. In general, the solid heat flux can also include the effect of radiation via an augmented flux that is due to the irradiation onto or out of the surface. Oftentimes, however, a full CHT coupling is not required. Instead, a 1D approximation can be made in which an overall heat balance at the interface is performed, such as:

$$q_{in}^r + q_{in}^c = q_{out}^r + q_{out}^c. \tag{74}$$

Therefore, in this equation, the radiation and fluid solvers provide the incoming energy fluxes while the user specifies surface properties, backside heat transfer coefficients, the backside reference temperatures, and the wall thickness. The above equation is solved via Newton's method, and the resulting temperature is applied for the fluid and radiation boundary condition.

4.4   Calore Code

Calore is a 3D conduction and radiation unstructured heat transfer code for solving linear and nonlinear thermal systems. It can model steady state and transients, multiple solid and fluid materials, heat sources, chemistry, thermal contact, and accounts for temperature-dependent material properties [Bova, Copps, and Newman, 2006].

4.5   Coupled Fuego-Calore Multiphysics Code

The Sierra code structure includes a set of diverse physics codes with a broad range of numerical schemes. Fuego and Calore are part of Sierra. The Sierra codes were

designed to be massively parallel, and to facilitate code-to-code coupling [Domino, 2006; Domino and Gianoulakis, 2007].

The coupling of the various Sierra codes can be done at various levels. The simplest is through user input, and is the level of coupling used for this research. In this case, Calore performs heat conduction and enclosure radiation. It passes Fuego surface temperatures. Then, Fuego uses the surface temperatures as boundaries, calculates the turbulent fluid dynamics, and passes a convective heat transfer coefficient, along with fluid temperatures, to Calore. Syrinx takes care of the PMR. See Figure 28 for a conceptual description of the code couplings.
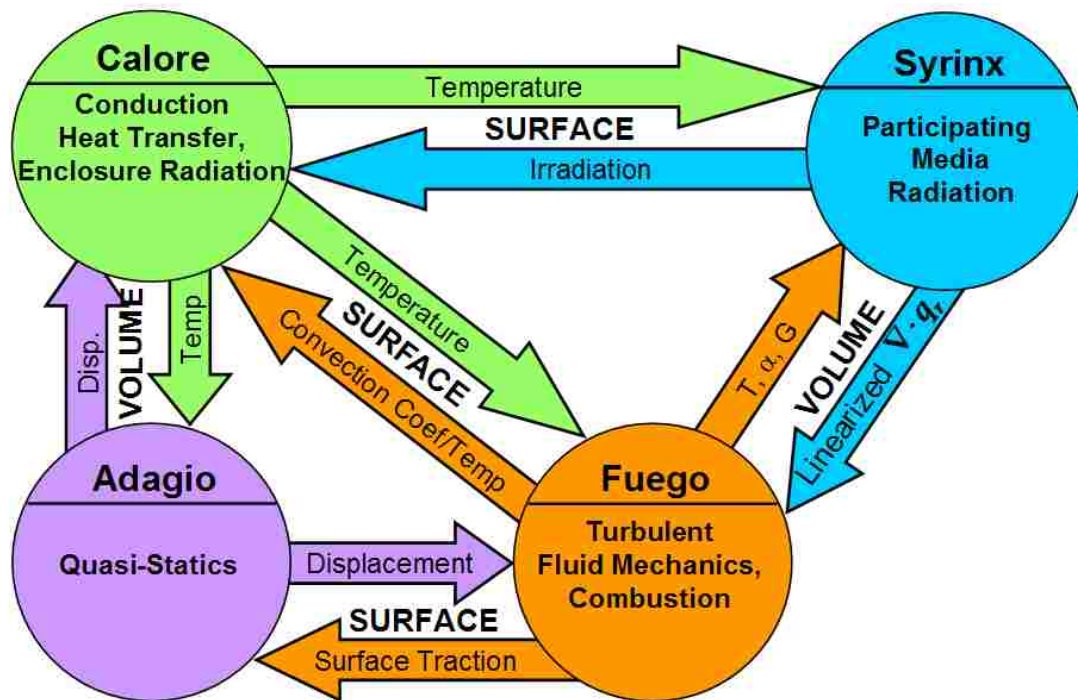
Figure 28. Fuego, Calore, Syrinx, and Adagio Coupling [Domino and Gianoulakis, 2007].

4.6 Fuego Validation and Verification of Single-Effect, Key Phenomena

A system model should undergo V&V of its sub-models in order to gain confidence when the tool is subsequently used to simulate a more complex system.

For this research, verification seeks to assess the correctness of the governing equations used for conservation of momentum, energy, and mass, as well as the associated equations, such as the equations of state, turbulence models, and so on. The goal of validation is to assess a code's quality and mathematical correctness. For example, a code can be validated by comparing its output with analytical solutions. By contrast, validation seeks to determine if the appropriate physical equations and domains are modeled properly by the code. For example, the code output could match experimental data.

A systematic process of V&V was conducted with the Fuego code on a set of key single-effect thermalhydraulic phenomena that are expected to occur in the LP. Basically, these simulations formed part of a crucial set of phenomena that must be modeled correctly before the complex flow in the VHTR LP can be modeled adequately.

As discussed previously, and shown in Figures 2 and 4, the LP involves rather complex geometry and thermalhydraulic conditions, and no integral thermalhydraulic experiment exists for the VHTR LP. Fortunately, there are many single-effect experiments and analytical solutions in the literature that adequately describe key phenomena found in the LP. So, if Fuego is able to simulate adequately the key single-effect phenomena, its output for the full-scale LP model ought to be more defensible. Details of the selected V&V single-effect models are found in Table 7, while the calculational results are found in Section 5.

4.7　　　　LP Modeling

Figure 29 shows the INL 1/2-symmetry LP model, which includes the supports posts, conventional jet exits, and wall structures. Results of a Fluent VHTR LP calculation run by General Atomics are shown in Figure 30 [McEligot and McCreery, 2004].

INL's nine region flow map of lower plenum and
corresponding RELAP5/ATHENA model components.
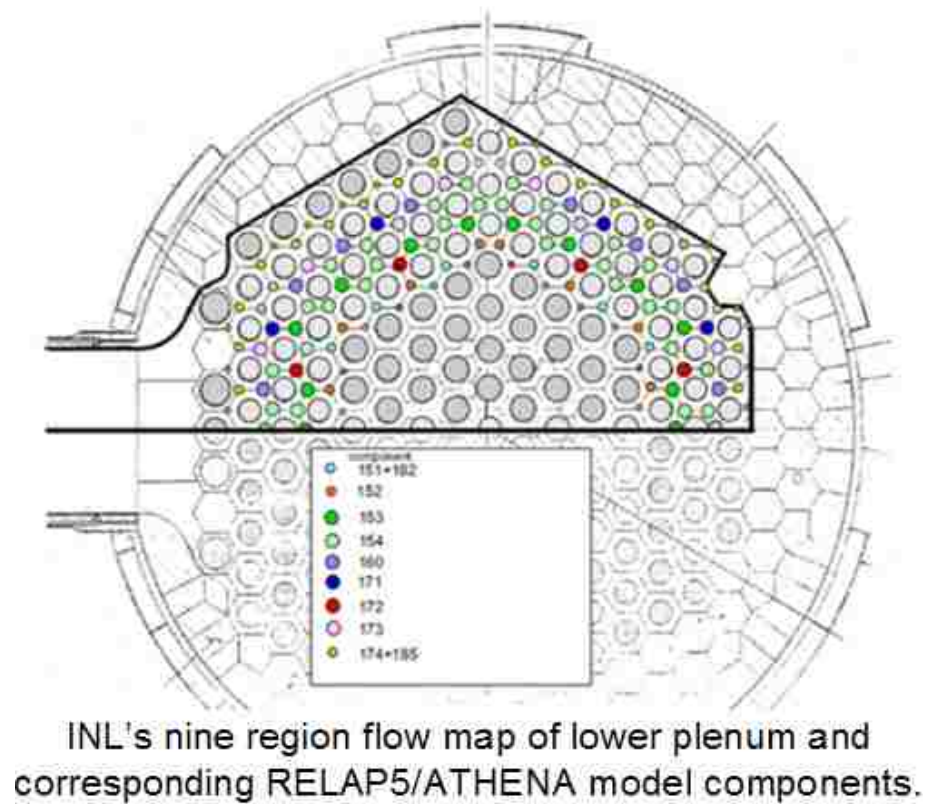
Figure 29. INL LP Model [McCreery and Condie, 2006].
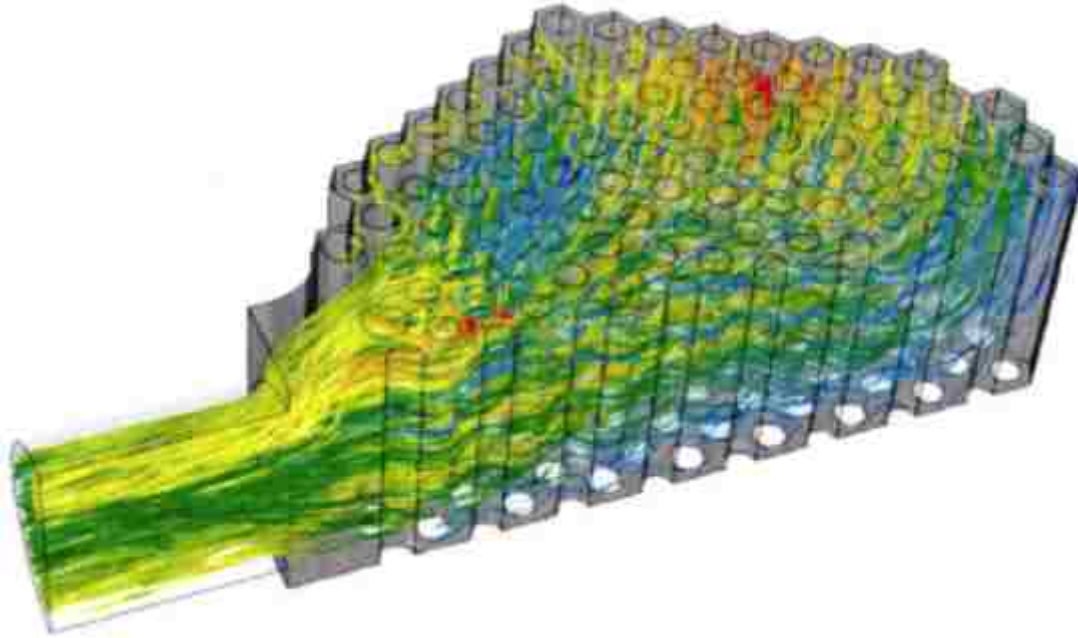
Figure 30. Fluent Temperature Overlayed on Velocity Streamlines for the VHTR LP [McEligot and McCreery, 2004].

The Fuego model used herein is based on the same INL geometry, and includes all the components that are enclosed by the solid black curve shown in Figure 29. Figure 31 shows a translucent view of the Fuego model. It includes 78 support posts with a diameter D=8"=0.203 m, 138 jet channels with three different diameters, the exterior wall, and the helium exit. Figure 32 shows a side view of the solid model, while Figure 33 shows the final version of the 1/2-symmetry model that includes geometric swirl devices. Note that this model does not include the lower insulation layer, which was incorporated later on in more advanced versions of the LP model.
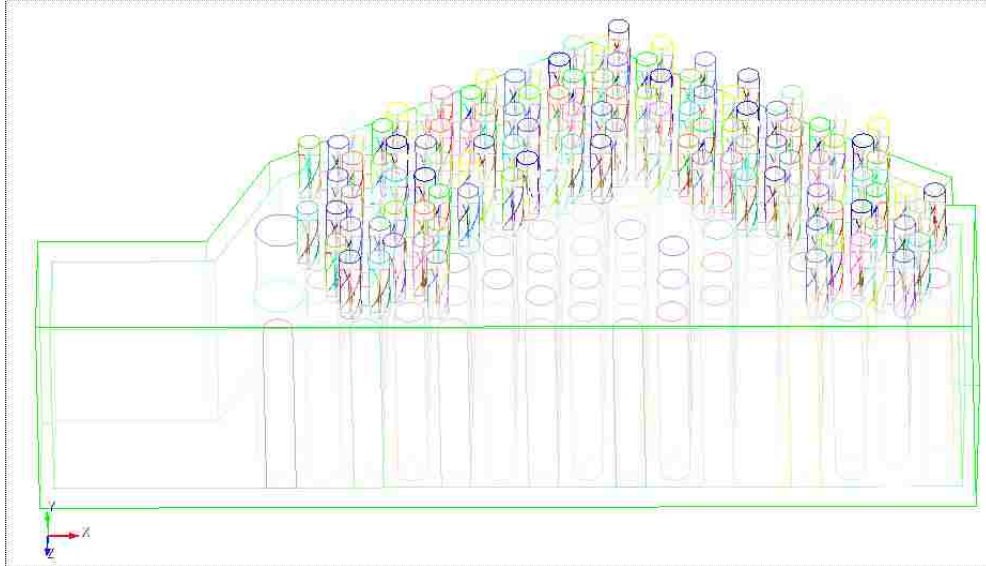
Figure 31. Translucent View of the Fuego LP Model with Support Posts and Geometric Swirl Devices.
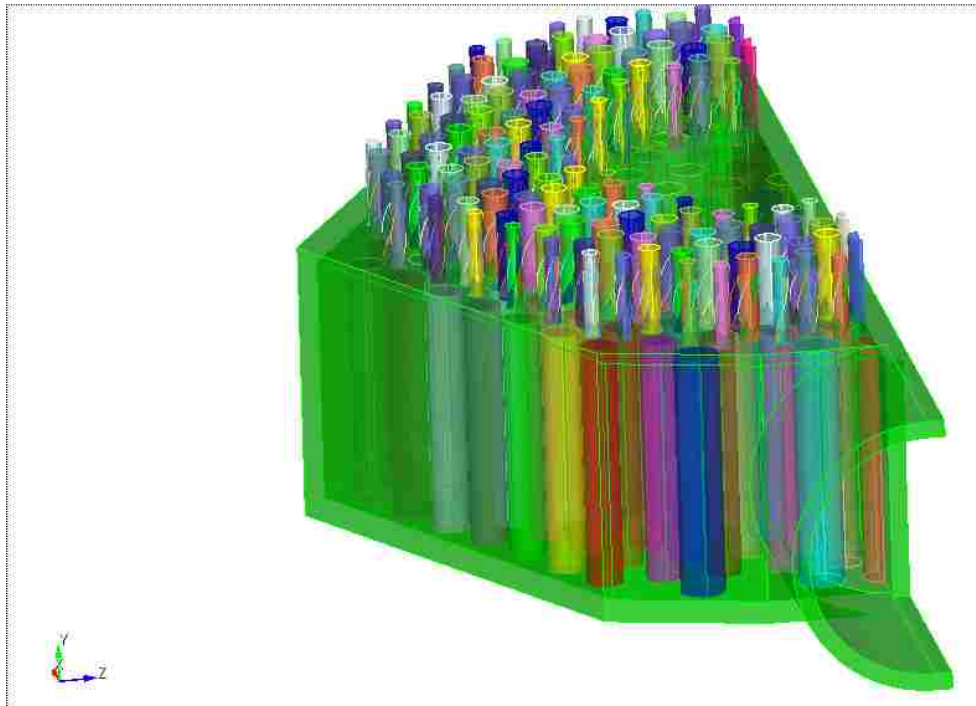
Figure 32. Side View of the Fuego LP Model with Support Posts and Geometric Swirl Devices.
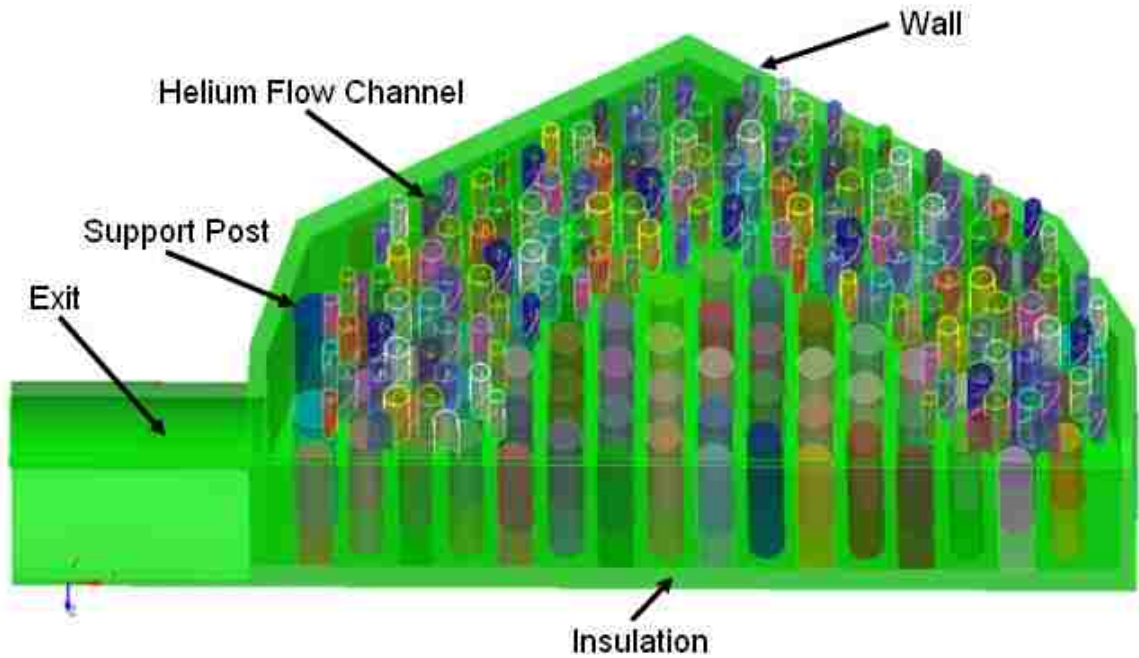
Figure 33. Final Version of the Half-Symmetry Model of the LP in a VHTR with Geometric Swirl Devices.

As noted in Section 4.2, the swirling helicoid geometry can be adequately modeled with swirling jet BCs. This more compact approach was eventually incorporated into the LP model, and its development is shown in the following figures. Figure 34 exhibits a translucent side view of the LP model with support posts and the swirl BCs, while Figure 35 shows a solid-model view for the half-symmetry model with only the support posts. Figure 36 shows the model with support posts and the swirl BCs. Finally, Figure 37 shows the final version of the 1/2-symmetry model with support posts and the BC-based swirl, including a lower plate that was included for the final set of calculations (*see* Section 5.3.4).
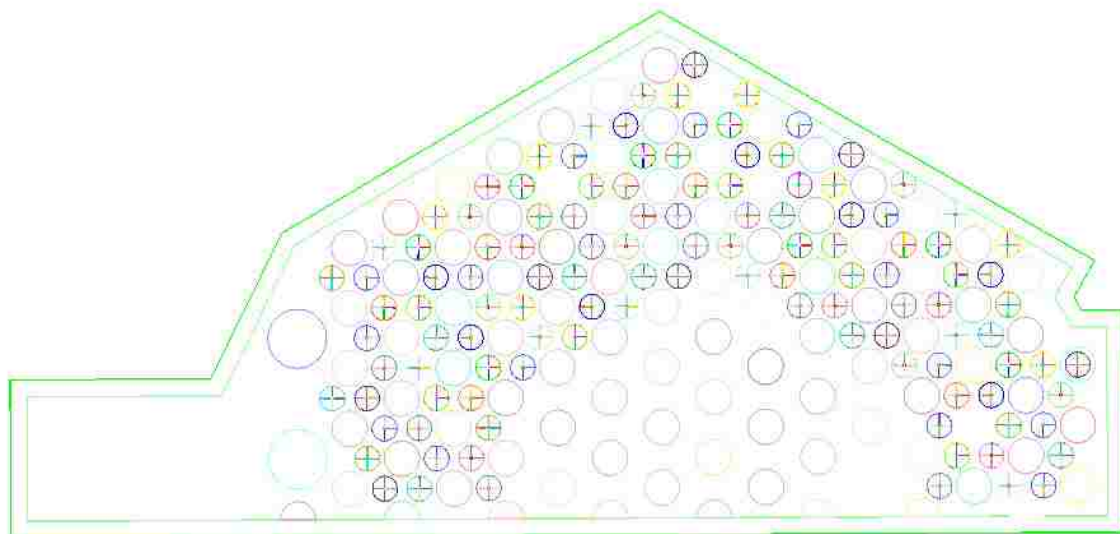
Figure 34. Translucent View of the Fuego LP Model with Support Posts and Swirl BCs.

Figure 35. Side View of the Fuego LP Model with Support Posts and Swirl BCs.
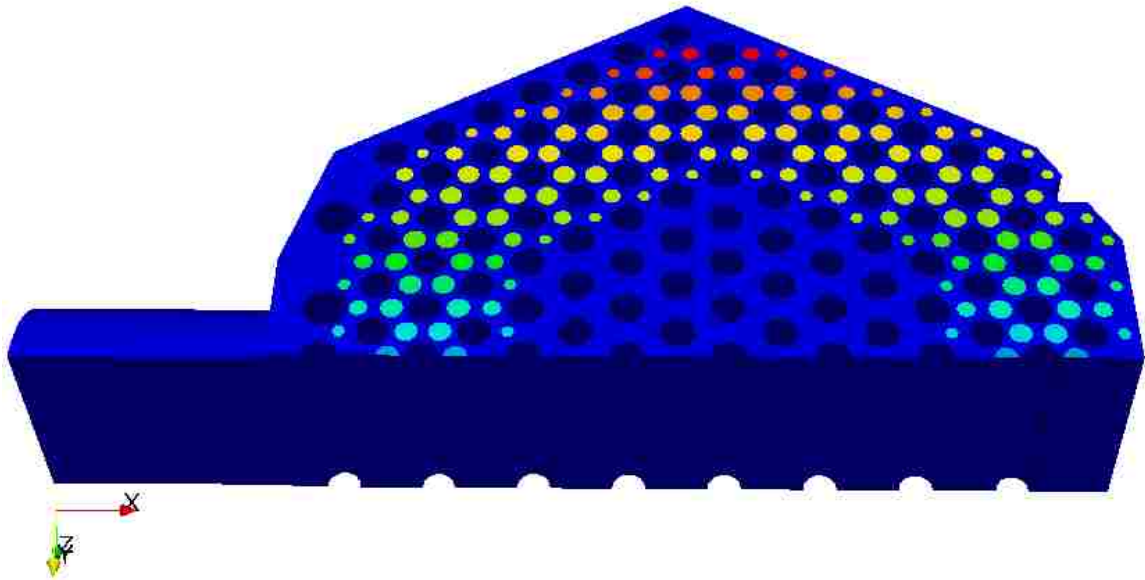
Figure 36. Half-Symmetry Model of the LP in a VHTR with Swirl BCs.
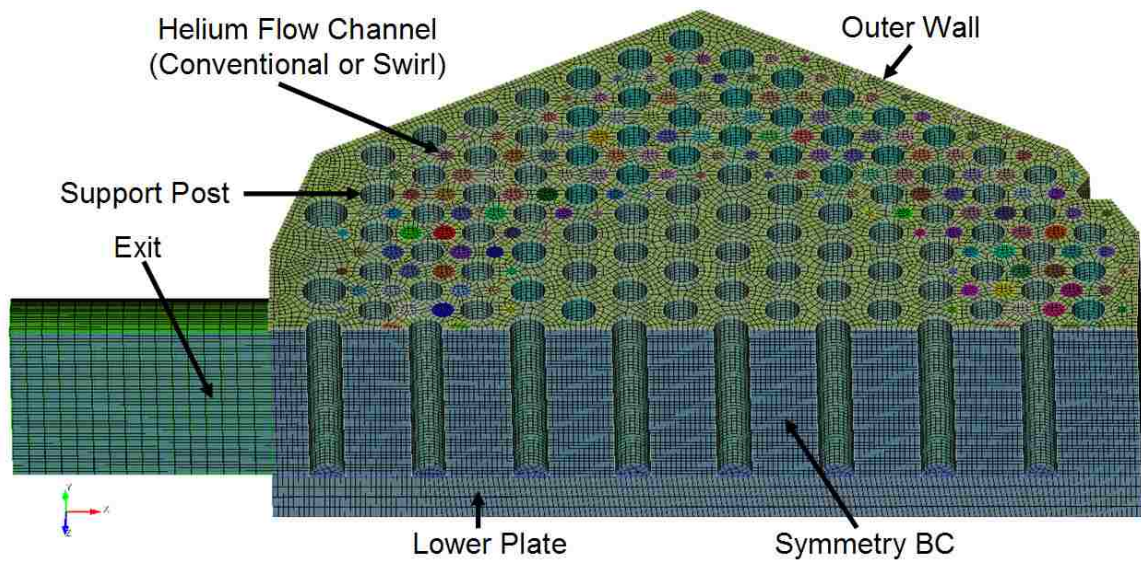
Figure 37. Final Version of the Half-Symmetry LP Model with Swirl BCs.

The LP meshes were generated using the Cubit code [Cubit, 2009] from geometry

developed with Pro/ENGINEER [Pro, 2009]. The temperature-dependent physical and

thermal properties for the helium were calculated using a CANTERA XML input file

(*see* Appendix G). The properties are based on the Chapman-Enskog formulation [Bird, Steward, and Lightfoot, 2007].

The initial time step used was 0.1 μs, and the simulation transient time varied from 100 ms to several seconds. The computation mesh used in the calculations consisted of 1 to 5.5 million hexahedral elements, which provided sufficient spatial discretization. For comparison purposes, a calculation performed for INL used approximately 750,000 elements [MacDonald, 2004]. Figure 38 shows a zoomed region of the fine mesh used for the jet flow and support rods. The largest circles are the support rods, which were modeled as cylindrical surfaces around which the helium flowed.

Figure 38. Zoom of the Fine Mesh Showing Resolution for the Small, Medium, and Large Jet Channels.

The LP models used in the simulations invoked the dynamic Smagorinsky LES turbulence model, and were run on the massively parallel Thunderbird and Red Sky machines at SNL. Because the jets can be modeled as swirl BCs, S was easily modified from 0 to 2.49 in order to observe its impact on heat transfer and gas mixing in the LP. The simulation results are found in Section 5.3.

5. NEW THEORY AND APPLICATIONS

The research presented herein led to advances in swirling jets and their eventual application in the LP calculations for optimal mixing and heat transfer. Three key areas were explored by the research conducted herein:

1. Axisymmetric vortex theory,

2. V&V of the Fuego CFD code for key phenomena expected to occur in the VHTR LP, and

3. Advanced LP calculations.

The key results that were obtained for this research are summarized as follows.

In the area of axisymmetric vortex theory:

- Development of the helicoid vortex swirl model,

- Formulation for the domain with the strongest impact of a swirling jet,

- Impact of S on the CRZ,

- Enhanced flow patterns from swirling jets,

- Impact of mixing and heat transfer as functions of Re and S for an unconfined jet,

- Unification of swirling axisymmetric jets,

- Series formulation of axisymmetric swirling jets,

- Development of a modified Chepura vortex,

- Development of a modified Newton vortex,

- Additional NS solutions for axisymmetric swirls,

- Transient S modeling, and

- Advanced swirling jet design.

In the area of Fuego V&V:

- Conventional jet,

- Swirling jet,

- Conventional jet in crossflow,

- Swirling jet in crossflow,

- Flow around a vertical cylinder,

- CRZ formation, and

- Staggered tubes in crossflow.

In the area of LP simulation:

- Basecase calculation with conventional jets,

- Impact of S on LP mixing and heat transfer,

- Impact of clockwise and counter-clockwise swirling jets, and

- Final calculation with multiphysics, advanced swirling-jet LP modeling.

The results from the three key areas are discussed in detail in Sections 5.1 through 5.3, respectively.

5.1   Axisymmetric Vortices

This section considers the theory of axisymmetric vortices, expands it, and develops new applications.

5.1.1   Helicoid Vortex Swirl Model

The primary motivation for this section is to develop a deeper mathematical and physical understanding of helicoids; the information will inevitably translate into better

understanding of the flow characteristics of the swirling jet, as well as the development of new swirling vortices, beginning with the helicoid swirl vortex.

The basic approach is to develop parametric equations that describe cylindrical and conical helices. That information will then be expanded to cylindrical and conical helicoids. Cylindrical helicoids are germane to the swirling device, while conical helicoids are relevant to the flow field of the jet as it exits the swirling device, as shown in Section 5.5 (Figure 66).

Parametric equations refer to equations where an arbitrary parameter, usually t, is used instead of independent variables. In turn, these representations calculate the value of the dependent variable by tracing (mapping) their values onto a coordinate system. Thus, as t changes, the vector changes as it traces a curve or surface. As an example, a curve may be represented parametrically on a Cartesian coordinate system with the following position vector

$$\vec{r}(t) = x(t)\vec{i} + y(t)\vec{j} + z(t)\vec{k} \tag{75}$$

where, for any value t_o of t, there is a point C on a curve denoted as $r(t_o)$ with coordinates $[x(t_o), y(t_o), z(t_o)]$. This is shown conceptually in Figure 39.
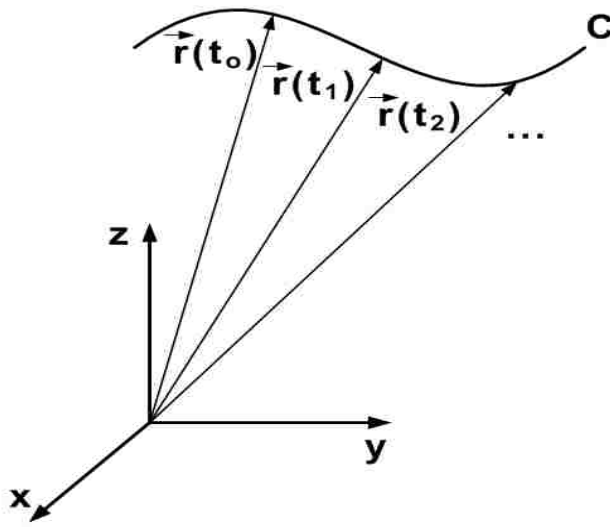
Figure 39. Mapping of Curve C onto Cartesian System Via Vector r(t).

Thus, the vector sketches the position of the curve onto the Cartesian coordinates, and as t increases, the vector continuously moves, with its arrow tip tracing every point along the curve.

As an example of parametric representation, consider a circle, for which

$$x = x(t) = a\cos(\omega t)$$
and   (76)
$$y = y(t) = a\sin(\omega t).$$

Then,

$$x^2 + y^2 = a^2\left[\cos^2(\omega t) + \sin^2(\omega t)\right] = a^2.$$ (77)

When solved, the two parametric equations collapse into a single equation that no longer has the arbitrary parameter t. The parametric vector notation can be used to describe a cylindrical helix in Cartesian coordinates as

$$\vec{r}(t) = a\cos(\omega t)\vec{i} + a\sin(\omega t)\vec{j} + ct\vec{k}.$$ (78)

The cylindrical helix is shown in Figure 40.
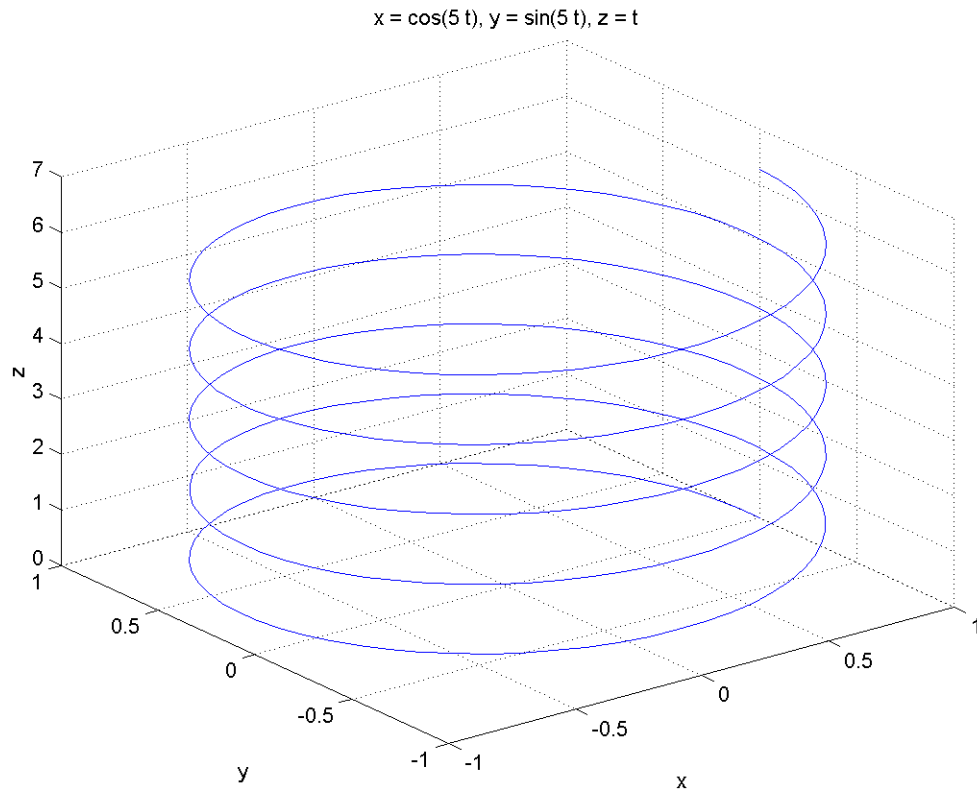
Figure 40. Cylindrical Helix Showing Five Complete Rotations.

In the above equation, *a* represents the radius and the height h is $2\pi c$. The pitch is the height of one full helical rotation. If c is positive, the helix is right-handed, while a negative c results in a left-handed helix. The number of helical turns is determined by ω. For example, 5ω means that the helicoid will complete five full rotations. Unless otherwise stated, $\omega = 1$.

The circular helix can be described as a twisted curve in space, as its surface is not confined to a flat plane. Because the helix has no self-intersections (i.e. points where the curve intersects itself), it is referred a simple curve [Kreyszig, 1979]. Furthermore, the helix has constant torsion and curvature. Another feature of the helix is that it is

93

geodesic. A geodesic is defined as the shortest path between points on a given curved

space. This feature will be exploited later in order to calculate the height of a helicoid.

In cylindrical coordinates, the cylindrical helix can be represented as

$$\vec{r}(t) = \vec{\delta}_r + t\vec{\delta}_\theta + t\vec{\delta}_z. \tag{79}$$

Additionally, the cylindrical helix can be described by using imaginary numbers,

$$\vec{r}(t) = e^{it}\vec{e}_k = \cos(t)\vec{i} + i\sin(t)\vec{j} , \tag{80}$$

where $\vec{e}_k$ is a mutually perpendicular unit vector.

The conical helix can be defined in Cartesian and cylindrical coordinates as follows,

respectively,

$$\vec{r}(t) = t\cos(t)\vec{i} + t\sin(t)\vec{j} + ct\vec{k} \tag{81}$$

And

$$\vec{r}(t) = t\vec{\delta}_r + t\vec{\delta}_\theta + t\vec{\delta}_z. \tag{82}$$

The conical helix is shown in Figure 41. Notice that the conical helix forms a spiral

when viewed from the top, as shown in Figure 42.

x = t cos(5 t), y = t sin(5 t), z = -t
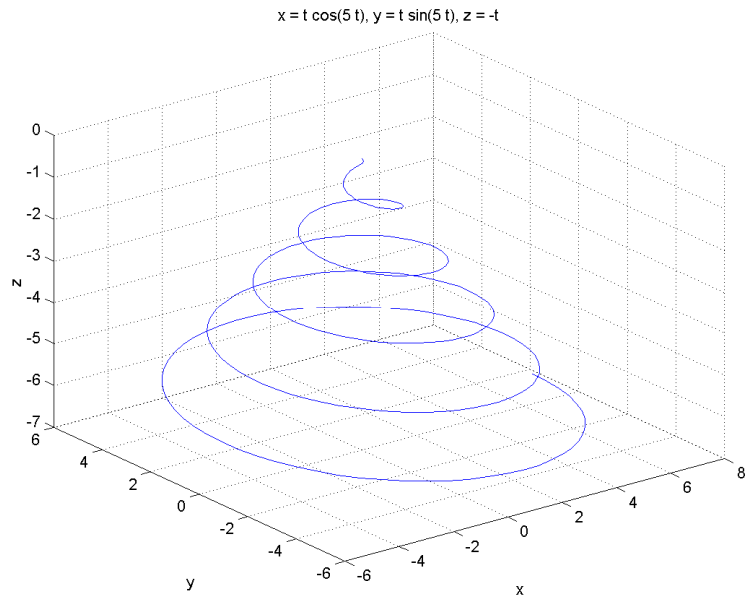
Figure 41. Conical Helix Showing Five Complete Rotations.

x = t cos(5 t), y = t sin(5 t), z = -t
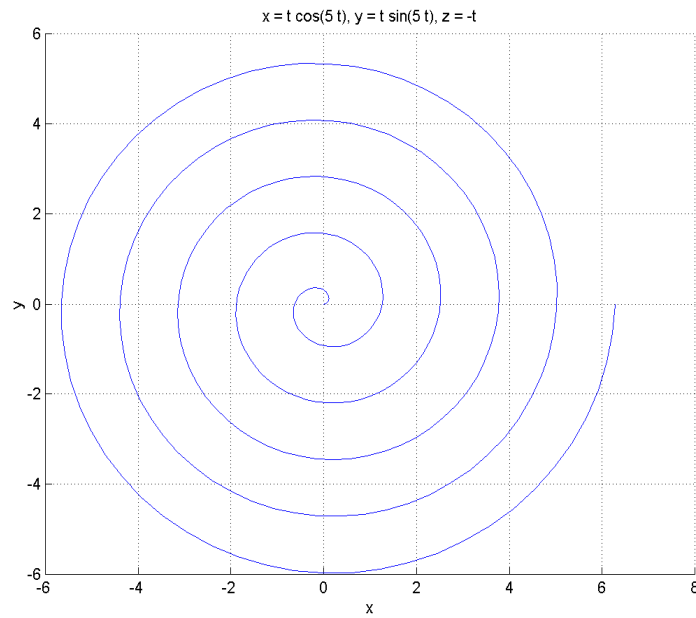
Figure 42. Top View of a Conical Helix Showing Five Complete Rotations.

95

Now, if instead of a helical curve confined within a cylindrical space one consider a helical three-dimensional ribbon that rotates symmetrically and periodically about the z axis, then such geometrical figure is defined as a helicoid; *see* Figure 43. Additionally, several ribbons can rotate about the axial axis, with an azimuthal off-set. Figures 44 through 45 show a helicoid system with quadruple ribbons that are off-set by 90°. A helicoid is also known as an Archimedes' screw, and was discovered by Jean Meusnier in 1776. The helical ribbon may be considered as having an infinite number of adjacent curves for which each follows a helical path. Stated differently, for any point on the helicoid's surface, there is a 3D helix that passes through such point. The geometric helicoid used in this research is shown in Figure 46. It consists of four helicoid ribbons spaced 90º apart that are attached onto a thin cylinder. The cylinder is capped with a sharp cone that is intended to minimize drag.
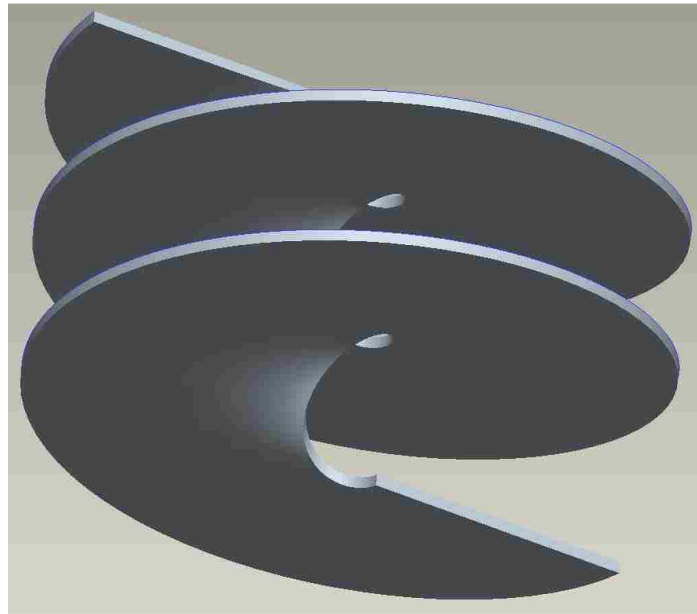
Figure 43. Single Ribbon Cylindrical Helicoid.

r-data = (3.9270e-001, 3.1416e+000, 20), theta-data = (4.7124e+000, 7.8540e+000, 20)
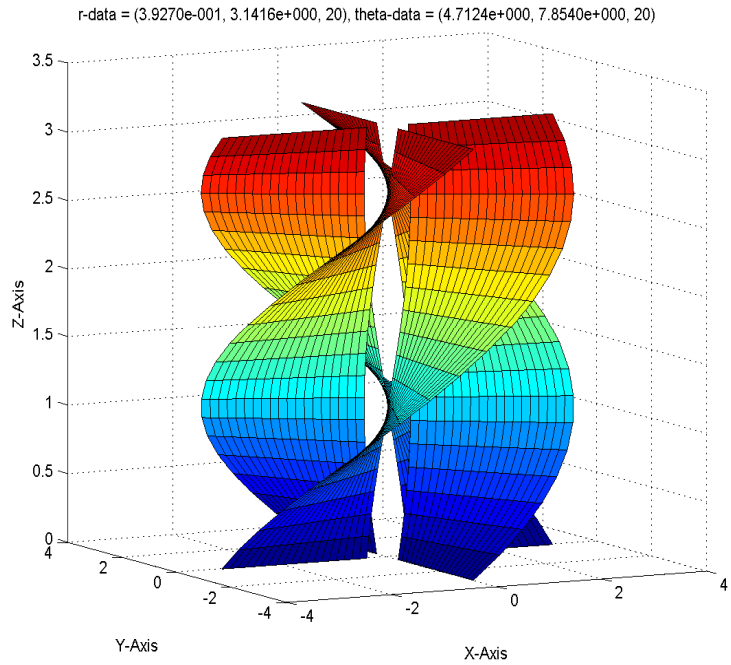
Figure 44. Side View of a Quadruple Ribbon Cylindrical Helicoid.

r-data = (3.9270e-001, 3.1416e+000, 20), theta-data = (4.7124e+000, 7.8540e+000, 20)
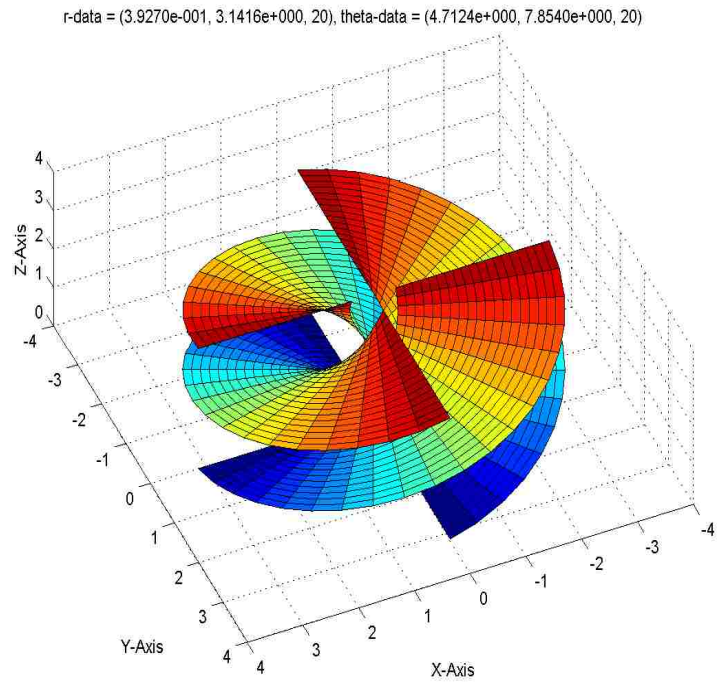
Figure 45. Top View of a Quadruple Ribbon Cylindrical Helicoid.

Figure 46. Swirl Inducing Device: Quadruple Ribbon Cylindrical Helicoid Attached to a Cone.

There are various types of three dimensional helicoids, of which the cylindrical and conical helicoid are of importance for this research. The cylindrical helicoid spirals about the surface of a cylinder with a constant radius, while the conical helicoid is defined by following an ever-increasing spiral along a cone's surface.

The helicoid may be defined by two angles, φ and θ. Here, φ represents the rotation of the helicoid's radius about a given coordinate, say z. In essence, it determines the number of rotations the helicoid makes about z, whether fractional or whole, while θ represents the descent angle of the 3D ribbon as it twists about the z axis.

The length s of the ribbon as it twists about the z axis can be obtained by marking the ribbon with n segments or chords, measuring each segment, and then summing the individual lengths. If n is very large, then the length of each chord approximates a straight line. Thus, as n approaches infinity, the chord length approaches zero. If the derivative for r(t) exists and is continuous, then the length of the sum s is equivalent to calculating the following integral,

$$s = \int_a^b \left(\dot{r} \cdot \dot{r} \right)^{1/2} dt \qquad (83)$$

In the case of a helicoid with height h,

$$\dot{r} = v(t) = -a\sin(t)\vec{i} + a\cos(t)\vec{j} + c\vec{k}. \qquad (84)$$

It then follows that

$$\dot{r} \cdot \dot{r} = a^2 + c^2 \qquad (85)$$

and so

$$s = \int_a^b \left(\dot{r} \cdot \dot{r} \right)^{1/2} dt = \int_a^b \left(a^2 + c^2 \right)^{1/2} dt = t \left(a^2 + c^2 \right)^{1/2}. \qquad (86)$$

s can be calculated from a different perspective if it is considered that the helicoid's height is a function of the angle θ, as shown in Figure 47. In particular, as

$$\theta \to 90°, h \to 0 \qquad (87)$$

and as

$$\theta \to 0°, h \to \infty. \qquad (88)$$

Figure 47 will now be used to determine h(θ). First, consider a case where the helicoid undergoes exactly ½ rotation (i.e. $\varphi = 180°$, or equivalently, $n_{rot} = 1/2$). This means that the arrow has covered half the circumference of a circle with radius a on the plane represented by z = constant. The distance covered by the helicoid as it travels the ½ rotation about the cylinder is the curve s. If the cylindrical surface thus spanned with radius = a is "flattened" onto a plane (i.e. consider half the cylinder, with symmetry with respect to the axial direction), then such surface will correspond to a 2D rectangle with height h and base πa, as shown in the right hand side (RHS) of Figure 47. The "flattening" or mapping of the cylinder with a helix on its surface results in the cylinder

yielding a flat rectangle, and the helix corresponds to a straight line. The line is straight because the helix is a geodesic, as discussed earlier. Now, the rectangle's base measures πa because it was formed from the mapping of the ½ circle, so half the circumference of the circle corresponds to πa.
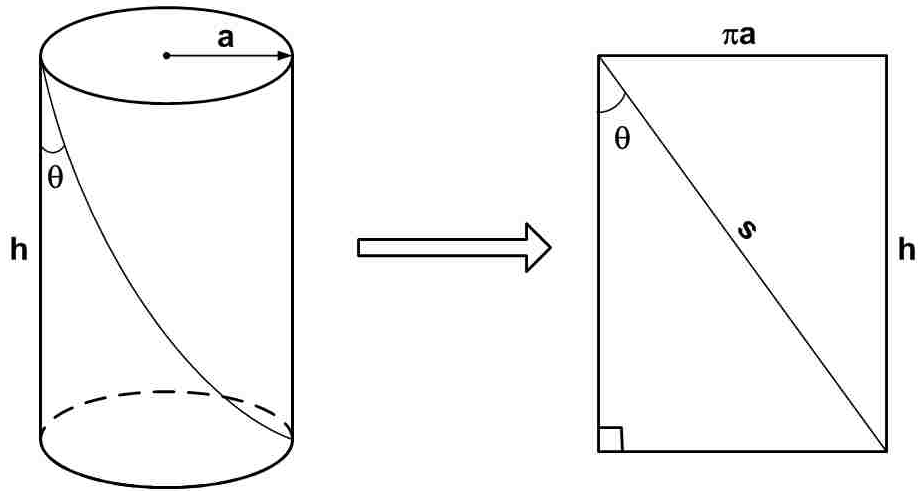
Figure 47. Mapping of a Half Cylinder and a Helix into a Rectangle and a Straight Line.

Taking a look at Figure 47, it follows that $\tan(\theta) = \pi a / h$. Therefore,

$$h = \frac{\pi a}{\tan(\theta)}.$$ (89)

A quick inspection of Equation 89 shows that it satisfies Equations 87 and 88. From Pythagoras' Theorem, the calculation of s is now more straightforward than previously (Equation 86),

$$s = \left[h^2 + (\pi a)^2 \right]^{1/2}$$ (90)

Equations 89 and 90 can be generalized for any fractional rotation or complete rotations as

$$h = \frac{2n_{rot}\pi a}{\tan(\theta)} \qquad (91)$$

and

$$s = \left[h^2 + (2n_{rot}\pi a)^2 \right]^{1/2}. \qquad (92)$$

Certain classes of vortex flows can be specified by the linearity of the azimuthal and axial velocity components [Fukumoto and Okulov, 2005; Okulov and Sorensen, 2010],

$$\frac{r'v}{L'} + w = \text{constant}, \qquad (93)$$

where r' is the radial distance from z (the symmetry axis), and L' is the length of a single helicoid revolution. The pitch is defined as

$$p = \frac{L'}{2\pi}. \qquad (94)$$

Note that helicoidal-type of vortex models are defined in the literature [Rossi, 2006; Chattot, 2006]. These helicoidal vortices primarily satisfy one or both of Equations 93 and 94. For example, the Rankine and Batchelor vortices are referred as helical (i.e. helicoidal) [Rossi, 2006; Okulov and Sorensen, 2010], as well as the Lamb and Burgers vortices [Hopfinger and Heijst, 1993; Alekseenko *et al.*, 1999]. Thus, the term "helicoid" or "helicoidal" vortex already carries meaning in the literature. For clarity, the helicoid swirl vortex developed here is referred as the "helicoid swirl vortex model" (HSVM), or simply as the "helicoid vortex". The usage of the term "helicoid" is appropriate here because, as will be shown shortly, the vortex follows a helical path. Furthermore, the HSVM has other helicoidal properties, such as a fixed pitch, as defined by Equation 94.

Like the Taylor-Green vortex [Taylor and Green, 1937], the helicoid vortex will first be defined in Cartesian coordinates, and then translated onto cylindrical coordinates. Note that most vortices are typically defined in cylindrical coordinates [Rankine, 1858; Lamb, 1932; Burgers, 1948; Loitsyanskiy, 1953; Gortler, 1954; Newman, 1959; Sullivan, 1959; Batchelor, 1964; Squire, 1965; Chepura, 1969; Martynenko, 1989; Aboelkassem, Vatistas, and Esmail, 2005].

The velocity components of a swirling jet can be approximated as 3D helicoids in a Cartesian coordinate system such as the one shown in Figure 48. For the swirl BCs, it is postulated that the helicoid velocity is the superposition of the azimuthal and axial velocities, where the azimuthal velocity is solely a function of x and y for the u- and v-velocity components. Therefore, consider that in its most generalized fashion, the Cartesian velocity field can be expressed as:

$$\vec{V}(x,y,z) = v_x(x,y,z)\vec{i} + v_y(x,y,z)\vec{j} + w_z(x,y,z)\vec{k}.$$ (95)

In a parameterized t-space, a 3D helicoid may be represented as [Kreyszig, 1979]:

$$\vec{V}(t) = v_{x,o}\sin(2\pi t)\vec{i} + v_{y,o}\cos(2\pi t)\vec{j} + v_{z,o}\vec{k}.$$ (96)

In the above equation, u_o, v_o, and w_o are constant. When translated into Cartesian variables x and y, the first two terms in Equation 96 become:

$$x = x(t) = v_{x,o}\cos(2\pi t)$$ (97)

and

$$y = y(t) = v_{y,o}\sin(2\pi t).$$ (98)

They describe a circle with radius u_o, if $v_{x,0} = v_{y,0}$. That is,

$$x^2 + y^2 = v_{x,0}^2 \cos^2(2\pi t) + v_{y,0}^2 \sin^2(2\pi t) = v_{x,0}^2,\tag{99}$$

which is akin to saying:

$$\left\| v_\theta \right\| = \left(\vec{v}_x \bullet \vec{v}_x + \vec{v}_y \bullet \vec{v}_y \right)^{\frac{1}{2}} = v_{x,0}.\tag{100}$$
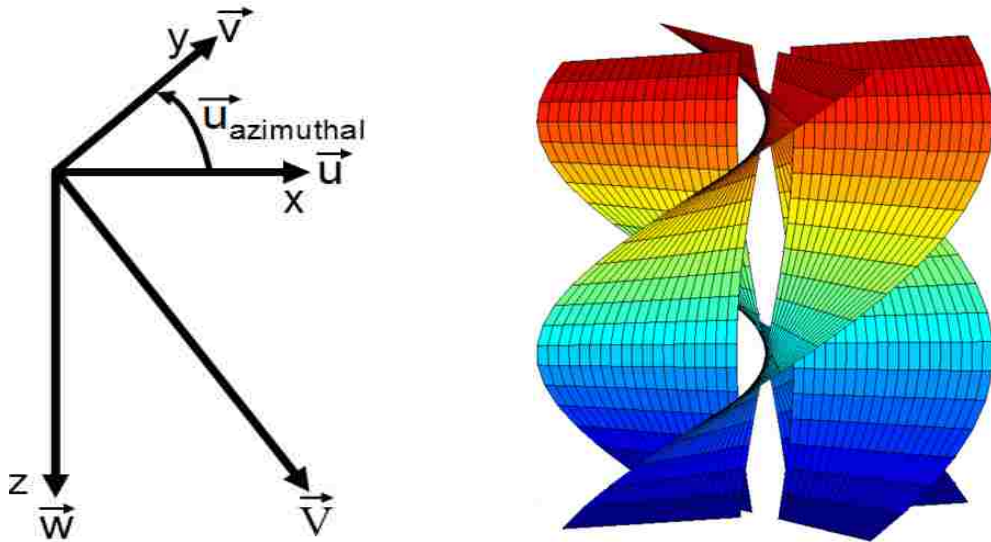
Figure 48. LHS: Schematic of the Azimuthal, Axial, and Net Velocities; RHS: Four Helicoid Surfaces Off-Set by 90º.

Because the helical velocity field includes a constant velocity component (w_o) that is normal to the azimuthal velocity plane, the overall motion of the superposed velocity forms 3D spiral surfaces (helicoids), *see* LHS of Figure 21. The Fuego code employs a Cartesian set of coordinates, where the u, v, and w velocity components are computed separately. *Accordingly, a non-parameterized Cartesian swirl BC is required to satisfy Fuego's velocity framework. This is attempted with a Cartesian sinusoidal helicoid approximation with superposition of the azimuthal and axial velocities. In particular, the first two terms of the parameterized velocity in Equation 95 collapse into the azimuthal velocity, while the third term is the axial velocity.*

103

For fully-developed, steady state flow that is symmetric about the z axis, the azimuthal velocity in a tube containing a geometric swirl device such as the one shown in the upper LHS of Figure 24 has v_x and v_y velocities that are functions solely of x and y, while the v_z velocity is constant with respect to z. This simplifies the helicoid velocity distribution as

$$\vec{V}(x,y,z) = v_x(x,y)\vec{i} + v_y(x,y)\vec{j} + v_{z,0}\vec{k}. \tag{101}$$

Now, because the geometry in consideration is helicoidal, it stands to reason that sinusoidal functions that conform to Equation 96 can be suitable approximations for the sought-after cylindrical helical swirl model. Based on analogy to an Eulerian helicoid sinusoidal velocity field, a proposed analytical swirl approximation is:

$$\vec{V}(x, y, z) = v_{x,0}\sin(2\pi y)\vec{i} - v_{y,0}\sin(2\pi x)\vec{j} + v_{z,0}\vec{k}. \tag{102}$$

Figure 49 is a 3D plot of the norm of the helicoid's first two velocity terms (the sines) and an intersection of a plane $z = v_{z,0} = $ constant. The figure shows that the plane intersects the sinusoidal function, forming the desired circular azimuthal velocity profile that in conjunction with a constant axial velocity, superposes to form the 3D swirling jet field. Note that as $v_{z,0}$ increases, the plane cut forming the circle becomes more and more "perfectly" shaped like a circle. Conversely, as $v_{z,0}$ decreases, the "circle" loses its circular symmetry, becoming more square-like. The best helicoid approximation using Equation 102 is obtained when $v_{z,0}$ is sufficiently large. It is worth noting that due to the stabilizing effect of the gas viscosity (which increases with temperature as noted in Equation 2), slightly square-like helicoids quickly become circular as the CFD

calculation proceeds. That is, as Fuego calculates the velocity field, the viscous effects quickly reshape the square-like vortex on the azimuthal plane into circles.
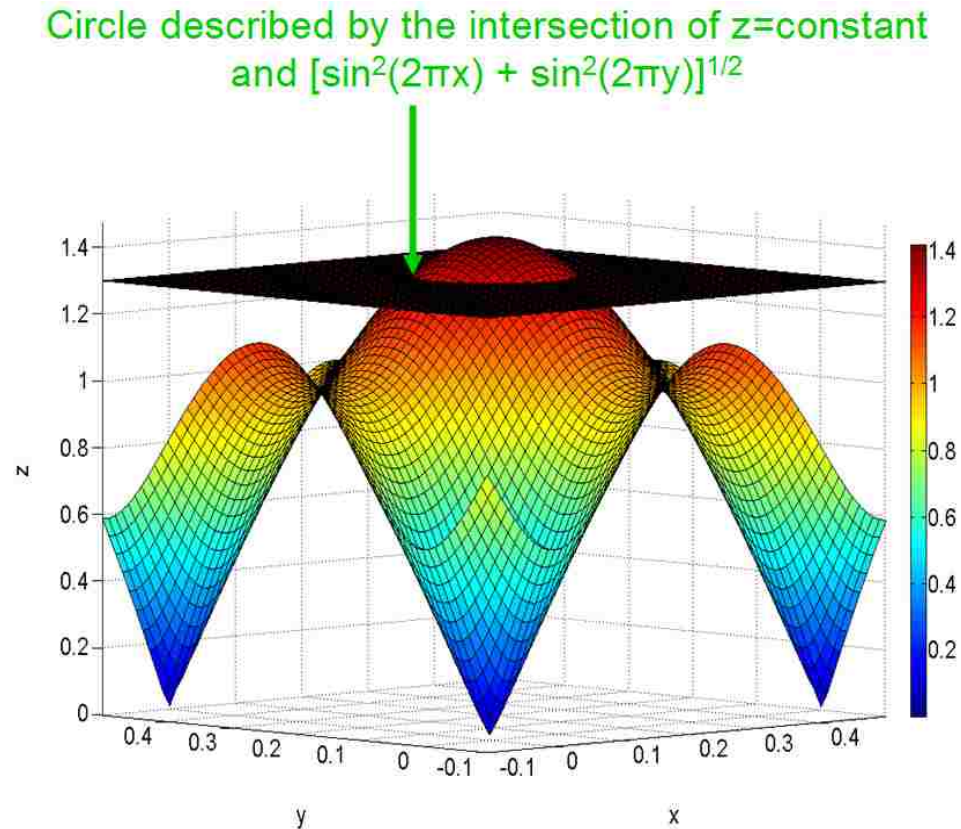
Figure 49. Intersection of Z = Constant Plane with the Norm of the First Two Velocity Terms.

From Figure 49, it is noted that:

- The u, v sinusoid is intersected by the flat plane, w.
- The intersections form circles on the x-y plane, which are extended by the w velocity. (The velocity w is normal to the x-y plane.)

Therefore, the superposition of the azimuthal and axial velocities forms the desired 3D, swirling helicoid velocity field.

105

The maximum value of the sinusoidal terms for Equation 102 is 1.0 (i.e., $\left|\sin(2\pi x)\right|_{max} = 1.0$ and $\left|\sin(2\pi y)\right|_{max} = 1.0$), while the minimum is 0. The first two terms of Equation 102 can be used to obtain the maximum azimuthal velocity at the exit of the swirling jet as:

$$\left\|v_{\theta,o}\right\|_{max} = \left[v_{x,0}^2 \left|\sin(2\pi y)\right|_{max}^2 + v_{y,0}^2 \left|\sin(2\pi x)\right|_{max}^2 \right]^{\frac{1}{2}} = \sqrt{2}v_{x,0} \tag{103}$$

Thus, the azimuthal velocity field can be considered as an infinite number of concentric circles on a flat plane having velocity ranging from 0 to $\sqrt{2}v_{x,0}$. From Figure 48:

$$\tan(\theta) = \frac{v_{\theta,0}}{v_{z,0}}, \tag{104}$$

and from Equations 103 and 104:

$$v_{z,0} = \frac{v_{\theta,0}}{\tan(\theta)} = \frac{\sqrt{2}v_{x,0}}{\tan(\theta)}. \tag{105}$$

From Equation 102, for a given $\vec{v}_o$,

$$v_{z,0} = \left(V_o^2 - 2v_{x,0}^2\right)^{\frac{1}{2}} \tag{106}$$

Combining Equations 105 and 106, and solving for u_o, gives:

$$v_{x,0} = \frac{V_0}{\left[2\left(1 + \frac{1}{\tan^2(\theta)}\right)\right]^{\frac{1}{2}}} \tag{107}$$

and $v_{y,0}$ is

$$v_{y,0} = \frac{V_0}{\left[2\left(1 + \frac{1}{\tan^2(\theta)}\right)\right]^{\frac{1}{2}}}. \tag{108}$$

The literature offers well over a dozen definitions for S [Leschziner and Rodi, 1984; Kilik and Finstad, 1986; Danitz, 1995; Billant *et al.*, 1998; Alekseenko *et al.*, 1999; Liang and Maxworthy, 2005; Bonaldo, 2007; Shiri, George, and Naughton, 2008; Jiang, Siamas, and Wrobel, 2008; Toh, Honnery, and Soria, 2010]. Key definitions for S have been summarized recently [Kihm, Chigier, and Sun, 1990; Chyang, Wan, and Chen, 1997; Toh, Honnery, and Soria, 2010].

For this research, the geometric S as defined in related applications for hubless swirlers will be used [Kerr and Fraser, 1965; Mathur and MacCallum, 1967; Lilley, 1977; Abujelala and Lilley, 1985; Kihm, Chigier, and Sun, 1990; Bilen *et al.* 2002; Fernandes, Heitor, and Shtork, 2006; Arzutug and Yapici, 2009]:

$$S = \frac{2}{3}\tan(\theta) \tag{109}$$

Thus, the swirl angle is defined as the descent angle θ of the helicoid surfaces, and the geometric S is a simple function of the angle. This allows Equations 107 and 108 to be combined with Equation 109, thus allowing $v_{x,0}$ and $v_{y,0}$ to be solely functions of S:

$$\frac{v_{x,0}}{V_0} = \frac{1}{\left[2\left(1 + \frac{4}{9S^2} \right) \right]^{\frac{1}{2}}} \cdot \tag{110}$$

Similarly, for the $v_{y,0}$ component,

$$\frac{v_{y,0}}{V_0} = \frac{1}{\left[2\left(1 + \frac{4}{9S^2} \right) \right]^{\frac{1}{2}}} \tag{111}$$

Finally, Equations 103 and 105 can be used to express the azimuthal and axial velocities, respectively, as functions of S:

$$\frac{v_{\theta,0}}{V_0} = \frac{1}{\left(1 + \dfrac{4}{9S^2}\right)^{\frac{1}{2}}} \tag{112}$$

and

$$\frac{v_{z,0}}{V_0} = \frac{2}{3S} \frac{1}{\left(1 + \dfrac{4}{9S^2}\right)^{\frac{1}{2}}}. \tag{113}$$

Taking the limits of Equations 112 and 113 shows that:

$$\lim_{S\to0+}\left(\frac{v_{\theta,0}}{V_0}\right) = 0.0, \quad \lim_{S\to\infty}\left(\frac{v_{\theta,0}}{V_0}\right) = 1.0, \quad \lim_{S\to0+}\left(\frac{v_{z,0}}{V_0}\right) = 1.0, \text{ and}$$

$$\lim_{S\to\infty}\left(\frac{v_{z,0}}{V_0}\right) = 0.0. \tag{114}$$

As noted in Figure 50 and also by the second limit in Equation 114, the azimuthal velocity increases rapidly with increasing S, but eventually reaches its asymptotic value. For example, at $S = 2.5$, the azimuthal velocity reaches 96.6% of its asymptotic value. Therefore, for $S > 2.5$, there is an insignificant increase in the azimuthal velocity. For instance, for $\theta = 85°$ and $89.5°$ (i.e. $S = 7.62$ and 76.4, respectively), the normalized azimuthal velocities are 99.6% and 99.9% of their asymptotic normalized values, respectively. The normalized axial velocities, however, are 8.7% and 0.87%, respectively. Clearly, not much is gained in terms of the azimuthal velocity for large θ, while the axial velocity drops by a factor of 10 (though θ increased by a mere 4.5°). Because the azimuthal velocity drops rapidly, the small change in its value is not warranted by the factor of 10 drop in the axial velocity. Figure 50 shows that the axial velocity drops rapidly as S increases, and approaches 0 as S approaches infinity. In fact, by the time S=10, the axial velocity is at merely 6.7% of its peak value. Table 3 summarizes the effect of S on the velocities based on V_O=60.0 m/s.
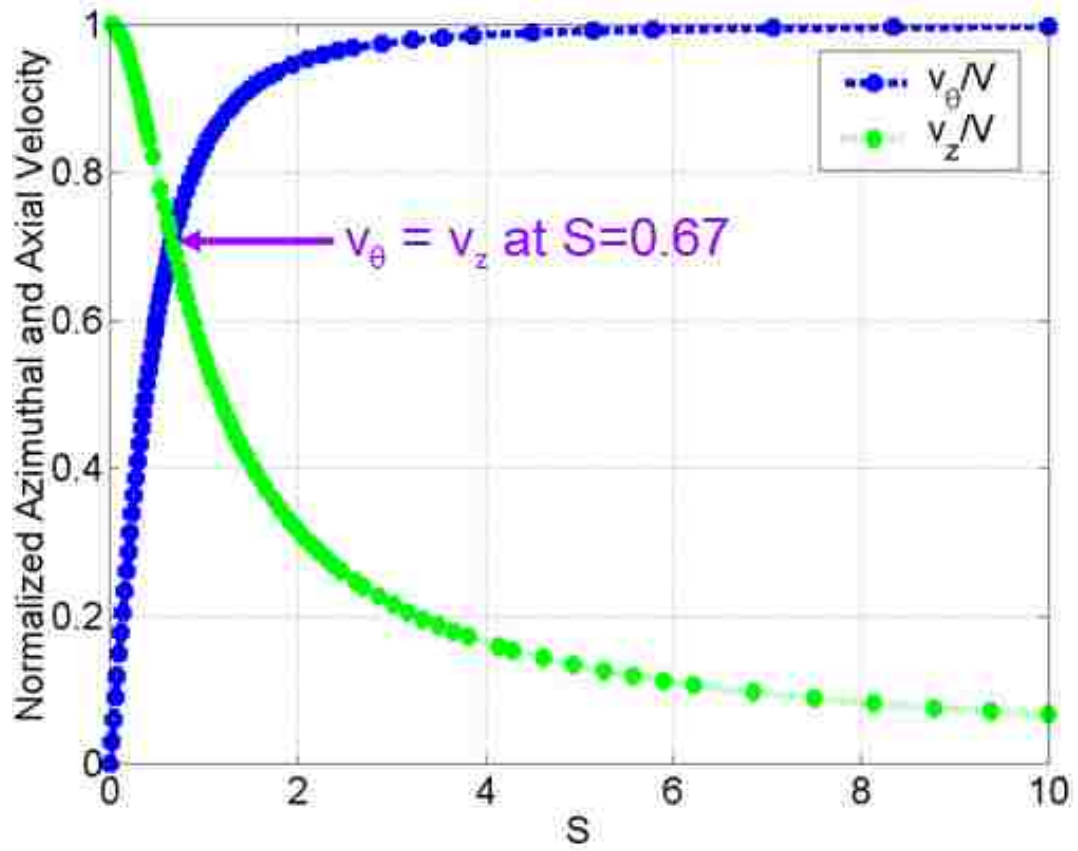
Figure 50. Normalized Azimuthal and Axial Velocities.

Table 3. Impact of S on Velocity (Based on V_0=60.0 m/s).

θ (°)	$S = \dfrac{2}{3}\tan(\theta)$	$\dfrac{v_{x,0}}{V_0} = \dfrac{1}{\left[2\left(1+\dfrac{4}{9S^2}\right)\right]^{\frac{1}{2}}}$ (m/s)	$\dfrac{v_{y,0}}{V_0} = \dfrac{1}{\left[2\left(1+\dfrac{4}{9S^2}\right)\right]^{\frac{1}{2}}}$ (m/s)	$\dfrac{v_{z,0}}{V_0} = \dfrac{2}{3S}\dfrac{1}{\left(1+\dfrac{4}{9S^2}\right)^{\frac{1}{2}}}$ (m/s)	$\dfrac{v_{\theta,0}}{V_0} = \dfrac{1}{\left(1+\dfrac{4}{9S^2}\right)^{\frac{1}{2}}}$ (m/s)
0	0	0	0	60.0	0
15	0.18	11.0	11.0	58.0	15.5
30	0.38	21.2	21.2	52.0	30.0
45	0.67	30.0	30.0	42.4	42.4
60	1.15	36.7	36.7	30.0	52.0
75	2.49	41.0	41.0	15.5	58.0
89	38.2	42.4199	42.4199	1.0471	59.9909
89.5	76.4	42.4248	42.4248	0.5236	59.9977
89.9	382.0	42.4263	42.4263	0.1047	59.9999

At this point, it should be asked, "Just how accurate is the helicoid norm approximation?" To that effect, the norm-based helicoid approximation was compared with the sine function; *see* Figure 51, LHS vs. RHS, respectively. A glance of Figure 51 shows that the two velocity distributions are remarkably similar, especially for small r. In order to gauge the error between the two approximations, their magnitudes were subtracted and plotted in Figure 52. A plane for z=0.018 was included to show the region where the error as a result of the approximation was less than 1.8%. This error range applies for $r < 0.21$, and shows that most of the helicoid surface approximation has less than 1.8% error. Finally, Figure 53 shows the positive and negative roots of the helicoid vortex.
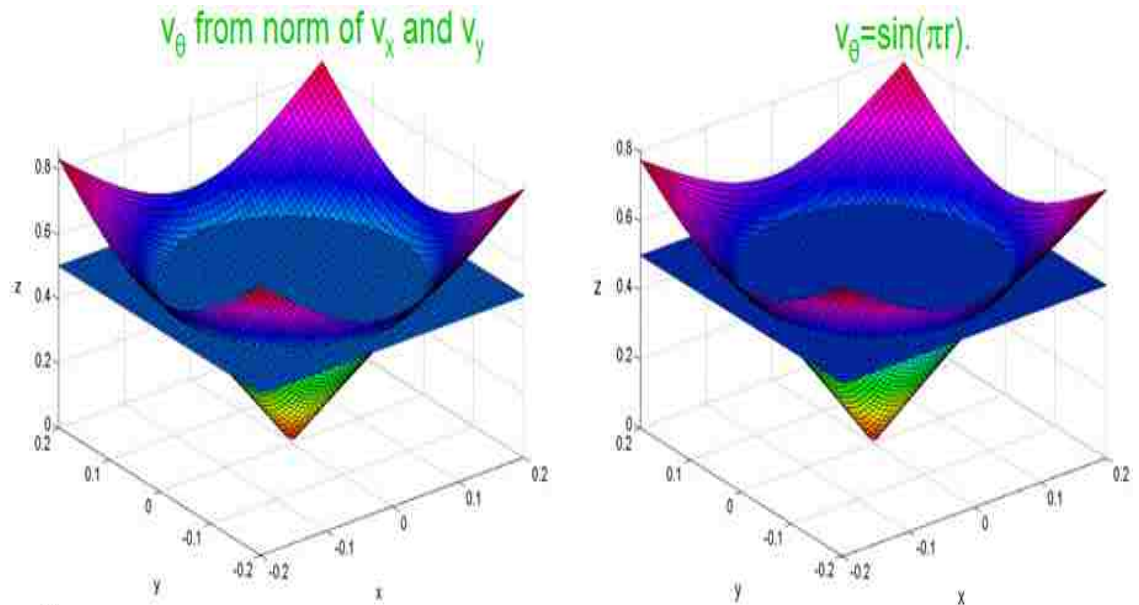
$$\left\| v_\theta \right\| = (v_x \cdot v_x + v_y \cdot v_y)^{1/2} = [\sin^2(\pi x) + \sin^2(\pi y)]^{1/2} \qquad \sin(\pi r) = \sin[\pi(x^2+y^2)^{1/2}]$$

Figure 51. Norm-Based Approximation of Helicoid Vortex vs. Sine Function.

$$\sin[\pi(x^2+y^2)^{1/2}] - [\sin^2(\pi x) + \sin^2(\pi y)]^{1/2}$$
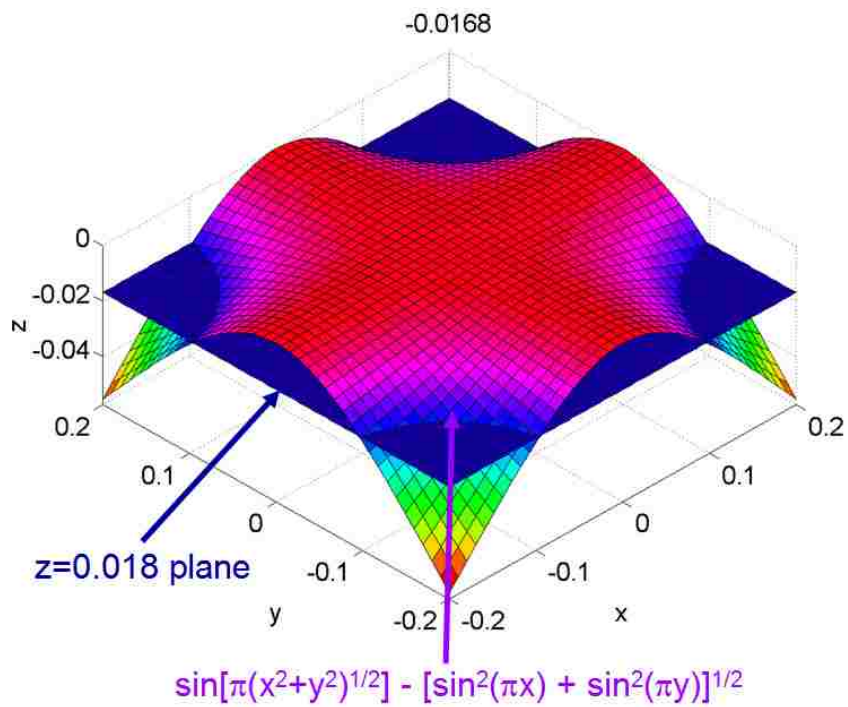
Figure 52. Error Due to the Sine Approximation of a Helicoid Vortex.

111

$$\sin(\pi r) = \sin[\pi(x^2+y^2)^{1/2}] \qquad \sin(-\pi r) = -\sin[\pi(x^2+y^2)^{1/2}]$$
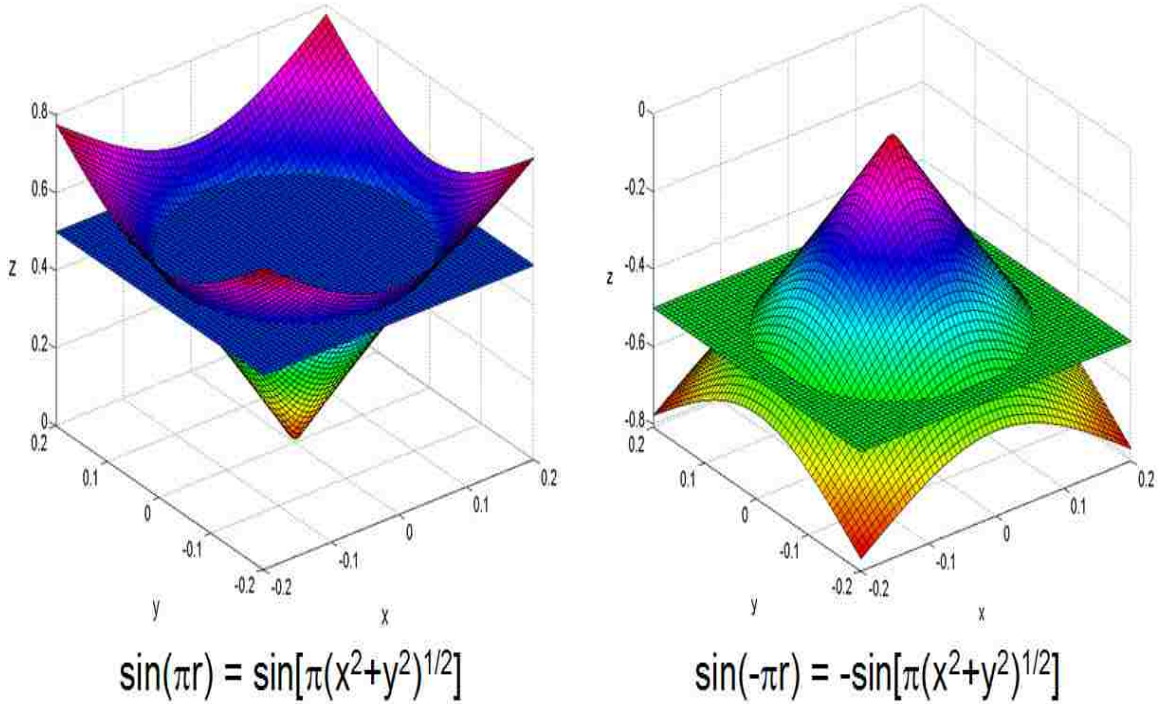
Figure 53. Positive and Negative Roots of the Helicoid Vortex.

5.1.2   Swirling Jet Strongest Domain

The present calculations agree with both theory and experimental data that for weak to

intermediate swirl (as defined in Equation 7), the peak azimuthal velocity v_θ of a swirling

jet decays as $1/z^2$ (*see* Figure 54) [Loitsyanskiy, 1953; Gortler, 1954; Mathur and

MacCallum, 1967; Chigier and Chervinsky, 1967; Blevins, 1992; Billant *et al*. 1998]. On

the other hand, the peak axial velocity w decays as $1/z$ [Loitsyanskiy, 1953; Gortler,

1954; Mathur and MacCallum, 1967; Chigier and Chervinsky, 1967; Blevins, 1992;

Billant *et al*. 1998]. This issue is referred as "swirl decay", and was first reported by

Loitsyanskiy. In particular, as z becomes large, the $1/z^2$ azimuthal velocity term decays

much faster (Equation 4). That is,

112

$$w = \frac{C_1}{z}, \tag{115}$$

and

$$v_\theta = \frac{C_2}{z^2}. \tag{116}$$

Based on a curve-fit of data presented in the literature [Blevins, 1992], it is possible to obtain $C_1 = -2.6S^3 + 12S^2 + 19S + 12$, while the reported value in the literature for $C_2 \sim 4$ to 11, and may be a function of S [Blevins, 1992]. Because the azimuthal velocity for a swirling jet decays faster than the axial velocity, there is a point, z^*, such that for $z \leq z^*$, $w \leq v_\theta$. Setting $z = z^*$ and solving for $v_\theta\left(z^*\right) = w\left(z^*\right)$,

$$z^* = \frac{C_2}{C_1} = \frac{C_2}{-2.6S^3 + 12S^2 + 19S + 12} \tag{117}$$

Clearly, the magnitude of z^* that maximizes the azimuthal momentum over the axial momentum depends strongly on the design value of S. For example, for S=0.2 and 0.6, z^*=1.3 and 2.6, respectively. Therefore, if the design seeks to optimize the mixing and heat transfer provided by swirl, a guideline is to have $w \leq v_\theta$, such that Equation 117 is satisfied.

Thus, a consequence of swirling jets is that they experience decay swirl. Therefore, there is a point beyond which the azimuthal velocity has decayed to a degree whereby it no longer significantly impacts the flow field. This factor is crucial in the design of swirling jets, and any applications that employ swirling jets for enhancing heat and mass transfer, combustion, and flow mixing.
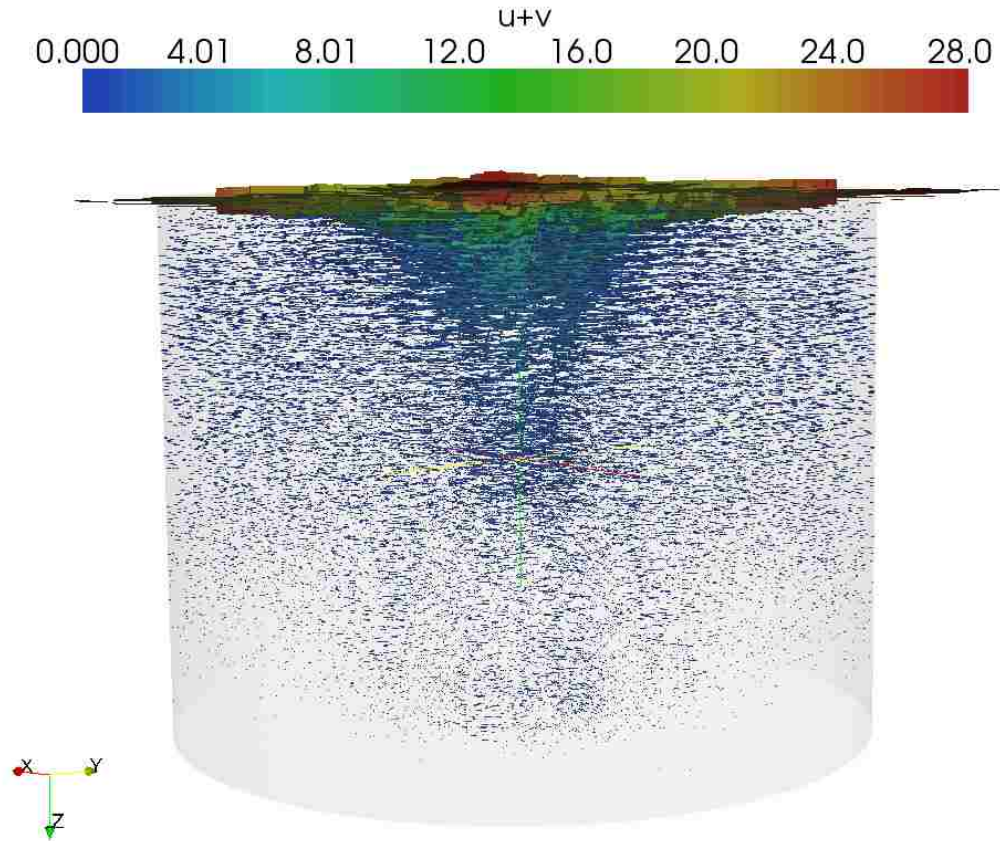
Figure 54. Fast Decay of the Azimuthal Velocity.

5.1.3 Impact of S on the Central Recirculation Zone

As shown by Figure 50, the maximum of the sum of the azimuthal and axial velocities

occurs when S=0.67 (i.e. θ=45º). This maximum is characterized by the intersection of

the azimuthal and axial velocities, that is, the point where $u_{\theta,o} = w_o$. As the azimuthal

velocity increases and exceeds the axial velocity, a low pressure region prevails near the

jet exit where the azimuthal velocity is the highest. The low pressure causes a reversal in

the axial velocity, thus producing a region of backflow. Because the azimuthal velocity

forms circular planes, and the reverse axial velocity superimposes onto it, the net result is

114

a pear-shaped CRZ. From a different point of view, for an incompressible swirling jet, as S increases, the azimuthal momentum increases at the expense of the axial momentum. This is consistent with literature data [Chigier and Chervinsky, 1967].

The CRZ formation resulted in a region where vortices oscillated, similar to vortex shedding from flow around a cylinder. The enhanced mixing associated with the CRZ is attributable to the back flow in the axial direction; in particular, the back flow acts as a pump that brings back flow for further mixing. The CRZ vortices tend to recirculate and entrain flow into the central region of the swirling jet, thus enhancing mixing and heat transfer within the CRZ. This subject matter should be studied in more detail.

Figures 55 and 56 shows the effect of swirl angle on the azimuthal and axial velocity for an unconfined swirling jet. Figure 57 shows the velocity vector, azimuthal velocity, and axial velocity as functions of weak swirl, while Figure 58 shows the same, but for moderate to strong swirl. *Note the dramatic changes that occurred in the axial and azimuthal velocity distributions as the CRZ formed—the most significant change occurred in the z-direction, which is the axis normal to the jet flow. For example, for θ=40º (no CRZ), the maximum azimuthal velocity at the bottom of the domain along the z axis was 15 m/s. But, when the CRZ formed at θ=45º, the maximum azimuthal velocity was essentially 0! The same effect can be observed for the axial velocity for pre- and post-CRZ velocity distributions.*

In effect, the region near the bottom of the z-axis for θ=45º formed a stagnant cone that was surrounded by azimuthal flow moving around the cone at ~15 m/s, and likewise for the axial velocity.
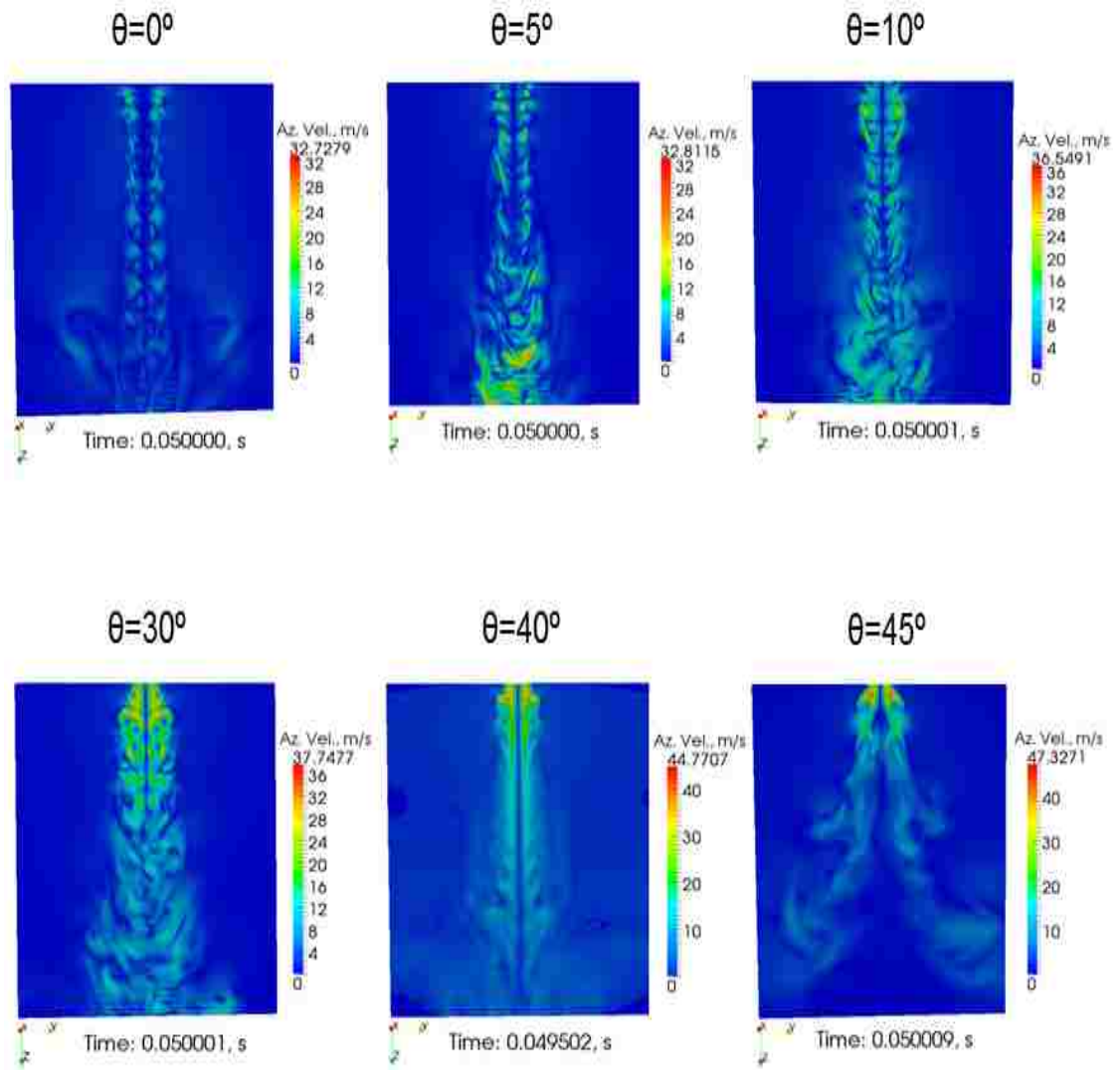
Figure 55. Effect of Swirl Angle on the Azimuthal Velocity.
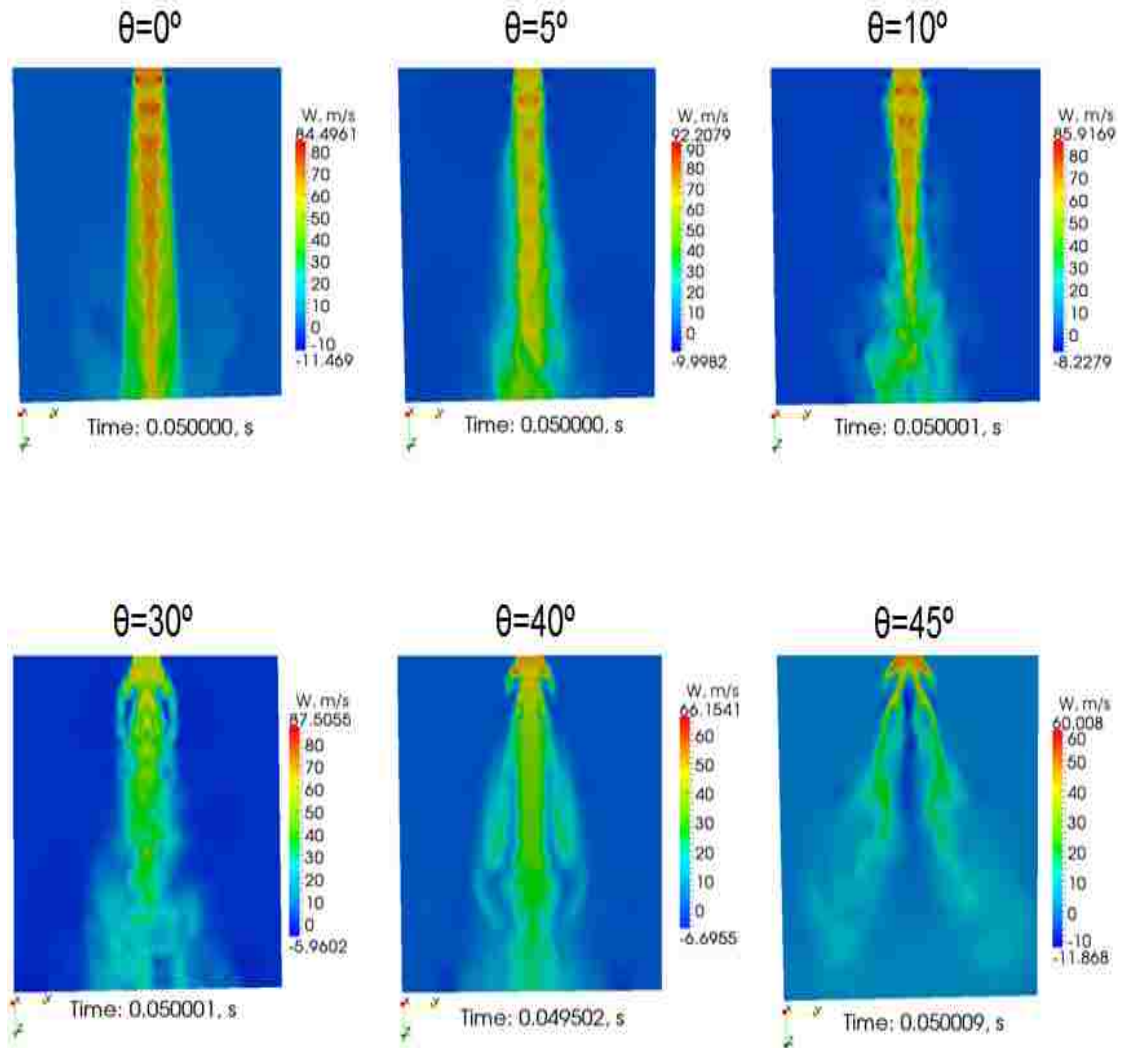
Figure 56. Effect of Swirl Angle on the Axial Velocity.
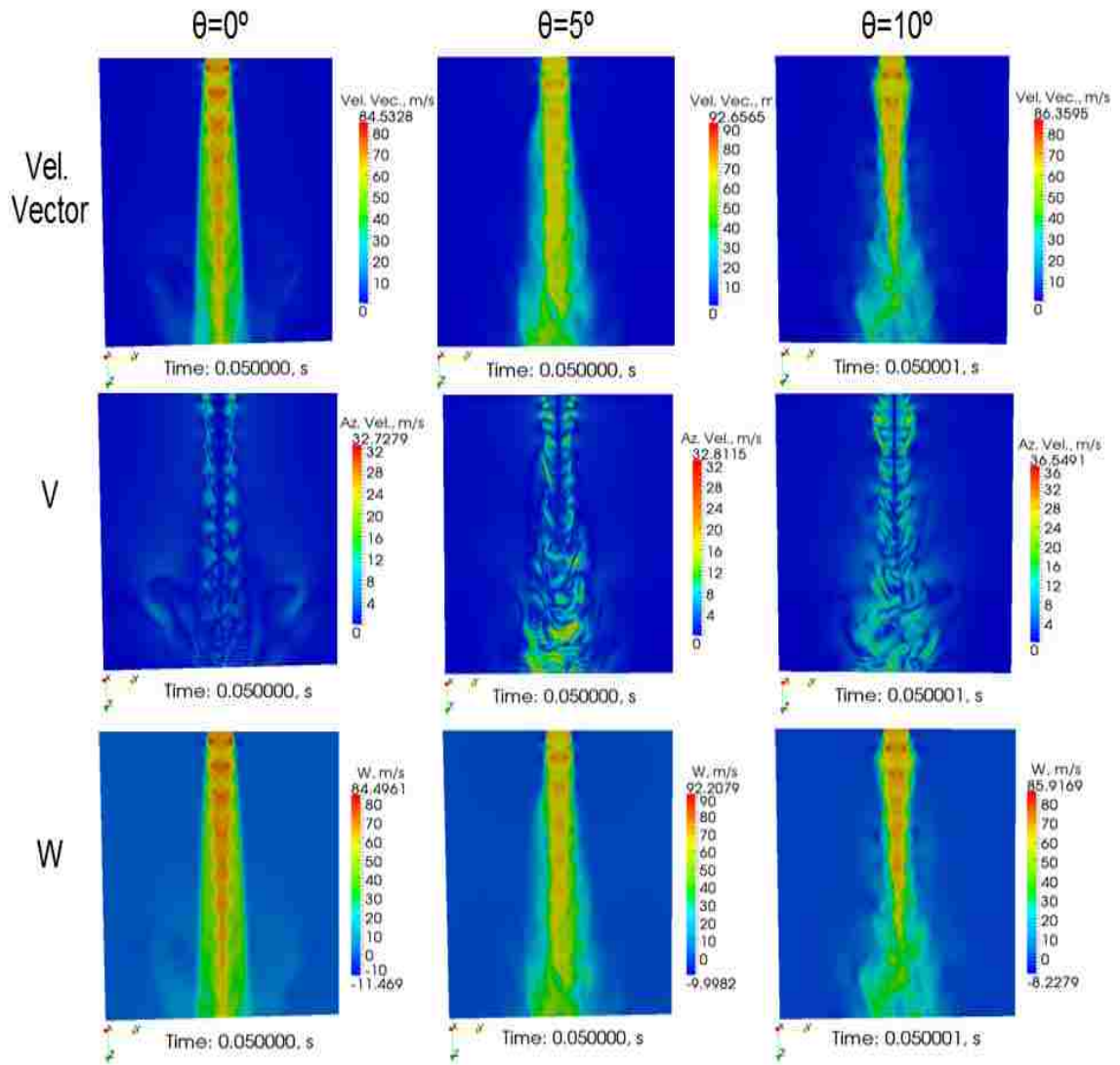
Figure 57. Velocity Vector, Azimuthal Velocity, and Axial Velocity as Functions of Small Swirl Angle.
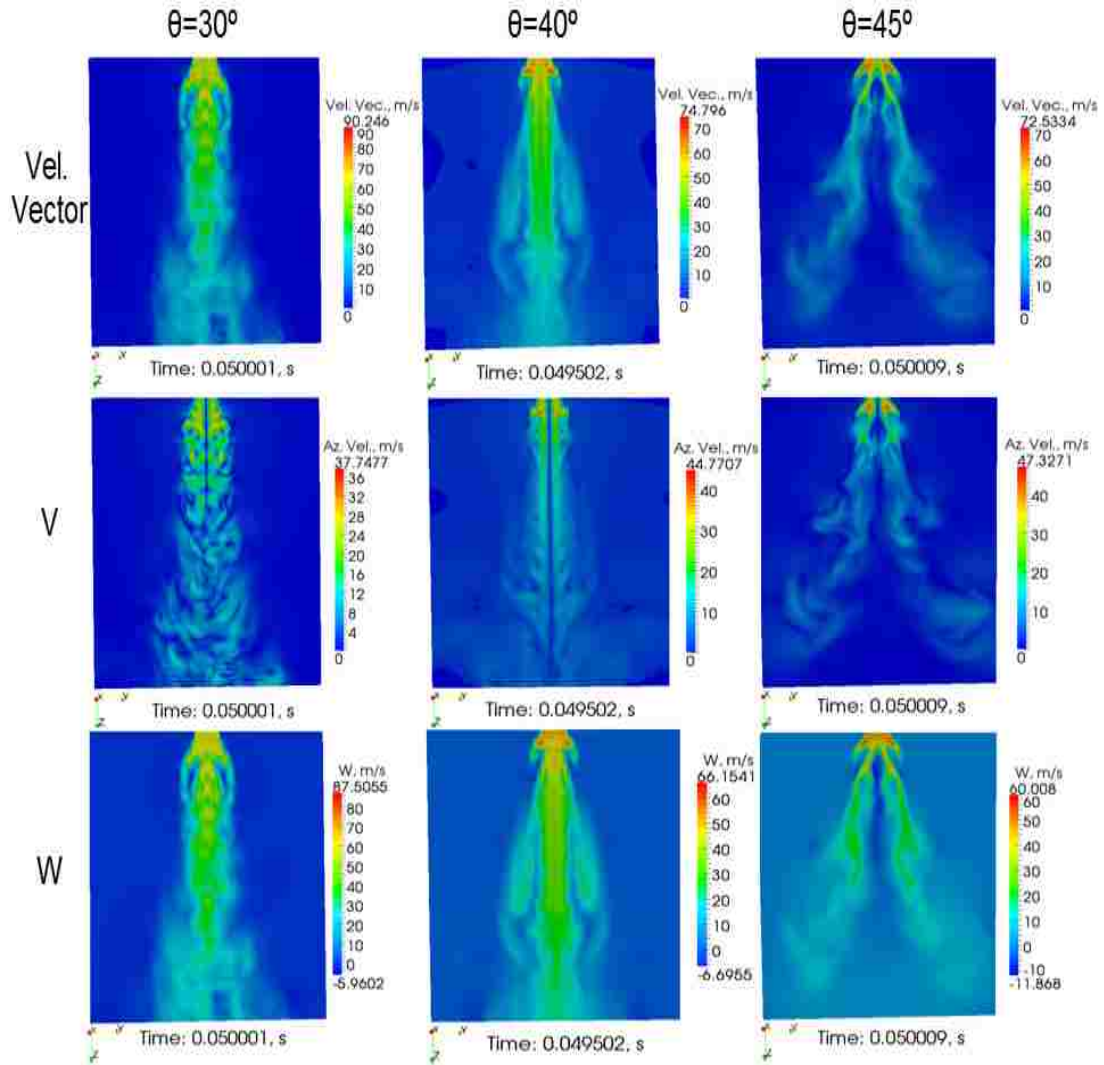
Figure 58. Velocity Vector, Azimuthal Velocity, and Axial Velocity as Functions of Moderate to Strong Swirl Angle.

From Figures 55 through 58, it is quite evident that the CRZ acts as a "solid" body around which the strong swirling jet flows. This is important, as the CRZ basically has two key impacts on the flow domain: 1) it diminishes the momentum along the flow axis and 2) both the axial and azimuthal velocities drop much faster than $1/z^2$. Therefore, whether a CRZ is useful in the design problem or not depends on what issue is being addressed. In particular, if it is desirable that a hot fluid be dispersed as rapidly as

possible, then the CRZ is useful because it more rapidly decreases the axial and azimuthal velocities of a swirling jet. However, if having a large conical region with nearly zero axial and azimuthal velocity is undesirable, then it is recommended that S<0.67. In the case of the VHTR, the lower plate temperatures were achieved as S increased, with S=2.49 achieving the coolest temperatures.

The "solid obstacle" analogy to a CRZ has been noticed in the literature. As so eloquently pointed by Hall,

> "Vortex cores have great powers of persistence: tornadoes travel many miles, and even the wing-tip vortices from aircraft trail for a few miles: and yet the concentrated structure can be dissipated abruptly; for example, the axial flow in the core of a leading-edge vortex can be brought from a value several times the free stream velocity to rest, while the core expands as if it had suddenly encountered a solid obstacle."

The blockage is also consistent with vortex shedding from a jet in a crossflow, and has been regarded "as if the flow were around a solid bluff body" [McMahon, Hester, and Palfery, 1971]. This feature of the CRZ will be explored further when using S > 0.67 in the LP calculations (Section 5.3.2).

5.1.4   Enhanced Flow Patterns from Swirling Jets

Certain swirling jet flow patterns not found in conventional jets promote mixing of the gas. These patterns arise from the high kinematic viscosity of helium gas at the VHTR operating temperature, as well as the swirling motion. For example, there is a toroidal helicoid pattern, as shown in Figure 59. The impact of this toroidal helicoid pattern is to continuously mix regions of colder gas into regions that are relatively hotter,

while at the same time the gas is transported around in a complex circular motion that involves both the azimuth angle and the inclination angle. Further, there are tertiary flow patterns, as shown in Figures 60 and 61 (the red and black arrows indicate the secondary and tertiary flow patterns, respectively). It is well-known that a conventional jet entrains surrounding gas [Bird, Steward, and Lightfoot, 2007]; this is the secondary flow pattern. However, for swirling jets, there is a secondary flow pattern that in turn induces a tertiary flow pattern. In short, these exotic flow patterns further enhance mixing and, thus, promote higher heat transfer rates.
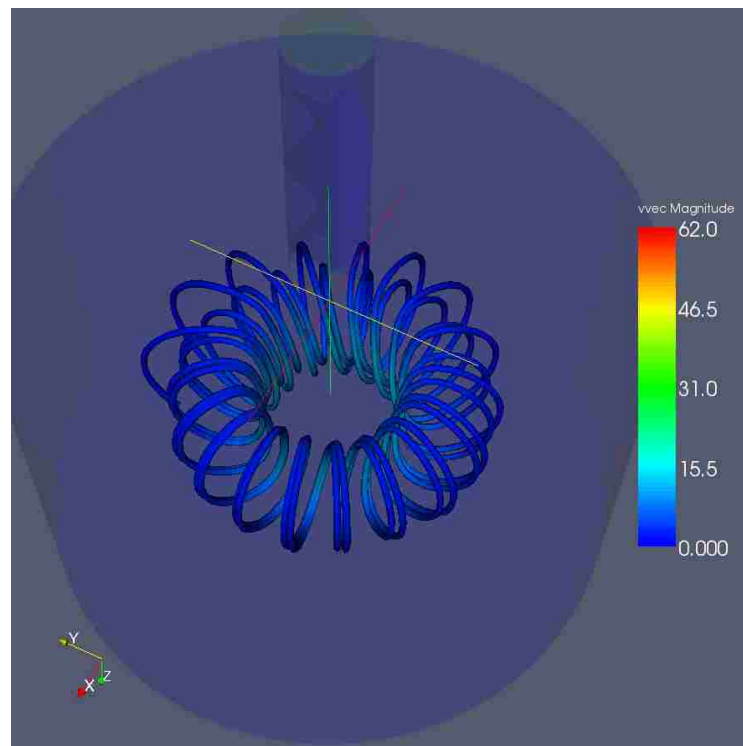
Figure 59. Toroidal Helicoid Flow Pattern.
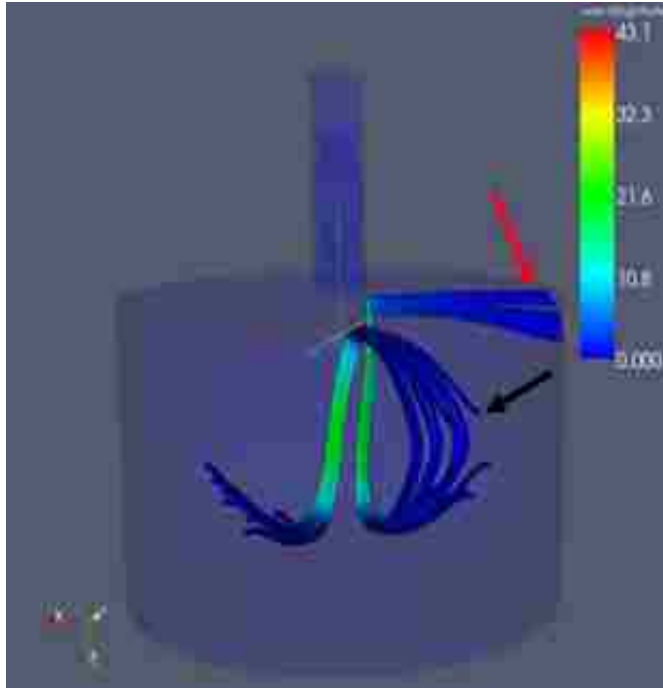
Figure 60. Secondary and Tertiary Flow Patterns—Lateral View. (The Red and Black Arrows Indicate the Secondary and Tertiary Flow Patterns, Respectively.)
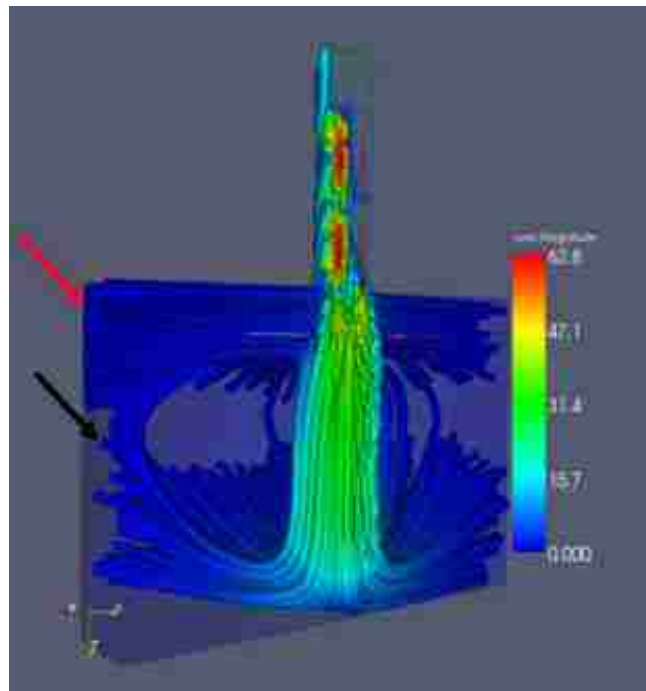
Figure 61. Secondary and Tertiary Flow Patterns—Jet Cross Section View. (The Red and Black Arrows Indicate the Secondary and Tertiary Flow Patterns, Respectively.)

There are several key flow patterns that are exhibited by the impinging, swirling jet. These can be better understood by visualizing the various distinct zones within the flow domain, and how they interact. For example, the gas from the upper, central, and lower lateral sides of the large plenum cylinder eventually forms part of the outermost regions of the swirling jet core. This is demonstrated progressively in Figures 62 – 65, which include 2, 100, 750, and 1,000 particle trace lines (streamlines) that show the gas particle path and velocity. Note that the four figures were obtained for the same transient time— they simply show various degrees of streamline layering that is included in each figure for enhanced visualization of the flow. The figures confirm that the gas is drawn inwardly in the radial direction from the upper, central, and lower lateral sides of the large cylinder, and then fed into the swirling jet. This can be shown by first observing Figure 62, which includes a long and a short streamline. The long streamline represents the gas that swirls as it flows through the quadruple helicoid swirling device. Upon exiting the device, the gas continues its downward, spiraling path until it nears the impingement plate. Thereafter, the long streamline basically ceases to rotate and spiral, and instead flows outwardly in the radial direction. On the other hand, at least initially, the short streamline behaves differently than the long streamline. It begins by flowing radially inward along the upper, lateral part of the large plenum cylinder. At this point, it is moving about two orders of magnitude slower than the jet. However, once it reaches the jet core, its path rotates approximately 90˚ downward as a result of the swirling jet's axial motion, which additionally causes its velocity to increase 10 to 100 times. At this moment, its motion follows that of the jet and the short streamlines collectively form gas shells that wrap around the outermost part of the jet core (*see* Figure 65). Upon nearing

123

the impaction plate, just like the long streamline, the short streamline transfers its axial

and azimuthal momentum into radial momentum (Figure 62). Thereafter, the radial flow

exits the large cylinder.
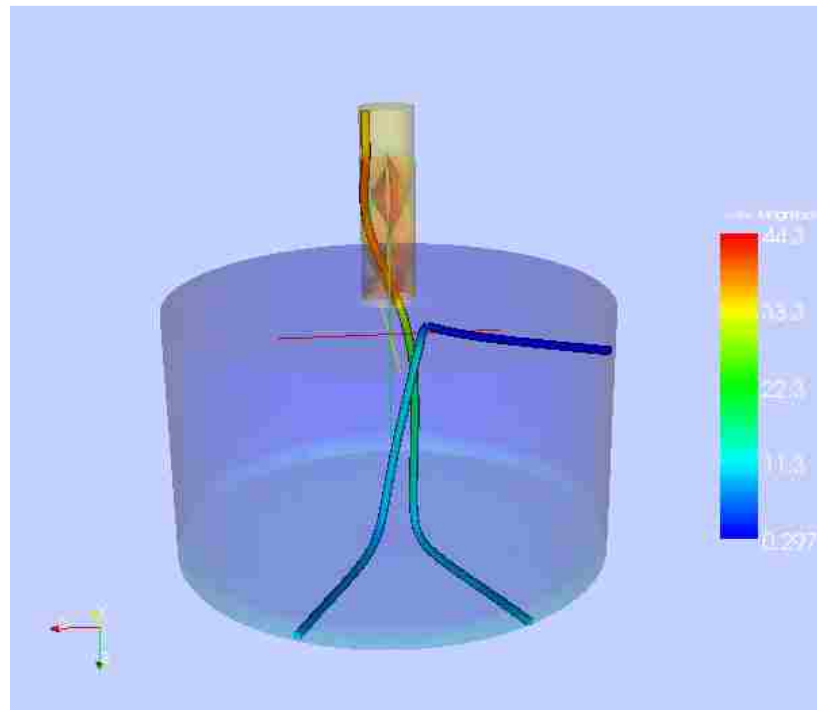
Figure 62. Two Streamlines Showing the Jet and Entrained Flow.
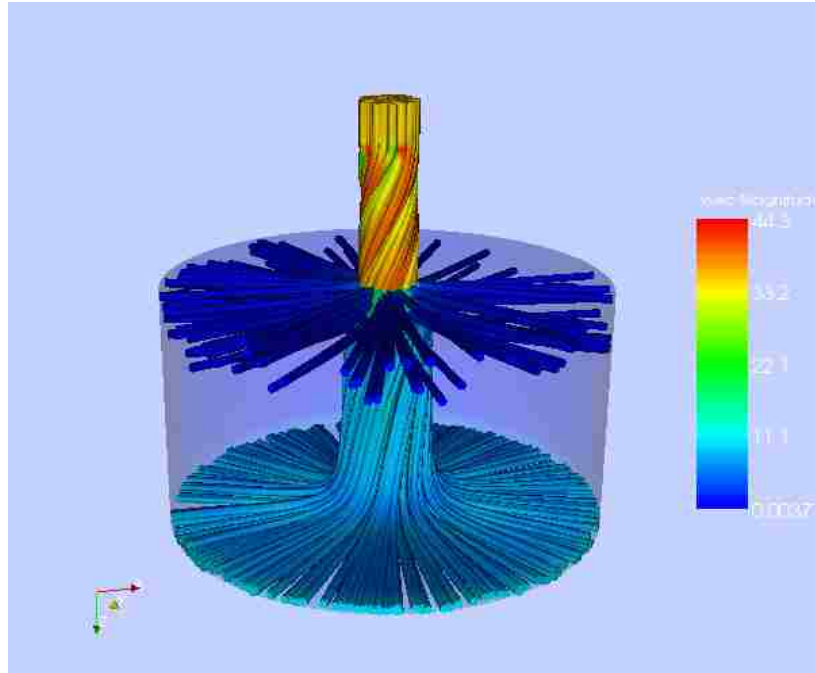
Figure 63. One Hundred Streamlines Showing the Jet and Entrained Flow.
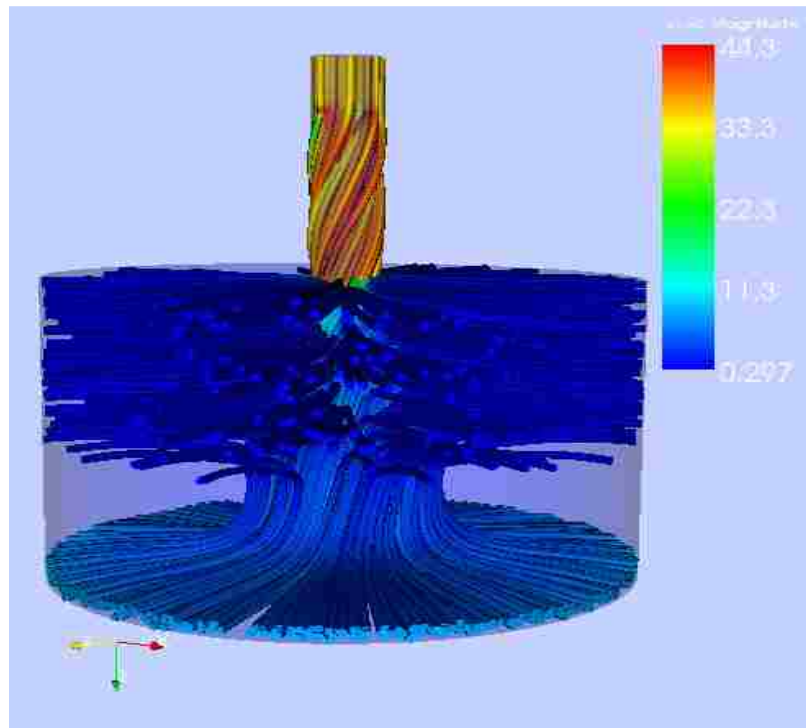
Figure 64. Seven Hundred Fifty Streamlines Showing the Jet and Entrained Flow.

Figure 64 shows that the entrained gas wraps around the outer layers of the swirling jet. The figure also shows that the entrained gas has a rotational nature as it flows down axially in cohesion with the well-established swirling jet core. As the flow nears the impingement plate at the bottom of the large cylinder, the gas slows down as it begins to flow predominantly in the radial direction. The progressive increase of trace lines in Figures 62 – 65 shows that the gas is entrained in the upper, central, and lower regions of the cylinder, with the circulation path of the entrained gas becoming increasingly smaller and smaller as the gas becomes entrained closer and closer to the impingement plate.
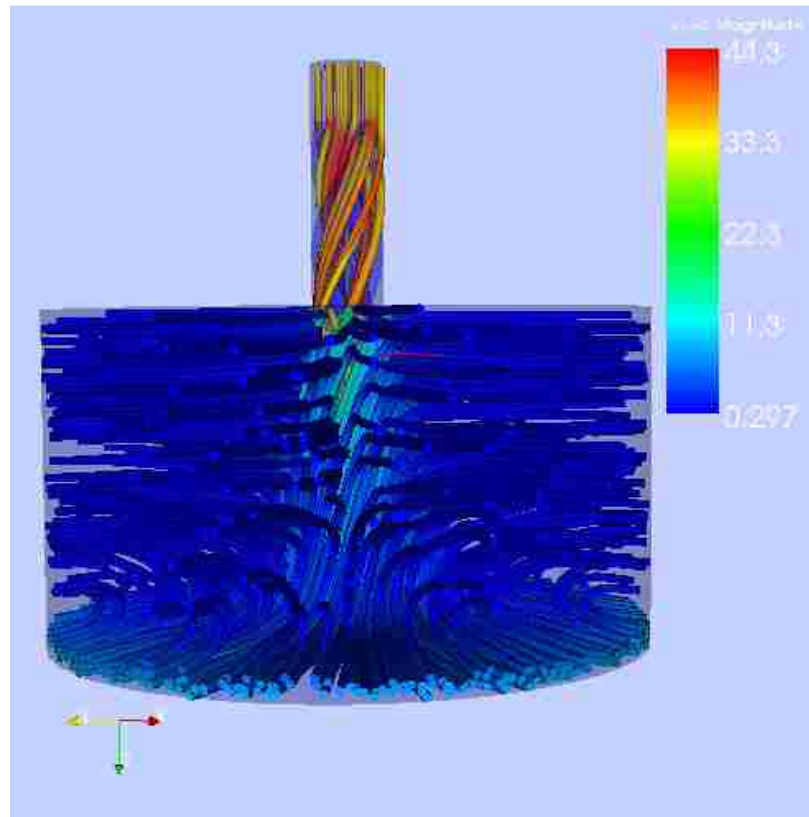
Figure 65. One Thousand Streamlines Showing the Jet and Entrained Flow.

The flow jet can be visualized by cutting the flow domain at the y=0 plane, as shown in Figure 66. The small inlet cylinder containing the quadruple helicoid swirling device

126

has two flow regions. Initially, the gas flows along the z axis through a cylindrical pipe with no obstructions. Then, the gas begins rotating in a cylindrical helicoid motion as it swirls around the four helicoid ribbons. Notice that there are four major flow regions within the large cylinder. The first is shown by the light green swirling jet core that simultaneously moves in the radial, azimuthal, and axial directions as it expands, swirls, and moves downwardly. Its motion is similar to a conical helicoid. The second region is comprised of a large set of blue layers of entrained gas that emanates radially inward from the upper, central, and lower lateral regions. Such gas forms layers that surround the jet and swirl around the jet core, as shown in Figure 67. The black arrows in the figure show where the relatively slower gas ceases to move primarily in the radial direction, and instead begins to accelerate axially (as well as azimuthally), following the swirling motion of the jet. The third region consists of the zone where the jet core and its numerous entrained surrounding layers approach the lower plate. At this point, the gas proceeds radially outward, forming a plate-like region (*see* Figure 66, bottom section). For convenience, the general flow directions are marked with gray arrows in the figure. Finally, the fourth region is at the bottom of the jet, centered about the z axis, where stagnation occurs.
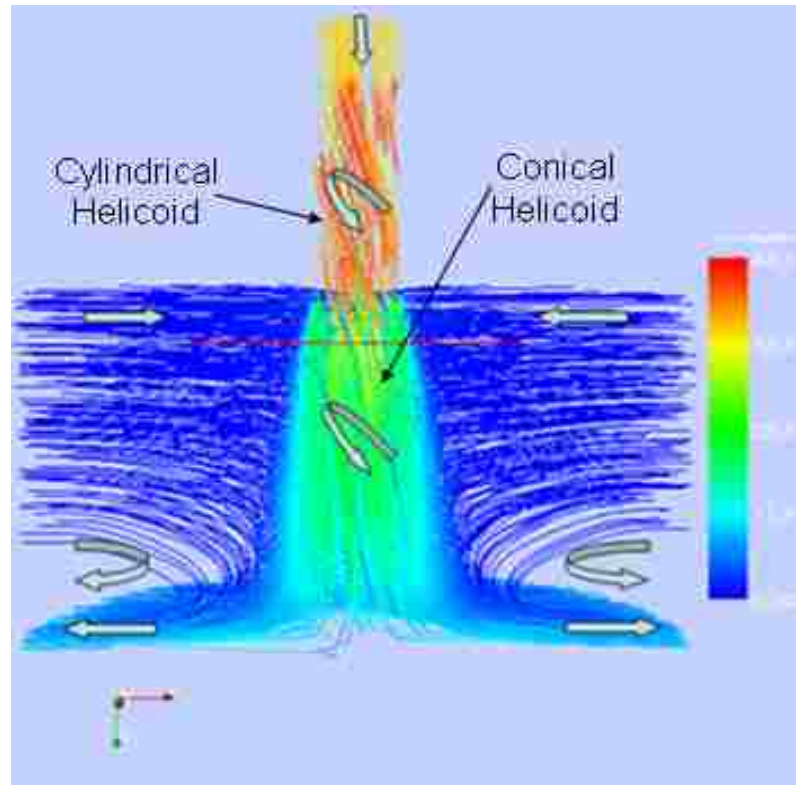
Figure 66. Velocity Streamline Cross-Section (Y=0 Plane).
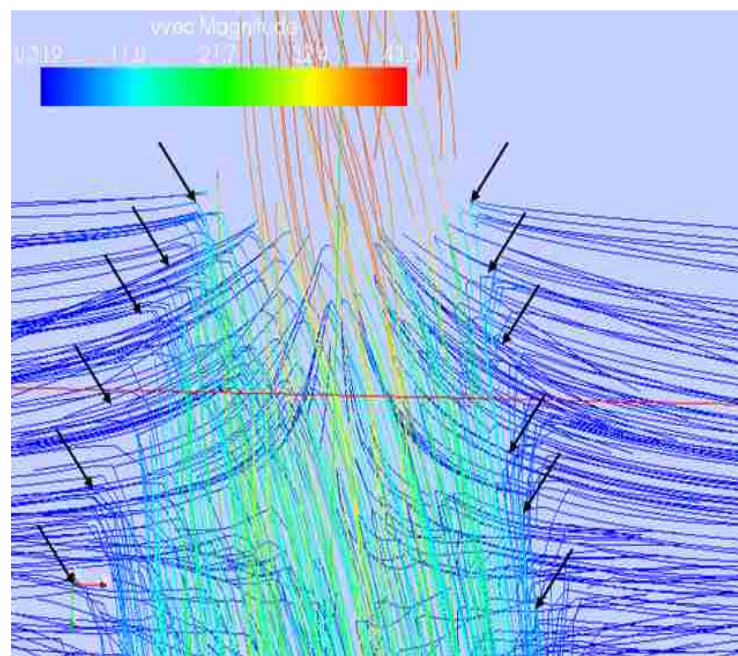
Figure 67. Zoom of Velocity Streamlines Showing Entrainment (Cross-Section at Y=0 Plane).

128

As discussed previously, the entrained gas begins by flowing radially inward towards the jet core, and then rotates approximately 90° downward as a result of the swirling jet's azimuthal motion. Now, after the 90° rotation occurs, the streamline begins swirling along with the motion of the rotating jet. Thus, in this example, by the time the streamline reaches the impingement plate, it has rotated about 75 to 80° about the vertical axis. This additional rotation is purely the result of the swirling motion of the flow, and therefore does not occur in the absence of the swirling device. To illustrate this phenomenon, Figure 68 shows a comparison of a regular jet with no swirling (orange streamline) and one with swirling (black streamline). The orange streamline represents a "C" shaped circulation path [Bird, Stewart, and Lightfoot, 2007] that eventually closes to form a loop that lies on a 2D plane; that is, the flow returns back to the top due to natural convection. On the other hand, the black streamline follows a "Z" path initially that does not close at the point where it originated, but is rather 3D, meaning that it reaches the top *significantly away* from the point where the fluid originated. Thus, its path closely resembles a Greek "σ", as shown in Figure 69.

An application of this phenomenon is for a system design configuration to take advantage of the "Z" twisted path by "pumping" away gas from hot zones to a location that is azimuthally away from the hot zone (75 to 80° in this example). In the case of the "C" path, the hot gas eventually can rise back up close to the point where it originated as a result of the buoyant forces, with the gas forming a vertical circular circuit, thus returning some of the energy to its initial location; not so the swirling jet. In short, the recirculation pattern acts as a "pump" that moves hot fluid from one region to another,

which in all likelihood is at a different temperature. It is therefore a mechanism that

serves to more efficiently transfer heat.
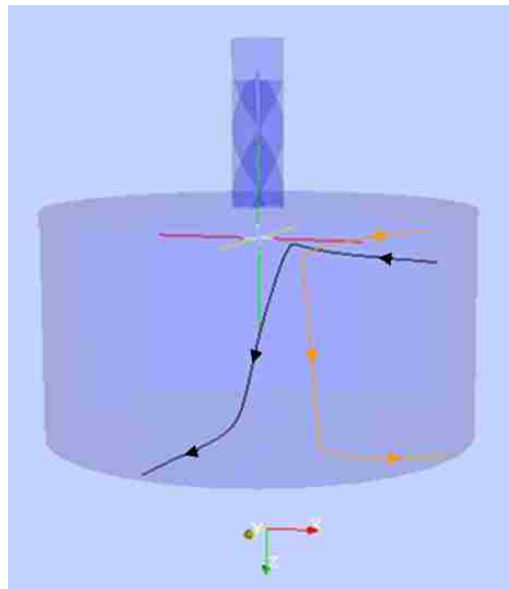
Figure 68. Comparison between Streamlines for an Entrained Gas in Conventional Jet (Orange) and a Swirling Jet (Black).
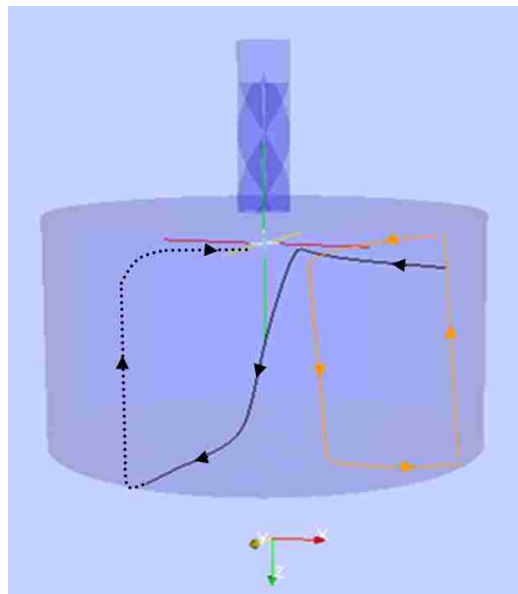
Figure 69. Comparison between Streamlines for an Entrained Gas in a Conventional Jet (Orange) and a Swirling Jet (Black). (The Dotted Lines Represent the Path Closure.)

Figure 70 shows a comparison between jet core streamlines for a regular jet (orange) and a swirling jet (black). Notice that by the time the swirling jet reaches the impingement plate, its diameter at a fixed plane in the z direction is larger than that of the jet with no swirling. This, then, is a measure of the increased heat transfer potential of the swirling jet, as its momentum is distributed across a larger domain.

Figure 71 shows the velocity magnitude of the radial and azimuthal velocities for a slice at z=constant, roughly 2/3 of the way down the large cylinder plenum. The swirling motion of the jet is evident in the central region. A zoom of the rotating region shows the adjacent fluid being entrained into the jet (*see* Figure 72). Figure 72 can be visualized as analogous to a limit cycle that happens to have a varying radius—the radius increases as the entrained layers of fluid wrap around the jet core. The fluid inside the jet core is flowing radially outward as it flows azimuthally, thus giving it a spiral-like counter-clockwise motion. Meanwhile, at the outer periphery of the jet core, the entrained flow rotates in a counter-clockwise fashion as it wraps around the jet core. Because both velocity fields move towards the limit cycle, it is therefore stable.
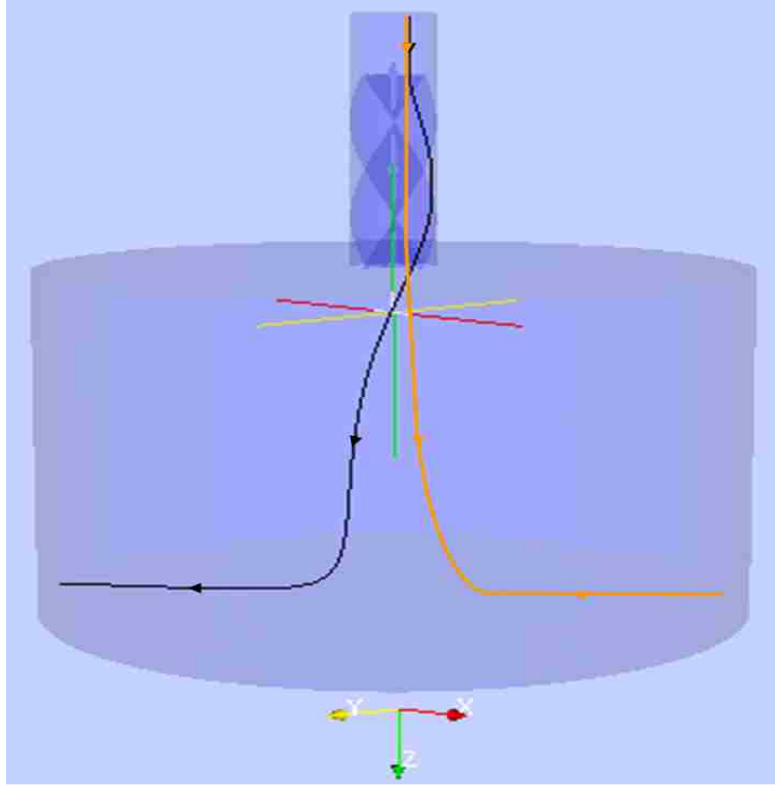
Figure 70. Comparison between Jet Core Streamlines for a Conventional Jet (Orange) and a Swirling Jet (Black).
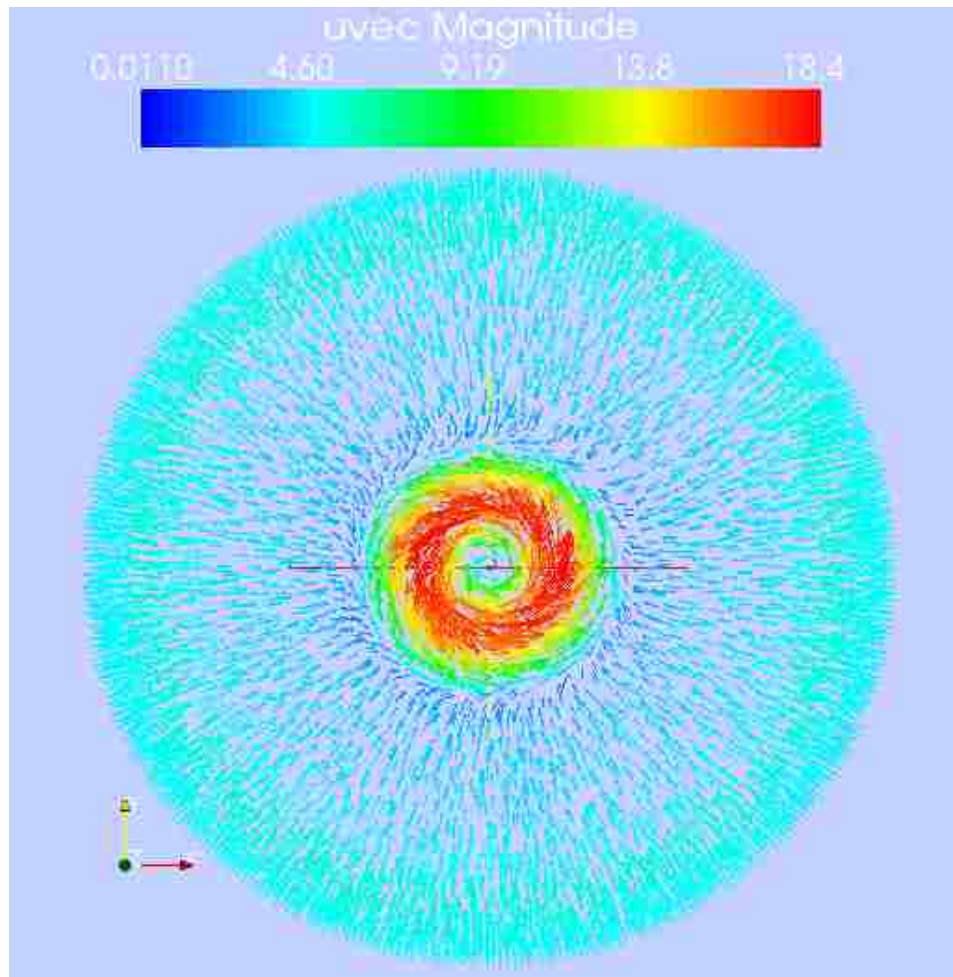
Figure 71. Radial and Azimuthal Velocity Magnitude.
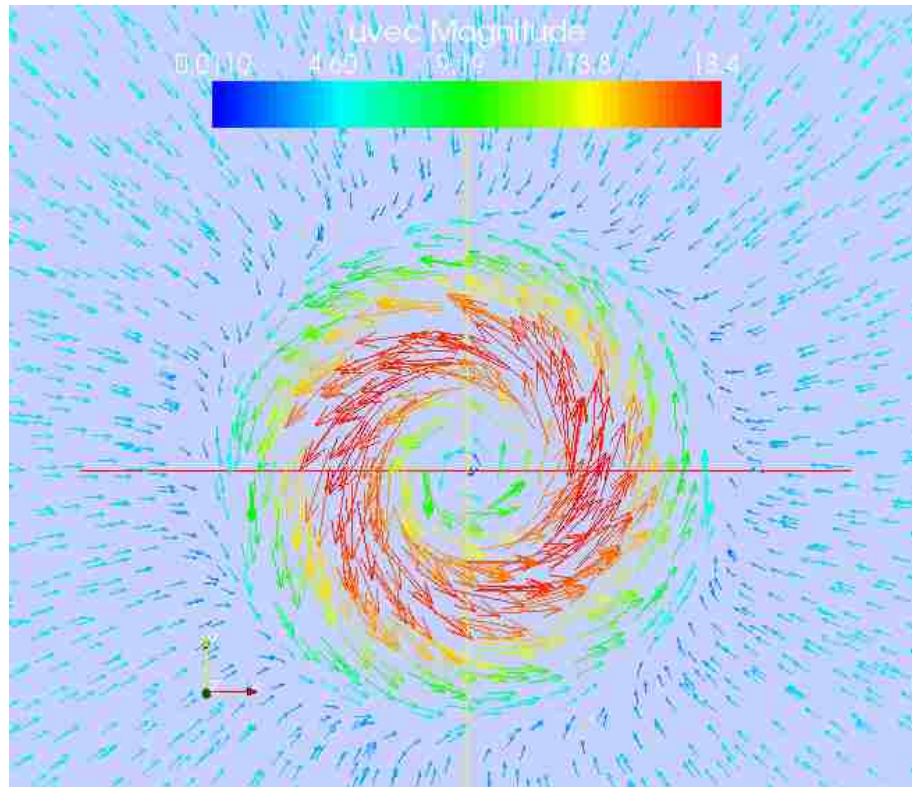
Figure 72. Zoom of Jet Vortex as it Entrains the Adjacent Gas.

Notwithstanding the enhanced flow patterns attributable to swirl, there is the concern

that a "stagnation" or "hurricane eye" analogy may exist. In particular, there would form

a centralized region along the z axis where there is nearly-zero velocity. As shown in

Section 5.1.3, that does not occur unless a CRZ forms. For example, note that Figure 61

shows that the jet core had velocities in the 15 to 50 m/s range. Now, the azimuthal

velocity distribution shows a region of stagnation in the center of the swirling jet (Figure

73, near the crosshairs). The azimuthal velocity at that point was about 0.03 m/s. The

figure was taken at a plane where z=constant, at half the height. But, the low azimuthal

velocity in the center of the swirling jet was offset by the relatively large axial velocity in

134

the z direction, as shown in Figure 74. Figure 74 shows a side view of the net velocity

magnitude, sqrt($v_x v_x + v_y v_y + v_z v_z$). As evidenced by the vector arrows and also from

Figure 73, most of the velocity is attributable to the axial component. Figure 73 shows

the large velocity magnitude field in the center of the jet with a peak central velocity

magnitude of 29.9 m/s. A top view of the overall magnitude is shown in Figure 75.

Figures 74 and 75 demonstrate that there was a large contribution of w in the z direction,

and therefore the central region was not stagnant. Figure 76 is the same as Figure 73,

except the slice was made at about z=2/3. The figure shows a more complex pattern,

though, with concentric rings of nearly stagnant flow in the radial and azimuthal

directions. Again, a look at the overall velocity magnitude side and top views shows that

the central region had peak velocity magnitudes approaching 25 m/s. Figures 77 and 78

are similar to Figures 74 and 75, except they were obtained for a slice at z=2/3.
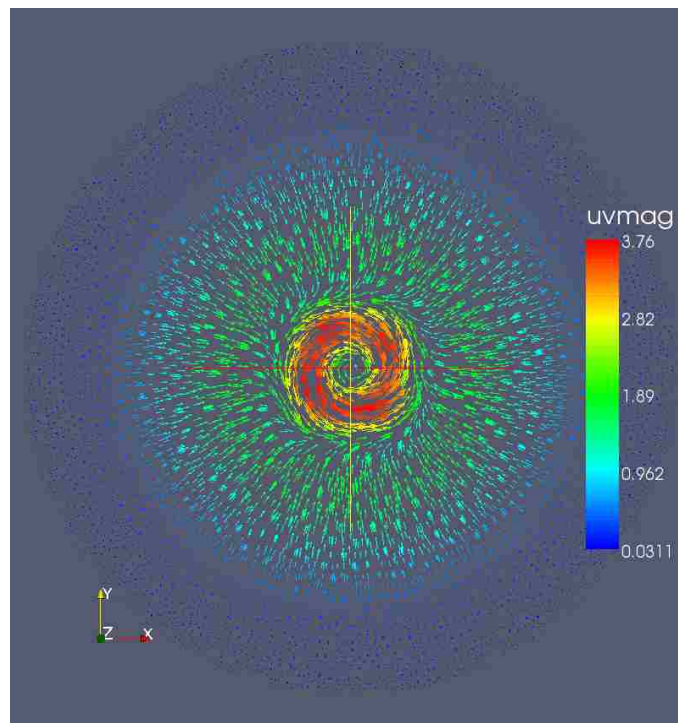
Figure 73. Velocity Magnitude of U and V at Z=1/2.

135
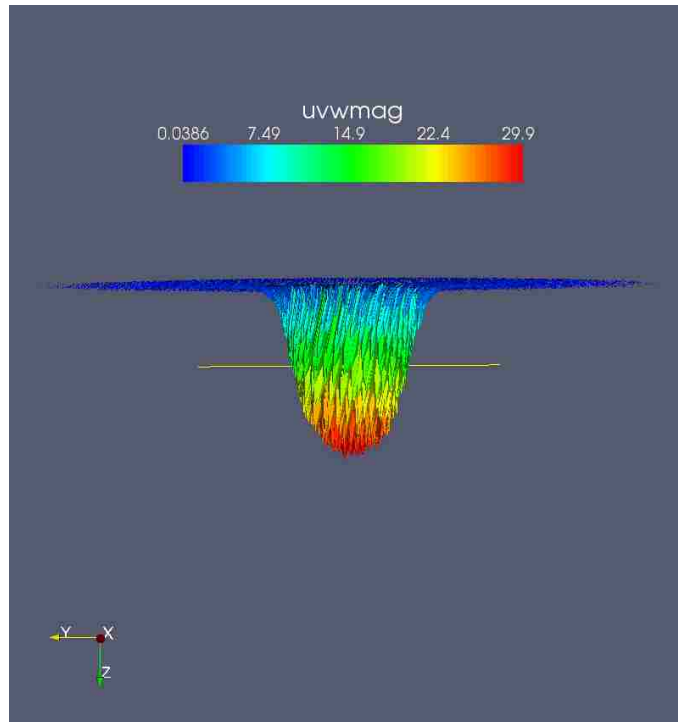
Figure 74. Side View of Velocity Magnitude for U, V, and W at Z=1/2.
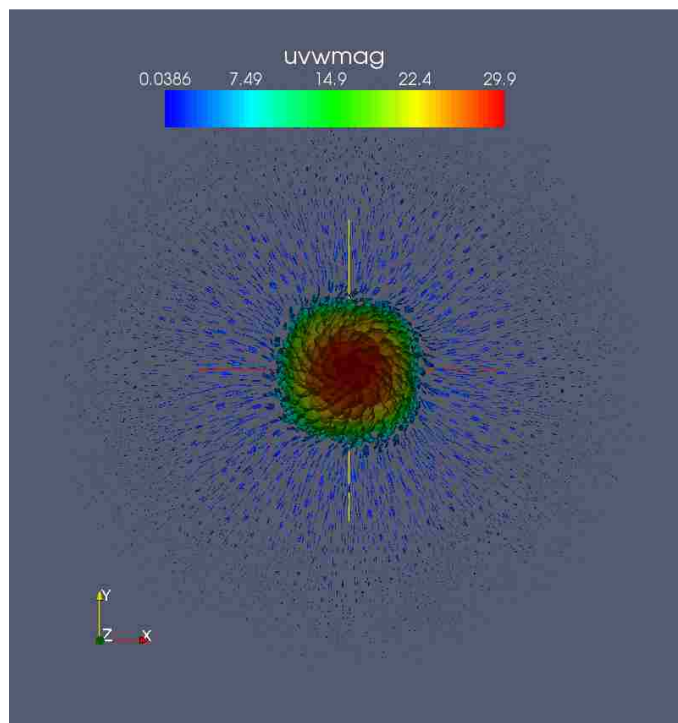
Figure 75. Top View of Velocity Magnitude for U, V, and W at Z=1/2.

136
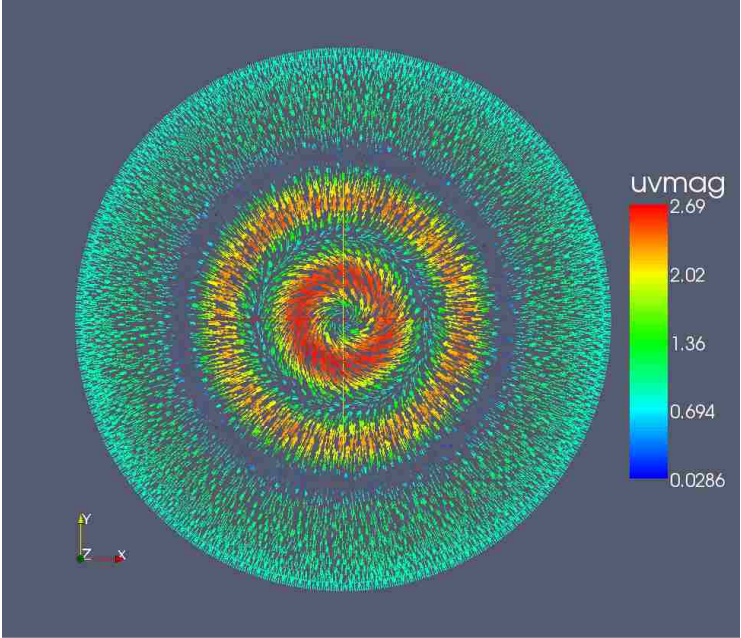
Figure 76. Velocity Magnitude of U and V at Z=2/3.
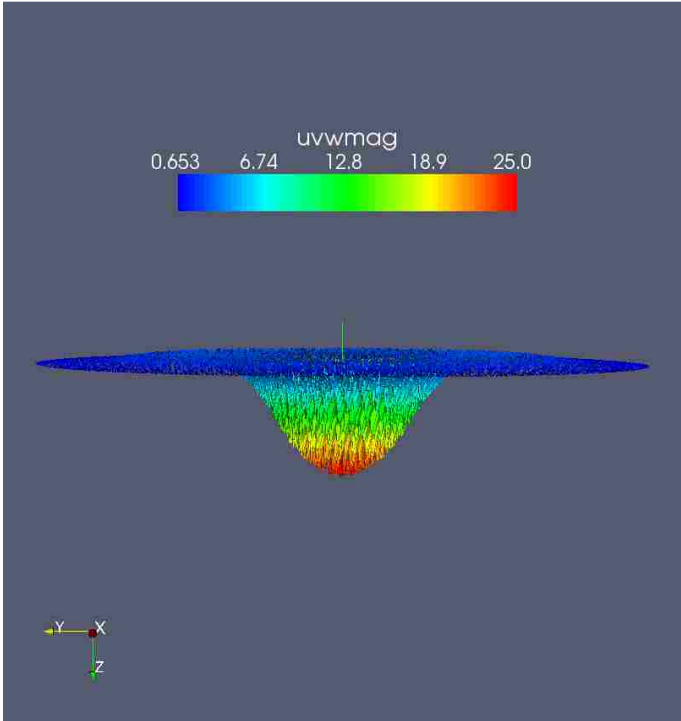
Figure 77. Side View of Velocity Magnitude for U, V, and W at Z=2/3.
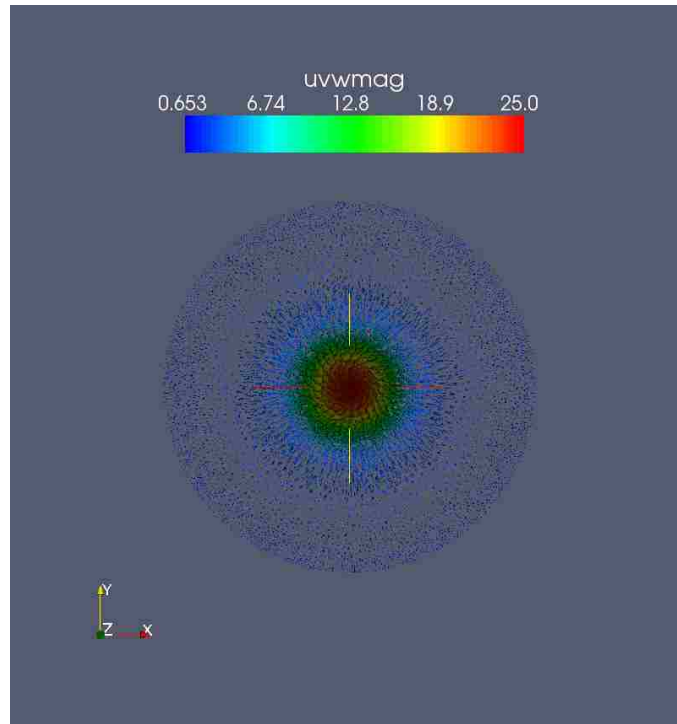
Figure 78. Top View of Velocity Magnitude for U, V, and W at Z=2/3.

5.1.5   Impact of Mixing and Heat Transfer as Functions of Re and S for Swirling Jets

Two models were employed to address this issue: 1) a cylindrical domain with a centrally-positioned swirling air jet and 2) a quadrilateral domain with six swirling jets. The single-jet model and its results are presented first, followed by the six-jet model discussion and results.

Both were run on the massively-parallel Thunderbird machine at SNL. The initial time step used was 0.1 μs, and the maximum Courant-Friedrichs-Lewy (CFL) condition of 1.0, which resulted in a time step on the order of 1 μs. The simulations were typically run for about 0.05 to several seconds of transient time. Both models were meshed using hexahedral elements with the CUBIT code [CUBIT, 2009]. The temperature-dependent

138

physical and thermal properties for air were calculated using a CANTERA XML input file that is based on the Chapman-Enskog formulation [Bird, Steward, and Lightfoot, 2007]. Finally, both used the dynamic Smagorinsky turbulence model.

The single-jet computation domain consisted of a right cylinder that enclosed a centrally-positioned single, unbounded, swirling air jet (Figure 79). The meshed computational domain consisted of 1 million hexahedral elements. The analysis varied the air inlet Re from $5x10^3$ to $5x10^4$ and the swirling angle, θ, from 0 to 75°, which corresponds to S from 0 to 2.49, respectively. The top surface (minus the jet BC) was modeled as a wall, while the lateral and bottom surfaces of the cylindrical domain were represented as open boundaries.
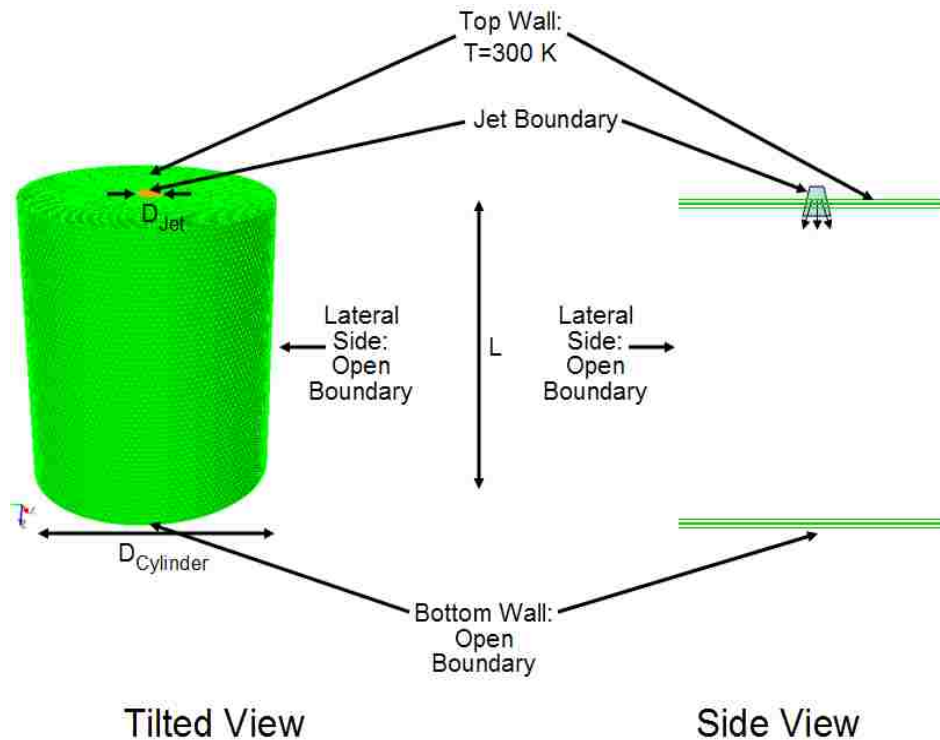
Figure 79. Cylinder with a Single Swirling-Jet Boundary.

Figure 80 shows the effect of the swirl angle and Re on the azimuthal velocity field

for θ=15, 25, 35, 50, 67, and 75º (S=0.18, 0.31, 0.79, 1.57, and 2.49, respectively). Re

was 5,000, 10,000, 20,000, and 50,000. As Re increased for fixed S, there was a higher

degree of azimuthal velocity turbulence, as well as a wider jet core. As S increased for a

fixed Re, the azimuthal velocity increased, consistent with Equation 112. The figure also

clearly shows the strong impact the CRZ formation has on how far the swirling jet travels

before it disperses. *Thus, as soon as the CRZ appears, the azimuthal velocity field does*

not travel as far, even at Re is increased substantially. In other words, although Re

increased 10-fold as shown on the figure, its impact was not as great on the flow field as

that of S once the CRZ developed.
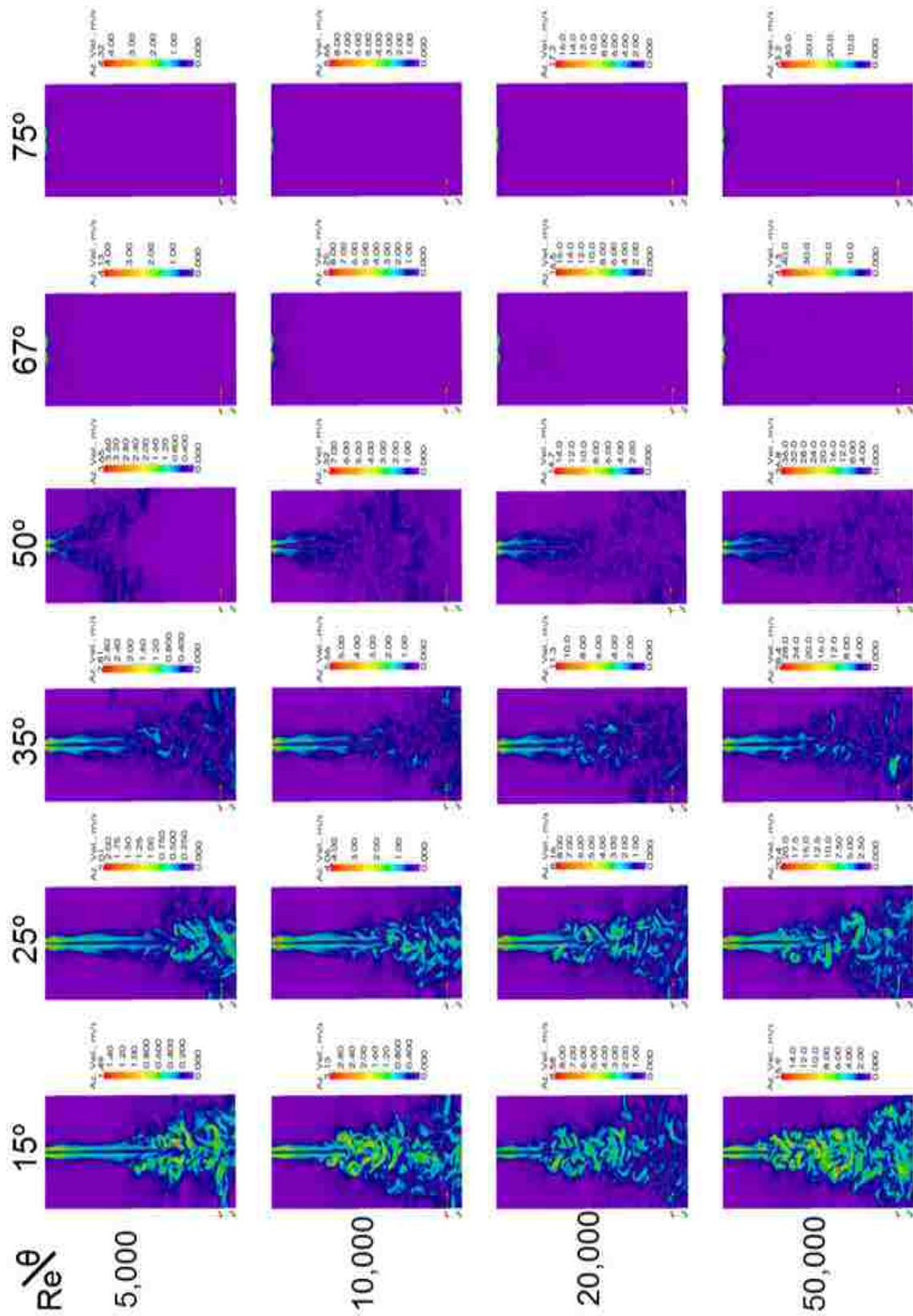
Figure 80. Impact of Re and θ on Azimuthal Velocity Field.

141

The computational mesh for the quadrilateral 3D domain for the set of six circular, swirling air jets is shown in Figure 81. The air temperature and approach velocity in the z direction for the jets was 300 K and 60 m/s. The numerical mesh grid in the computation domain consisted of 2.5×10^5-5×10^6 hexahedral elements.
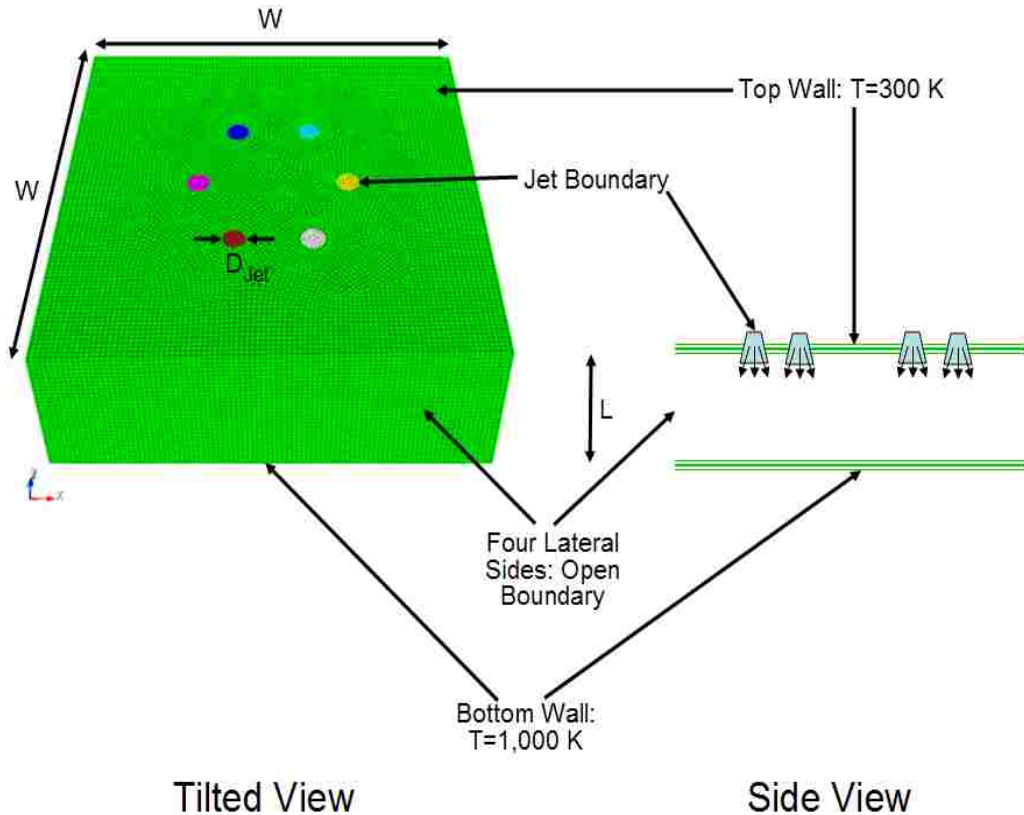
Figure 81. Quadrilateral with Six Swirling-Jet Boundaries.

The top surface of the domain (minus the jet BCs), was modeled as an adiabatic wall. The lateral quadrilateral sides were open boundaries that permitted the air to continue flowing outwardly. The bottom of the domain was an isothermal wall at 1,000 K. The air swirling out the six jets through the computation domain eventually impinged upon the bottom surface, thereby removing dissipated heat. The hot air at the surface of the hot

142

plate was entrained by the swirling and mixing air above the plate. The calculations were conducted for θ=0 (conventional jet), 5, 10, 15, 20, 25, 50, and 75º (the corresponding S were 0, 0.058, 0.12, 0.18, 0.24, 0.31, 0.79, and 2.49, respectively). With the exception of varying the swirl angle, the calculations used the same mesh, Fuego version, and input.

As a way to quantify S vs. cooling, all the hexahedral element cell-averaged temperatures were grouped according to a linear temperature distribution ("bins"). The calculated temperature bins are shown in Figures 82 and 83, which show that for S in a certain range at a given L/D, there were a higher number of hotter finite elements in the flow field; this is indicative of the swirling jet enhanced ability over a conventional jet to remove heat from the isothermal plate. For example, Figure 82 shows that for L/D=12, and S ranged from 0.12 to 0.31, the swirling jets removed more heat from the plate, and were thus hotter than the case with S=0. Additionally, the best cooling was achievable when S=0.18. However, Figure 83 shows that for L/D=3, and S ranged from 0.12 to 0.79, the swirling jets removed more heat from the plate, and were thus hotter than the case with S=0. The best cooling was achievable when S=0.79. The results confirmed that for S≤0.058, the flow field closely approximated the flow field for S=0, so there were insignificant enhancements to the heat transfer.

The back flow zone, the CRZ, appears to enhance the heat transfer compared to swirling flow with no CRZ, as evidenced by the multiple-jet calculations shown in Figures 82 and 83. As noted previously, the azimuthal velocity of the swirling jet decays as $1/z^2$. Therefore, the largest heat transfer of the swirling jets over conventional jets occurred within a few jet diameters as evidenced by Figures 82 and 83. Thus, it was not surprising that the multiple jets enhanced cooling of the bottom isothermal plate if and

only if the azimuthal velocity had not decayed before reaching the intended target (i.e. the isothermal plate in this case).
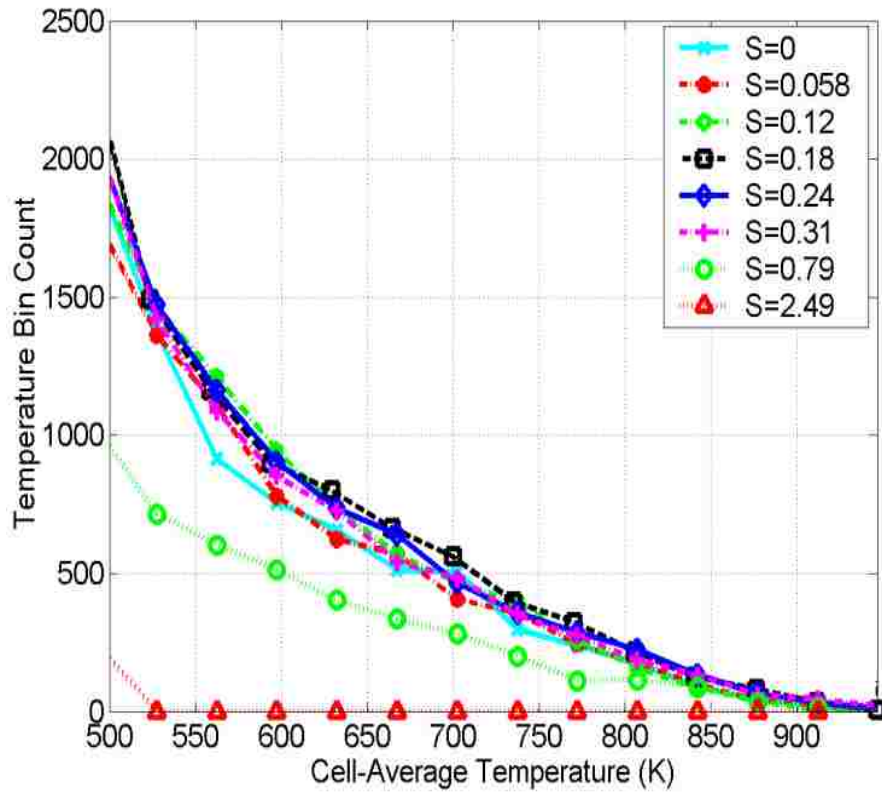
Figure 82. Temperature Bin Count for All Elements with L/D=12 Mesh.

144
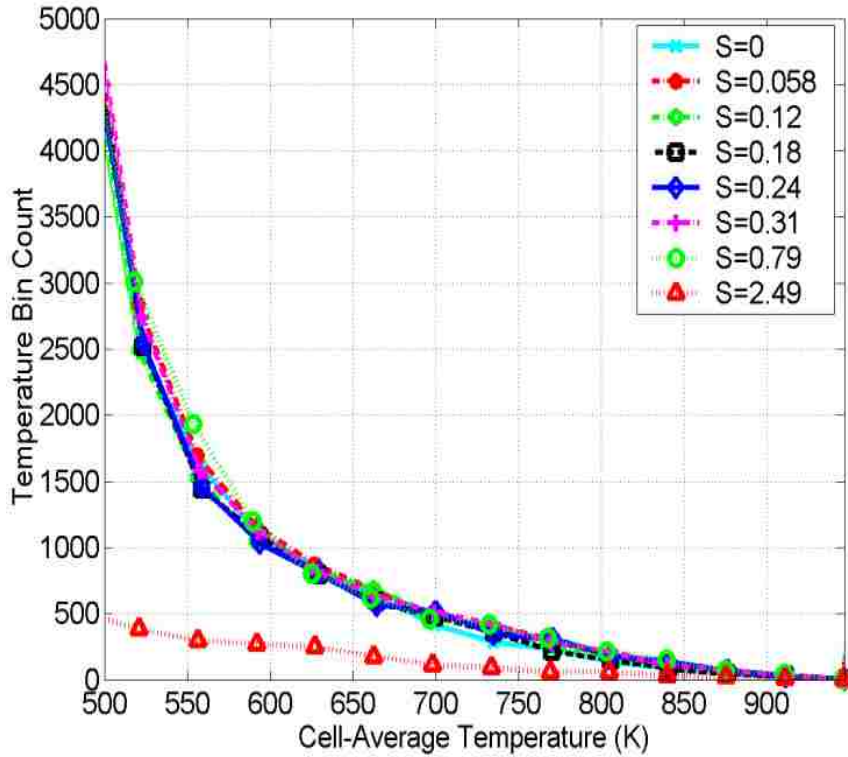
Figure 83. Temperature Bin Count for All Elements with L/D=3 Mesh.

The velocity field for L/D=3 and S=0.79 is shown in Figure 84. The upper figure

shows the velocity distribution at the top of the computation domain near the nozzle exit,

while the bottom figure shows a cross-section view of the domain. The circulation roles

appear as a result of the interaction of the multiple jets, rather than the value of S (the

roles for S=0.0 are very similar to those for S=0.79). Notice that the flow field shows

that the jets impinge on the isothermal plate at velocities ranging from 25 to 35 m/s,

which is a significant fraction of the initial velocity of 60 m/s. Thus, the azimuthal

momentum is significant, and induces significant swirl that results in more mixing and

therefore more cooling of the plate.
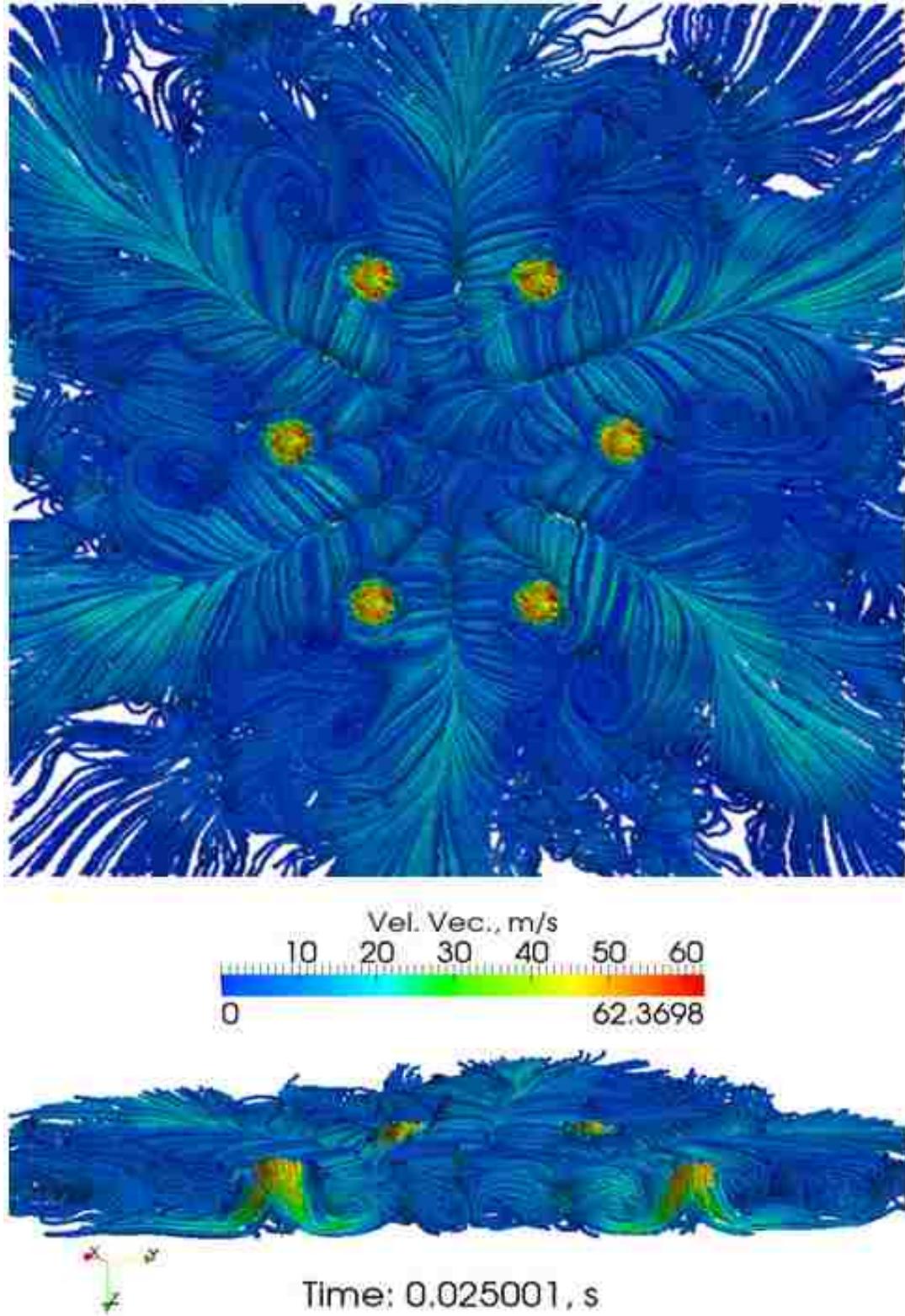
Figure 84. Velocity Flow Field for the Mesh with L/D=3 and S=0.79. Top Image: Domain View of Top; Bottom Image: Domain Cross-Section.

The reason for this high degree of cooling and mixing can be better understood by comparing the azimuthal flow fields shown in Figure 85 for S=0.79 (the top has L/D=3 and the bottom has L/D=12). Note that for L/D=3, the azimuthal velocity was approximately 25 to 35 m/s by the time it reached the isothermal plate, but for the case with L/D=12, the azimuthal velocity was 15 to 25 m/s. The temperature field for S=0.79 and L/D=3 is shown in Figure 86.

Thus, because the azimuthal velocity decays rapidly with distance from the nozzle exit, the value of L/D determines if there will be a significant azimuthal flow field by the time the jet reaches the isothermal bottom plate. Therefore, smaller L/D results in more heat transfer enhancement as S increases.

Results show that the swirling jet flow field transitions to that of a conventional jet beyond a few jet diameters. For example, according to weak swirl theory, at L/D=10, the swirling jet azimuthal velocity has decayed to 1% of its initial value, so the azimuthal momentum becomes negligible at this point; instead, the flow field exhibits radial and axial momentum, just like a conventional jet. Therefore, a free (unconstrained) swirling jet that becomes fully developed will eventually transition to a conventional jet, which is consistent with the recent similarity theory of Ewing [Semaan, Naughton, and Ewing, 2009]. Clearly, then, the advantages offered by swirl are only available within a few jet diameters from the nozzle exit, depending on the value of S and Re.
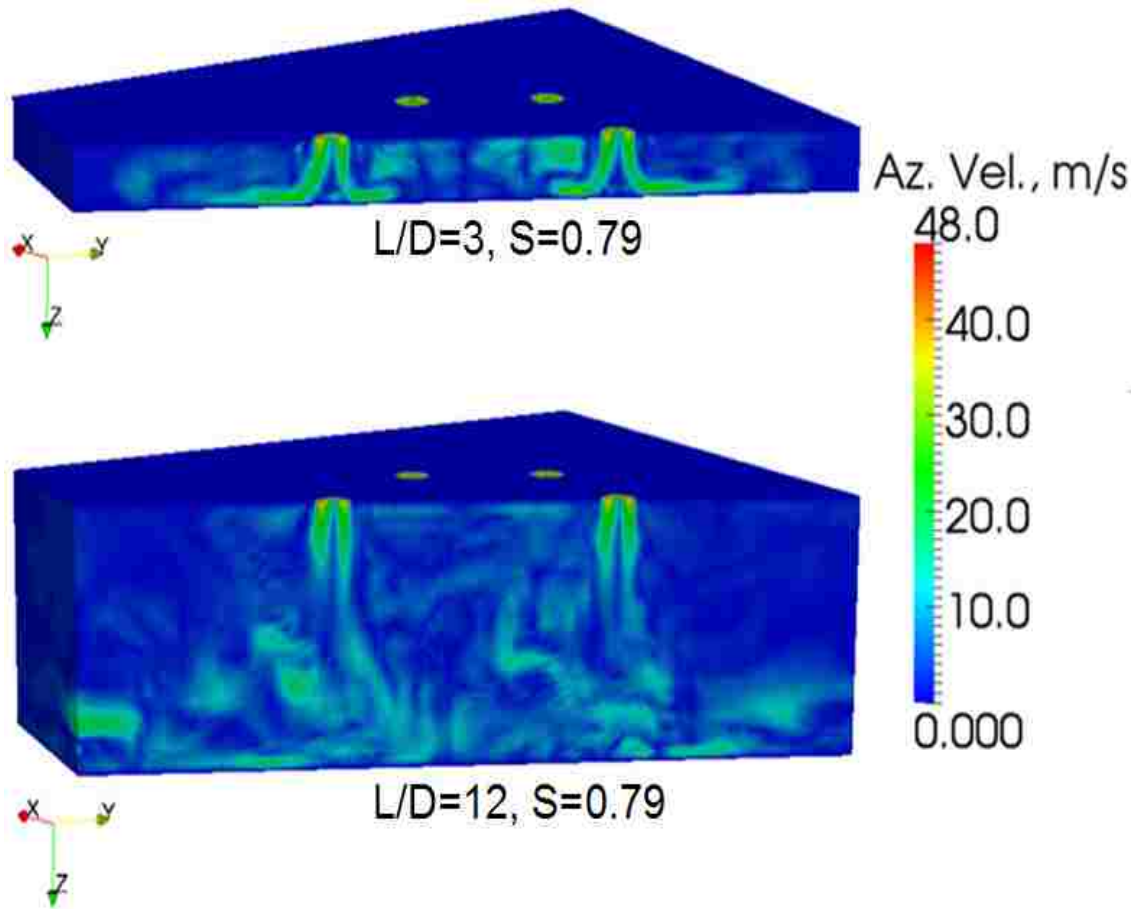
Figure 85. Azimuthal Flow Field for S=0.79. Top Image: L/D=3; Bottom Image: L/D=12.
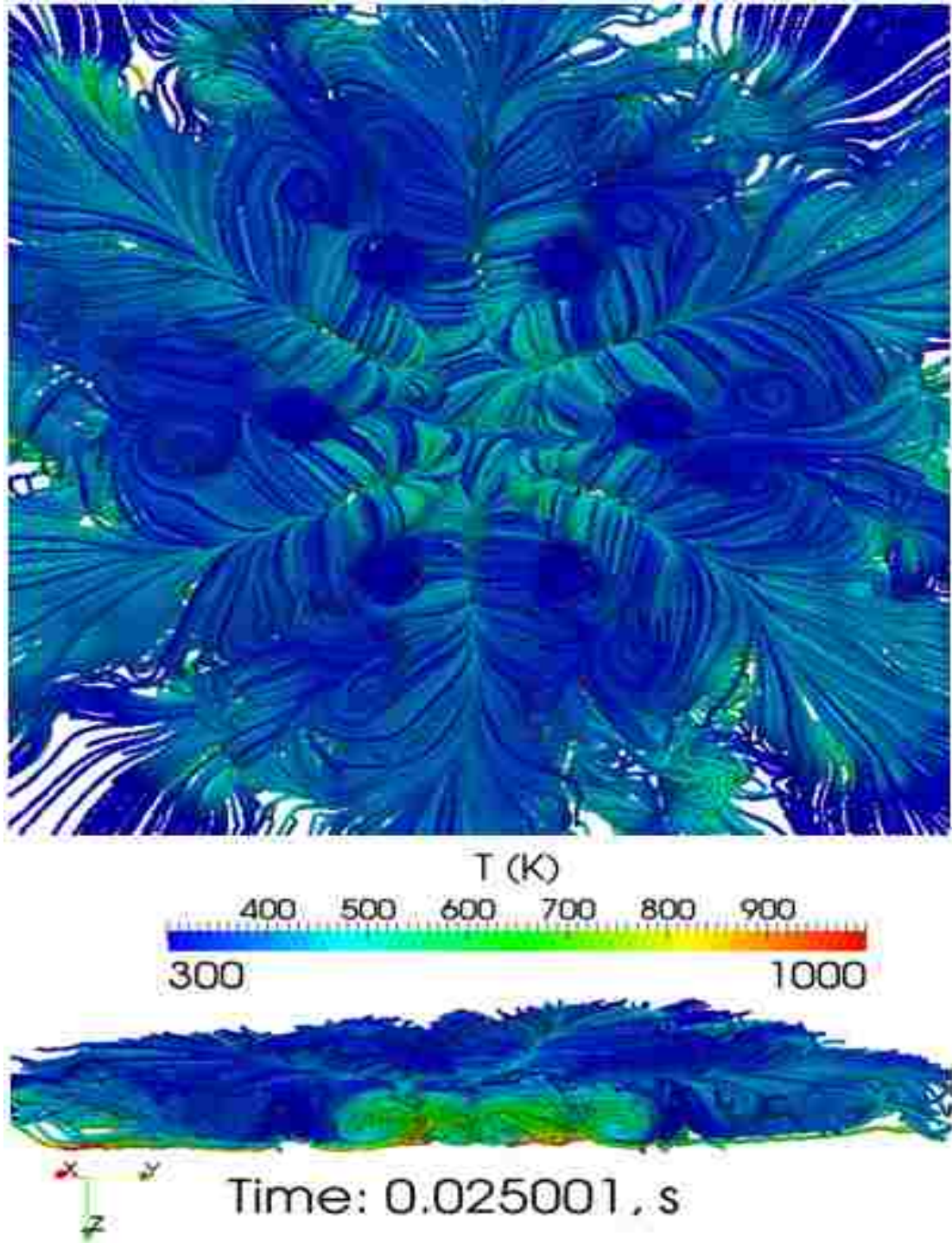
Figure 86. Temperature Field for the Mesh with L/D=3 and S=0.79. Top Image: Domain View of Top; Bottom Image: Domain Cross-Section.

5.1.6 Toward Unification of Swirling Jets—Axisymmetric Family of Swirling Vortex Jets

In summary, the 15 axisymmetric, Newtonian vortices have the following characteristics

in common:

1. $v_\theta(r=0) = 0$

2. Similar $v_\theta(r)$ velocity profiles (sine-like)

3. The $v_\theta(r)$ profile is asymmetric about r. That is, $v_\theta(r) = v_\theta(-r)$: odd functions

4. There are at most four distinct types of axisymmetric vortices

5. All vortices collapse to the Rankine vortex bound

6. The other bound is a Lamb-Oseen-like sine bound

Furthermore, as will be shown in the following Section 5.1.7:

7. All the v_θ profiles can be expressed as an alternating series that expands

   geometrically with odd exponents.

Items 5 and 6 are evident from the series expansions in Table 6. In particular, the

azimuthal velocity approaches the Rankine solid-body azimuthal velocity for large C_1

and small C_3, C_5, etc. The Lamb-Oseen-like sine limit is approached when $C_1 \rightarrow \pi$,

$C_3 \rightarrow \dfrac{\pi^3}{3!}$, $C_5 \rightarrow \dfrac{\pi^5}{5!}$, *and so on.*

Table 4. Vortex Velocity Definitions.

Vortex	Radial Velocity	Azimuthal Velocity	Axial Velocity
Rankine 1 field, f(r)	0	$\Omega r, r \leq a$ ("solid body") $\dfrac{\Omega a^2}{r}, r > a$ ("free") $\Omega = \dfrac{\Gamma}{2\pi a^2}$	0
Lamb-Oseen 1 field, f(r,t)	0	$\dfrac{\Gamma}{2\pi r}\left(1 - e^{-\frac{r^2}{4\nu t}}\right)$	0
Burgers 3 fields, f(r,z)	$-ar$	$\dfrac{\Gamma}{2\pi r}\left(1 - e^{-\frac{ar^2}{2\nu}}\right)$ $\dfrac{1}{r}\left(\dfrac{1 - e^{-\frac{1}{2}\mathrm{Re}\,r^2}}{1 - e^{-\frac{1}{2}\mathrm{Re}}}\right)$ $\mathrm{Re} = \dfrac{bV_{rb}}{\nu}$	$2az$
Loitsyanskiy 3 fields, f(r,z)	$\dfrac{\alpha\sqrt{\nu}}{z}\dfrac{\alpha\eta\left(1 - \dfrac{\alpha^2\eta^2}{4}\right)}{\left(1 + \dfrac{\alpha^2\eta^2}{4}\right)^2}$ $\eta = \dfrac{1}{\sqrt{\nu}}\dfrac{r}{z}$	$\dfrac{1}{z^2}\dfrac{\alpha\gamma\eta}{\left(1 + \dfrac{\alpha^2\eta^2}{4}\right)^2}$	$\dfrac{2\alpha^2}{z}\dfrac{1}{\left(1 + \dfrac{\alpha^2\eta^2}{4}\right)^2}$
Gortler 3 fields, f(r,z)	$\dfrac{\gamma\nu}{z}\dfrac{\xi - \dfrac{\xi^2}{4}}{\left(1 + \dfrac{\xi^2}{4}\right)^2} \sim 0$ $\xi = \dfrac{\gamma r}{z}$	$\dfrac{\gamma\nu}{z}\dfrac{\xi}{\left(1 + \dfrac{\xi^2}{4}\right)^2}$	$\dfrac{\gamma^2\nu}{z}\dfrac{2}{\left(1 + \dfrac{\xi^2}{4}\right)^2}$

Vortex	Radial Velocity	Azimuthal Velocity	Axial Velocity
Newman 3 fields, f(r,z)	$-\dfrac{Ar}{2z^2}e^{-\frac{Wr^2}{4\nu z}}$	$\dfrac{A}{r}\left(1-e^{-\frac{Wr^2}{4\nu z}}\right)$ $\dfrac{\Gamma}{2\pi r}\left(1-e^{-\frac{Wr^2}{4\nu z}}\right)$	$\dfrac{A}{z}e^{-\frac{Wr^2}{4\nu z}}$
Sullivan 3 fields, f(r,z)	$-ar+\dfrac{6\nu}{r}\left(1-e^{-\frac{ar^2}{2\nu}}\right)$	$\dfrac{\Gamma}{2\pi r}\left[\dfrac{H\left(\dfrac{ar^2}{2\nu}\right)}{H(\infty)}\right]$ $H(x)=$ $\displaystyle\int_0^x e^{-t+3\int_0^t\left[(1-e^{-\tau})/\tau\right]d\tau}\,dt$ Alternatively: $\dfrac{\Gamma}{r}\left(1-e^{-\frac{r^2}{f^2}}\right),\ 0\le r<c$	$2az\left(1-3e^{-\frac{ar^2}{2\nu}}\right)$
Batchelor 2 fields, f(r)	0	$\dfrac{C_0}{r}\left(1-e^{-\frac{Ur^2}{4\nu z}}\right)$ (original Batchelor formulation) and $\dfrac{\Gamma}{2\pi r}\left[1-e^{-\left(\frac{r}{a}\right)^2}\right]$ (max. at r=1.121; $u_{\theta,max}=$ 0.639q) (stable vortex for q > 1.5 [Mayer and Powell, 1992; Sipp, Coppens, Jacquin, 1999]) ($q=\dfrac{\Gamma}{2\pi}$, Γ=circulation)	$W_0 e^{-\left(\frac{r}{a}\right)^2}$
Squire 1 field, f(r,z)	0	$\dfrac{K}{2\pi r}\left[1-e^{-\frac{W_0 r^2}{4(\nu+aK)z}}\right]$	0

Vortex	Radial Velocity	Azimuthal Velocity	Axial Velocity
Chepura 1 field, f(r)	0	$\dfrac{kr}{2}\left[2-\left(\dfrac{r}{r_t}\right)^2\right],\ 0\le r\le r_t$ $\dfrac{kr_t}{2r},\ r_t\le r\le r_c$	0
Martynenko 3 fields, f(r,z)	$\sim\dfrac{1}{z}$	$\dfrac{\alpha^{\frac{3}{2}}L_0}{4\pi\mu}\left(\dfrac{K_0}{\pi\rho\nu^2}\right)^{\frac{1}{2}}\dfrac{(\alpha\eta)^{\frac{1}{2}}}{(1+\alpha\eta)^2}\omega$ where $\eta=\dfrac{K_0r^2q}{4\pi\rho\nu^2}$ $\zeta=\dfrac{L_0^2}{16\pi\rho\nu^2K_0}\dfrac{1}{z^2}$ $\gamma=\left(1+\sqrt{1-\dfrac{1}{2}\zeta^3}\right)^{\frac{1}{3}}$ $+\left(1-\sqrt{1-\dfrac{1}{2}\zeta^3}\right)^{\frac{1}{3}}$ $q=\dfrac{1}{2^{\frac{2}{3}}}\dfrac{1}{z^2}\gamma^2$ $\omega=\dfrac{1}{2^{\frac{1}{3}}}\dfrac{1}{z^2}\gamma$	$\dfrac{K_0}{\pi\mu}\dfrac{2\alpha}{(1+\alpha\eta)^2}zq$
AVE Vortex 1 field, f(r,t)	0	$\beta^2 r-\displaystyle\sum_{n=1}^{\infty}A_nJ_1(\lambda_n\beta r)e^{-\lambda_n^2\beta t}$	0
Helicoid 2 fields, f(r)	0	$\sin(\pi r)$, for small r	W_0
Modified Chepura 1 field, f(r)	0	$k\left(\dfrac{r}{r_t}\right)-\dfrac{k}{3!}\left(\dfrac{r}{r_t}\right)^3+\dfrac{k}{5!}\left(\dfrac{r}{r_t}\right)^5,$ $0\le r\le r_t$	0
Modified Newman 3 fields, f(r,z)	$-\dfrac{Ar}{2z^2}e^{-\frac{Wr^2}{4\nu z}}$	$Ae^{-\frac{Wr^2}{4\nu z}}$ "free vortex" domain	$\dfrac{A}{z}e^{-\frac{Wr^2}{4\nu z}}$

Certainly, the velocity components vary according to which NS terms were included during the original derivation of the solution. Upon a casual search in the literature, one notes that there are not just the 15 axisymmetric vortices mentioned here, but many more, with more are being added at a fast rate. There seems to be a proliferation of vortices, to a degree that baffles (and perhaps even annoys!), rather than provides a higher degree of confidence in vortex modeling. And indeed, such sentiments have already been expressed in the literature [Aboelkassem and Vatistas, 2007]. After all, which vortex is "better" (more fundamental), and based upon what criteria? Many literature reports mention that a given vortex was used because it is "widely used…" [Vatistas, Kozel, and Mih, 1991; Alekseenko, *et al.*, 1998; Mao and Sherwin, 2009; Okulov and Sorensen, 2009; Ortega-Casanova and Fernandez-Feria, 2009]. Further, how do the results from a given axisymmetric vortex apply to the others, if at all? Most importantly, are the vortices related to each other, in some form of vortex family, wherein they share certain mathematical characteristics? This subsection highlights various similarities that have been briefly hinted in the literature, or that plainly have not been discussed previously.

Some researchers have noted that some of the most "popular" vortices share some basic characteristics. Perhaps the earliest example of this was noted by Chepura, where he overlayed the normalized azimuthal velocity of his newly-formulated vortex (the Chepura vortex) with the Rankine vortex [Chepura, 1969]. This showed that the two velocity profiles were similar (e.g. both had zero velocity at r=0 and their velocity profiles were quite similar, as noted in Figure 87. In the figure, the dashed and solid lines are the Rankine and Chepura vortices, respectively. Further, it has also been shown that a vortex formulation with azimuthal velocity represented as a function of r and n very

closely matched the Burgers vortex for n=2 and was Rankine-like for n=∞ [Vatistas, Kozel, and Mih, 1991]. In this context, n is an exponential value for r. As another example, the azimuthal velocity for the Rankine, Scully, and Lamb vectors were normalized and overlayed, only to show that their profiles were quite similar [Alekseenko *et al.*, 1999]. Finally, the normalized azimuthal velocity for the Rankine, Oseen-Lamb, Burgers-Rott, and Sullivan vortices were also plotted [Batterson, Maicke, and Majdalani, 2007]; *see* Figure 88. Interestingly, the authors called such plot a "unified normalization".

Note that there are two versions of the Sullivan vortex, depending on the number of "cells". The single-cell Sullivan vortex is included in this research. The "two-cell" model and (also called "bidirectional) [Batterson, Maicke, and Majdalani, 2007], consists of an inner downflow region coexists with a downward-flowing region. In other words, the swirling flow has "nested" regions with reversed flow interspersed upon the swirling field [Donaldson and Sullivan, 1960]. Note that characteristic 1 above applies for "one-cell", but not for "two-cell" types.
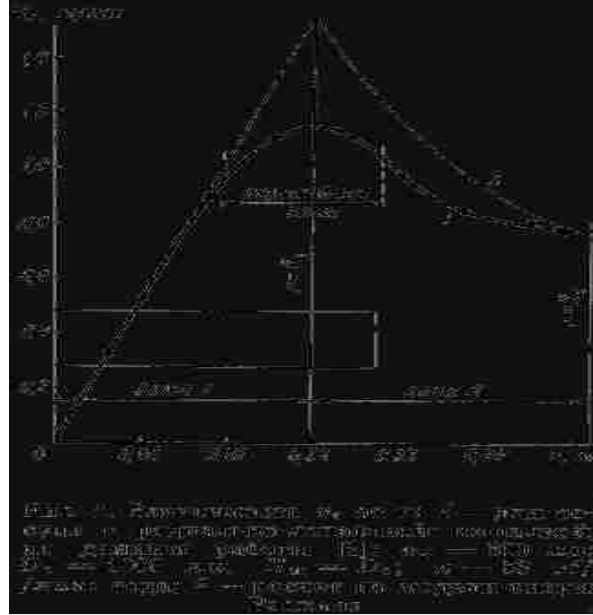
Figure 87. Chepura and Rankine Vortices: Normalized Azimuthal Velocity Overlay [Chepura, 1969].
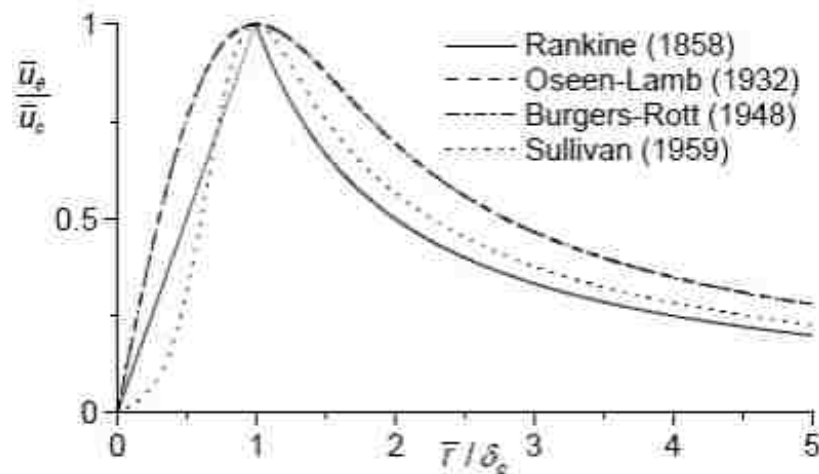
Figure 88. Rankine, Oseen-Lamb, Burgers-Rott, and Sullivan Vortices: Normalized Azimuthal Velocity Overlay [Batterson, Maicke, and Majdalani, 2007].

Figure 89 expands the work of the previous researchers just discussed by showing that

the Rankine, Burgers, Loitsyanskiy, Gortler, Newman, Sullivan, Batchelor, Chepura,

AVE, and Rodriguez/El-Genk Helicoid (and indeed all 15 vortices discussed here) are

part of a vortex family whose normalized azimuthal velocity is sine-like. It is also quite

noteworthy that sinusoidal azimuthal velocity distributions have already been used in

recent experiments found in the literature [Semaan and Naughton, 2010]. For

comparison purposes, the axial velocity profile of three vortices is shown in Figure 90;

the radial, azimuthal, and axial velocity equations for all 15 vortices are found in Table 4.
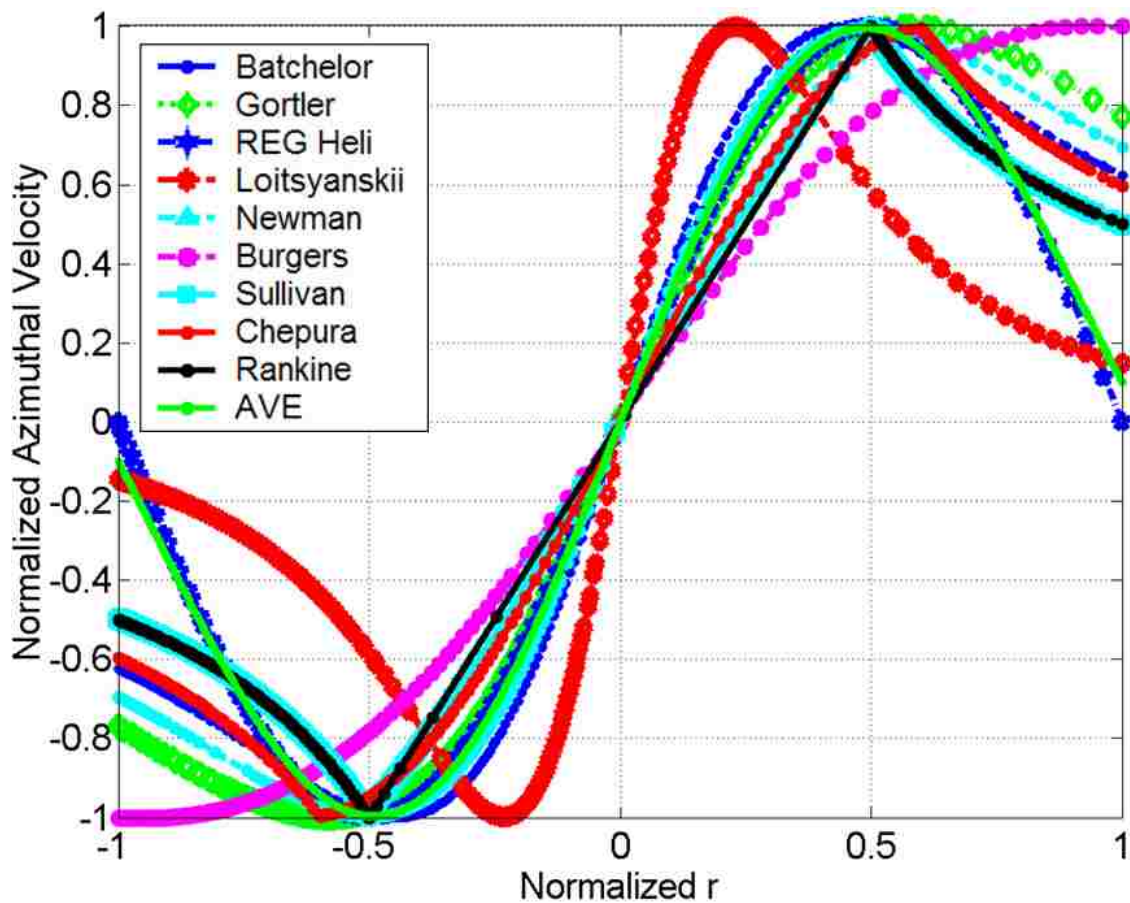
Figure 89. Rankine, Burgers, Loitsyanskiy, Gortler, Newman, Sullivan, Batchelor, Chepura, AVE, and Rodriguez/El-Genk Helicoid: Normalized Azimuthal Velocity Overlay.
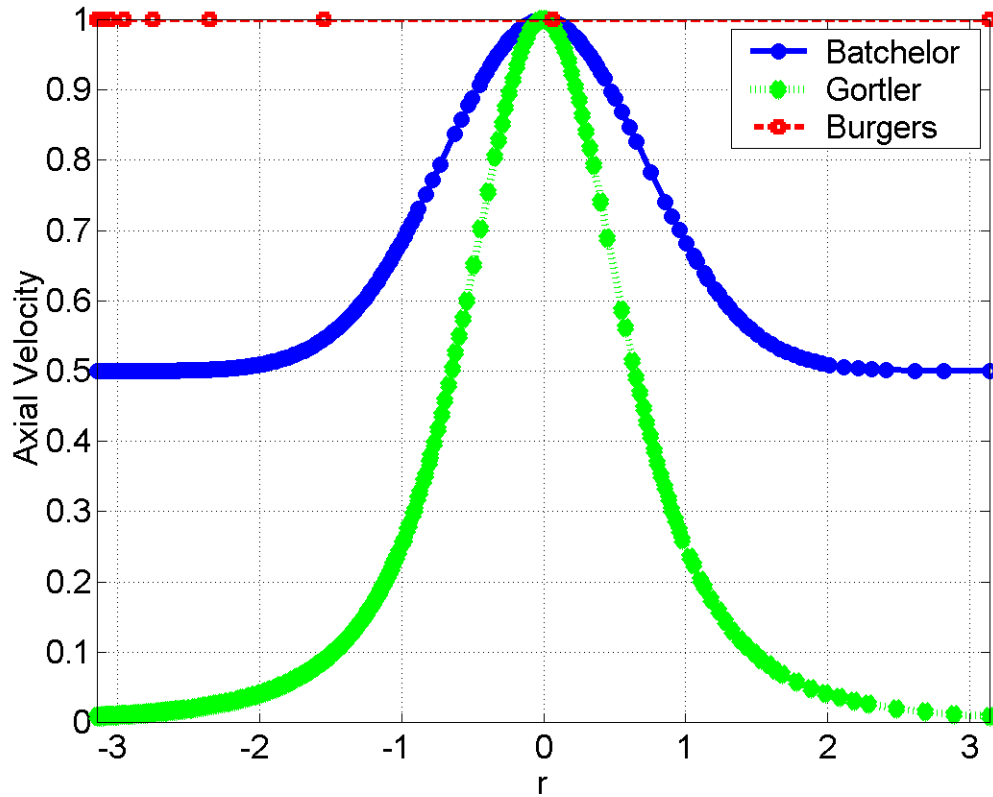
Figure 90. Batchelor, Gortler, and Burgers Vortex Axial Velocity Overlay.

Note that a 3D generalized velocity field in cylindrical coordinates can be expressed as

$$\vec{V}(r,\theta,z)=\vec{V}\left[u(r,\theta,z),v(r,\theta,z),w(r,\theta,z)\right]. \tag{118}$$

If the flow is symmetric about the axial coordinate z, then it moves about in circles around the z axis [Lamb, 1932]. Thus, the flow field is still 3D, but is axisymmetric about z. In such case, the above equation reduces to

$$\vec{V}(r,z)=\vec{V}\left[u(r,z),v(r,z),w(r,z)\right]=u(r,z)\vec{\delta}_r+v(r,z)\vec{\delta}_\theta+w(r,z)\vec{\delta}_z. \tag{119}$$

Even swirling flows that have a θ dependence eventually become axisymmetric as a result of viscous effects [Loitsyanskiy, 1953]. In any case, when axisymmetry is assumed, the Navier-Stokes conservation of momentum PDE is simplified considerably, as all partials with respect to θ vanish. Note that the overall flow field must retain the v velocity component in order to induce a vortex (swirl), but that none of the velocity components retain the θ dependency, as shown by the four equations that follow. *Thus, there are at most four distinct types of axisymmetric flows:*

$$\vec{V}(r,z)=\vec{V}\big[u(r,z),v(r,z),w(r,z)\big], \tag{120}$$

$$\vec{V}(r,z)=\vec{V}\big[0,v(r,z),w(r,z)\big], \tag{121}$$

$$\vec{V}(r,z)=\vec{V}\big[u(r,z),v(r,z),0\big], \text{ and} \tag{122}$$

$$\vec{V}(r,z)=\vec{V}\big[0,v(r,z),0\big]. \tag{123}$$

Table 5. Categories of Axisymmetric Vortices.

Vortex Category	Radial Velocity, u	Azimuthal Velocity, v	Axial Velocity, w
$\vec{V}(r,z)=\vec{V}\big[u(r,z),v(r,z),w(r,z)\big]$ Example: Burgers	-ar	$\frac{\Gamma}{2\pi r}\left(1 - e^{-\frac{ar^2}{2\nu}}\right)$	2az
$\vec{V}(r,z)=\vec{V}\big[0,v(r,z),w(r,z)\big]$ Example: Batchelor	0	$\frac{C_0}{r}\left(1-e^{-\frac{Ur^2}{4\nu z}}\right)$	$W_0 e^{-\left(\frac{r}{a}\right)^2}$
$\vec{V}(r,z)=\vec{V}\big[u(r,z),v(r,z),0\big]$ Example: *none found in the literature*	u(r,z)	v(r,z)	0
$\vec{V}(r,z)=\vec{V}\big[0,v(r,z),0\big]$ Example: Rankine	0	$\Omega r, r \le a$ $\frac{\Omega a^2}{r}, r > a$	0

It is noteworthy that many examples were found in the literature for the first, second, and fourth categories, but none for the third. This should be investigated further.

5.1.7　　　Series Formulation of Axisymmetric Swirling Jets

From Table 4, it is evident that the v_θ vortex distributions can be classified according to five mathematical functions:

1. Series (Rankine, Chepura, Modified Chepura),

2. Exponential (Lamb-Oseen, Burgers, Newman, Sullivan, Batchelor, Squire, Modified Newman),

3. Polynomial (Loitsyanskiy, Gortler, Martynenko),

4. Bessel (AVE), and

5. Sine (Rodriguez/El-Genk helicoid).

A casual inspection of the five mathematical forms shows suggests that the mathematical forms are quite different. However, that is not the picture suggested by Figure 89, with its 10 vortices that seemingly share a similar sine-like profile. Upon further thought, the Rankine, modified Chepura, and Rodriguez/El-Genk helicoid actually have the following in common: the formulation for Rankine vortex for r≤a and the modified Chepura for r≤a have similar series terms when compared to an expansion of the Rodriguez/El-Genk helicoid. In particular:

For the Rankine Domain 1,

$$v_{Rankine}(r) = C_1 r. \tag{124}$$

Here, Domain 1 refers to the "solid body" part of the vortex, where the fluid essentially behaves as if attached to a rotating, solid body. Domain 2 refers to the "free" vortex, away from the solid body region, where the vortex velocity decays.

The modified Chepura for Domain 1 is

$$v_{Chepura}(r) = \frac{k}{1!}\left(\frac{r}{a}\right) - \frac{k}{3!}\left(\frac{r}{a}\right)^3 = C_1 r - C_3 r^3. \tag{125}$$

And a series expansion of sine for the Rodriguez/El-Genk helicoid yields

$$v(r) = \sin(\pi r) = \pi r - \frac{\pi^3}{3!}r^3 + \frac{\pi^5}{5!}r^5 - \frac{\pi^7}{7!}r^7... = C_1 r - C_3 r^3 + C_5 r^5 - C_7 r^7... \tag{126}$$

Next, by noting from Figure 89 that 1) the Rodriguez/El-Genk helicoid and the AVE vortex [Aboelkassem, Vatistas, and Esmail, 2005] are very similar in profile and 2) that the Bessel function of the first kind has long been observed to behave as the sine function, one is tempted to also do a series expansion for it. By searching for the most sine-like series expansion for the Bessel function (*see* Figure 91), and setting t=to and n=1, Maple calculated the series expansion as

$$v_{AVE} = series\left[\beta^2 r - \sum_{n=1}^{\infty} A_n J_1(\lambda_n \beta r) e^{-\lambda_n^2 \beta t}\right] \tag{127}$$

$$= 3.173r - 5.5r^3 + 3.06r^5 - 0.869r^7... = C_1 r - C_3 r^3 + C_5 r^5 - C_7 r^7...$$

Indeed, the AVE vortex can uniquely be expressed as Fourier-Bessel series [Aboelkassem, Vatistas, and Esmail, 2005].
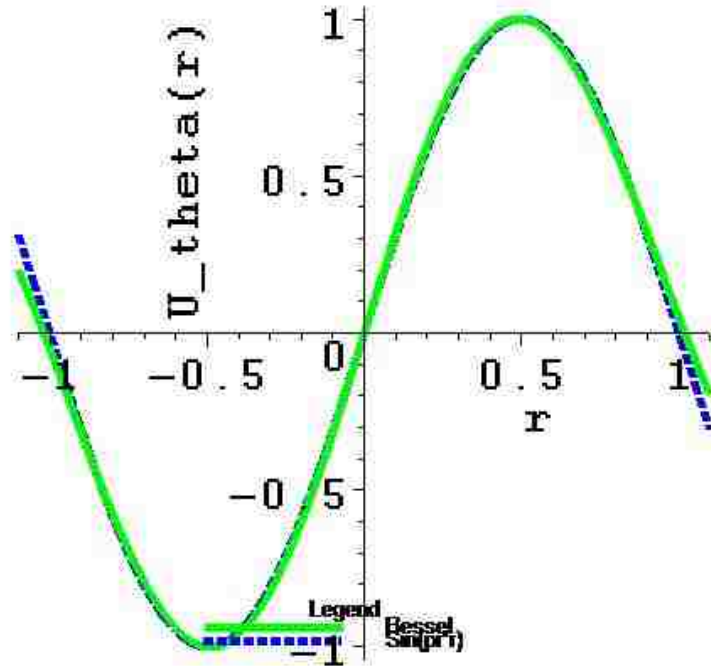
Figure 91. Bessel and Sine Azimuthal Velocities.

Therefore, this shows that the Rankine, modified Chepura, Rodriguez/El-Genk helicoid, and the AVE vortex can be collapsed into a single mathematical series form! Will all the vortices follow? By using Maple, one easily obtains series expansions for the polynomial and exponential forms. Not quite surprisingly (at this point, anyway), it is found that

$$v_{exponential} \; = \; series\left[\frac{C_1}{r}\left(1 \; - \; e^{-C_2 r^2}\right)\right] \; = \; C_1 r \; - \; C_3 r^3 + C_5 r^5 \; - \; C_7 r^7... \tag{128}$$

and likewise,

$$\begin{aligned} v_{polynomial} &= \; series\left[\text{polynomial}\left(\text{Loitsyanskiy, Gortler, or Martynenko}\right)\right] \\ &= \; C_1 r \; - \; C_3 r^3 + C_5 r^5 \; - \; C_7 r^7... \end{aligned} \tag{129}$$

162

Figure 92 shows that Loitsyanskiy vortex with parameters that make it the most "sine-like" (LHS). In fact, it is easy to observe that such is the case for small r, say $r \leq 0.7$. The RHS of Figure 92 shows the relative error between the most sine-like Loitsyanskiy and $\sin(\pi r)$. The same analysis was performed for the Newman vortex, as shown in Figure 93. The figure shows that same conclusions can be made with the Newman vortex as was done with the Loitsyanskiy vortex.

Therefore, all the vortices presented herein can be represented as alternating geometric series with odd exponents!

Interestingly, for non-Newtonian swirling fluids, the axial and azimuthal velocities were assumed to be representable as series expansions with alternating signs exponential power [Som, 1983]:

$$v_{\text{non-Newtonian,Som}}(r) = -C_0 + C_1 r - C_2 r^2 \tag{130}$$

and

$$w_{\text{non-Newtonian,Som}}(r) = -C_0 + C_1 r - C_2 r^2 + C_3 r^3. \tag{131}$$
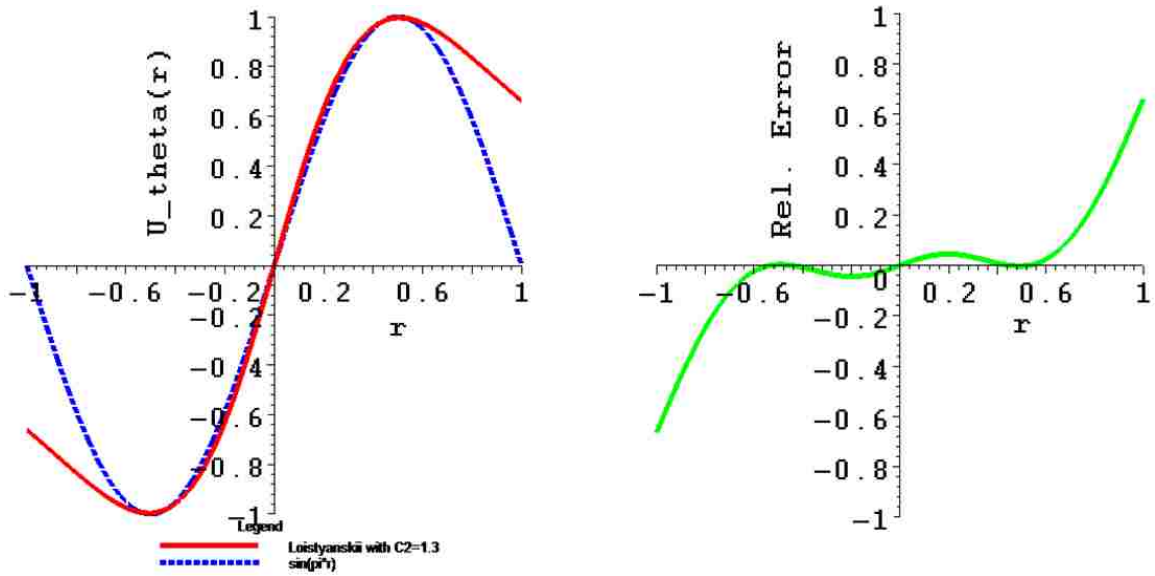
Figure 92. LHS: Loitsyanskiy and Sine Azimuthal Distributions. RHS: Relative Error between Both Distributions.
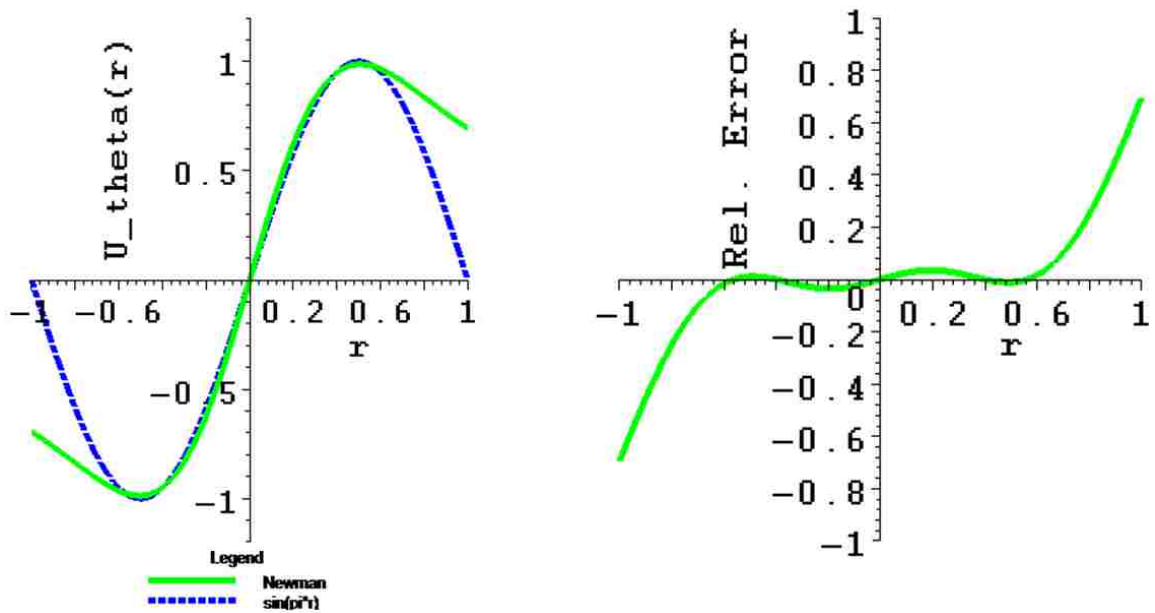
Figure 93. LHS: Newman and Sine Azimuthal Distributions. RHS: Relative Error between Both Distributions.

Table 6. Towards Vortex Unification.

Vortex Name	Azimuthal Velocity	Mathematical Form($z=z_0$; $t=t_0$, const.)	Series Expansion
Rankine ("solid body") [Rankine, 1858]	$\Omega r, r \le a$ $\dfrac{\Omega a^2}{r}, r > a$ $\Omega = \dfrac{\Gamma}{2\pi a^2}$	Series	$\dfrac{C_0}{r}$ $C_1 r$
Lamb-Oseen ("Oseen-Lamb") [Lamb, 1932]	$\dfrac{\Gamma}{2\pi r}\left(1 - e^{-\frac{r^2}{4\nu t}}\right)$	Exponential	$C_1 r - C_3 r^3 + C_5 r^5 - C_7 r^7 ...$
Burgers [Burgers, 1948]. (The vortex has also been referred as the "Burgers-Rott", though Rott's paper was published 10 years later) [Rott, 1958]	$\dfrac{1}{r}\left(\dfrac{1-e^{-\frac{1}{2}\mathrm{Re}\,r^2}}{1-e^{-\frac{1}{2}\mathrm{Re}}}\right)$ $\mathrm{Re} = \dfrac{bV_{rb}}{\nu}$	Exponential	$C_1 r - C_3 r^3 + C_5 r^5 - C_7 r^7 ...$
Loitsyanskiy [Loitsyanskiy, 1953]	$\dfrac{1}{z^2}\dfrac{\alpha\gamma\eta}{\left(1 + \dfrac{\alpha^2\eta^2}{4}\right)^2}$ $\eta = \dfrac{1}{\sqrt{\nu}}\dfrac{r}{z}$	Polynomial	$C_1 r - C_3 r^3 + C_5 r^5 - C_7 r^7 ...$
Gortler [Gortler, 1954]	$\dfrac{C_1 z_0^2}{z^2}\dfrac{\dfrac{2r}{r_0}}{\left[1 + \left(\dfrac{r}{r_0}\right)^2\right]^2}$	Polynomial	$C_1 r - C_3 r^3 + C_5 r^5 - C_7 r^7 ...$
Newman [Newman,	$\dfrac{\Gamma}{2\pi r}\left(1 - e^{-\frac{Wr^2}{4\nu z}}\right)$	Exponential	$C_1 r - C_3 r^3 + C_5 r^5 - C_7 r^7 ...$

Vortex Name	Azimuthal Velocity	Mathematical Form(z=z₀; t=t₀, const.)	Series Expansion
1959]	$\dfrac{C_1}{r}\left(1 + C_2 e^{-C_3 \nu r^2}\right)$		
Sullivan ("2 cell") [Sullivan, 1959]; alternate form as a combination of two vortices: [Chuah and Kushida, 2007]	$\dfrac{\Gamma}{2\pi r}\left[\dfrac{H\left(\dfrac{a r^2}{2\nu}\right)}{H(\infty)}\right]$ $H(x) =$ $\displaystyle\int_0^x e^{-t+3\int_0^t \left[(1-e^{-\tau})/\tau\right]d\tau}\, dt$ Alternatively: $\dfrac{\Gamma}{r}\left(1 - e^{-\frac{r^2}{f^2}}\right),\ 0 \le r < c$ and $\dfrac{(1-a)R V_R}{r} +$ $\dfrac{a\Gamma\left(1-e^{-\sigma}\right)}{r}$ $c \le r < R$	Exponential	$C_1 r - C_3 r^3 + C_5 r^5 - C_7 r^7 ...$
Batchelor ("q") [Batchelor, 1964]	$\dfrac{C_0}{r}\left(1-e^{-\frac{Ur^2}{4\nu z}}\right)$	Exponential	$C_1 r - C_3 r^3 + C_5 r^5 - C_7 r^7 ...$
Squire [Squire, 1965]	$\dfrac{K}{2\pi r}\left[1 - e^{-\frac{W_0 r^2}{4(\nu + aK)z}}\right]$	Exponential	$C_1 r - C_3 r^3 + C_5 r^5 - C_7 r^7 ...$
Chepura [Chepura, 1969; Chepura 1971]	$\dfrac{kr}{2}\left[2 - \left(\dfrac{r}{a}\right)^2\right],\ 0 \le r \le a$ $\dfrac{ka}{2r},\ a \le r \le r_c$	Series	$C_1 r - C_3 r^3$

Vortex Name	Azimuthal Velocity	Mathematical Form($z=z_0$; $t=t_0$, const.)	Series Expansion
Martynenko [Martynenko, 1989]	$\dfrac{\alpha^{\frac{3}{2}}L_0}{4\pi\mu}\left(\dfrac{K_0}{\pi\rho\nu^2}\right)^{\frac{1}{2}}\dfrac{(\alpha\eta)^{\frac{1}{2}}}{(1+\alpha\eta)^2}\omega$ where $\eta=\dfrac{K_0 r^2 q}{4\pi\rho\nu^2}$ $\zeta=\dfrac{L_0^2}{16\pi\rho\nu^2 K_0}\dfrac{1}{z^2}$ $\gamma=\left(1+\sqrt{1-\dfrac{1}{2}\zeta^3}\right)^{\frac{1}{3}}$ $\quad +\left(1-\sqrt{1-\dfrac{1}{2}\zeta^3}\right)^{\frac{1}{3}}$ $q=\dfrac{1}{2^{\frac{2}{3}}}\dfrac{1}{z^2}\gamma^2$ $\omega=\dfrac{1}{2^{\frac{1}{3}}}\dfrac{1}{z^2}\gamma$	Polynomial	$C_1 r - C_3 r^3 + C_5 r^5 - C_7 r^7 ...$
AVE Vortex [Aboelkassem, Vatistas, and Esmail, 2005]	$\beta^2 r - \sum_{n=1}^{\infty} A_n J_1(\lambda_n \beta r)\, e^{-\lambda_n^2 \beta t}$	Bessel	$C_1 r - C_3 r^3 + C_5 r^5 - C_7 r^7 ...$
Helicoid [Rodriguez and El-Genk, 2008a, 2010d]	$\sin(\pi r)$, for small r	Sine	$C_1 r - C_3 r^3 + C_5 r^5 - C_7 r^7 ...$
Modified Chepura [Rodriguez, El-Genk, 2010]	$\dfrac{k}{1!}\left(\dfrac{r}{a}\right) - \dfrac{k}{3!}\left(\dfrac{r}{a}\right)^3 + \dfrac{k}{5!}\left(\dfrac{r}{a}\right)^5$, $0\le r\le a$	Series	$C_1 r - C_3 r^3 + C_5 r^5$
Modified Newman [Rodriguez, El-Genk, 2011]	$C_2 e^{-C_3 \nu r^2}$	Exponential	$-\dfrac{C_{-1}}{r}$ $+ C_1 r - C_3 r^3 + C_5 r^5 - C_7 r^7 ...$

167

5.1.8   Modified Chepura Vortex

Chepura and coworkers developed an azimuthal velocity distribution based on data fit to vorticity data and then solving the NS vorticity equation in 1D [Chepura *et al.*, 1969; Chepura, 1971; Akira, 1993]. According, the following relationships were obtained:

$$v(r) = \frac{kr}{2}\left[2 - \left(\frac{r}{a}\right)^2\right], \ 0 \leq r \leq a \ \text{(Domain 1)} \tag{132}$$

and

$$v(r) = \frac{ka}{2r}, \ a \leq r \leq r_c \ \text{(Domain 2)}. \tag{133}$$

Because vorticity data was used obtain the formulation, some issues arise. In particular, the solution does not satisfy NS. Further, the experimental data is not captured adequately near r=a (Domain 1), as shown in Figure 94. An expansion of Chepura's azimuthal velocity shows that

$$v(r) = \frac{kr}{2}\left[2 - \left(\frac{r}{a}\right)^2\right] = kr - \frac{k}{2}\left(\frac{r}{a}\right)^3, \ 0 \leq r \leq a, \tag{134}$$

which looks like the first two terms of a sine expansion. With this in mind, the original Chepura form was revised to make the terms more sine-like, with the hypothesis based on the notion that axisymmetric vortices share a sine-like series expansion. With that in mind, one obtains the modified Chepura vortex,

$$v_{\text{Mod, Chepura}}(r) = \frac{k}{1!}\left(\frac{r}{a}\right) - \frac{k}{3!}\left(\frac{r}{a}\right)^3 + \frac{k}{5!}\left(\frac{r}{a}\right)^5 ..., \ 0 \leq r \leq a. \tag{135}$$

Figures 94 and 95 show that for Domain 1, the modified Chepura vortex (as third and fifth order sine expansions) provided a much better fit to the experimental data. For comparison, the Rankine Domain 1 formulation was also included. The Rankine and the

third and fifth order modified Chepura vortices well better able to capture the experimental data. Both figures also show that the Chepura Domain 2 formation, the Rankin Domain 2 formulation, and the modified Newman vortex (to be discussed in the following subsection) quite excellently fit the experimental data. This further corroborates the hypothesis that the axisymmetric vortices follow sine-like series.
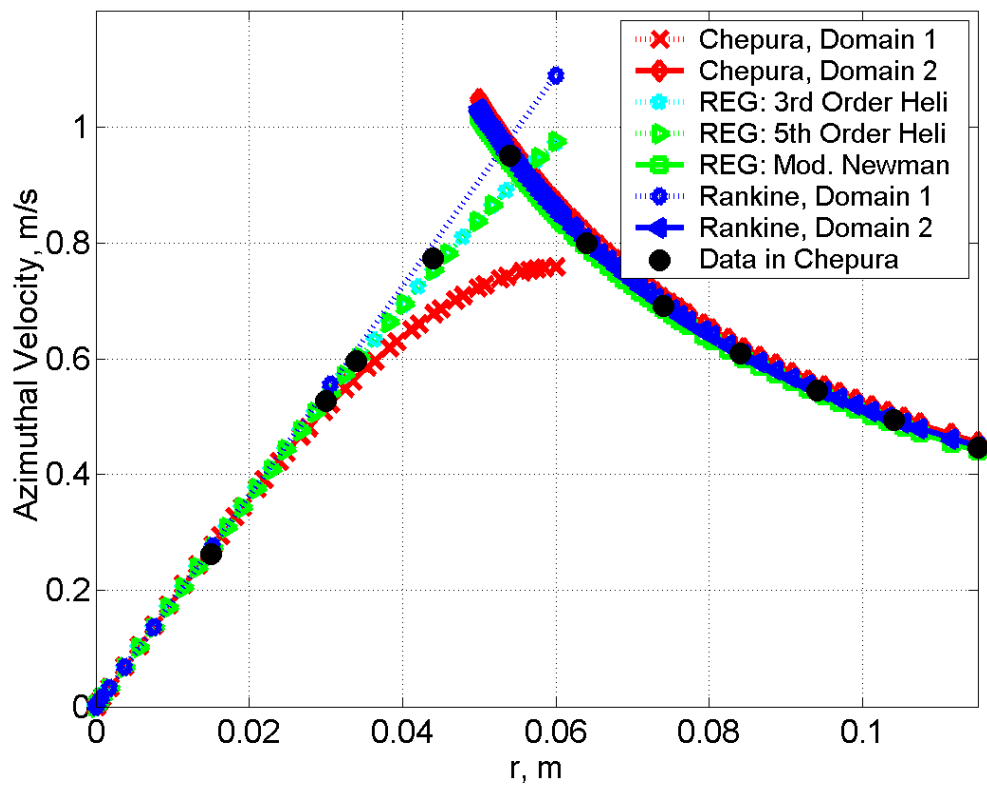
Figure 94. Comparison of Original Chepura Vortex with the Modified Chepura Vortex: Data Set 1.
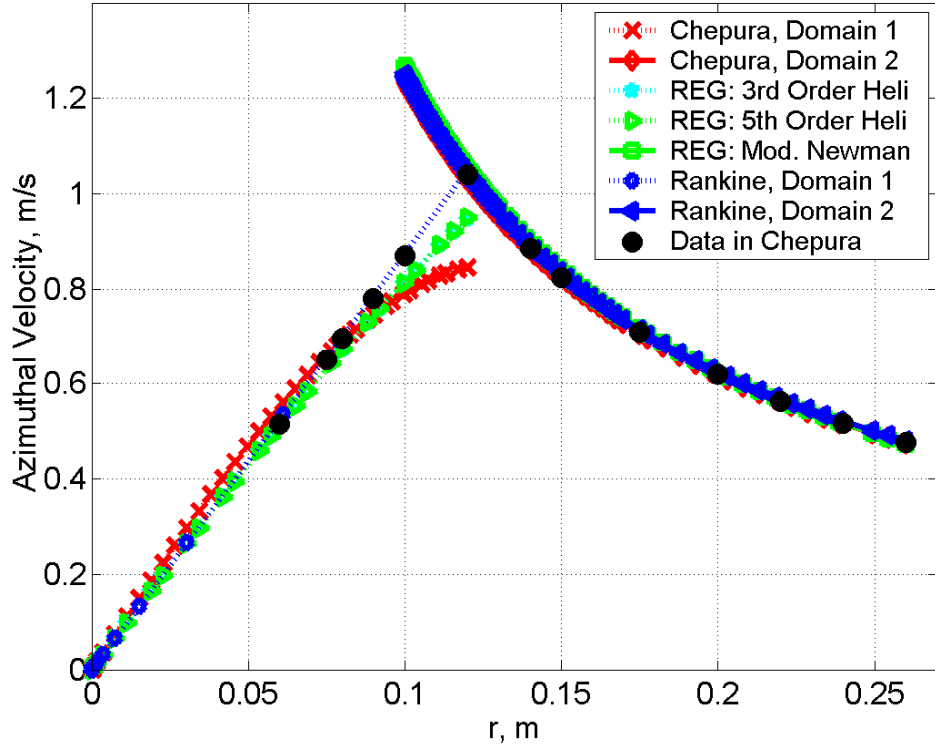
Figure 95. Comparison of Original Chepura Vortex with the Modified Chepura Vortex: Data Set 2.

5.1.9　　Modified Newton Vortex

One can further exploit the sine-like series characteristic of axisymmetric by applying

an expansion to the Neman vortex:

$$v\left(r, z=z_O\right) \;=\; \frac{\Gamma}{2\pi r}\left(1 - e^{-\frac{W_O r^2}{4\nu z_O}}\right) \;=\; \frac{\Gamma}{2\pi r} \;-\; \frac{\Gamma}{2\pi r}e^{-\frac{W_O r^2}{4\nu z_O}}$$

$$=\; \frac{\Gamma}{8\pi}\left(\frac{W_O}{\nu z_O}\right)r \;-\; \frac{\Gamma}{64\pi}\left(\frac{W_O}{\nu z_O}\right)^2 r^3 \;+\; \frac{\Gamma}{768\pi}\left(\frac{W_O}{\nu z_O}\right)^3 r^5 \;-\; \frac{\Gamma}{12288\pi}\left(\frac{W_O}{\nu z_O}\right)^4 r^7 ... \qquad (136)$$

$$=\; C_1 r \;-\; C_3 r^3 \;+\; C_5 r^5 \;-\; C_7 r^7 ...$$

Note that for convenience, u_θ is taken at $z=z_O$ where z_O is a constant. That is, a slice of the azimuthal velocity is taken at a plane $z=z_O$, which lies within the vortex near field. Now take a series for the proposed modified Newman vortex:

$$v_{\text{Mod Newan}}\left(r, z=z_O\right) = \frac{\Gamma}{2\pi r} e^{-\frac{W_O r^2}{4\nu z_O}}$$

$$= -\frac{\Gamma}{2\pi} r^{-1} + \frac{\Gamma}{8\pi}\left(\frac{W_O}{\nu z_O}\right) r - \frac{\Gamma}{64\pi}\left(\frac{W_O}{\nu z_O}\right)^2 r^3 + \frac{\Gamma}{768\pi}\left(\frac{W_O}{\nu z_O}\right)^3 r^5 - \frac{\Gamma}{12288\pi}\left(\frac{W_O}{\nu z_O}\right)^4 r^7 \ldots \quad (137)$$

$$= -C_{-1} r^{-1} + C_1 r - C_3 r^3 + C_5 r^5 - C_7 r^7 \ldots$$

Note that both series are the same, except for one term (the first term of the modified Newman series is not part of the Newman vortex). So, the modified Newman expansion includes a Rankine Domain 2 term! Because the modified Newman formulation satisfies NS, and it cannot be applied at r=0 (just like the Rankine Domain 2 formulation), this suggests that the modified Newman be used in Domain 2. As Figure 96 in the previous subsection shows, the modified Newman vortex is able to capture experimental data adequately.

Figure 96 shows that various degrees of azimuthal velocity decay can be modeled by the modified Newman vortex. Interestingly, the modified Newman slow decay collapses to the Rankine Domain 2 formulation. The other extreme is the very fast decay that can be obtained, as required by the type of vortex being analyzed. This notion leads to the following idea:

> *It is possible to engineer vortices in order to approximate a desired profile for the swirling jet flow field, so long as NS and conservation of mass are satisfied.*

This will be considered in Section 5.1.12 (Advanced Swirling Jet Design Guidelines).
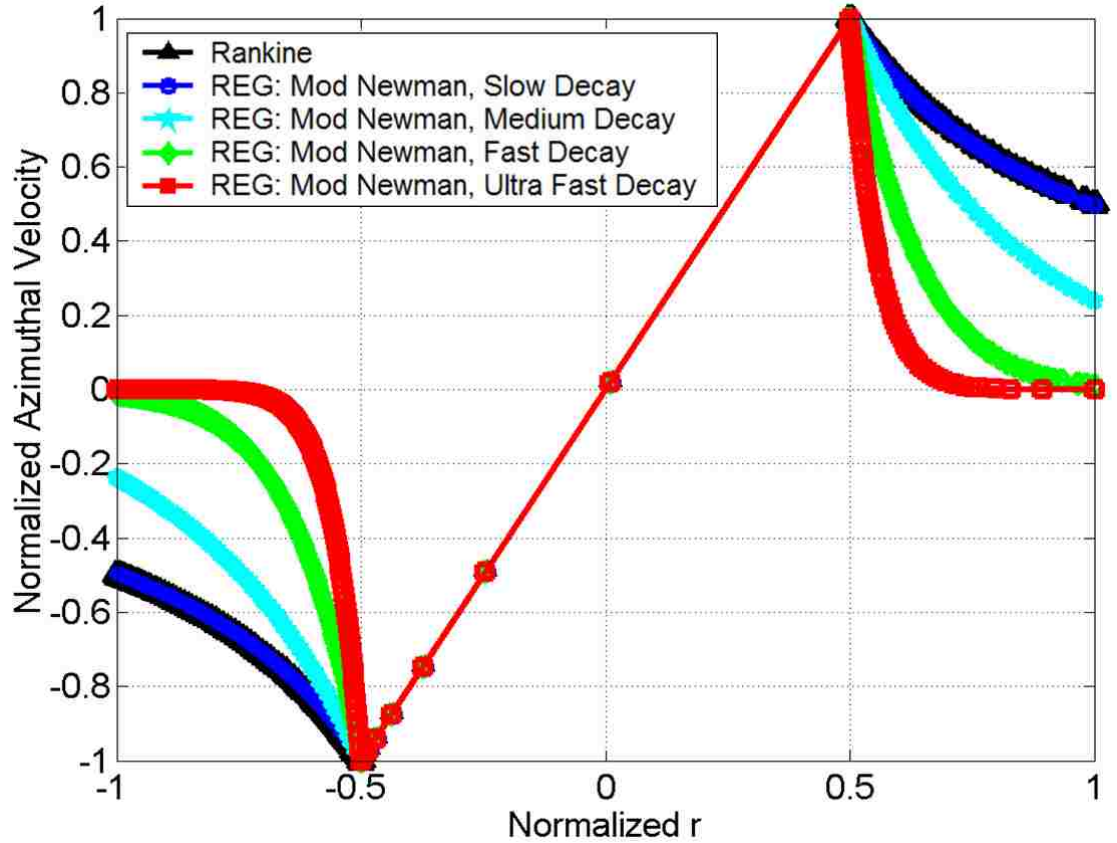
Figure 96. Modified Newman Vortex with Various Degrees of Decay.

5.1.10 Additional Navier-Stokes Solutions for Axisymmetric Swirls

Sections 5.1.7 – 5.1.9 show that it is possible to express vortices as series. That, in turn, allows one to surmise that new NS solutions for swirling axisymmetric flows can be represented as simple series that are functions of r. This will be developed here for 1D and 2D solutions having two and three flow velocity components (fields).

For a steady state, incompressible, negligible gravitational term, symmetry about the z axis (axisymmetry), Newtonian fluid with weak swirl [Gortler, 1954], the NS equations in cylindrical coordinates simplify to the following equations in r, θ, and z, respectively:

$$u\frac{\partial u}{\partial r} - \frac{v^2}{r} + w\frac{\partial u}{\partial z} = v\left(\frac{\partial^2 u}{\partial r^2} + \frac{1}{r}\frac{\partial u}{\partial r} - \frac{u}{r^2} + \frac{\partial^2 u}{\partial z^2}\right),$$ (138)

$$u\frac{\partial v}{\partial r} + \frac{uv}{r} + w\frac{\partial v}{\partial z} = v\left(\frac{\partial^2 v}{\partial r^2} + \frac{1}{r}\frac{\partial v}{\partial r} - \frac{v}{r^2} + \frac{\partial^2 v}{\partial z^2}\right),$$ (139)

$$u\frac{\partial w}{\partial r} + w\frac{\partial w}{\partial z} = v\left(\frac{\partial^2 w}{\partial r^2} + \frac{1}{r}\frac{\partial w}{\partial r} + \frac{\partial^2 w}{\partial z^2}\right),$$ (140)

while conservation of mass reduces to

$$\frac{\partial u}{\partial r} + \frac{u}{r} + \frac{\partial w}{\partial z} = 0.$$ (141)

It is already known in the literature that for any velocity field described as

$$\vec{V} = \left[\vec{0}, \vec{v}(r), \vec{w}(r)\right],$$ (142)

the steady-state Euler momentum equation simplification for NS is satisfied [Rossi, 2006], leaving only the following θ and z terms:

$$w\frac{\partial v}{\partial z} = 0,$$ (143)

$$w\frac{\partial w}{\partial z} = 0$$ (144)

Note also that such $\vec{V}$ also conserves mass. Other NS solution forms have been proposed [Donaldson and Sullivan, 1960; Vatistas, Kozel, and Mih, 1991; Park and Han, 2009].

If u and w are negligible, the NS equations collapse to the simplified 1D conservation of momentum equation in the azimuthal direction. This yields the simple ordinary differential equation (ODE),

$$\frac{d^2 v}{dr^2} + \frac{1}{r}\frac{dv}{dr} - \frac{v}{r^2} = 0,$$ (145)

which can be solved for the single-field velocity, v_θ, as a function of r only. The solution is the well-known Rankine vortex [Rankine, 1858]:

$$v(r) = \frac{c_1}{r} + c_2 r \tag{146}$$

In Sections 5.1.10.1, new solutions will be sought to the NS equations based on the notion that the solutions for axisymmetric swirling flows have a peculiar tendency to be expressible as series solutions.

5.1.10.1   Azimuthal and Radial Velocity Field Solutions

For the two fields $u(r) \neq 0$ and $v(r,z) \neq 0$, the 2D NS radial and azimuthal velocity momentum PDEs can be simplified as follows,

$$\frac{\partial^2 u}{\partial r^2} + \frac{1}{r}\frac{\partial u}{\partial r} - \frac{u}{r^2} + \frac{\partial^2 u}{\partial z^2} = 0 \tag{147}$$

$$u\frac{\partial v}{\partial r} + \frac{uv}{r} - \nu\left(\frac{\partial^2 v}{\partial r^2} + \frac{1}{r}\frac{\partial v}{\partial r} - \frac{v}{r^2}\right) = 0 \tag{148}$$

An inspection of the above two PDEs shows that they are no longer linear. A proposed series solution is as follows:

$$u(r) = \frac{2n\nu}{r} \tag{149}$$

and

$$v(r) = \frac{B_0(z)}{r} + B_1(z)r^{(2n+1)} \tag{150}$$

Substitution of Equation 149 into 147 shows that the first, second, and third terms produce nontrivial partials, respectively, that cancel, as shown below:

$$-\frac{4n\nu}{r^3} + \frac{2n\nu}{r^3} + \frac{2n\nu}{r^3} = 0 \tag{151}$$

Substitution of Equations 149 and 150 into 148 shows that all five terms produce nontrivial partials that also cancel, respectively, as shown below, and their sum is simplified using Maple (the Maple script used in this derivation is shown in full detail in Appendix C). Thus, the sum of Equations 152 through 156 is 0.

$$2n\nu \left[-\frac{B_0(z)}{r^3} + (2n+1) B_4(z) r^{(2n-1)} \right] \tag{152}$$

$$2n\nu \left[\frac{B_0(z)}{r^3} + B_4(z) r^{(2n-1)} \right] \tag{153}$$

$$-\nu \left[2\frac{B_0(z)}{r^3} + (2n+1)^2 B_4(z) r^{(2n-1)} - (2n+1) B_4(z) r^{(2n-1)} \right] \tag{154}$$

$$-\nu \left[-\frac{B_0(z)}{r^3} + (2n+1) B_4(z) r^{(2n-1)} \right] \tag{155}$$

$$\nu \left[\frac{B_0(z)}{r^3} + B_4(z) r^{(2n-1)} \right] \tag{156}$$

Applying Equations 149 and 150 to the following conservation of mass equation, Equation 141, yields two nontrivial terms that also cancel out:

$$-\frac{2n\nu}{r^2} + \frac{2n\nu}{r^2} = 0. \tag{157}$$

Therefore, Equations 149 and 150 are solutions to NS of the form in Equations 147 and 148, and also satisfy conservation of mass in the form of Equation 141.

5.1.10.2   Azimuthal, Radial, and Axial Velocity Field Solutions

For the three fields $u(r) \neq 0$, $v(r) \neq 0$, and $w(r) \neq 0$, the 1D NS radial, azimuthal, and axial velocity momentum PDEs can be simplified as follows, respectively:

$$w \frac{\partial u}{\partial z} - \nu \left(\frac{\partial^2 u}{\partial r^2} + \frac{1}{r} \frac{\partial u}{\partial r} - \frac{u}{r^2} + \frac{\partial^2 u}{\partial z^2} \right) = 0 \tag{158}$$

$$u \frac{\partial v}{\partial r} + \frac{uv}{r} + w \frac{\partial v}{\partial z} - \nu \left(\frac{\partial^2 v}{\partial r^2} + \frac{1}{r} \frac{\partial v}{\partial r} - \frac{v}{r^2} \right) = 0 \tag{159}$$

$$u \frac{\partial w}{\partial r} + w \frac{\partial w}{\partial z} - \nu \left(\frac{\partial^2 w}{\partial r^2} + \frac{1}{r} \frac{\partial w}{\partial r} + \frac{\partial^2 w}{\partial z^2} \right) = 0 \tag{160}$$

Based on the same reasoning discussed in Section 5.1.10.1, a proposed series solution is proposed:

$$u(r) = \frac{2n\nu}{r} \tag{161}$$

$$v(r) = B_1 r^{(2n+1)} \tag{162}$$

$$w(r) = -C_1 r^{2n} \tag{163}$$

Substitution of Equations 161 and 162 into 158 produces three nontrivial terms whose sum is zero:

$$-\frac{4n\nu^2}{r^3} + \frac{2n\nu^2}{r^3} + \frac{2n\nu^2}{r^3} = 0 . \tag{164}$$

Substitution of Equations 161 through 163 into Equation 159 yields five nontrivial terms (Equations 165 through 169) whose sum is also zero according to Maple:

$$2n\nu(2n+1) B_1 r^{(2n-1)} \tag{165}$$

$$2n\nu B_1 r^{(2n-1)} \tag{166}$$

$$-\nu \left[(2n+1)^2 B_1 r^{(2n-1)} - (2n+1) B_1 r^{(2n-1)} \right] \tag{167}$$

$$-\nu(2n+1) B_1 r^{(2n-1)} \tag{168}$$

$$\nu B_1 r^{(2n-1)}$$

$$(169)$$

Next, substitution of Equations 161 and 163 into Equation 160 yields three nontrivial terms (Equations 170 through 172) whose sum is zero:

$$-4n^2 \nu C_1 r^{2n-2}$$

$$(170)$$

$$-\nu\left(-4n^2 C_1 r^{2n-2} + 2n C_1 r^{2n-2}\right)$$

$$(171)$$

$$2n\nu C_1 r^{2n-2}$$

$$(172)$$

Finally, substitution of Equations 161 and 163 into 141 produces two nontrivial terms of equal and opposite magnitude that are identical to Equation 157, thus showing that mass is also conserved. The Maple script used in this derivation is shown in full detail in Appendix C.

Therefore, Equations 161 through 163 are solutions to NS of the form in Equations 158 through 160, and also satisfy conservation of mass in the form of Equation 141.

Further, that new two and three field solutions are expressible in certain series forms that satisfy NS provides additional corroborating evidence that axisymmetric solutions are expressible as series.

5.1.11 Transient S Modeling

The literature is teeming with swirling jet experiments and calculations where S=constant. However, no dynamic S calculations or experiments were found where the swirl angle changes geometrically. There are simulations were S is dynamic in the sense that it is the ratio of the angular and axial momentum, so it is possible to modify either to get a "dynamic" S [Najim, Styles, and Syred, 1981; Merker *et al*., 2006]. Nevertheless

dynamic S may be applicable in nanotechnology applications, as well as propulsion and exotic heat transfer, and has various theoretical implications, including new flow patterns and CRZ formation hysteresis, which have additional applications in combustion.

Because a formulation was developed in Section 5.1.1 that specifies the v_x, v_y, and v_z velocities as functions of S (*see* Equations 110, 111, and 113, respectfully), it is now possible to specify S as a varying function of time, S(t). Because S is a function of θ (Equation 109), then

$$S = S(\theta) = S\big(\theta(t)\big). \tag{173}$$

Clearly, $\theta(t)$ may be any reasonable, analytical function. As an example, consider a function that increases linearly with time, starting at $\theta=0°$, peaks at $\theta=89°$ (θ_{max}); and then decreases linearly back to 0° thereafter. The function may not reach 90° so that S=∞ is avoided. Based on the calculations already conducted herein, a time ramp was chosen such that it allowed the flow field sufficient time for the CRZ to form and expand as θ changed. With that in mind,

$$
\begin{aligned}
\theta(t) &= \ 0 \ \text{for } t \leq t_1 \\
\theta(t) &= \ \left(\frac{\theta_{max}}{t_2 - t_1}\right)(t - t_1) \ \ \text{for } t \leq t_2 \\
\theta(t) &= \ -\left(\frac{\theta_{max}}{t_3 - t_2}\right)(t - t_3) \ \ \text{for } t \leq t_3 \\
\theta(t) &= \ 0 \ \text{for } t \leq t_4
\end{aligned}
\tag{174}
$$

The function is shown in Figure 97. The function, as well as the velocities as functions of S, can be linked into the Fuego executable by using FORTRAN user-subroutines. As time advances in Fuego, the swirl angle changes, causing S to change,

which in turn causes the lead coefficients in the helicoid swirl velocities to change. Note that the lead-coefficient changes uniquely specify the swirl angle at any given time.

The stand-alone jet model was used with CFL=1.0. As a starting point, the following values were used for time: t_1=1.0, t_2=11.0, t_3=21.0, and t_4=23.0 s.
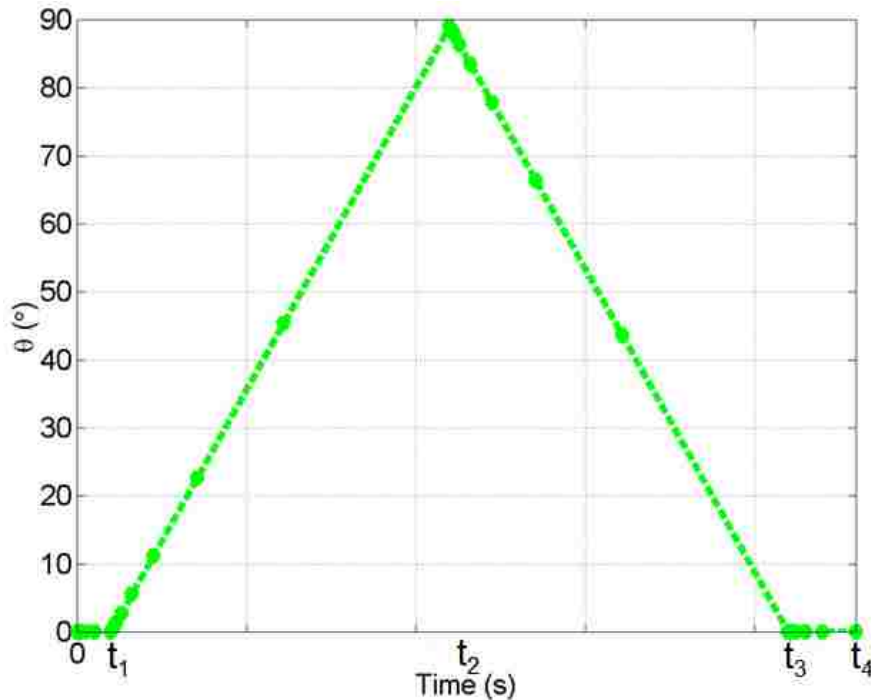
Figure 97. Dynamic Swirl Angle.

For the calculation, Re remained fixed at 1,600; only S changed as a function of time. Due to the long calculational time period, the simulation was run on a coarse grid (36,440 hexahedral elements) to scope out the calculational behavior. Thereafter, the calculation was run on a mesh with 124,745 hexahedral elements, and found to have sufficient discretization to show the details of the vortex flow, including the CRZ.

The calculation showed that as S increased, the CRZ initially formed at ~42°; that is, it formed ~3° sooner than when a static S was used. Because Re was fixed, the output as S increased followed that of Figure 80. As the calculation proceeded, it was noted that

179

the CRZ closed at ~59º, quite more than the 45º at which it first appeared with S was

static. The first formation of the CRZ at less than 45º and its subsequent closure at > 45º

are attributable to the higher degree of turbulence that occurred as the vortex opened at a

rather fast rate, without allowing the flow field to reach steady state. The same applies to

its closure. For comparison purposes, another calculation was run with static S at θ=45º

using the same mesh, initial and boundary conditions, as well as CFL number. Figure 98

shows the CRZ that was formed with a static S at θ=45º (LHS), and the CRZ as it first

formed (middle frame) and closed (RHS) during the transient S calculations. Notice that

the overall flow profile looked similar.
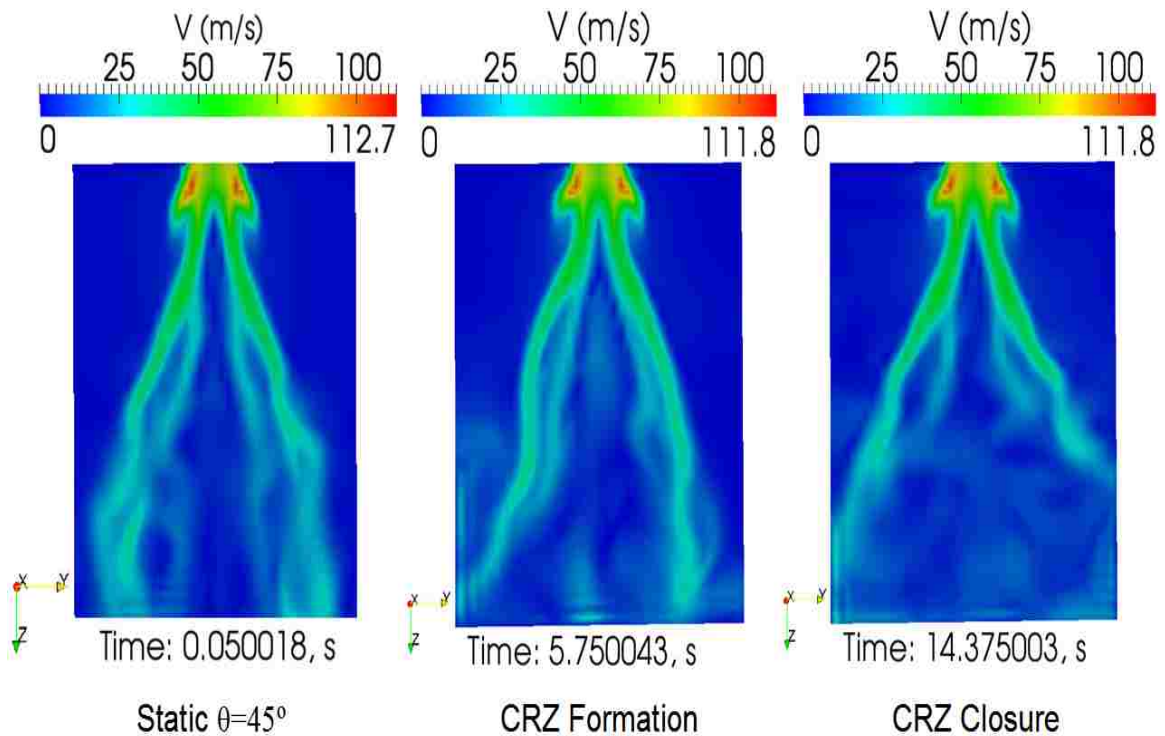
Figure 98. Comparison of CRZs Formed during Static and Transient S.

5.1.12 Advanced Swirling Jet Design Guidelines

Jet design has many practical applications, such as the modification of the CRZ for reduction of NOx during combustion, as well as control of the leading edge vortices that destabilize a swirling jet [Saghbini and Ghoniem, 1997]. Therefore, it is profitable to seek ways to design jets for optimal mixing, heat transfer, etc.

Now, without doubt, recent swirling vortex research involves complex and diverse findings, such as:

- The existence of critical points and manifolds in the Lamb vector [Kollmann and Umont, 2004; Kollmann, 2006],

- Energetic modes [Jung, Gamard, and George, 2004],

- Vortex rings and vortical structures [Fuchimoto *et al.*, 2009],

- Similarity theory for weak swirls [Semaan and Naughton, 2009; Semaan, Naughton, and Ewing, 2009],

- Compressible and incompressible jet instabilities studies [Rusak and Wang, 1996; Rusak and Lee, 2002],

- The existence of hairpin vortices in the near-field that enhance mixing [Elavarasan and Meng, 2000; Matsuda and Sakakibara, 2005],

- For swirling jets in crossflow, the generation of counter-rotating vortex pairs (CVP) that promote a pumping action from *low-speed* fluid regions onto the *high-speed* outer shear layer [Elavarasan and Meng, 2000],

- Centrifugal instabilities yield CVPs that have opposing sign and that tend to disappear as the streamwise velocity increases, with one ring being amplified and the other decaying as a result of the Kelvin-Helmholtz axial flow instability [Martin and Meiburg, 1996],

- Small structures in fine scale eddies [Buxton and Ganapathisubramani, 2009], and

- 30 to 40% of the fluctuations that occur in the swirling jet are due to organized motion related to coherent structures [Frohlich, Garcia-Villalba, and Rodi, 2008].

Clearly, some of the above insights can be applied to enhance mixing and turbulence. Another important feature of swirling jets is that as S increases, the velocity field inevitably becomes unstable (also known as jet "breakdown") [Lucca-Negro and O'Doherty, 2001]. Swirling jet breakdown was first studied by Elle and Werle in the 1960s and continues to generate much research energy and enthusiasm [Elle, 1960; Werle, 1960; Benjamin, 1962; Lopez, 1990; Brown and Lopez, 1990; Lopez and Perry, 1992; Shtern and Hussain, 1999; Lee and Rusak, 2004; Liang and Maxworthy, 2004]. Others have investigated the recirculation zone length and the S vs. Re dependency of the CRZ [Young, Liao, and Sheen, 1999].

Therefore, jet instability can also be used as a jet design parameter. In terms of vortex breakdown phenomena, researchers have recently noted the following:

- The upstream BCs can impact the onset of axisymmetric vortex breakdown [Leclaire, Sipp, and Jacquin, 2008],

- Vortex breakdown in annular swirling jets is well-documented [Sheen, Chen, and Jeng, 1996],

- Exotic breakdown shapes have been identified, such as the trident and Celtic cross vortex [Billant, Chomaz, and Huerre, 1998; Gallaire, Rott, and Chomaz, 2004], and

- The successful calculation of two stationary CRZ bubbles [Serre and Bontoux, 2002].

An excellent review of vortex breakdown was recently conducted [Lucca-Negro and O'Doherty, 2001], and a useful map for vortex breakdown vs. S was recently compiled [Liang and Maxworthy, 2008]. Although various theoretical studies have been conducted to explain vortex breakdown of axisymmetric swirling flows, there currently is no "consistent description of this complicated phenomenon" [Rusak and Wang, 1996].

Therefore, it is clear that there are various ways swirling jets can be designed. And indeed, some researchers have already worked in this area; among some of the design parameters are mode selection [Gallaire and Chomaz, 2003] and adjustment of rotational Re to move the CRZ [Atvars, Thompson, and Hourigan, 2009]; this latter approach will be considered later in this Section. In addition, others have modified the azimuthal velocity distribution (e.g. Bessel function) and shown that the axial velocity decreased as a result of swirl [Itoh *et al*., 2003] (this result is not surprising, as shown in Section 5.1.1).

Consequently, even despite the complexity of recent vortex phenomena, there are aspects of swirling jets that readily lend themselves to judicious engineering design. For example, it is possible to modify a swirling jet flow field in order to reach a desired engineering goal. That argument was explored in Section 5.1.2, where it was noted that for weak to intermediate S, there exists a domain z^* where the azimuthal velocity exceeds the axial velocity. That insight in turn allows the optimum usage of weak to intermediate swirl.

Then, at this point, there are some additional parameters that may be explored further with the purpose of optimizing the swirling jet flow field. Among these are the:

1. Azimuthal velocity shape,

2. Ratio of the azimuthal and axial velocities, and

3. Modification of the CRZ.

That the azimuthal velocity distribution can take numerous shapes as a function of r and Re has already been shown [Donaldson and Sullivan, 1960]; some of these families of curves include rather "wild" azimuthal velocity profiles that are disjointed and approach infinity as r approaches 0. Other researchers have also proposed a varied set of azimuthal velocity profiles [Knowles and Carpenter, 1988; Knowles and Carpenter, 1990; Larocque, 2004]. In addition, controllable initial tangential velocity distribution (solid body vs. free) indicated that in the near-field, the solid-body vortex for S=0.48 (moderate swirl) exhibited the classical velocity decay, while the free vortex (which had a sine-like shape) and that had the same S "was on the verge of vortex breakdown". Remarkably, such behavior ought not to occur unless $S_{crit} \geq 0.6$ [Farokhi, Taghavi, and Rice, 1988], and, as shown in this research, $S_{crit} \geq 0.67$ (Section 5.1.1).

As examples of azimuthal velocity designs, suppose θ=0°. Then the flow would be principally in the z direction, with expansion in the r direction. In this case, there would be no azimuthal flow, and this would occur at the expense of maximizing the momentum in the r and z directions. By contrast, if θ=90°, then there would be no axial flow. The flow field would have momentum exchange between the azimuthal and radial directions only. The lack of flow in the z direction in this case would be at the expense of maximizing the azimuthal and radial momenta. Clearly, then, there ought to be an angle θ whereby the axial and azimuthal mixing can be maximized.

Furthermore, by adjusting S, the magnitude of the radial, azimuthal, and axial velocities are uniquely specified once the vortex type is chosen (e.g. Batchelor, AVE,

etc.; *see* Table 4). Then, the shape of the azimuthal velocity can be optimized such that the desired feature is attained. For example, the mixing in the central region and surrounding areas can be increased. Figure 99 shows an example of the AVE vortex whose parameters (the lead coefficient and argument of the Bessel function) were modified in order to show that the azimuthal velocity can be shifted towards the origin (z) or away from it. Because only the coefficients were modified, the azimuthal distributions still satisfy NS.

Recall that the CRZ formation occurs as a result of the azimuthal velocity being greater than or equal to the axial velocity (Section 5.1.1). Then, it follows that by shifting the azimuthal velocity as shown in Figure 99, it is possible to also change the S at which the CRZ will occur.

Furthermore, Figure 96 shows that it is possible to substantially modify the degree of decay for the free domain of the vortex. Because only the lead and exponential coefficients for the Modified Newman vortex were adjusted, the rate of decay in the azimuthal velocity satisfies NS in the free domain.
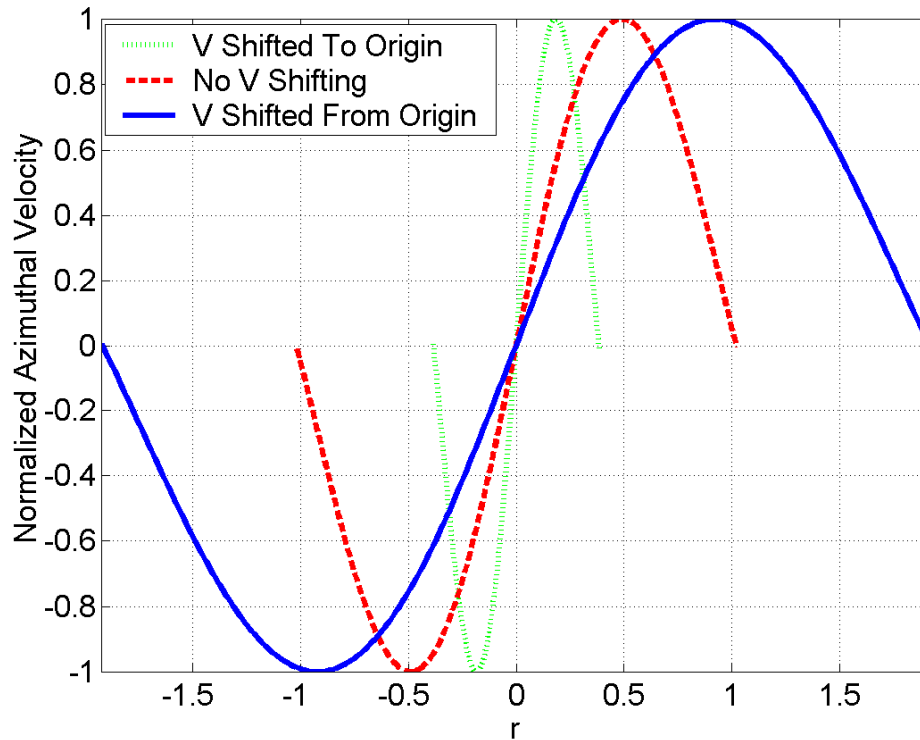
Figure 99. Shifting of the Azimuthal Velocity for the AVE Vortex.

5.2   Fuego Validation and Verification (V&V)

The literature indicates that the development of a PIRT-like (phenomena identification and ranking table) approach has a strong likelihood for identifying the key phenomena in the LP [Vilim, Pointer, and Wei, 2006; Lee *et al.*, 2007; Olivier and Nowlen, 2008]. Indeed, various attempts have been made recently for the VHTR LP, and this research focuses on many of those that have been identified already [McEligot, D. M. *et al*, 2005; Vilim, Pointer, and Wei, 2006]. Based on the literature and a desire to include simplified to more complex fluid phenomena, a set of key fluid phenomena were selected for CFD simulations. The cases that were selected for V&V are listed in Table VI, and are as follows [Rodriguez and El-Genk 2010a]:

1. Conventional jet,

2. Swirling jet,

3. Conventional jet in crossflow,

4. Swirling jet in crossflow,

5. Flow around a vertical cylinder,

6. CRZ formation, and

7. Staggered array of tubes in crossflow.

The above seven phenomena are strongly related to flow distribution, as well as thermal mixing and stratification. Furthermore, they received a "high" ranking in a recent VHTR PIRT study that was conducted by Argonne National Laboratory [Vilim, Pointer, and Wei, 2006].

Table 7. Fuego Validation and Verification for Key Phenomena Relevant in the LP.

Flow Type	Key Variables / Phenomena	Data / Theory	Fuego V&V
Conventional Jet	Axial velocity distribution	Chevray and Tutu, 1978; Schlichting, 1979; Falcone and Cataldo, 2003; Singh, Sundararajan, and Bhaskaran, 2003; Bird, Stewart, and Lightfoot, 2007	Rodriguez and El-Genk, 2010a
	Radial velocity distribution	Reichardt, 1942; Witze and Dwyer, 1976; Falcone and Cataldo, 2003; Bird, Stewart, and Lightfoot, 2007	Rodriguez and El-Genk, 2010a
	Jet spread angle	Labus and Symons, 1972; Witze and Dwyer, 1976; Bird, Stewart, and Lightfoot, 2007; Blevins, 1992	Rodriguez and El-Genk, 2010a
Swirling Jet	Axial velocity	Blevins, 1992; Chigier and Chervinsky, 1967	Rodriguez and El-Genk, 2010a

Flow Type	Key Variables / Phenomena	Data / Theory	Fuego V&V
	Azimuthal velocity	Mathur and MacCallum, 1967; Chigier and Chervinsky 1967; Billant *et al*. 1998; Blevins, 1992	Rodriguez and El-Genk, 2010a
Conventional Jet in Crossflow	Jet propagation	Pratte and Baines, 1967; Nirmolo, 1970; Chassaing *et al.*, 1974; Kamotani and Greber, 1974; Sucec and Bowley, 1976; Patankar, Basu, and Alpay, 1977; Goldstein and Behbahani, 1982; Kavsaoglu and Schetz, 1989; Blevins, 1992; Rivero, Ferre, and Giralt, 2001; Kiel *et al.*, 2003; Kawai and Lele, 2007	Rodriguez and El-Genk, 2010a
	Jet velocity	Pratte and Baines, 1967; Chassaing, P. *et al.*, 1974; Sucec and Bowley, 1976; Patankar, Basu, and Alpay, 1977; Blevins, 1992; Lim, New, and Luo, 2001	Rodriguez and El-Genk, 2010a
	Production of counter-rotating vortices	Pratte and Baines, 1967; Blevins, 1992	Rodriguez and El-Genk, 2010a
	Jet cross section (kidney)	Kavsaoglu and Schetz, 1989; Blevins, 1992	Rodriguez and El-Genk, 2010a
Swirling Jet in Crossflow	Jet propagation	Kavsaoglu and Schetz, 1989; Denev, Frohlich, and Bockhorn, 2009; Kamal, 2009	Rodriguez and El-Genk, 2010a
	Jet velocity	Kavsaoglu and Schetz, 1989; Denev, Frohlich, and Bockhorn, 2009; Kamal, 2009	Rodriguez and El-Genk, 2010a
Flow Around a Cylinder	Stagnation pressure	White, 1991	Rodriguez, Domino, and El-Genk, 2010
	Vortex shedding frequency	Ribner and Etkin, 1958; Roshko, 1961; Williamson, 1989; Kravchenko and Moin, 2000; Afgan, 2007; Doolan,	Rodriguez, Domino, and El-Genk, 2010

Flow Type	Key Variables / Phenomena	Data / Theory	Fuego V&V
		2010	
CRZ	Swirl angle at which CRZ is first formed.	Mathur and MacCallum, 1967; Chigier and Chervinsky, 1967; Billant *et al.,* 1998; Rodriguez and El-Genk, 2010b	Rodriguez and El-Genk, 2010b
Staggered Array of Tubes in Crossflow	Flow distribution.	Grimison, 1937; Blevins, 1992; Liang and Papadakis, 2007	Present study

Note that the stand-alone model involved 500,000 to 5.5 million hexahedral elements. As noted in Section 5.2, the fine nodalization was not extrapolated linearly to the LP model. This was a necessary compromise, as discretizing the LP to the level of the stand-alone models would have resulted in calculations that would have required prohibitive calculational times, even on massively parallel computer systems.

5.2.1 Conventional Jet

Figure 100 shows the experimental data for a cylindrical jet [Reichardt, 1942]. A solution for turbulent, conventional jets evaluates the axial velocity as [Schlichting, 1933; Bird, Stewart, and Lightfoot, 2007],

$$w(r,z) = \frac{\nu_t}{z} \frac{2C_3^2}{\left[1 + \frac{1}{4}\left(\frac{C_3 r}{z}\right)^2\right]^2} \tag{175}$$

An empirical velocity distribution for cylindrical jets can also be applied to the data with excellent results [Tollmein, 1926],

$$w(r,z) = W_{max} e^{-0.65\left(\frac{r}{z}\right)^2}. \tag{176}$$

The width b as the jet spreads is [Blevins, 1992],

(4.1) $b(z) = 0.086z$

while others report a similar expression [Reichardt, 1942; Bird, Stewart, and Lightfoot, 2007],

$b(z) = 0.0848z$ (177)
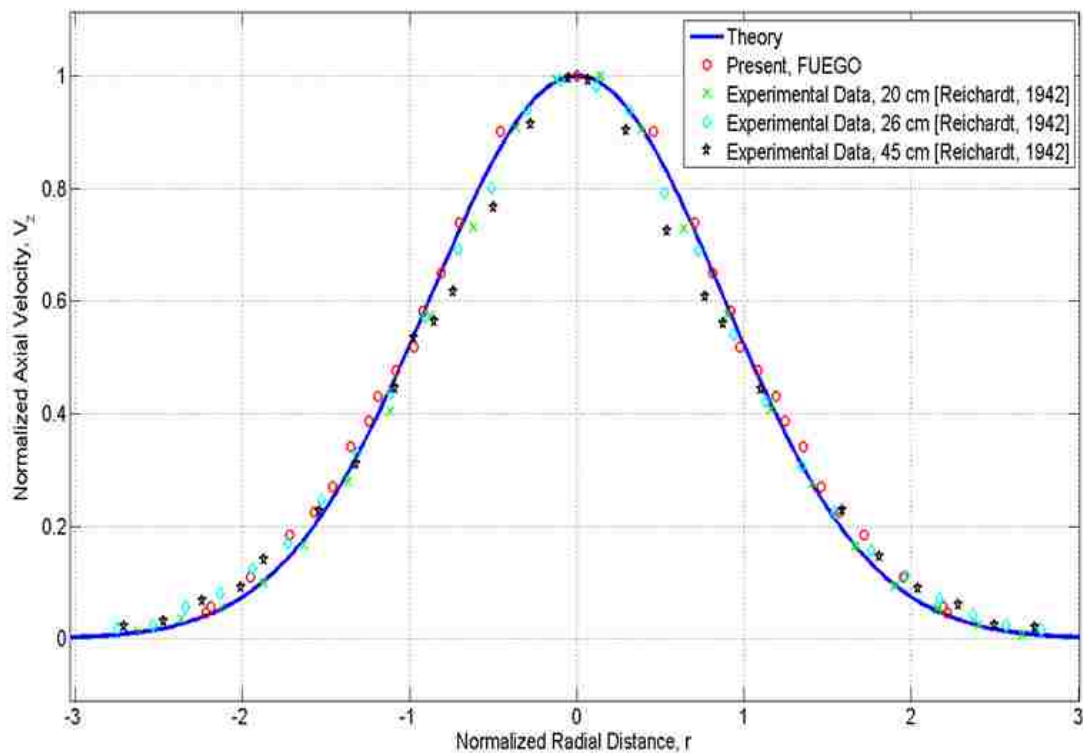
Figure 100. Normalized Axial Velocity vs. Normalized Radial Distance for a Conventional Jet: Theory, Fuego, and Data.

A free, conventional (symmetric) jet of hot helium was modeled with Fuego. The calculated normalized axial velocity as a function of the normalized radial distance was compared with boundary layer theory and experimental data, as shown in Figure 100 [Schlichting, 1979; Goldstein and Seol, 1991; Bird, Stewart, and Lightfoot, 2007]. The

comparisons show that Fuego, theory, and the experimental data are reasonably close, even when the axial velocity has decayed substantially.

Figure 101 shows Fuego's axial velocity distribution for a fully-developed conventional jet. The two super-imposed green arrows show the location where, at a given point in the z axis, the ratio of the axial velocity at radius r, and its associated centerline velocity, equal half. (The axial velocity profiles are taken at z = constant planes.) The experimentally-measured spread angle is 4.85º [Schlichting, 1979; Bird, Stewart, and Lightfoot, 2007], while that of the Fuego calculation is about 5º.
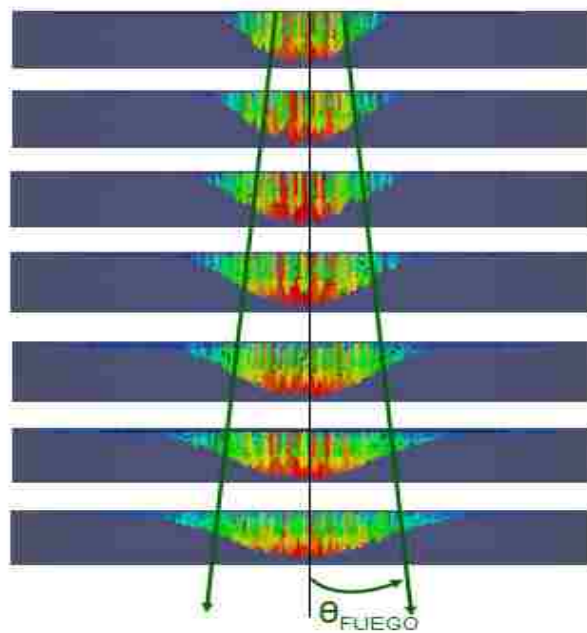
Figure 101. Fuego Cross-Sections of Axial Velocity-Distribution for a Symmetrical Jet.

5.2.2   Swirling Jet

For this calculation, a single, round, axisymmetric swirling jet field was computed; experimental data for a cluster of nine swirling jets was recently obtained [Boutazakhti *et al.*, 2007], while data for circular, elliptic, square, rectangular, equilateral triangular, and isosceles triangular jets was measured recently [Singh, Sundararajan, Bhaskaran, 2003]. Researchers have observed that a swirling impinging jet decreases the maximum pressure near the plate [Herrada, Pino, and Ortega-Casanova, 2009]. The jet considered for this calculation was unconfined.

The swirl angle was set by adjusting the swirl BCs to match the experiment hardware angle reported by Blevins [Blevins, 1992]. The calculated centerline axial velocity for the asymmetric, swirling-jet is shown in Figure 102. The theoretical velocity decreased linearly as the axial distance increased away from the jet exit nozzle [Rajaratnam, 1976; Blevins, 1992]. The figure shows that there is very good agreement with Fuego's predictions and theory that the centerline (maximum) axial velocity varies as 1/z, as reported in the literature [Loitsyanskiy, 1953; Gortler, 1954; Blevins, 1992],

$$w(z) = C_1(S)\left(\frac{r_0}{z}\right)w_0. \tag{178}$$

where [Blevins, 1992]

$$C_1(S) = -2.6S^3 + 12S^2 - 19S + 12. \tag{179}$$

Note that the 1/z dependency applies for weak to moderate S (*see* Section 2.2).

As shown in Figure 103, the present CFD calculations confirm the literature experimental data and theory that the azimuthal velocity of a swirling jet decays as $1/z^2$

[Loitsyanskiy, 1953; Gortler, 1954; Mathur and MacCallum, 1967; Chigier and Chervinsky, 1967; Rajaratnam, 1976; Blevins, 1992; Billant *et al.*, 1998]:

$$v(z) = C_2 \left(\frac{r_0}{z} \right)^2 v_0 \tag{180}$$

where [Blevins, 1992] noted a wide significant variation for C_2, $4 < C_2 < 11$, which may be a function of S.

Thus, the azimuthal velocity decays much faster than the axial velocity—a factor that is crucial in the design of an LP with swirling jets, and for that matter, any system application that employs swirling jets for cooling, heating, combustion, and mass transfer.
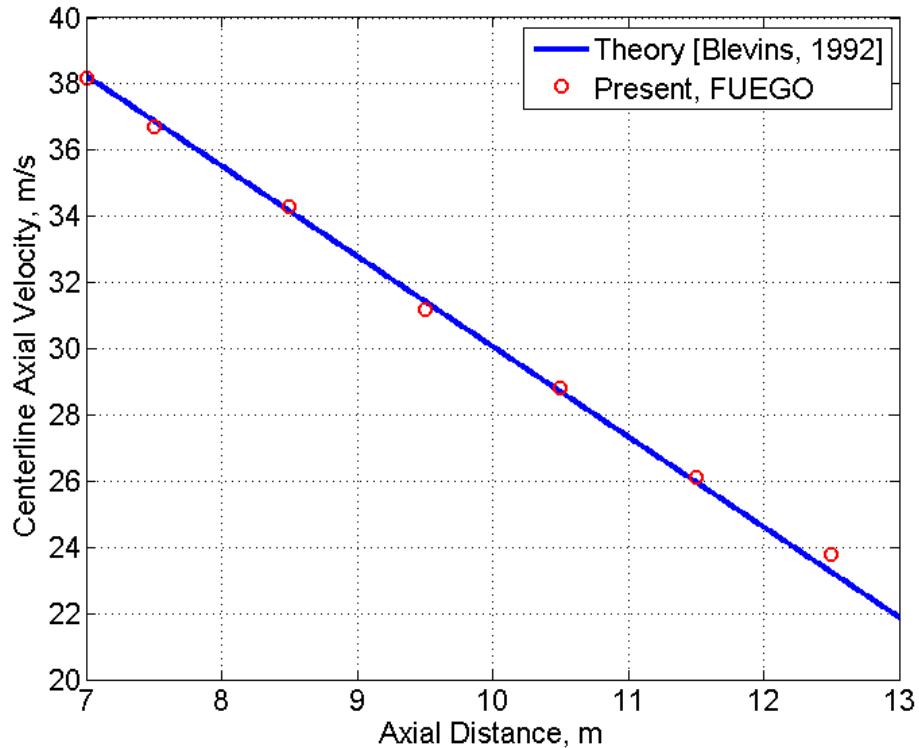
Figure 102. Swirling Jet—Axial Velocity vs. Axial Distance.
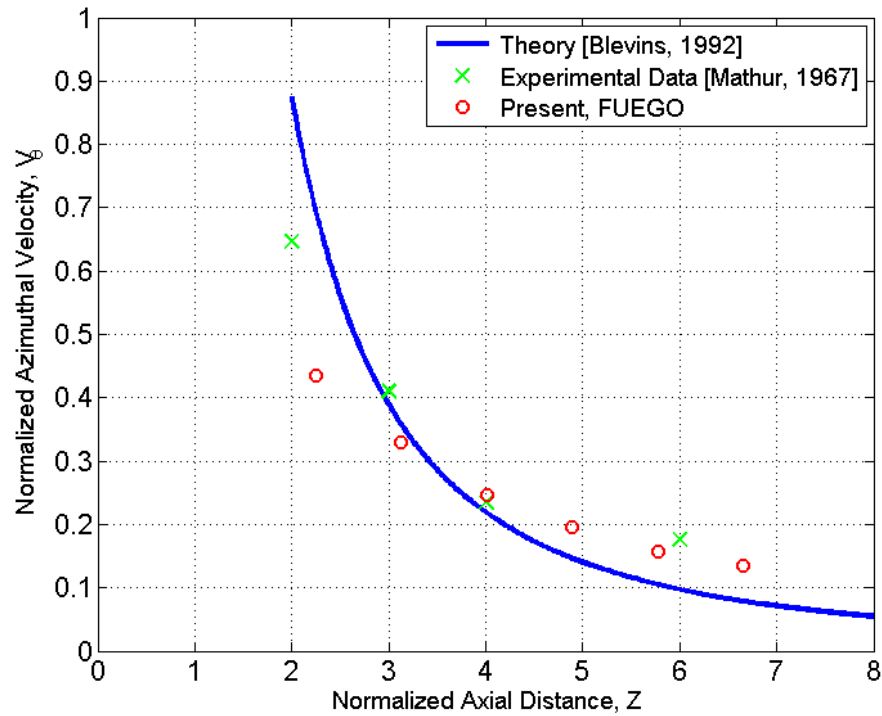
Figure 103. Swirling jet—Azimuthal Velocity vs. Axial Distance.

5.2.3 Conventional Jet in Crossflow

An unconfined helium conventional jet in crossflow was modeled with Fuego. As noted by researchers some time ago, a conventional jet in crossflow has a parabolic-like trajectory that is a function of the ratio of the jet nozzle and crossflow velocities [Keffer and Baines, 1963; Pratte and Baines 1967; Blevins, 1992; Kiel *et al.*, 2003]; *see* Figure 104. Kiel and coworkers considered Re in the range of 3,000 to 18,000. The literature describes the jet trajectory as,

$$\frac{z}{r_o} = c_1 \left(\frac{u_o}{u_1} \right)^{0.72} \left(\frac{x}{r_o} \right)^{0.28} \tag{181}$$

where c_1 is 3.87, 2.9, and 1.89 for the top, centerline, and lower jet trajectory, respectively.

For the simulations, the jet nozzle velocity was 35 m/s, while the uniform crossflow velocity was 5.0 m/s. Figure 105 compares the semi-empirical correlations with the present numerical results for a conventional jet in crossflow. Note the good agreement between Fuego results and the semi-empirical correlations for the centerline and bottom profiles. The top profile qualitatively follows the Fuego output, though the agreement is not as good in the region where the flow is not fully developed. The predicted flow fluid using Fuego spreads out a little more than the correlations. As noted by Blevins, the length of the jet core is a function of the jet nozzle radius, the crossflow velocity, and the jet nozzle velocity. The core length as calculated by Fuego is $3.5r_o$, while experimental data indicates that it should be about $3.75r_o$. Experimental results have shown that as soon as the jet leaves the core zone, into the transition region, it develops a characteristic "kidney shape" (Figure 106) and two counter-rotating vortices take form where there was previously a circular jet cross section [Blevins 1992]. The kidney shape is quite evident in the calculations when using velocity contours. The Fuego-calculated counter-rotating vortices are shown in Figure 107; they are obtained by taking a planar slice that is normal to the crossflow field (yz-plane). The experimental value for the ratio of the width to height for the kidney cross section is 1.4, which is the same as indicated by the present numerical results (Figure 106). A cross-section of the calculated counter-rotating vortices is shown in Figure 107.
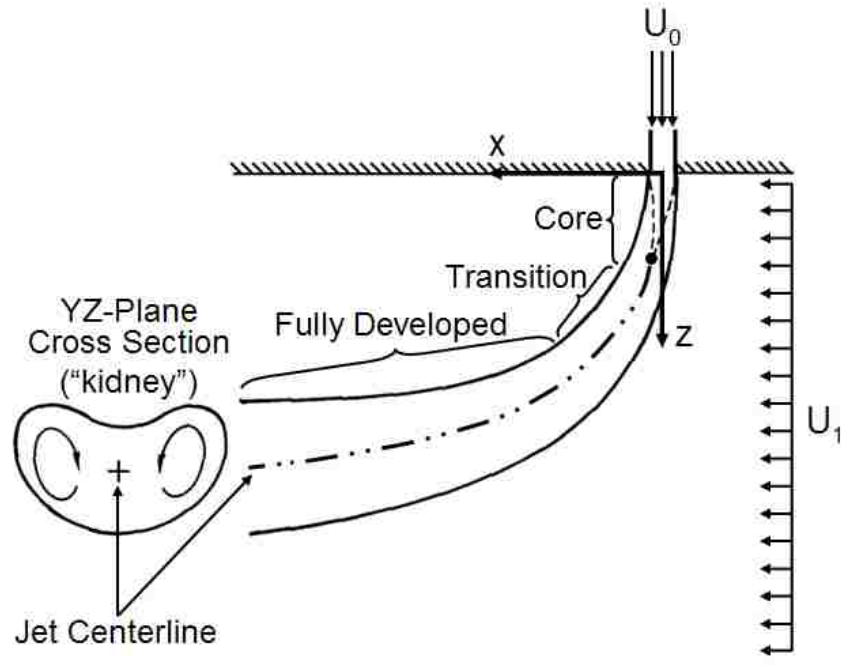
Figure 104. Crossflow Jet Schematic.
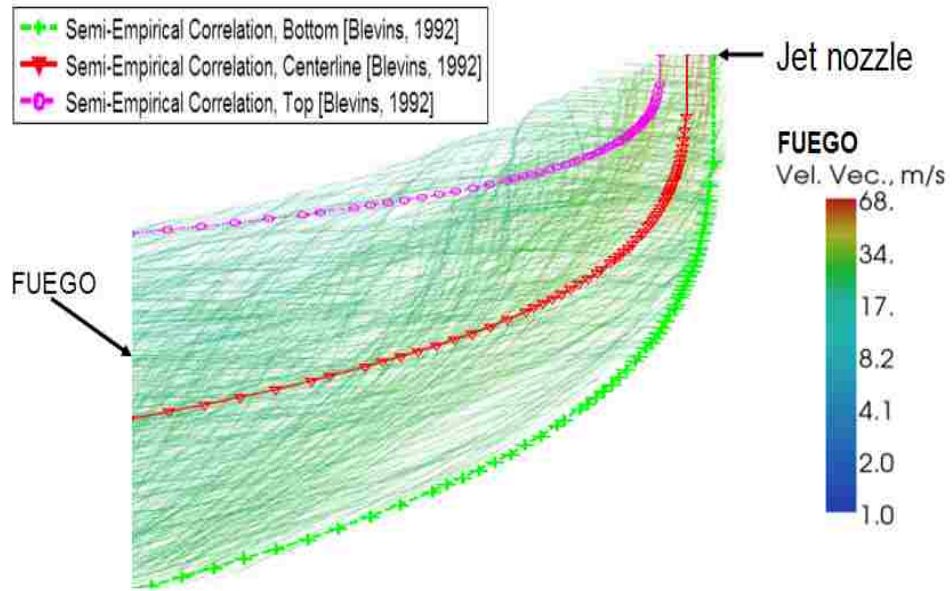
Figure 105. Conventional Jet in Crossflow—Fuego Output vs. Semi-Empirical Data Correlations.
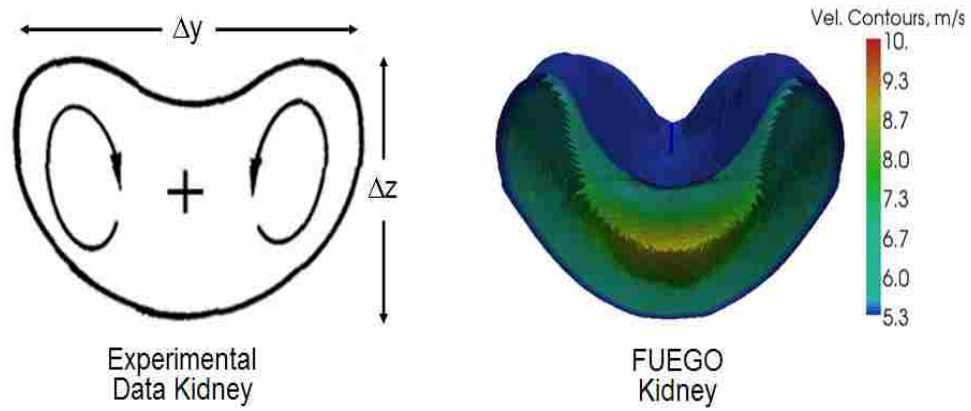
Figure 106. Cross-Section of Kidney Shape for Jet in Crossflow.
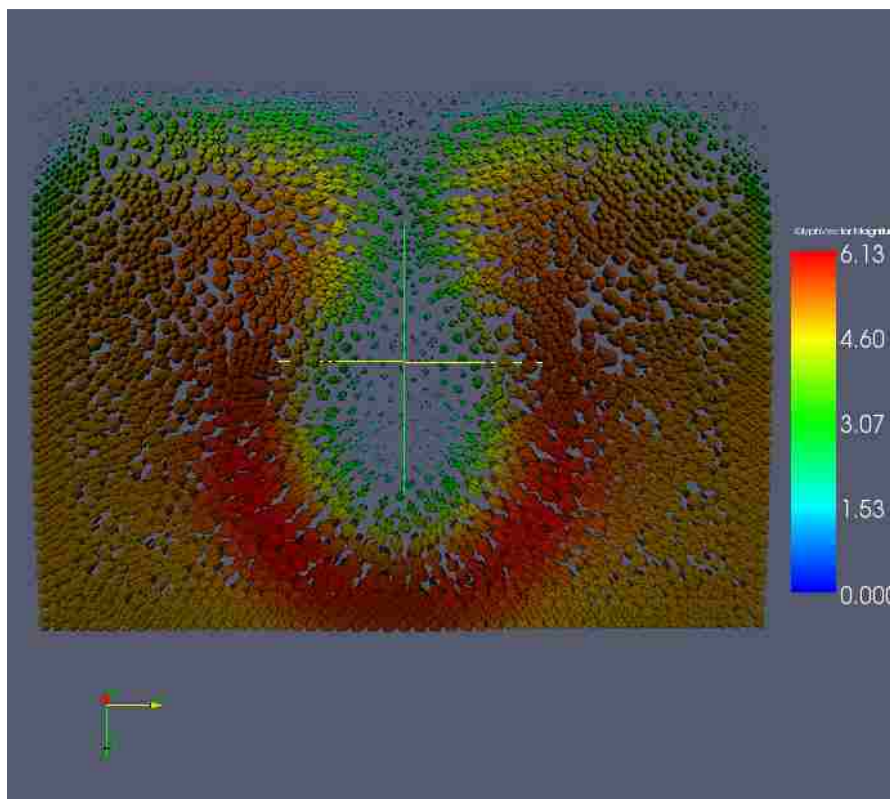
Figure 107. Counter-Rotating Vortex Pairs of a Conventional Jet in Crossflow.

Figures 108 and 109 show that the crossflow streamlines flow around the jet, as if the jet were an obstruction. Further, the crossflow adjacent to the outer parabolic region "wraps" around the parabolic jet, producing regions with strong mixing (*see* Figure 110). Notice the twin vortices that form on the LHS of the figure, creating additional mixing.
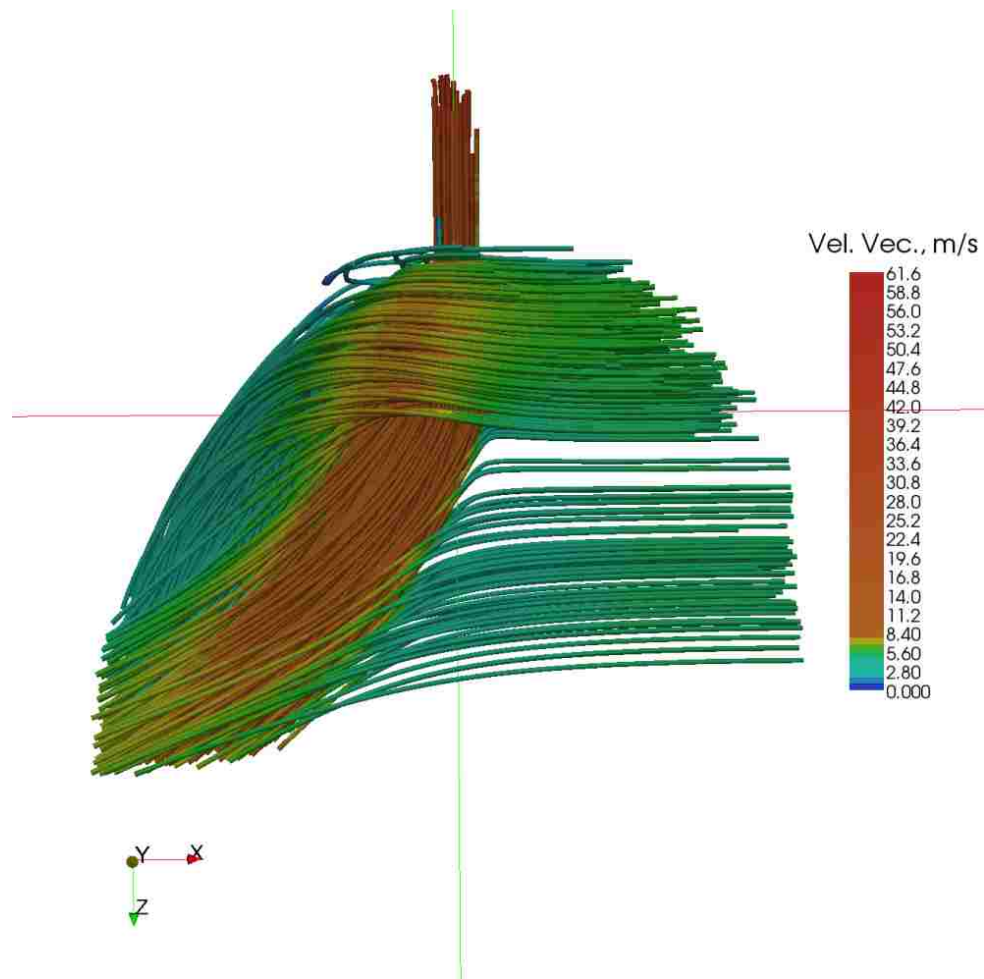
Figure 108. Crossflow Flowing around the Jet, Side View.
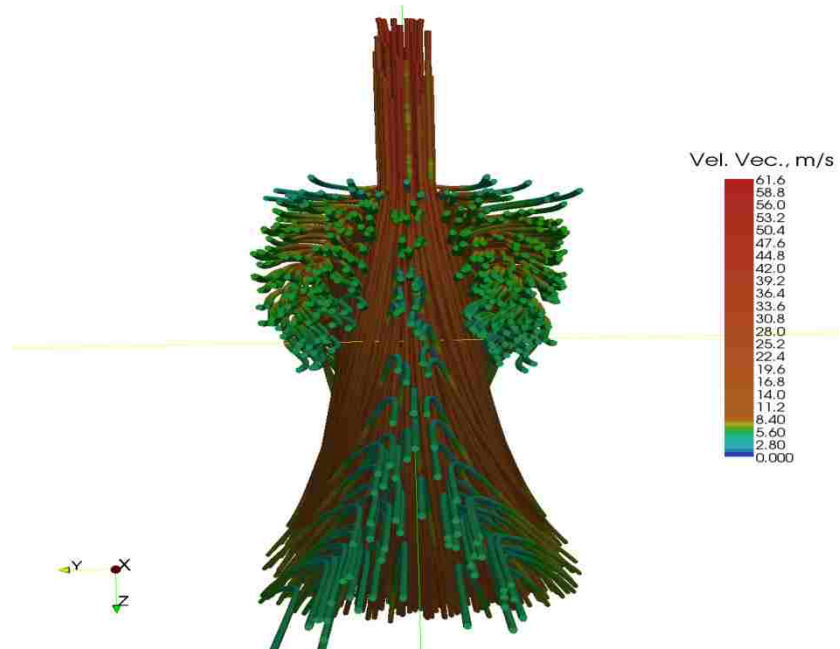
Figure 109. Crossflow Flowing around the Jet, Back View.
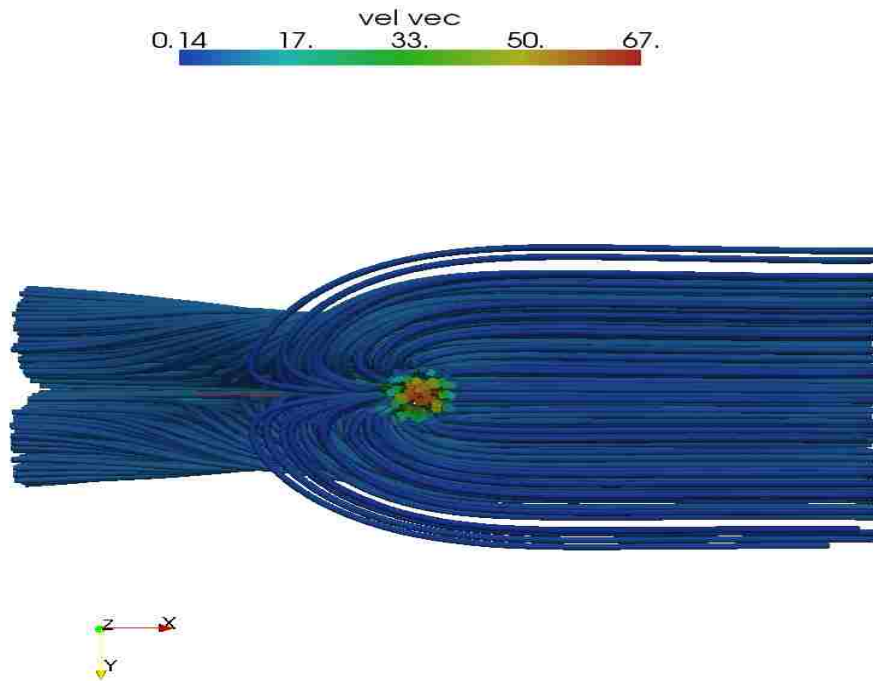
Figure 110. Strong Mixing Associated with Jets in Crossflow, Top View.

5.2.4   Swirling Jet in Crossflow

An unconfined, helium swirling jet in crossflow was simulated. Unfortunately, there is limited experimental data in the literature for swirling jets in crossflow. The literature includes a handful of papers with jet propagation, jet velocity, and vortex features were studied [Kavsaoglu and Schetz, 1989; Denev, Frohlich, and Bockhorn, 2009].

A radial swirler with crossflow was considered recently, but its geometry is sufficiently different from the LP jet in crossflow that it will not be considered here [Kamal, 2009]; the LP jets swirl azimuthally as they travel in the z-direction. Nevertheless, the work of Kamal showed that the swirling jet with crossflow increased mixing—and a desired feature sought after in this research. A more prototypic swirling jet in crossflow experiment was conducted for jet to crossflow velocity ratios of 2.2, 4, and 8 [Kavsaoglu and Schetz, 1989]; *see* Figure 111. They defined a swirl ratio as the "maximum peripheral velocity near the nozzle wall divided by the average axial velocity". Their data included swirl ratios of 0, 40, and 58%, as well as the characteristic parabolic velocity profile of a conventional jet in crossflow, and the kidney shape. Finally, recent work in this area has led to jet trajectories for $0 \leq S \leq 0.6$ using LES simulations [Denev, Frolich, and Bockhorn, 2009]. The authors also calculated the kidney shape.

However, there are some issues with the data, as discussed by a recent study [Denev, Frolich, and Bockhorn, 2009]. Denev and coworkers performed a set of simulations using LESOCC2, which is a LES code. Their output can be compared qualitatively with Fuego as a code-to-code comparison (Figure 112). A preliminary comparison shows good qualitative agreement between the LESOCC2 calculations and Fuego for the jet trajectories. *Most importantly, the figure shows that as S increases, the penetration depth*

of the jet is smaller. This is a desirable feature for the LP design, as higher S will

decrease the chances of a hot jet impinging on the LP plate.
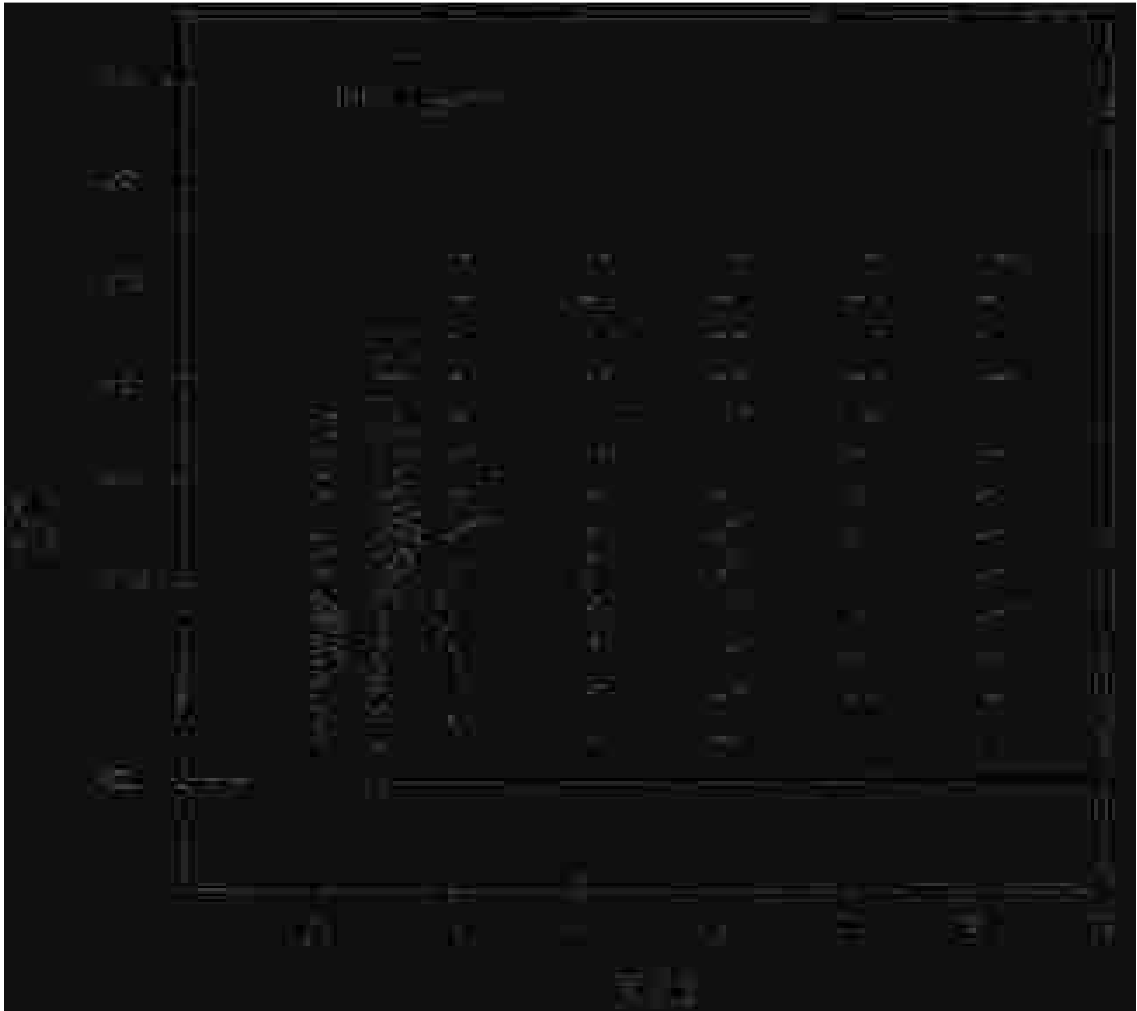
Figure 111. Swirling Jet in Crossflow Data [Kavsaoglu and Schetz, 1989].
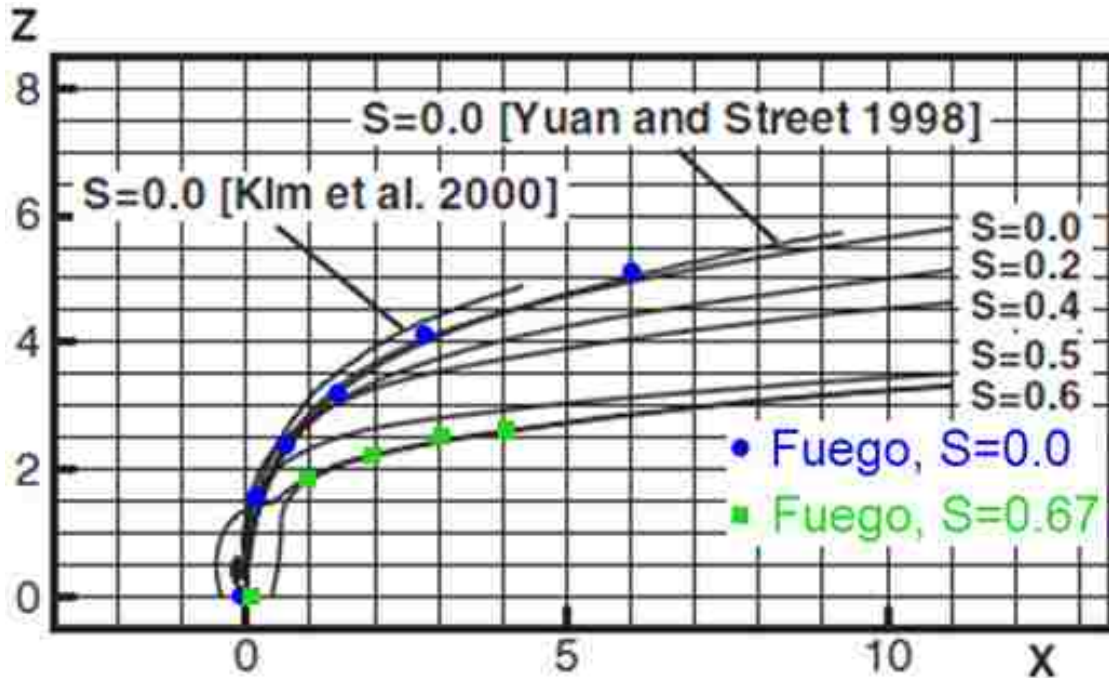
Figure 112. Swirling Jet in Crossflow: Comparison of Various LES Simulations [Kavsaoglu and Schetz, 1989 (Lines); Rodriguez and El-Genk, 2011 (Points)].

5.2.5   Flow around a Vertical Cylinder

The VHTR LP contains a large number of cylindrical graphite support posts that are approximately 8" in diameter. Due to their proximity to each other (as defined by the pitch to diameter ratio), the LP flow field is actually more similar to that around a large set of staggered tubes than to flow around a single tube. For staggered tubes, the flow around the individual tubes interferes with the flow field, whereby the flow near the tubes never attains the approach velocity.

Flow around a vertical cylinder has been researched extensively, yielding a large experimental database and CFD simulation results [Ribner and Etkin, 1958; Williamson, 1989; White, 1991; Tutar and Holdo, 2001; Afgan, 2007]. In light of the simplicity of modeling the flow around a single tube and the ability to compare CFD results to well-known theory, a single-cylinder flow calculation was added to the set of key Fuego V&V

calculations. In the meantime, it could be argued that if a CFD code cannot adequately simulate the simplified flow field around a single cylinder, it most likely cannot successfully model the flow for staggered cylinders applicable to the VHTR LP.

A set of coarse and very fine rectangular meshes were generated for simulating the flow around a vertical cylinder. The meshes consisted of 4,000, 16,000, 64,000, 256,000, and 1 million hexahedral elements, which resulted in an average cell length of 2.3×10^{-2}, 1.2×10^{-2}, 5.7×10^{-3}, 2.9×10^{-3}, and 1.4×10^{-3} m, respectively. It was noted that the solution was sufficiently converged spatially by 64,000 elements, as Fuego and theory differed by <2%. The cylinder diameter (D) was 0.203 m, the expected diameter of the graphite posts in the LP of a VHTR. The mesh dimensions were L = 15D and W = 10D. The mesh thickness was one element. The boundaries on the x-z planes were open, and so was the boundary on the opposite end of the inflow boundary; *see* Figure 113. The x-y planes had symmetry boundary conditions. The cylinder was placed 5D away from the constant velocity inflow boundary. The mesh dimensions were chosen primarily to avoid far field effects from interfering with the wake around the cylinder, and secondarily to calculate a reasonably-sized vortex street. (Note that in the actual LP, the cylinders would be much closer to each other.) The mesh dimensions were consistent with an LES calculation found in the literature [Tutar and Holdo, 2001]. The CFL number was fixed at 1.0, which resulted in time steps of 2.7×10^{-4}, 1.4×10^{-4}, 4.5×10^{-5}, 2.7×10^{-5}, and 1.4×10^{-5} s, respectively. The calculations were run with eight to 256 processors on the SNL Red Sky cluster.

The calculations used helium gas at 1,273 K, which yielded a gas density of 0.0386 kg/m^3, and a kinematic viscosity of 1.36×10^{-3} m^2/s. The helium gas approach velocity

(inflow boundary) for the calculations was fixed at 13.4, 67.0, and 134 m/s, which yielded Re of 2,000, 10,000, and 20,000. No calculations with variation in temperature were conducted for these set of calculations. However, temperature directly affects the kinematic viscosity, which affects Re, and for such reason and others, the calculations considered a 10-fold range in Re.

The problem can be better understood by using the Strouhal number (St), defined as:

$$St = \frac{fD}{U_\infty}, \qquad (182)$$

where D is the cylinder diameter, f is the vortex shedding frequency, and U_∞ is the approach velocity. Figure 113 shows the vortices generated as the flow swept around the cylinder, which is known as vortex shedding [White, 1991]. For a long cylinder, St can be approximated as [Wikipedia, 2010b]

$$St = A\left(1 - \frac{B}{Re}\right), \qquad (183)$$

for $250 < Re < 2\times10^5$, which covers the regime from transition turbulence to the subcritical regime. The Wikipedia article suggests A = 0.198 and B = 19.7. However, a better data fit for the data of Ribner and Etkin [Ribner and Etkin, 1958] was found by setting A = 0.21 for $250 \leq Re \leq 20{,}000$, while B remained unchanged, as shown in 114. It is noteworthy that this fit also covers the low Re laminar region quite well, which is approximated by Williamson as [Williamson, 1989]

$$St = \frac{A}{Re} + B + CRe, \qquad (184)$$

where A=-5.1064, B=0.2175, and C=0. Note that the streamline that is normal to the cylinder eventually impacts the cylinder wall, and because the wall is rigid, the fluid velocity is zero. The impact point is called the stagnation point [White, 1991],

$$P_S - P_\infty = \frac{1}{2}\rho U_\infty^2,$$ (185)

where P_S and P_∞ are the stagnation pressure and pressure far away from the cylinder, respectively. The fluid density is ρ.

Because the pressure fluctuates with time, a Reynolds average with a 0.5 s time filter was used for the calculations. The calculated (P_S - P_∞) are shown in Table 8, while the computed St vs. Re are shown in Figure 114. It is noteworthy that the Fuego results and theory pressure were within 0.1%, while the Fuego vortex shedding frequency was within 5% of the experimental data.
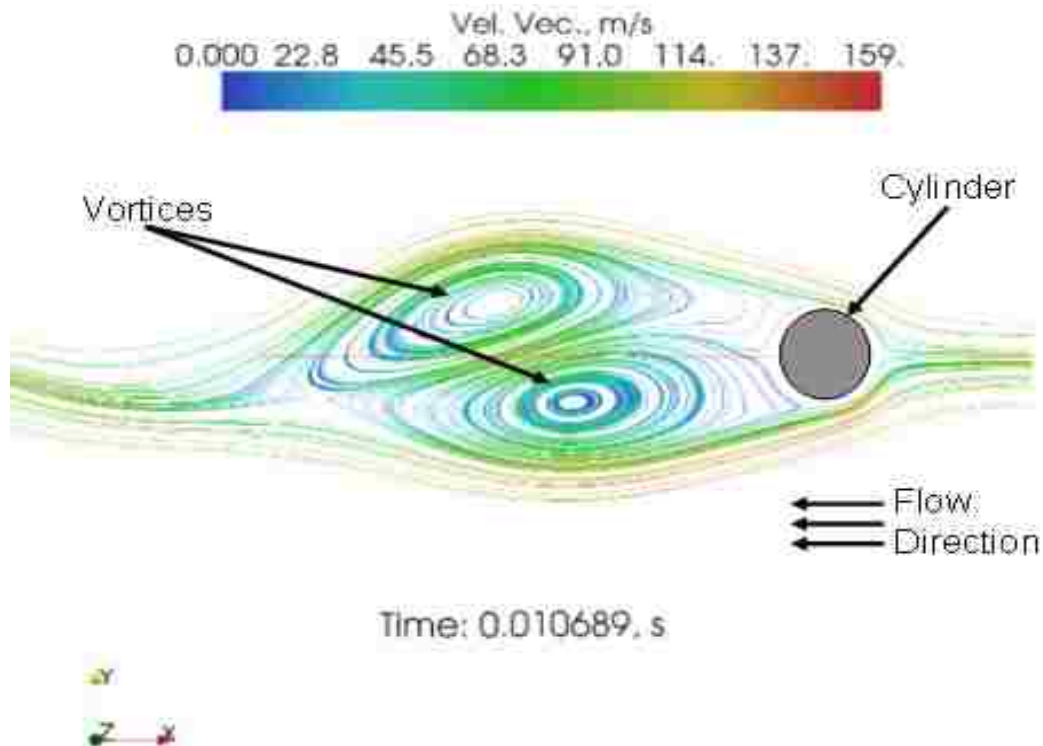
Figure 113. Vortices Generated by Flow around a Cylinder.
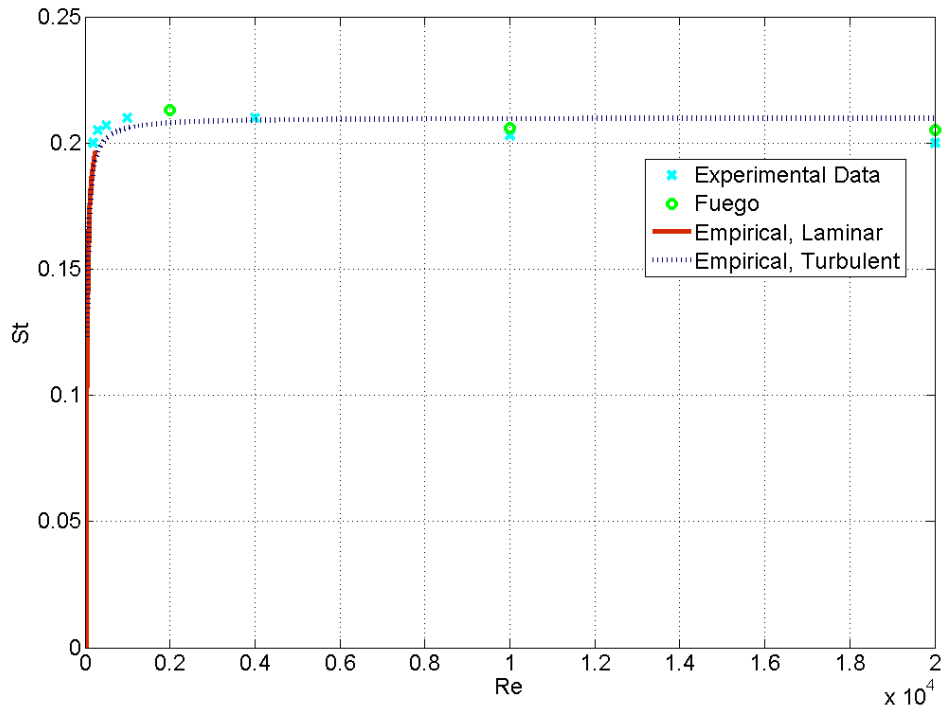
Figure 114. Strouhal Number vs. Reynolds Number.

Table 8. Fuego P_S - P_∞.

Number of Elements	P_S - P_∞, Pa (Theory=86.6)
4,000	81.2
16,000	83.5
64,000	85.3
256,000	86.1
1,000,000	86.5

5.2.6   Central Recirculation Zone (CRZ) Formation

For an incompressible jet, the azimuthal momentum is greater than or equal to the axial

momentum when S≥0.67 (θ≥45°), as indicated by Figure 50 (and also Equations 112 and

206

113). When the relative magnitude of the azimuthal momentum reaches or exceeds that of the axial momentum, the CRZ forms. Swirling jets can experience large azimuthal velocity fluctuations upstream of the CRZ, and even in its absence for a swirling jet [Menke and Gursul, 1997]. Researchers have also noted that the CRZ length is strongly dependent on axial and azimuthal velocity distribution [Dong and Lilley, 1993]. Furthermore, the superposition of the axial and azimuthal velocities over the CRZ is known to be an important element in its formation [Leibovich, 1978]. An excellent overview of CRZ formation theories and experimental data was recently compiled [Lucca-Negro and O'Doherty, 2001].

The azimuthal momentum consists of a circular motion on flat planes normal to the axial direction, while the axial velocity moves the fluid in the direction normal to the azimuthal plane. Note that the azimuthal velocity varies radially: it is zero at r=0, increases sinusoidally as r increases, peaks, and then drops off sinusoidally. On the other hand, the axial velocity peaks along the z axis and drops as a function of r in a Gaussian-like distribution. This means that the axial velocity peak (the z axis), occurs exactly where the azimuthal velocity is zero! On the other hand, as the axial velocity decays radially, the azimuthal velocity increases and peaks. The low azimuthal velocity near the z axis causes a high pressure that, when overcome by the axial velocity, results in back flow, and the subsequent formation of the CRZ.

By using parallel visualization with Paraview, one is able to obtain some good snapshots (anatomy) of a CRZ. For example, the CRZ region (the back flow region) has a negative pressure, as shown in Figure 115. The upper portion of the figure corresponds to the CRZ, and is reminiscent of a backbone structure. The positive pressure is shown in

Figure 116, which corresponds to the remainder of the swirling jet (non-CRZ portion).

Figure 117 shows an overlay of the negative and positive pressure domains within the

swirling jet. Figure 118 shows the negative axial velocity, whose upper part is the CRZ.

Again, note the backbone type of structure shown in the upper part of the figure. The

non-CRZ (positive) axial velocity is shown in Figure 119. In order to visualize the

azimuthal velocity in the interior, a meridional cut was made, as shown in Figure 120.

Upon a close-up inspection, one can *see* the hollowed-out CRZ domain residing along the

z axis (which had a negative velocity, and was therefore excluded for visualization

purposes).
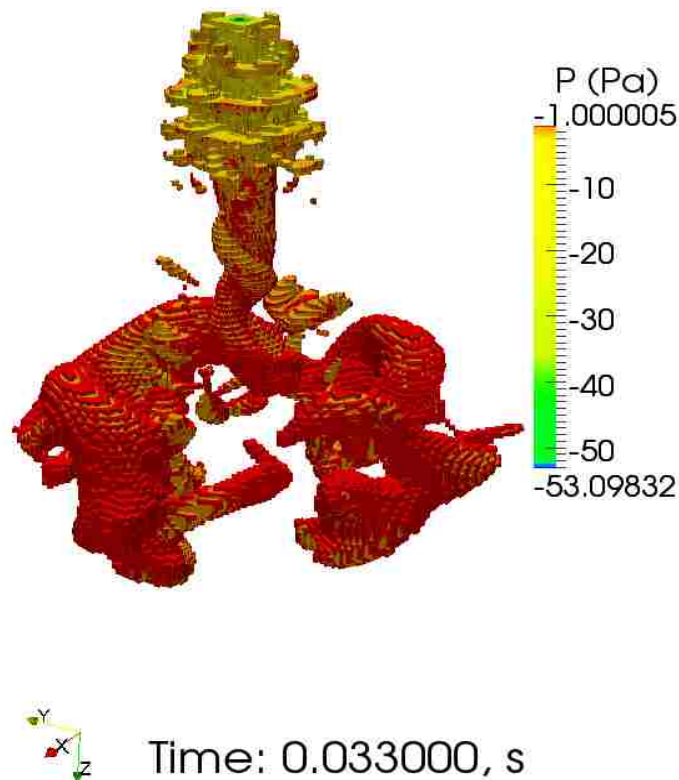
Figure 115. CRZ Domain with Negative Pressure.
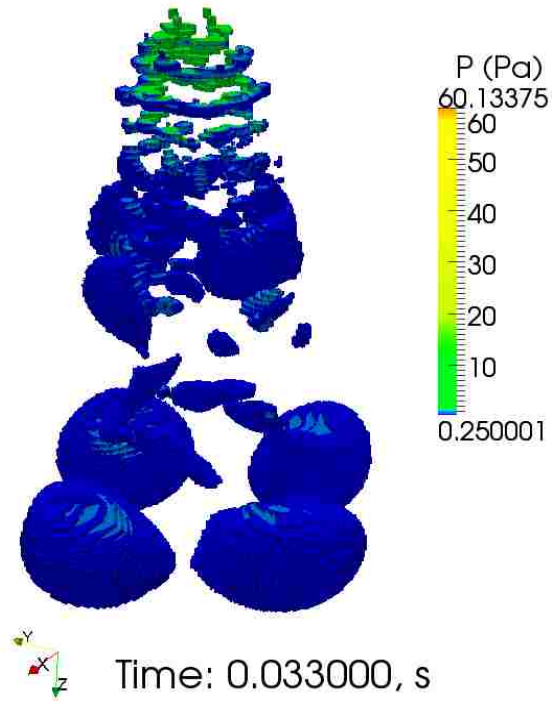
Figure 116. CRZ Domain with Positive Pressure.
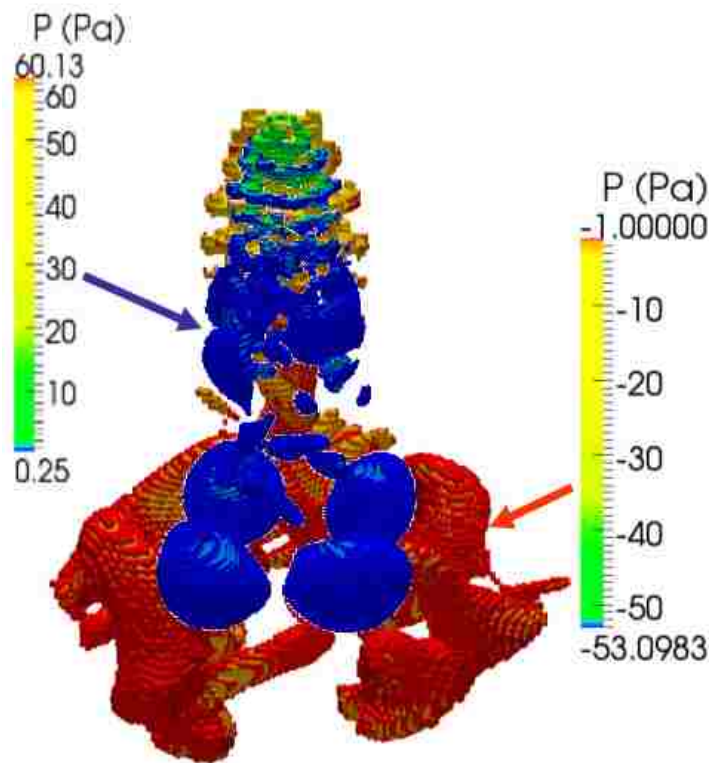
Figure 117. CRZ Domain with Overlay of Positive and Negative Pressure.
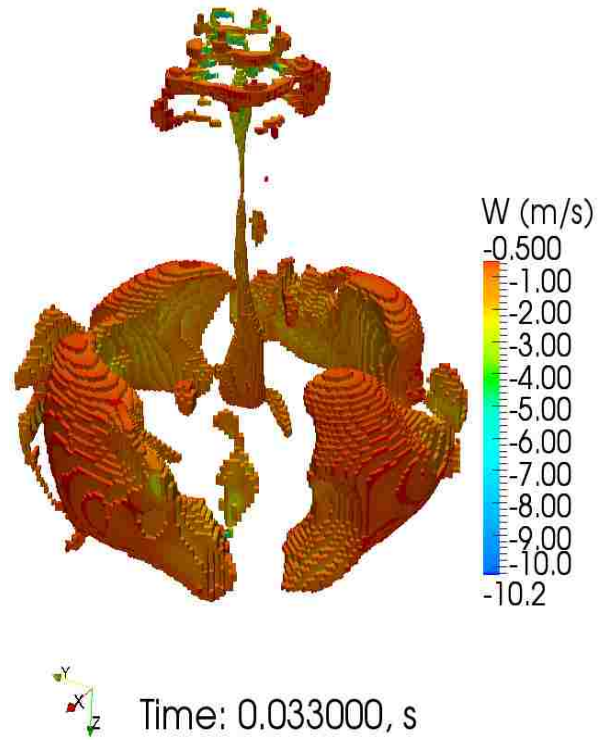
Figure 118. CRZ Domain with Negative Axial Velocity.
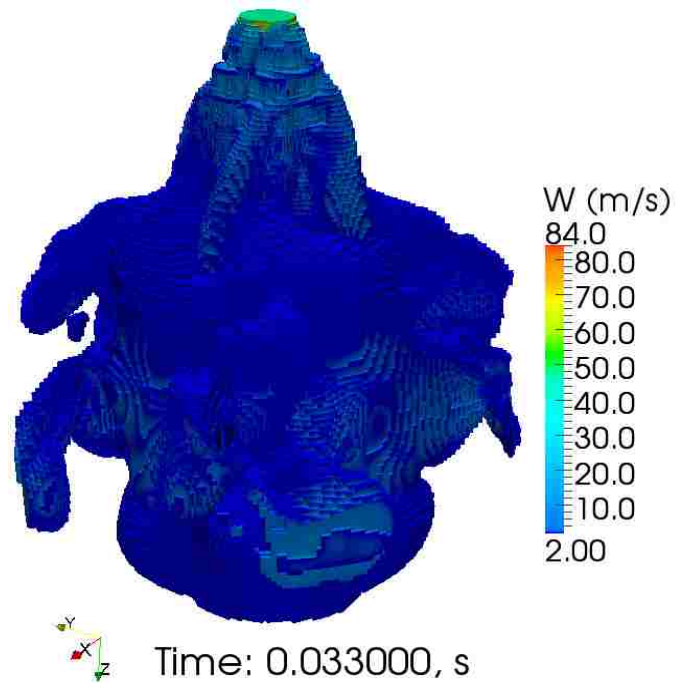
Figure 119. CRZ Domain with Positive Axial Velocity.
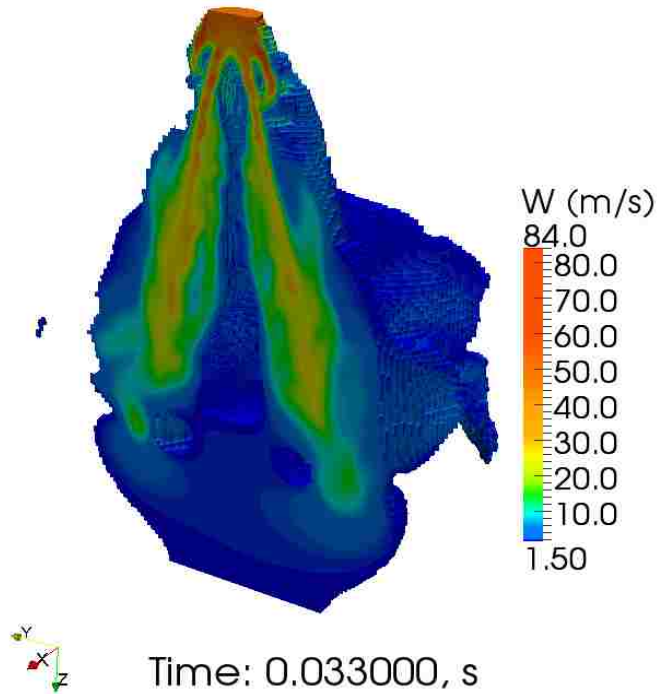
Figure 120. CRZ Domain with Positive Axial Velocity—Meridional Cut.

Various experiments [Mathur and MacCallum, 1967; Chigier and Chervinsky, 1967; Feyedelem and Sarpkaya, 1997; Billant *et al.* 1998] confirm that the CRZ first forms when S≥0.67 (θ≥45°) for hubless swirlers.

A set of Fuego calculations was conducted with a cylindrical domain that had a swirl BC. The calculations showed that the CRZ first formed when θ=45°. Figures 121 and 122 show the axial and azimuthal velocity, respectively, for S=0.56 (θ=40º) and S=0.67 (θ=45º), while Figure 123 shows the axial velocity for weak to moderate S. It is interesting to note that a set of Fuego calculations were also conducted for θ=40 through 44º, in increments of 1º, to see when a stable CRZ would first appear. Here, "stable" refers to a CRZ that forms, and does not disperse as the flow becomes fully developed. For example, for θ=40 through 43º, no CRZ formed. However, for θ= 44º, a CRZ formed

211

initially, but was pushed away in the axial direction while its length steadily decreased. This occurred as the flow became fully developed. *Thus, a "stable" CRZ was not formed in the calculations unless S≥0.67 (θ≥45°).*
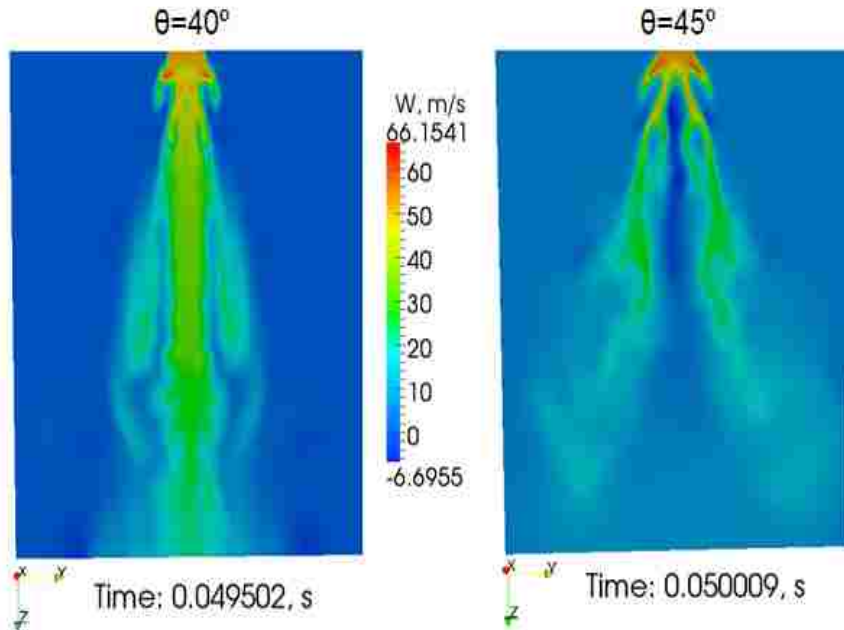
Figure 121. Axial Velocity for Single Jet with S=0.56 (θ=40º) and S=0.67 (θ=45º).
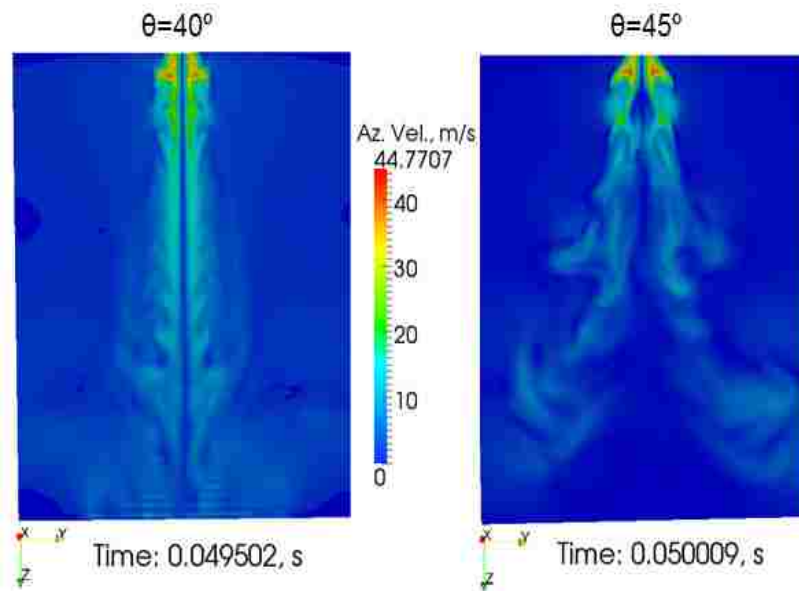
Figure 122. Azimuthal Velocity for Single Jet with S=0.56 (θ=40º) and S=0.67 (θ=45º).
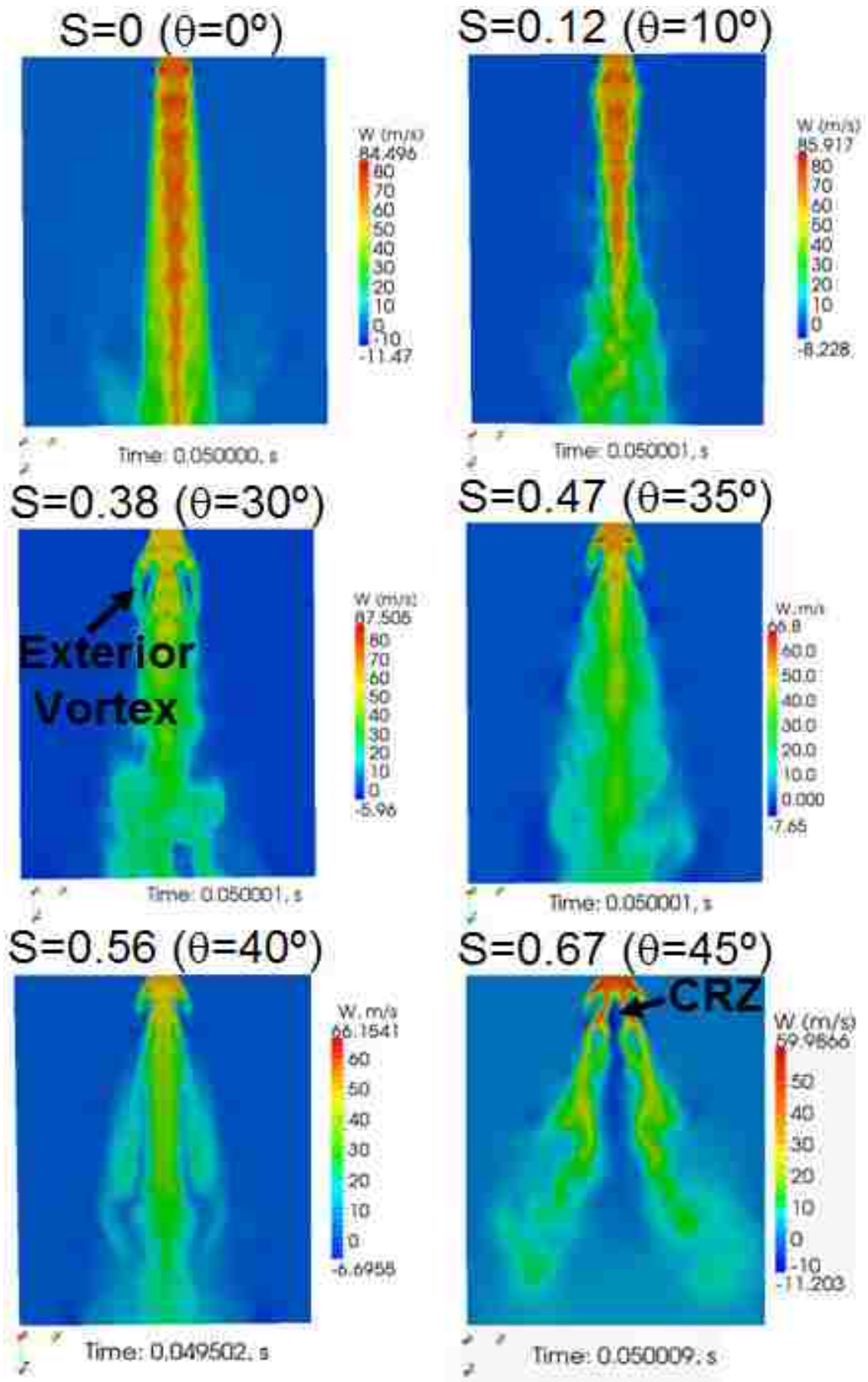
Figure 123. Axial Velocity for Weak to Moderate S.

213

5.2.7   Staggered Array of Tubes in Crossflow

As a final V&V calculation, a staggered array of tubes in crossflow was simulated. From Figure 33, it is evident that the 78 support posts in the ½-symmetry model form an array of staggered vertical tubes arranged in a triangular grid. Considerable crossflow occurs within the LP [McEligot and McCreery, 2004], so this calculation considered a crossflow boundary with no jets. This allows a comparison of the velocity distributions found in the literature [Liang and Papadakis, 2007]. Further comparisons can also be made for the pressure drops, if desired [Grimison, 1937; Blevins, 1992].

For the LP, P/D=1.7, which is about 30% larger than for PWRs [Todreas and Kazimi, 1990]. However, the ratio is sufficiently small that the support posts are close enough to impact the flow field of adjacent support posts (for an equilateral triangle array with $P/D > 2\sqrt{3}$, a single tube approximation is valid) [Blevins, 1992].

The model is shown in Figure 124. Its geometry was based to a large extent on the recent work of Liang and Papadakis [Liang and Papadakis, 2007]. The model consisted of a 3D rectangular cuboid with 78,111 hex elements for the coarse mesh (the fine mesh had 527,475 hex elements). D=0.01 m. The LHS lateral boundary was inflow at 0.62 m/s, while the RHS lateral side was open. The other two lateral surfaces were modeled as walls, while the top and bottom surfaces used symmetry BCs. The model consisted of six rows in a triangular array, for a total of 12 tubes. CFL was 1.0, and included the dynamic Smagorinsky turbulence model. The working fluid, water at 300 K, had ν= 9.83×10^{-7} m^2/s and ρ=997.4 kg/m^3. Blevins suggests that Re be calculated with the velocity through the minimum gap between the tubes (~0.83 m/s). Thus, the approach Re and gap Re were 6,307 and 8,444, respectively.

Figure 125 (top) shows the streamline flow distribution across the staggered tubes. As the flow went around the tubes, four distinct, primary, high-velocity "channels" formed (see the yellow-blue-green streamlines). By contrast, the RHS of the cylinders had low-velocity regions that consisted of large blue CVPs that were on the order of D to 2D. Thus, the highest velocity occurred as the constricted gas proceeded through the most direct paths between the tubes. It is noteworthy that the first three rows (LHS of the domain) experienced minimal oscillation, while the last three rows experienced much oscillation due to vortex shedding. Figure 125 (LHS and RHS) shows the velocity vectors from Liang and Papadakis, and Fuego, respectively. Note that although both figures used different colors to represent the velocity magnitudes, their values at comparable regions are typically within ±10%.
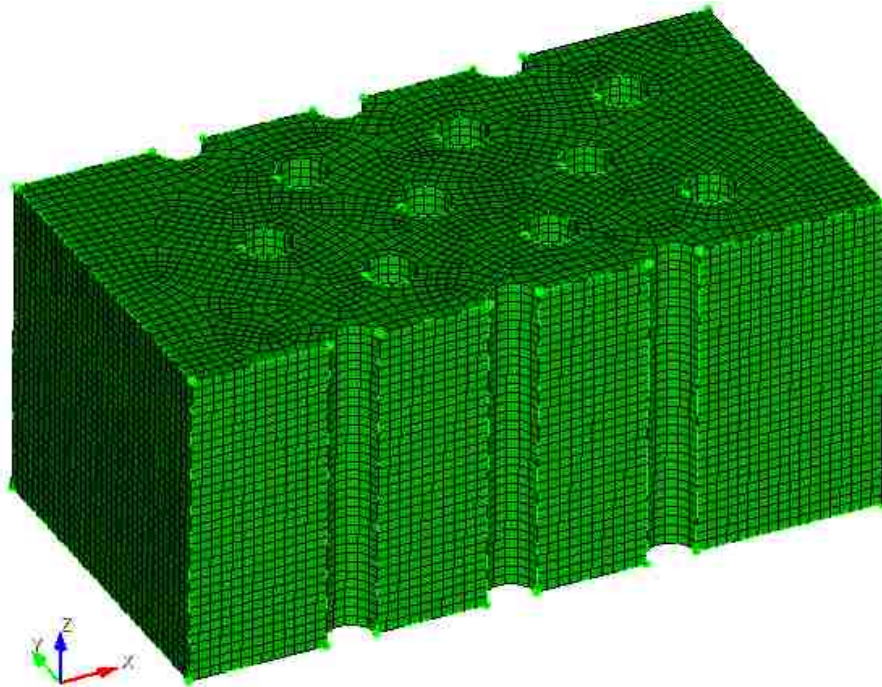
Figure 124. Staggered Array of Tubes Model.
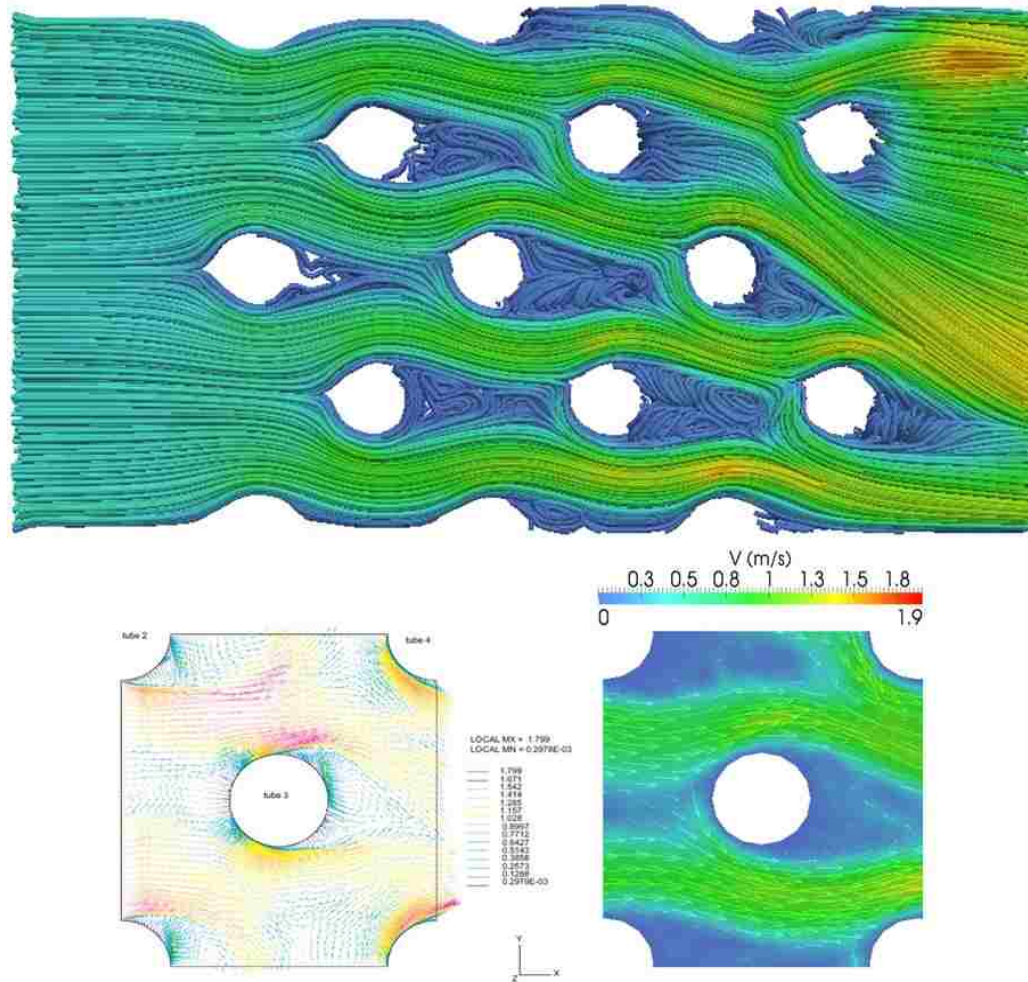
Figure 125. Flow Distribution for the Staggered Array of Tubes. Top: Fuego Velocity Streamlines. LHS: Liang and Papadakis Velocity. RHS: Fuego Velocity.

5.3　　　LP Calculations

The final set of Fuego and Fuego-Calore calculations are discussed in detail in this section. First, a basecase calculation was conducted, and thereafter a set of calculations were completed and analyzed to address issues such the impact of S on mixing and heat transfer, the impact of swirl rotation direction, the effect of multiphysics, and the behavior of the advanced swirling jet models.

216

5.3.1   Basecase Calculation

The Fuego-Calore VHTR LP model (Figure 37) used in the simulations invoked the

dynamic Smagorinsky LES turbulence model, and was run on the Thunderbird massively

parallel supercomputer at SNL.

The initial time step used was 0.01 μs, and the simulation transient time varied from

100 ms to several seconds. The time step was calculated by setting the maximum CFL to

1.0, resulting in a time step of 1.2×10^{-5} s.

The computational meshes of 1 to 12 million hexahedral elements used in the present

calculations provided sufficient spatial discretization. They were generated using the

CUBIT code from geometry developed with Pro/ENGINEER [Pro, 2009].

Note that the geometry, and the thermal and flow BCs used for this research were

based on reasonable values, because no final, official VHTR design has been published in

the literature as of Winter 2010 [Johnson and Schultz, 2010; Kinsey, 2010; ORNL, 2010;

Wikipedia, 2010a; World Nuclear News, 2010]. Nevertheless, the values used herein are

consistent with those found in the literature. Thus, the results can be easily extrapolated

to those of the final design.

The basecase calculation employed conventional jets, so θ=0º (S=0). 135 helium jets

were at 1,273 K, and three jets were 200 K hotter. The hotter jets were placed at strategic

locations within the LP to gauge the impact of hot channels (shown with red circles in

Figure 130).

Using the helicoid swirling jet methodology, the jets can be modeled as either

conventional or swirling jet BCs. That is, S can easily be changed to the desired

magnitude in order to observe its impact on heat transfer and gas mixing in the LP. The

results for the basecase calculation were compared with calculations with jets at S>0 in order to gauge the effectiveness of swirl (*see* Section 5.3.2).

The calculational meshes were generated using the CUBIT code [CUBIT, 2009] from the geometry developed with Pro/ENGINEER [Pro, 2009]. The temperature-dependent physical and thermal properties for the helium were calculated using a CANTERA XML input file that was based on the Chapman-Enskog formulation [Bird, Steward, and Lightfoot, 2007].

The results of the calculation are shown in Figures 126 through 132. Figure 126 shows the calculated velocity streamlines. The figure also shows a significant acceleration of the fluid as it travels through the LP, and approaches the exit. This acceleration is due to conservation of mass: more and more gas from the jets enters the limited flow area of the LP chamber. The small streamlines at the top are the 138 conventional jets. Because they posses no swirl, the streamlines basically show as cylindrical bundles that flow in the +z direction. However, due to crossflow, the jets begin to form classical parabolic trajectories, as discussed in Sections 5.2.3 and 5.2.4. Figure 127 shows the velocity streamlines at the opposite end of the LP exit (the RHS). It is clear that because of the lower crossflow, the jets were able to penetrate much deeper. *By the same token, having a hot spot in this part of the LP will result in hotter bottom plate temperature.* Figure 128 shows a top view of the net velocity streamlines emanating at the RHS of the LP. Once again it can be seen that the jets on the RHS follow a very selective path—they tend to impinge on the bottom plate and thereafter flow across the lower parts of the LP, near the bottom plate. That the paths are quite narrow is shown in Figure 129, which shows the net velocity streamlines for two jets at

the RHS of the LP. By contrast, the central and LHS jets do not penetrate the LP

chamber as much, as shown in Section 5.3.4.
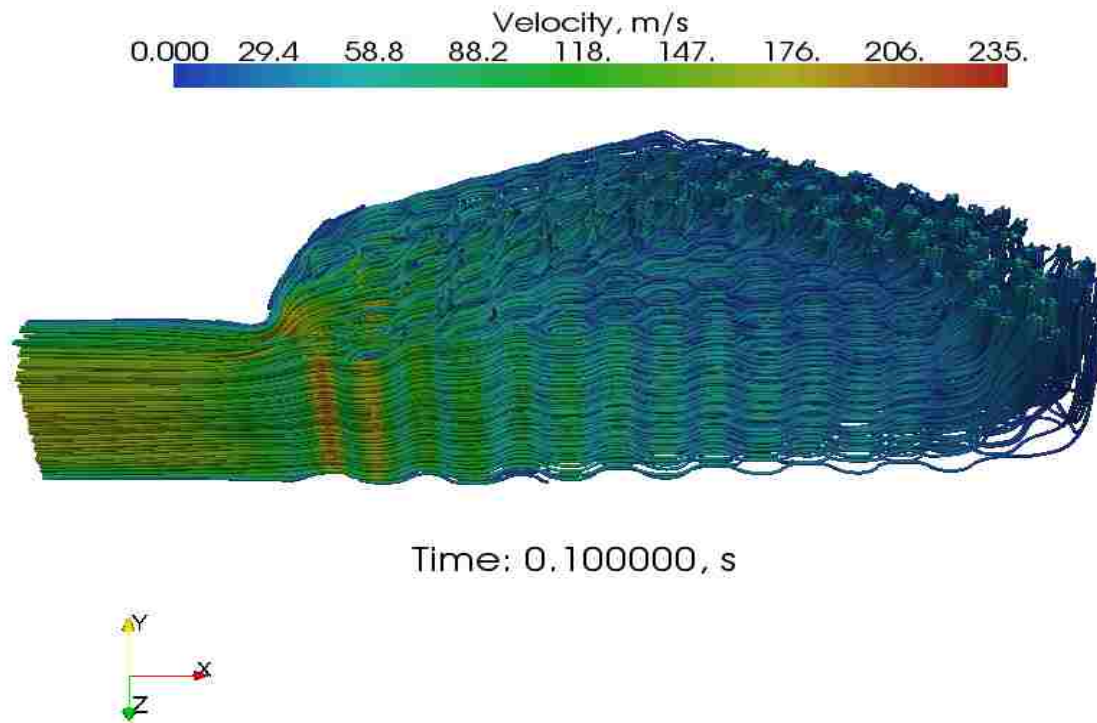
Figure 126. LP Net Velocity Streamlines.
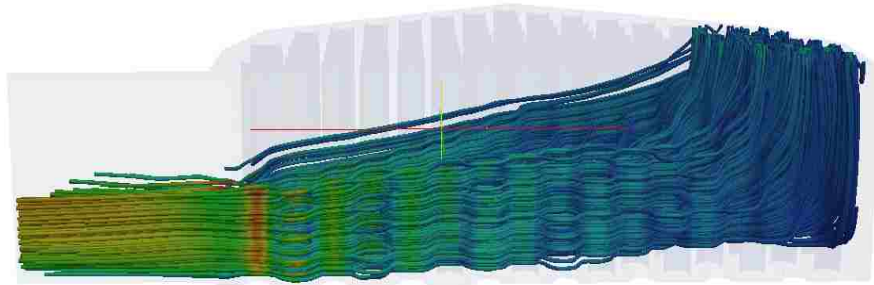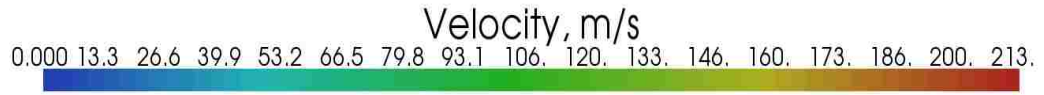
Figure 127. Net Velocity Streamlines at the Opposite End of the LP Exit—Side View.
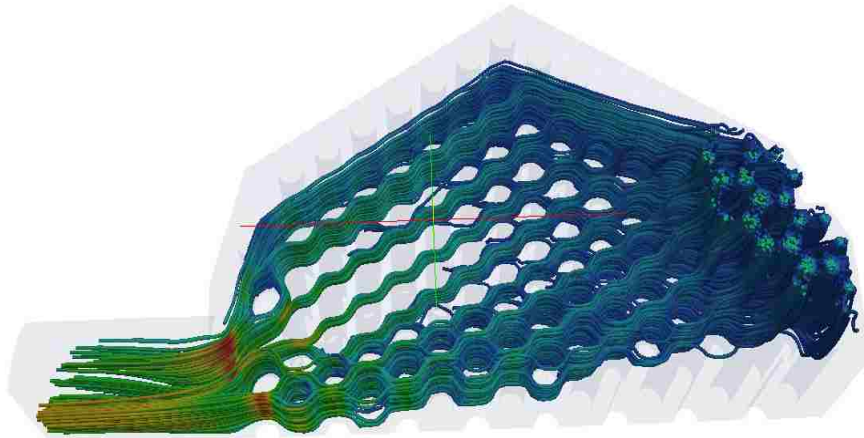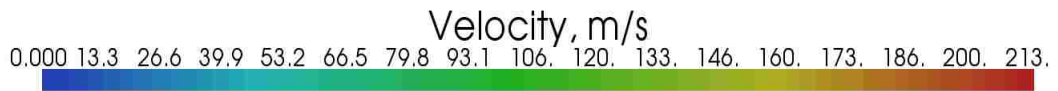
Figure 128. Net Velocity Streamlines Emanating from the Opposite End of the LP Exit—Top View.
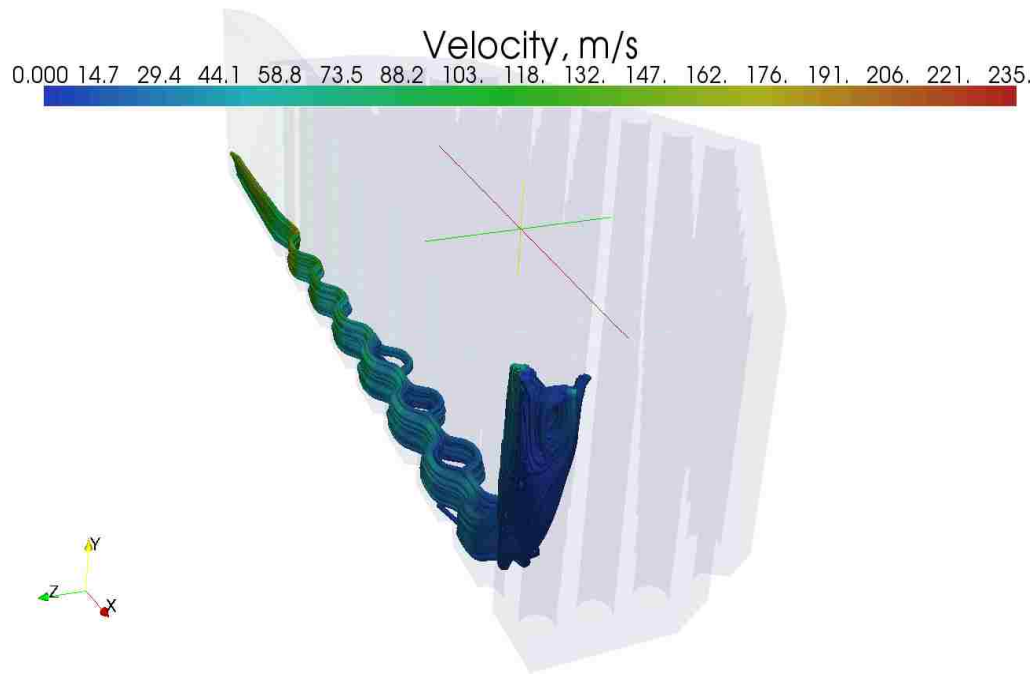
Figure 129. Net Velocity Streamlines for Two Jets at the Opposite End of the LP Exit.

The velocity streamlines were colored with fluid temperature in Figure 130, where the three hot jets are readily observable. Consistent with the tight flow paths followed by the jets, the hot channel temperature also follows a narrow path, with limited mixing. Figure 131 shows a zoom of the velocity streamlines that were colored with fluid temperature for a single hot channel. Its initial temperature was 1,473 K, but had dropped to about 1,325 by the time it impinged on the lower plate. Figure 132 shows the velocity streamlines colored by fluid temperature for the hot channel jet. The upper, circular region was at 1,473 K, and was surrounded by streamlines at various approach angles that were formed as cooler, surrounding gas was entrained by the jet.
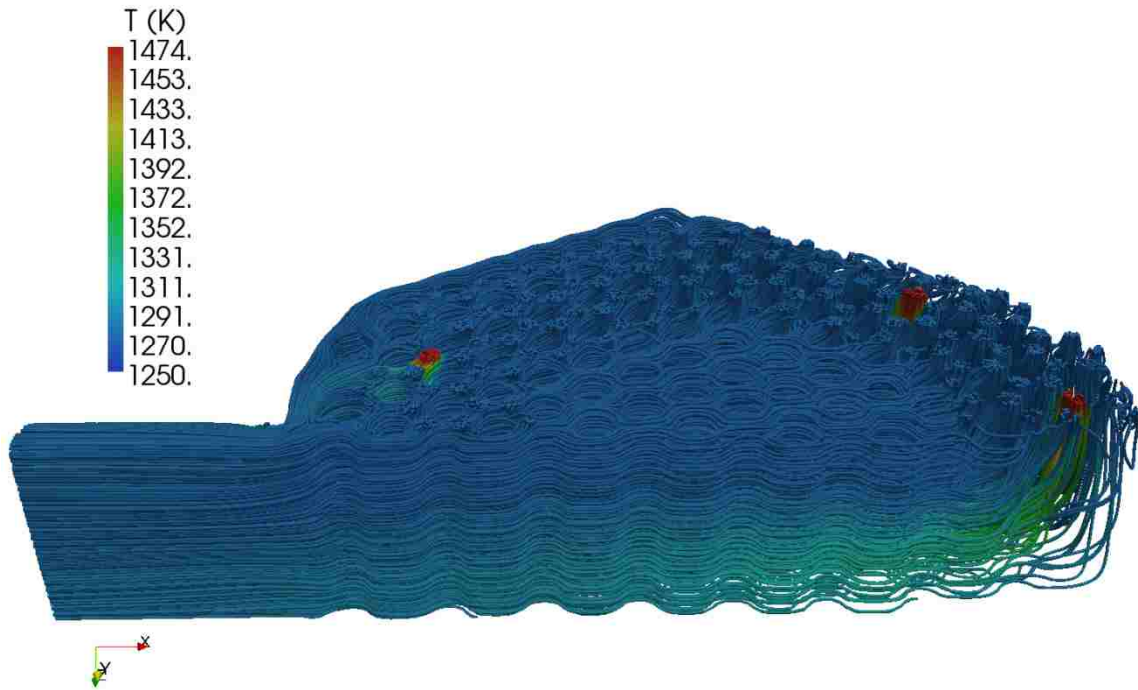
Figure 130. Velocity Streamlines Colored by Fluid Temperature—Hot Channel Locations.
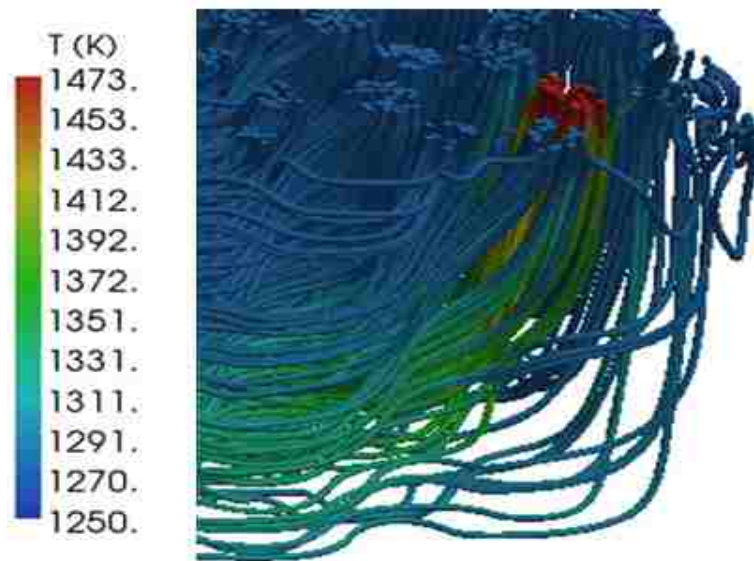
Figure 131. Zoom of Velocity Streamlines Colored by Fluid Temperature for a Single Hot Channel Surrounded by Channels with Average Fluid Temperature.
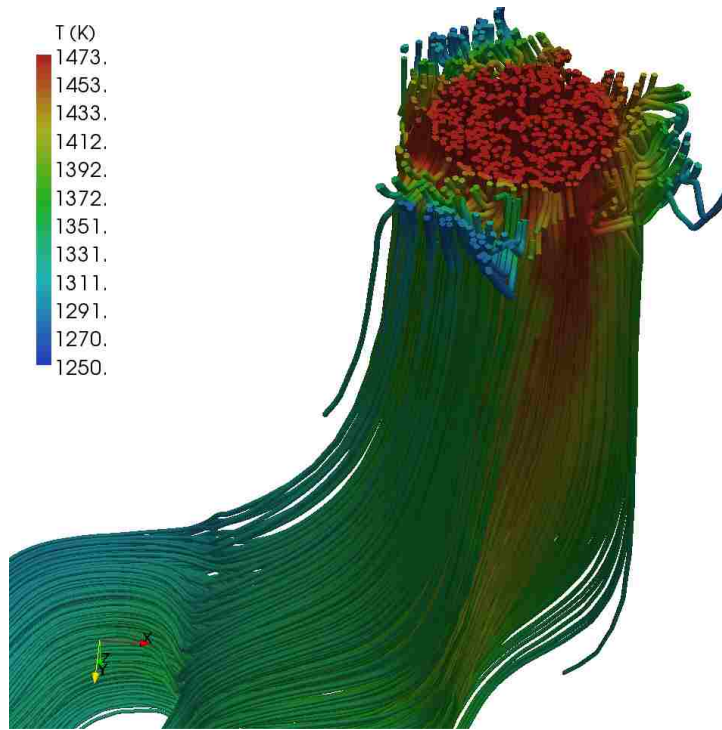
Figure 132. Velocity Streamlines Colored by Fluid Temperature for a Single Hot Channel.

5.3.2 Impact of S on LP Mixing and Heat Transfer

Researchers have shown that the CRZ formation impacts the heat transfer [Uddin *et al*., 2009]. To investigate that effect in the LP, flow field calculations were performed to investigate the effect of S on mixing, as well as enhancements to turbulence and heat transfer, and the impact of the CRZ. Calculations were performed for S=0 (i.e., θ=0º, conventional jet) and for swirling jets for which S=0.38, 0.67, 1.15, and 2.49 (i.e., θ=30, 45, 60, and 75º, respectively). The five calculation sets were conducted with the same helium temperatures as the basecase (i.e., three channels were hotter than the other 135 channels) (*see* Section 5.3.1). The locations for the hot channels are shown in Figure 133. The streamlines for the velocity distributions for S=0.67 for the front and back sides of the LP are shown in Figures 134 and 135, respectively. Unlike Figure 130, Figure 134

223

shows that the jet streamlines now have swirl, and therefore achieve more mixing in the

upper parts of the LP. Figure 136 shows the velocity domain for a slice taken at half the

LP height for S=0.67. Once again, the flow acceleration towards the LP exit is evident.

Figure 137 shows volume rendering of the temperature distribution for S=0.67. *Because*

of the large variation in crossflow across the LP, it is clear that hot jet location is a

significant factor that determines if it can adversely heat-up the lower plate; this is the

case because the crossflow Re varies by as much as 70 times, depending on its location

within the LP.
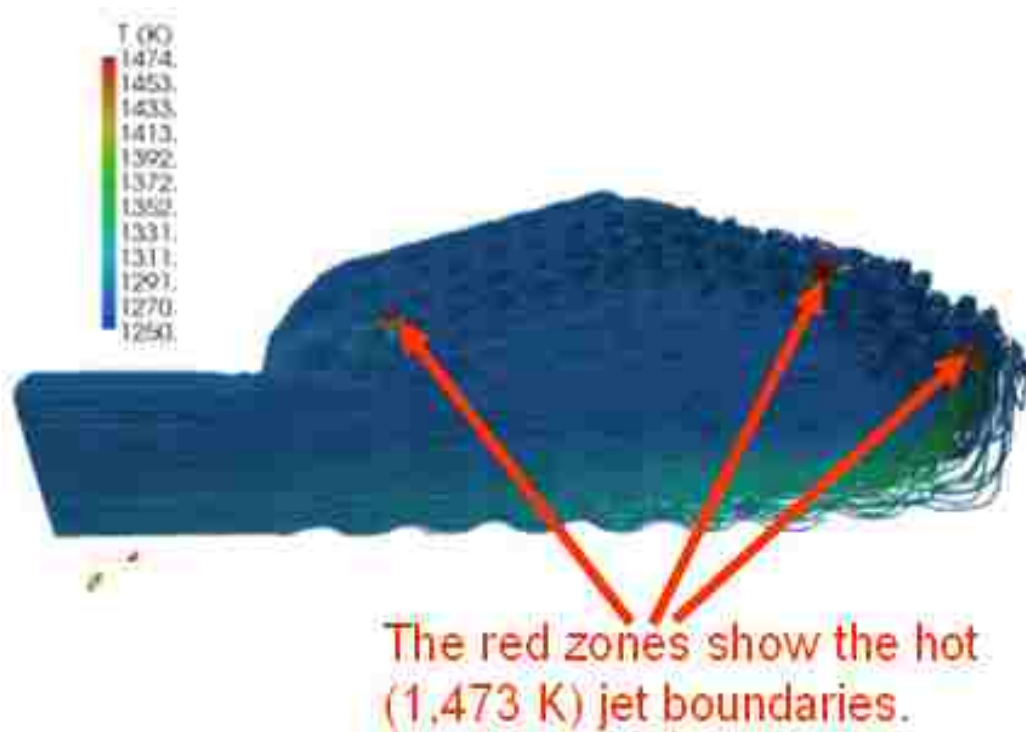
Figure 133. Location of the Hot Channels in the LP Model.
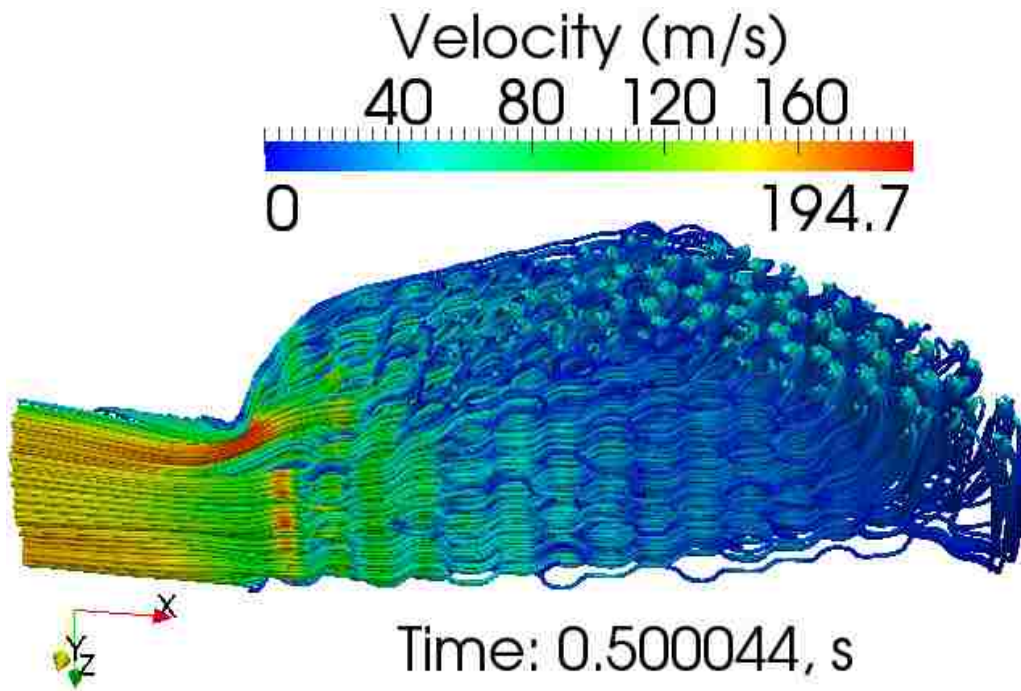
Figure 134. Velocity Distribution for S=0.67.
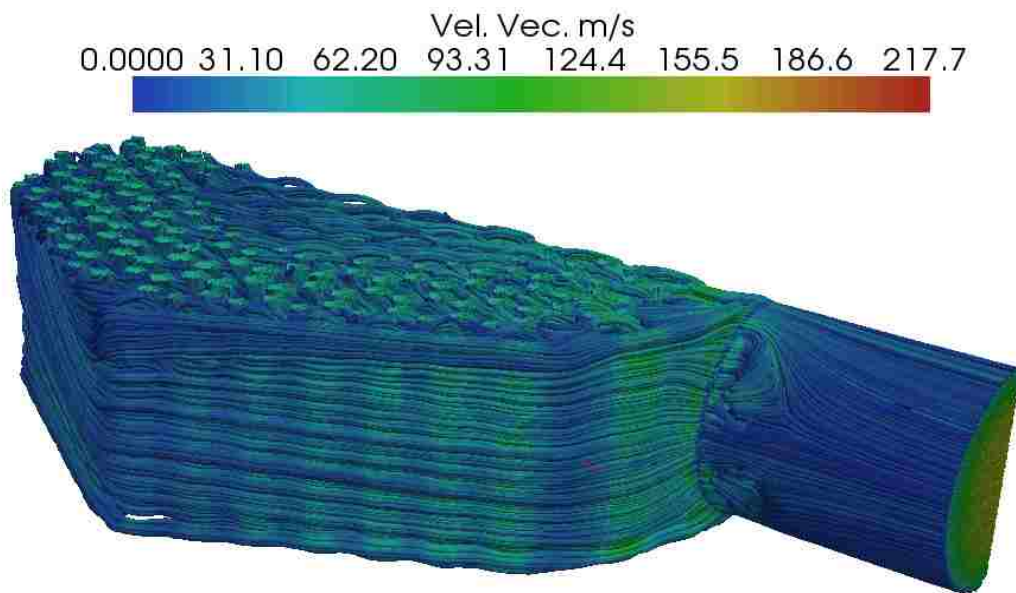
Figure 135. Velocity Streamlines for S=0.67—Back View.
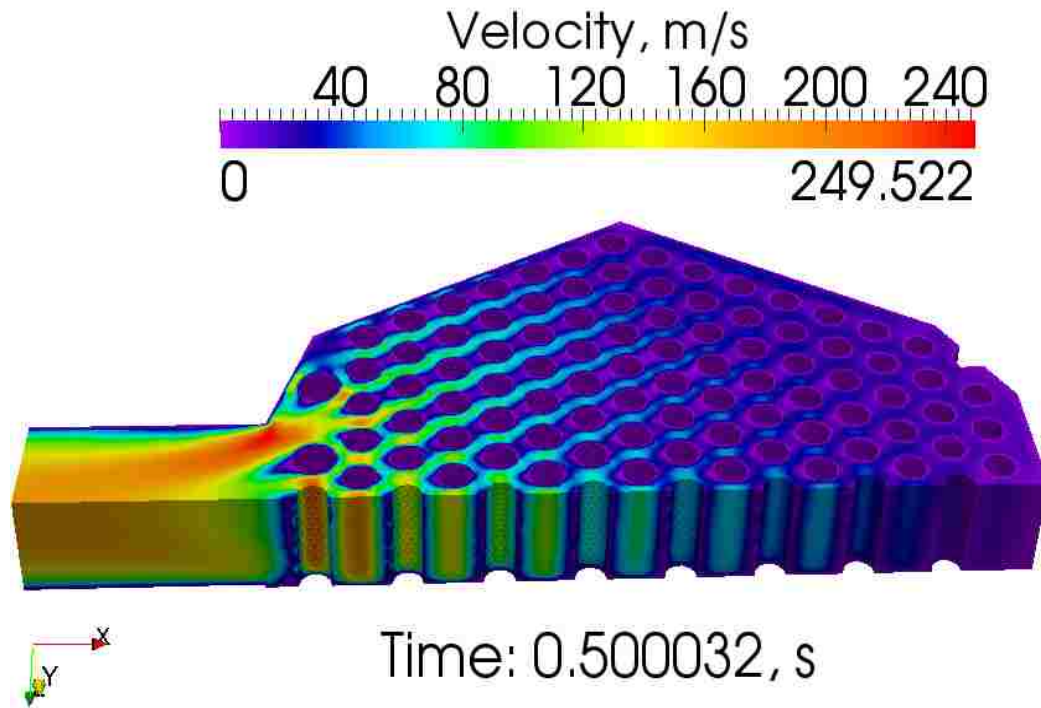
Figure 136. Velocity Domain for a Slice Taken at Half LP Height for S=0.67.
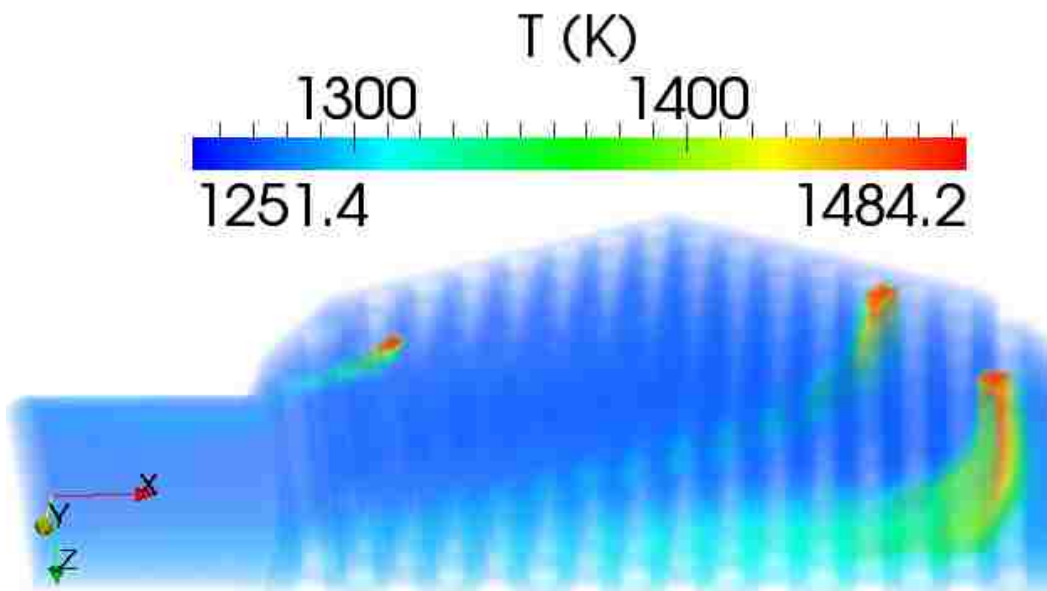
Figure 137. Volume Rendering of Temperature Distribution for S=0.67.

Figure 138 shows the temperature contours for the three hot channels for S=0.67. It is clear that most of the energy imparted by the hot channels remained in confined sections of the LP. Figures 139 and 140 show the pressure difference domain for a slice taken at half the LP height and a back view of the pressure difference overlayed on velocity streamlines, respectively. The figures show that the overall pressure drop in the LP was small, about 4,500 Pa, and that most of the pressure drop was concentrated near the LP exit.
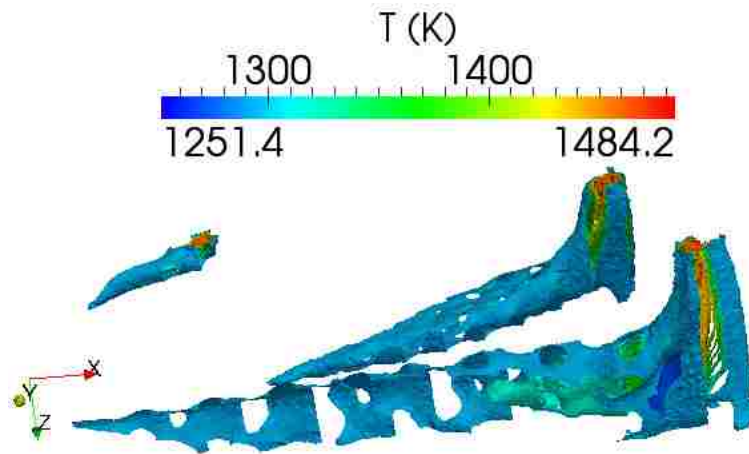
Figure 138. Temperature Contours for the Three Hot Channels for S=0.67.
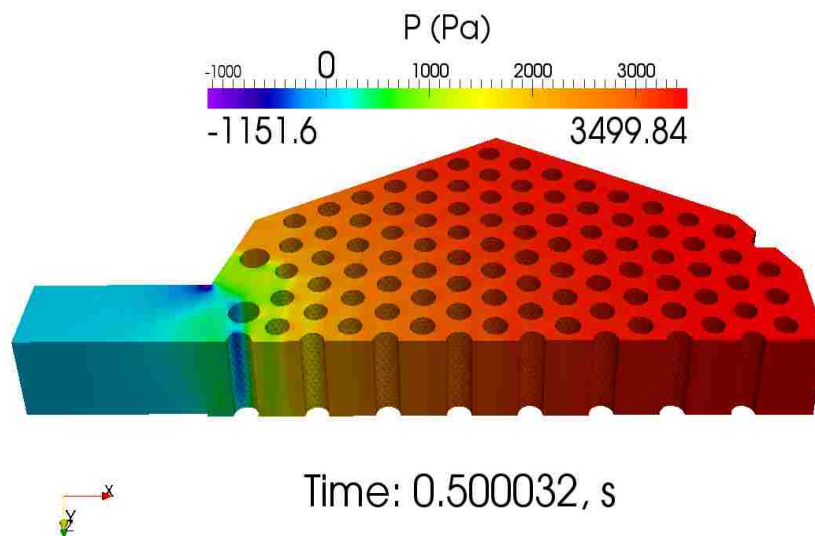
Figure 139. Pressure Difference Domain for a Slice Taken at Half LP Height.
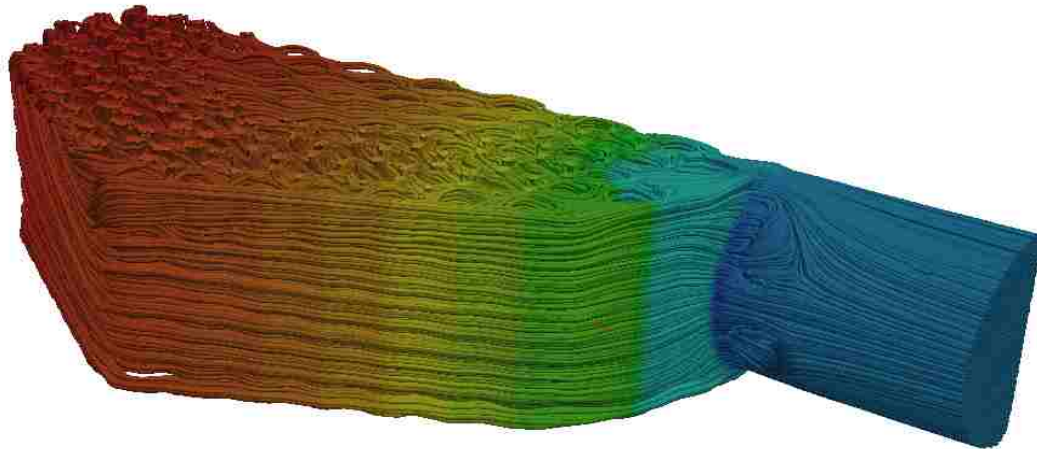
Figure 140. Pressure Difference Overlayed on Velocity Streamlines—Back View.

Figure 141 presents the cooling effect on the bottom plate when using conventional jets (top) and swirling jets (bottom). Note that for S=0, the flow field of the hottest helium conventional jets eventually reached the bottom plate at a slightly lower temperature of ~1,325 K. However, with the swirling jets at S=2.49, the gas thoroughly mixed, decreasing the temperature of the helium reaching the bottom plate by an additional 52 K, that is, to ~1,273 K. Furthermore, the spatial distribution in the bottom plate was not only lower but also more uniform, as shown by the arrows in the figure.
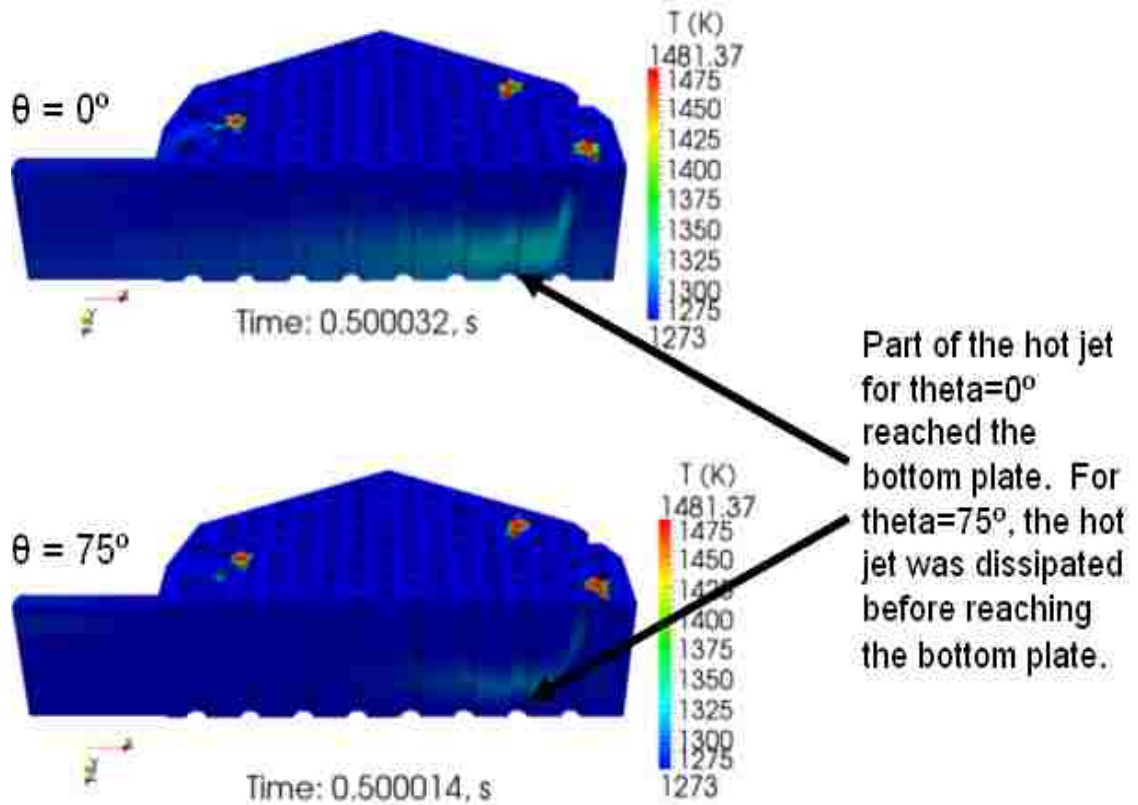
Figure 141. Comparison of Fluid Temperature for Conventional vs. Swirling Jets. Top: Conventional ($\theta=0^\circ$, S=0). Bottom: Swirling ($\theta=75^\circ$, S=2.49).

To quantify the effect of S on heat transfer at the bottom plate in the VHTR LP, the hexahedral element cell-averaged temperatures of a planar slice at the bottom plate (the opposite end of the jet exits) were calculated and grouped according to a linear temperature distribution ("bins"). The calculated temperature bins are shown in Figure 142. The figure shows that as S increased, the number of finite elements in the bottom plate with cooler temperature increased, as evidenced by the relative magnitudes of the temperature bins (see arrow on LHS of Figure 142). In addition, there were fewer hotter finite elements (as shown by the arrow pointing downward, on the RHS of Figure 142). Figure 143 shows the effect of S on heat transfer enhancement at the bottom plate by

showing the relative number of elements in bar format. In particular, S=2.49 had a larger quantity of cooler elements than the case for S=1.15, and so forth progressively until reaching S=0. Conversely, S=2.49 had fewer hotter elements than the case with S=1.15, and so forth.

In order to quantify the net change between the calculations, the difference of number of elements n for all the temperature bins for each case i (i.e. S>0) and the basecase (S=0) were computed. In particular,

$$n(T_{bin,S>0})_i - n(T_{bin,S=0}). \tag{186}$$

The results were plotted in Figure 144. The solid blue line with circles shows the net difference in elements for each of the 40 temperature bins for the calculations with S=2.49 and S=0, and so forth. The figure shows that as S increased, the number of finite elements in the bottom plate with cooler temperature increased dramatically. For example, the case with S=2.49 had 2,573 more elements at 1,273.5 K than when S=0; the next case, S=1.15, had 889 more, while the cases for S=0.38 and 0.67 each had about 340 more such elements. Given that the planar slice consisted of 3,602 elements, the number of cooler elements as a result of the enhanced swirl field was quite significant. (Note: negative temperature-bin count for this figure means that there were more of a given bin element for the case S=0 than for S>0.)
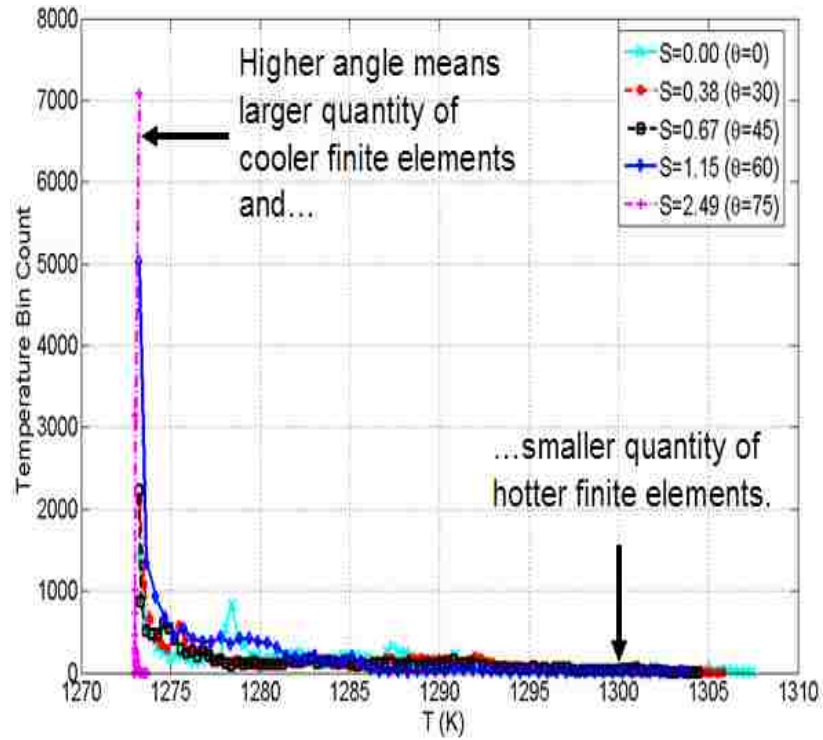
Figure 142. Effect of S on Heat Transfer Enhancement at the Bottom Plate in the LP.
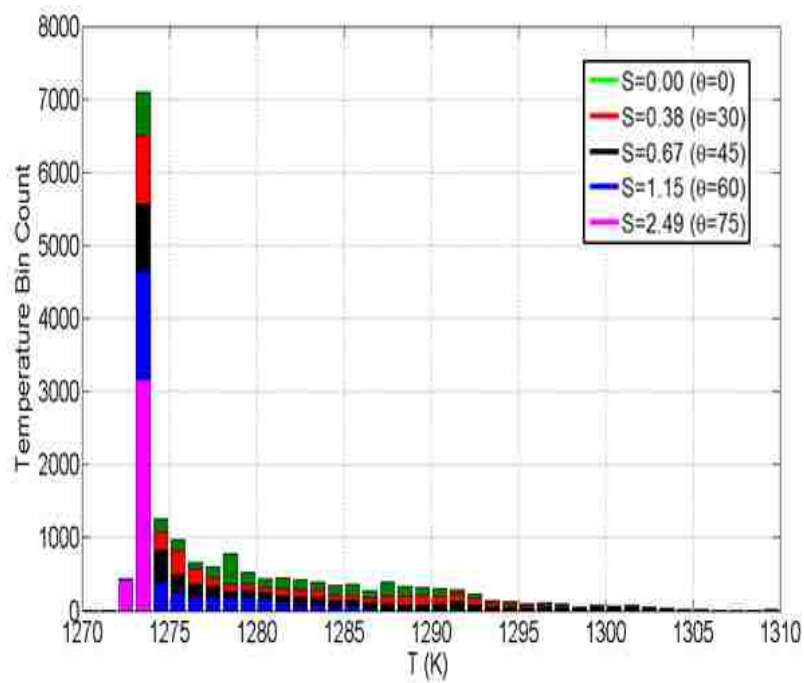
Figure 143. Effect of S on Heat Transfer Enhancement at the Bottom Plate in the LP—Stacked Bars.

231
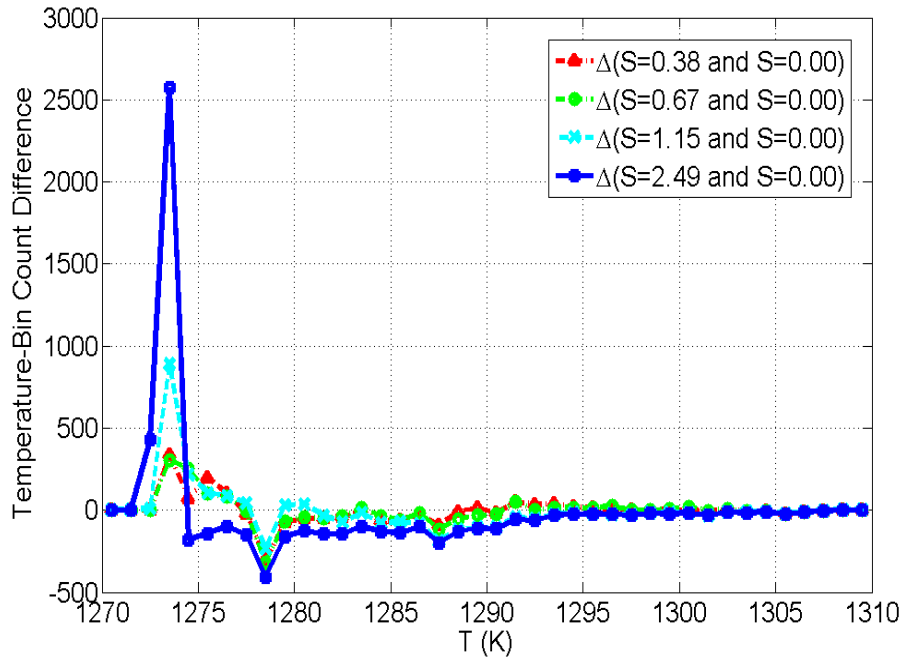
Figure 144. Effect of S on Heat Transfer Enhancement at the Bottom Plate of the LP—Net Bin Count.

The calculations showed that as S increased, the entrainment of the surrounding helium increases linearly, in agreement with the literature. In particular, the literature shows that the entrainment, as defined by the entrainment constant K_e, increases linearly as S increases [Kerr and Fraser, 1965]:

$$K_e = 0.35 + 1.4S \tag{187}$$

and [Chigier and Chervinsky, 1967]:

$$K_e = 0.32 + 0.8S. \tag{188}$$

Consequently, by the time S=2.49, all the finite elements in the temperature slice were only within 1 - 2 K of the surrounding, cooler helium jets (~1,270 K vs. ~1,325 K for the basecase), as evidenced by Figures 142 through 144.

Figure 138 shows how rapidly the swirling flow jets mixed. In particular, by the time the swirling jets had travelled approximately 60% of the distance to the bottom plate, the peak helium temperature had dropped 100 K, and by the time the jets impinged the bottom plate, the gas temperature had reached that of the surrounding, cooler gas (1,273 K). By comparison, setting $S = 0$ (i.e., conventional jets) with the same BCs resulted in the jet impinging on the bottom plate at ~1,325 K [Rodriguez and El-Genk, 2010c]. This is a good performance metric of the entrainment and mixing capacity of the swirling jets when compared with conventional jets. Furthermore, Figure 138 shows the temperature contours for the three hot channels. The figure shows that the hot gas quickly reached the colder, surrounding gas temperature within about seven jet diameters. (Note: the holes in the figure are the support post locations.)

The vorticity, $\bar{\omega}$, is defined as

$$\bar{\omega} = \bar{\nabla} \times \bar{V}, \tag{189}$$

and is a measure of a fluid's rotation. Paraview calculates vorticity once the velocity vector is calculated via its "calculator" filter and plotted using velocity streamlines. Figure 145 shows velocity streamlines colored with vorticity for S=0.0, 0.3, 0.45, and 0.75. The images show that the jets with highest S have the highest vorticity at the jet outlet. This is reasonable, since vorticity is basically the azimuthal circulation divided by the flow area; as S increases, so thus the azimuthal velocity.
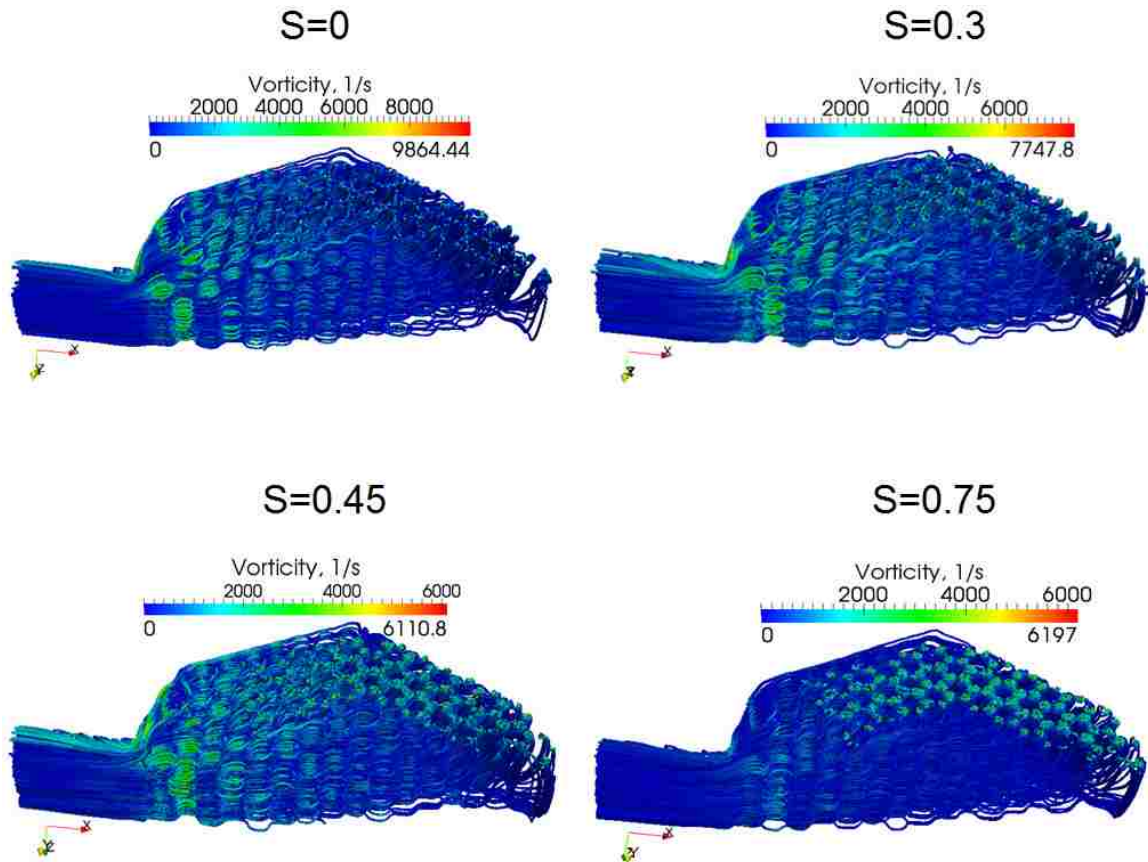
Figure 145. Streamlines Colored with Vorticity for S=0.0, 0.30, 0.45, and 0.75.

5.3.3　　　　Clockwise and Counter-Clockwise Swirling Jets

A set of calculations was performed to investigate the impact of swirl rotation direction of the hot helium exiting the LP coolant channels. A second set of calculations was performed to investigate the impact of S on the mixing and heat transfer in the LP. The results of these calculations are presented next.

Three calculations are performed to compare the effect of S and the swirling jet rotation direction: conventional jets (base-case), clockwise (CW) swirling jets, and counter-clockwise (CCW) swirling jets. The base-case calculation has 138 conventional helium jets (S=0). The second calculation involves the same number of swirling jets, but

has S=0.67 and all jets rotate in the CW direction. The third calculation is the same as the second, except that all the jets swirl in the CCW direction. For all three calculations, 135 jets are at 1,273 K, while the three hot channel jets are at 1,473 K.

The rotation direction of a helicoid is based on the sign of the u and v velocity components, as shown in Figure 146.

Case CCW about +z:
$v_x = 21.2\sin(2\pi y)$ m/s
$v_y = -21.2\sin(2\pi x)$ m/s
$v_z = 51.96$ m/s

Case CW about +z:
$v_x = -21.2\sin(2\pi y)$ m/s
$v_y = 21.2\sin(2\pi x)$ m/s
$v_z = 51.96$ m/s
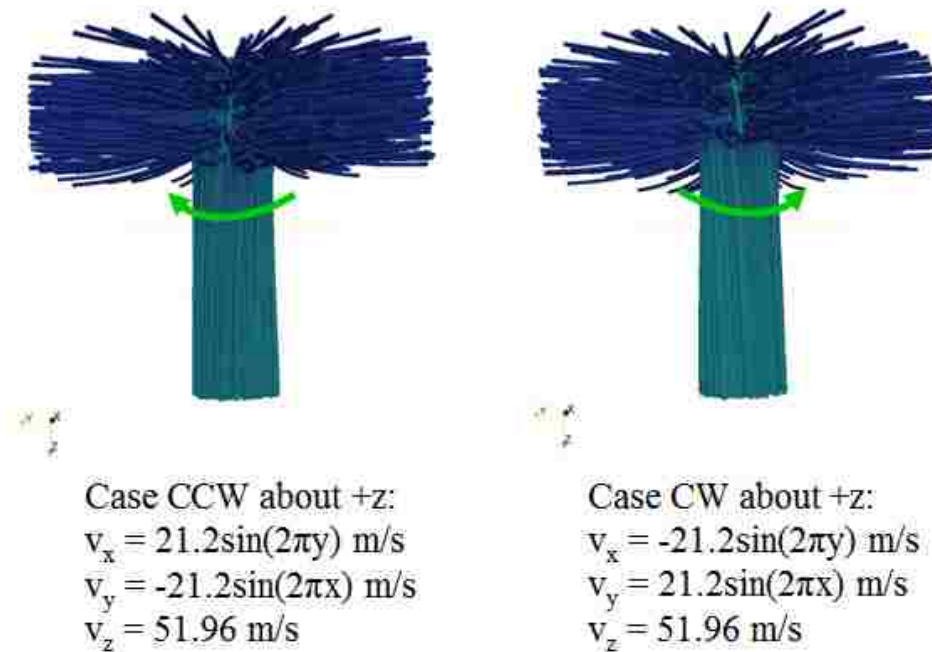
Figure 146. Determination of CCW and CW Helicoid Rotation.

For the basecase calculation, the principal velocity components for the 138 jets were:

$$(v_x, v_y, v_z)_{conv} = (0.0, 0.0, 60.0) \tag{190}$$

The velocity distribution follows the helicoidal velocity field distribution found in Equation 2. However, because the conventional jet field does not rotate, the sinusoidal terms are set to 0. The velocities were in m/s.

For the CW swirling jets calculation, the velocity components for the 138 jets were given as:

$$(v_x, v_y, v_z)_{CW} = \left[-21.2\sin(2\pi y),\ 21.2\sin(2\pi x),\ 51.96\right] \tag{191}$$

For the CCW swirling jet calculation, the velocity components for 135 jets were given as:

$$(v_x, v_y, v_z)_{CCW} = \left[21.2\sin(2\pi y),\ -21.2\sin(2\pi x),\ 51.96\right] \tag{192}$$

Thus, except for the jet boundary conditions, the three calculations used the same input deck, mass flow rate per BC, mesh, code version, and number of parallel processors.

To simplify the comparison process, Figure 147 shows the streamlines for a single jet in the basecase (conventional jet) vs. a single CCW swirling jet (the entire flow field for all 138 jets is found in Figure 150).

As shown in Figure 147, the swirling jet diameter was wider throughout the LP than the conventional jet. To gauge more explicitly this difference, the jet diameters at the midpoint of the LP in the axial direction (i.e. in the primary flow direction) were evaluated. Thus, by midpoint into the LP, the swirling jet was ~70% wider than the conventional jet. This result is consistent with the literature, which shows that swirling jet entrainment increases linearly as a function of S [Kerr and Fraser, 1965; Chigier and Chervinsky, 1967], and as entrainment increases, so does the jet diameter.

Thus, as Figure 147 shows, the advantages of the CCW swirling jets at S=0.67 over the conventional jets are: (1) the CCW swirling jet diameter was ~70% wider and therefore distributed its thermal energy over a wider volume within the LP, (2) the upper

portion of the swirling jet's flow field showed ~50% more entrainment of the surrounding helium in the LP, and (3) at half the jet height, the swirling jet was ~50 K cooler at the jet core. Because the swirling jets entrained more of the surrounding gas that subsequently mixed with the hotter gas of the jet, the thermal stratification observed with conventional jets was reduced.

A comparison of the calculated flow fields in the LP with CW and CCW jets is shown in Figure 148. As expected, the helicoid's CCW motion in the +z direction effectively opposes the general flow direction in the LP (towards the LP exit as the gas flows to the energy conversion assembly); *see* Figure 150. The green arrows in Figure 150 serve as a visual aid to help show the general flow direction of the CFD calculation. The figure also includes the streamlines of a typical single jet. For convenience, the jet streamlines were shifted to the bottom of the figure so the swirling jet's individual behavior can be more evident. A visualization of other swirling jets within the LP showed similar behavior: the opposing azimuthal flow increases turbulence and mixing, and therefore enhances heat transfer. The enhanced turbulence is manifested by an increased magnitude in the Reynolds shear stresses, which in turn is attributed to the near head-on collision of the swirling-jet azimuthal velocity with the general LP velocity vector, as shown conceptually on the RHS of Figure 150. Recall that the jet azimuthal velocity is composed of the v_x and v_y terms of the swirling jet, and that both v_x and v_y increase as S increases, as shown by Equations 110 and 111 (a conventional jet has neither a v_x nor a v_y velocity component). As shown in Figure 148, the CW swirling motion resulted in less enhancement in turbulence, mixing, and heat transfer than the CCW swirling motion.

Nevertheless, its impact was higher than conventional jets (base-case), as Figure 149 shows.
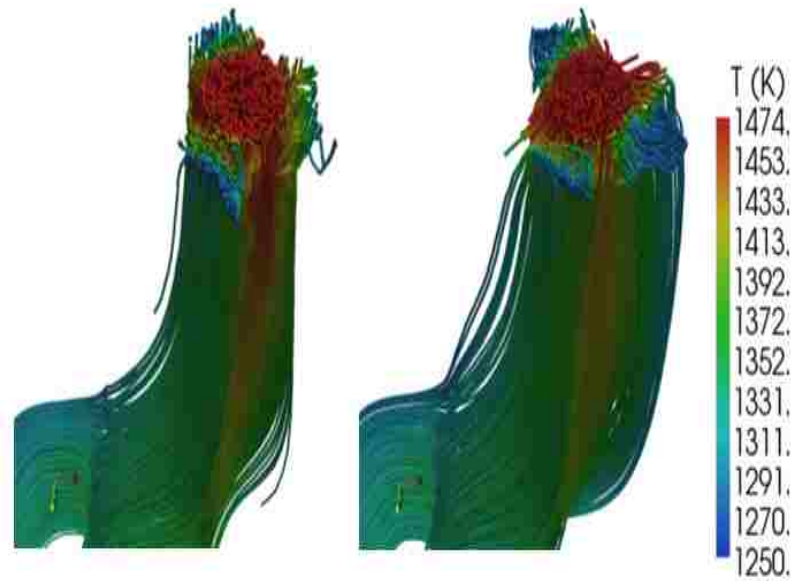
Figure 147. Comparison of the Calculated Jet Streamlines: Single Jet View. LHS: Basecase (Conventional Jet). RHS: CCW Swirling Jet.
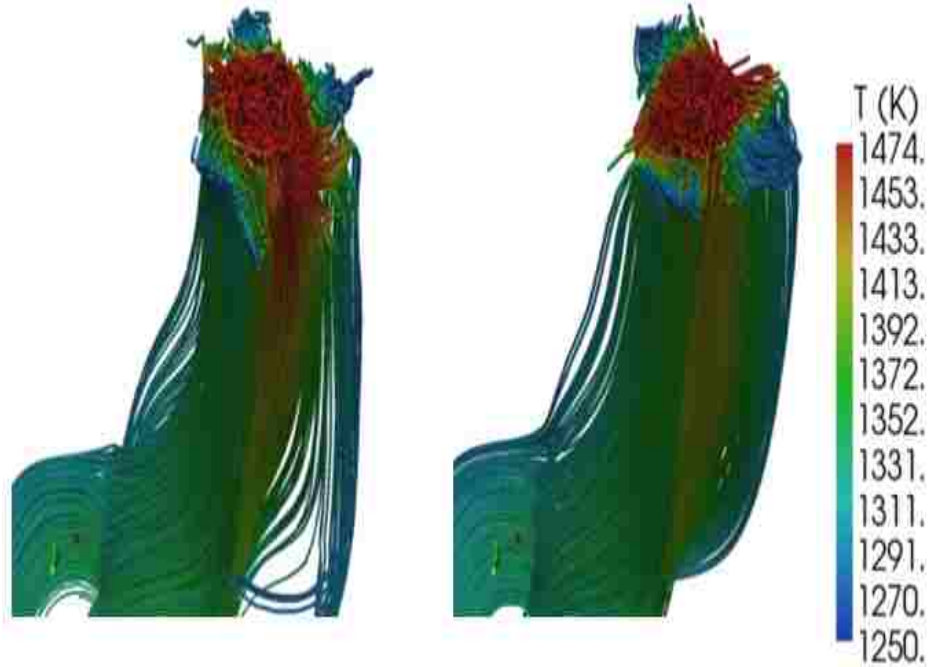
Figure 148. Comparison of the Calculated Swirling Jet Streamlines: Single Jet View. LHS: CW Jet. RHS: CCW Jet.
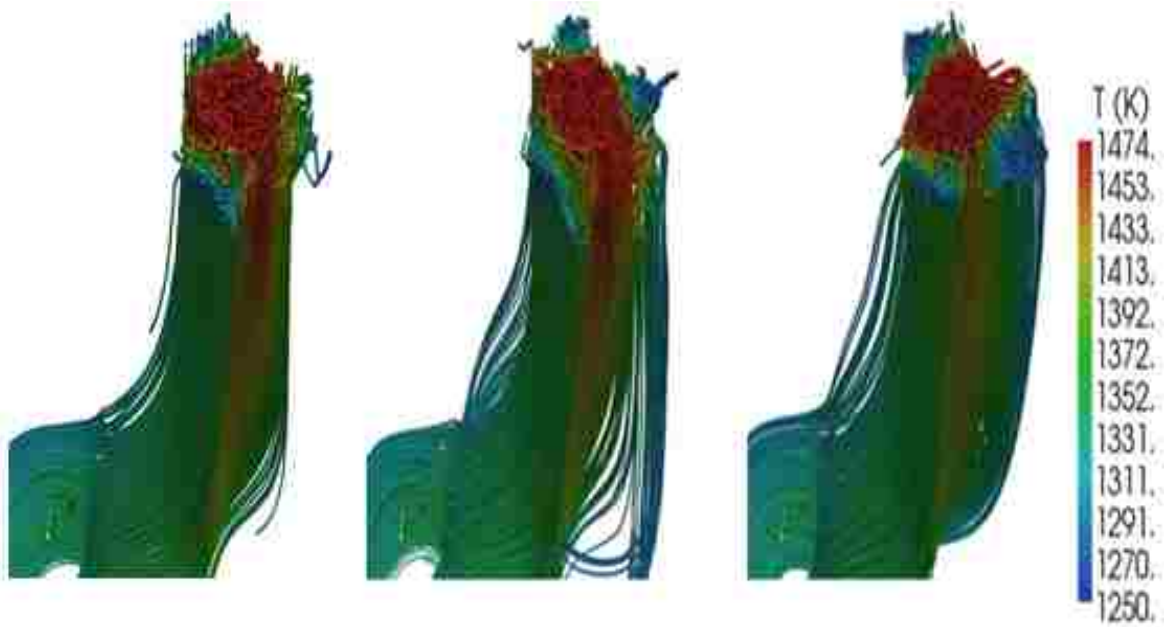
Figure 149. Comparison of the Calculated Swirling Jet Streamlines: Single Jet View. LHS: Conventional Jet. Center: CW Jet. RHS: CCW Jet.
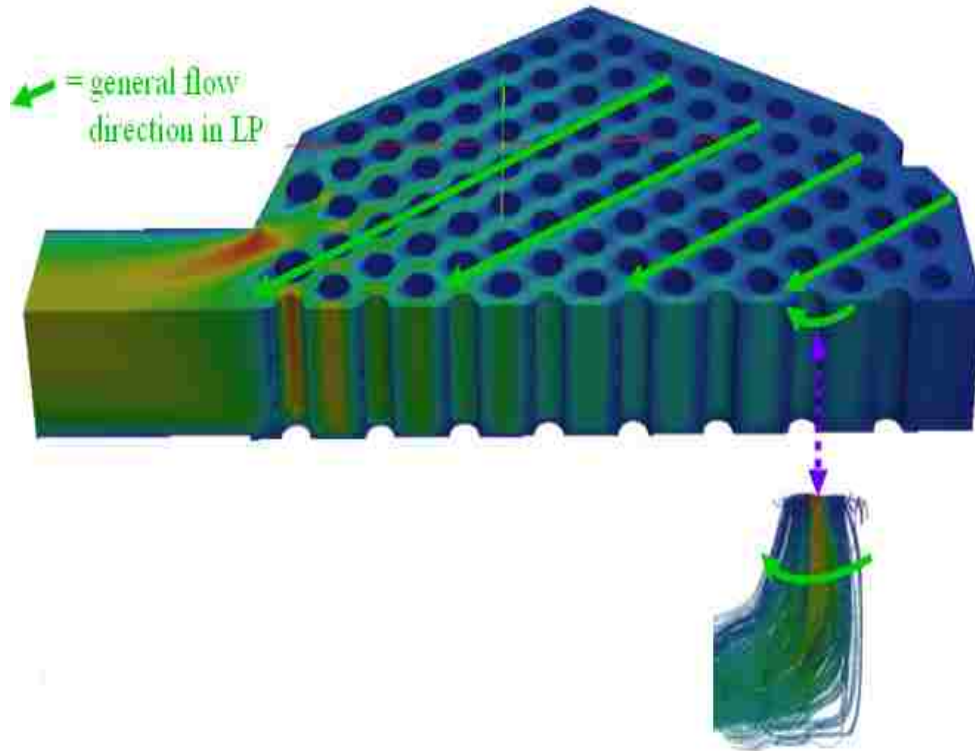
Figure 150. Importance of Rotation Direction for the Swirling Jets.

5.3.4   Multiphysics, Advanced Swirling-Jet LP Modeling

The final calculations used herein included the following:

- Fuego-Calore couple code,

- Helicoid vortex swirl model,

- Dynamic Smagorinsky LES turbulence model,

- PMR,

- 1D CHT, and

- Insulation plate at the bottom of the LP.

The PMR model calculated the impact of radiation heat transfer for the high

temperature helium gas behavior as a participating media. For the CHT, it was assumed

that the LP wall conducted heat, which was subsequently convected to the ambient as a result of natural convection.

The full-scale, half-symmetry mesh used in the LP simulation had unstructured hexahedral elements and accounted for the graphite posts, the helium jets, the exterior walls, and the bottom plate with an insulating outer surface [Allen, 2004]. The impact of using various swirl angles on the flow mixing and heat transfer in the LP was investigated.

For the final simulations, the jet exit velocity for the conventional jets was chosen as $V_0 = 67$ m/s in the +z direction. The emerging gas flow from the coolant channels in the Cartesian x, y, and z directions had v_x, v_y, and v_z velocity components, respectively, whose magnitude depended on the swirl angle of the insert, θ (*see* Figure 48, Section 5.1.1).

The initial time step used was 0.01 μs, and the simulation transient time was five to 25 s, with the CFL condition set to 1.0. Three helium jets were set to 1,473 K in order to investigate their tendency to form hot spots and thermally-stratified regions; the rest of the jets were at 1,273 K. S was set to 0.67.

Figure 151 shows key output from the coupled calculation, including the velocity streamlines (A), plate temperature distribution (B), fluid temperature as seen from the top (C), and fluid temperature shown from the bottom side (D). At steady state, Re in the LP ranges from 500 to 35,000. The lower RHS region in the LP had the lowest crossflow velocity (Re ~ 500), as shown in Figure 151A. As a consequence of the low crossflow, the hot jet that was placed strategically in that vicinity was able to reach the bottom plate with higher temperature (Figure 151B) than the other two hot channels that injected onto

regions with much higher crossflow. Consequently, Figure 151C shows that the two jets

were unable to reach the lower plate. This is a basic effect of conventional jets in

crossflow [Pratte and Baines, 1967; Nirmolo, 1970; Chassaing, P. *et al*., 1974; Kamotani

and Greber, 1974; Sucec and Bowley, 1976; Patankar, Basu, and Alpay, 1977; Goldstein

and Behbahani, 1982; Kavsaoglu and Schetz, 1989; Blevins, 1992; Rivero, Ferre, and

Giralt, 2001; Kiel *et al.*, 2003; Kawai and Lele, 2007] and swirling jets in crossflow

[Kavsaoglu and Schetz, 1989; Denev, Frohlich, and Bockhorn, 2009; Kamal, 2009]: the

higher the ratio of crossflow velocity to jet velocity, the faster the jet will bend in a

parabolic profile. Figure 151D shows the fluid temperature as seen from the bottom.
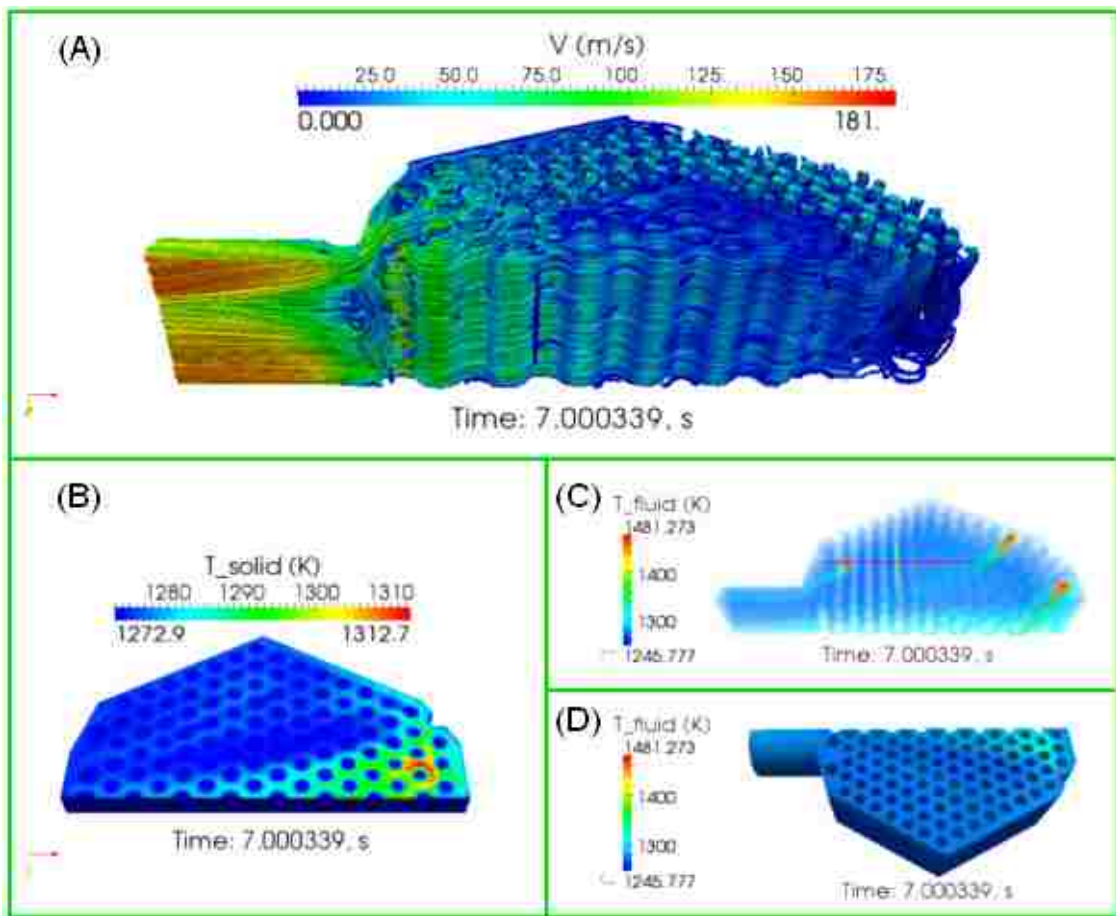
Figure 151. Fuego-Calore Output Showing: (A) Velocity Streamlines. (B) Plate Temperature Distribution, (C) Volume Rendering of Fluid Temperature, and (D) Fluid Temperature at the Bottom Side.

Figure 152 shows the velocity distribution at half the LP height. There is a noticeable acceleration of the fluid as it travels through the LP towards the exit. This is due to conservation of mass: as more mass from the jets enters the chamber, it must travel across fixed flow area.

Figure 153 shows the velocity threshold for the three hot channels. The figure confirms that despite the fact that there were a total of 138 jets in the half-symmetry model, each jet followed a rather narrowly-defined path that widened two to seven times the initial jet diameter, and followed the classic parabolic trajectory of a jet in crossflow. Figure 154 shows the fluid temperature (based on thresholds) for the hot channels. Due to mixing, the fluid temperature dropped 100 K within a few jet diameters. Figure 155 is similar, but is based on volume rendering of the fluid temperature. These figures allow the systematic tracing of velocity and temperature profiles of selected jets, without obstruction from other jets.
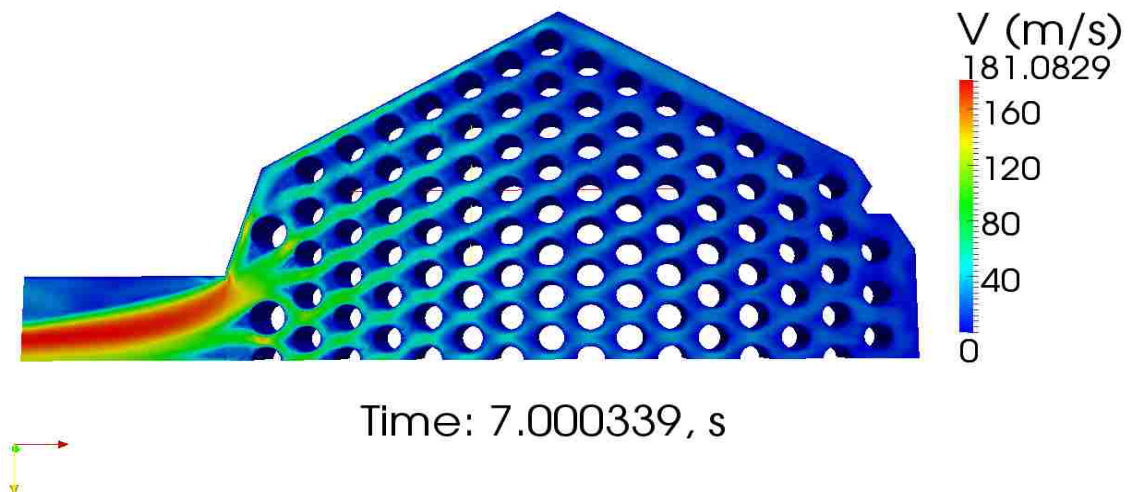
Figure 152. Velocity Distribution at Half the LP Height.

For low S, there is less mixing in the region adjacent to the jet exit, but the jet is able to reach the bottom plate. Conversely, for higher S, there is more mixing near the jet exit, but significantly less of the jet's azimuthal momentum reaches the bottom plate. For a sufficiently large S and tall LP, the azimuthal momentum will have decayed before reaching the bottom plate. The optimal height for swirling jets (with no crossflow) can be calculated via z* in Section 5.1.2. Figures 153 through 155 indicate that the jet penetration in the axial direction is a strong function of the crossflow. So, the lower the crossflow (RHS of figures), the deeper the jets are able to penetrate, and vice-versa (LHS of figures). Therefore, due to swirl decay and crossflow issues, S needs to be adjusted according to the local flow field conditions and desired LP height.
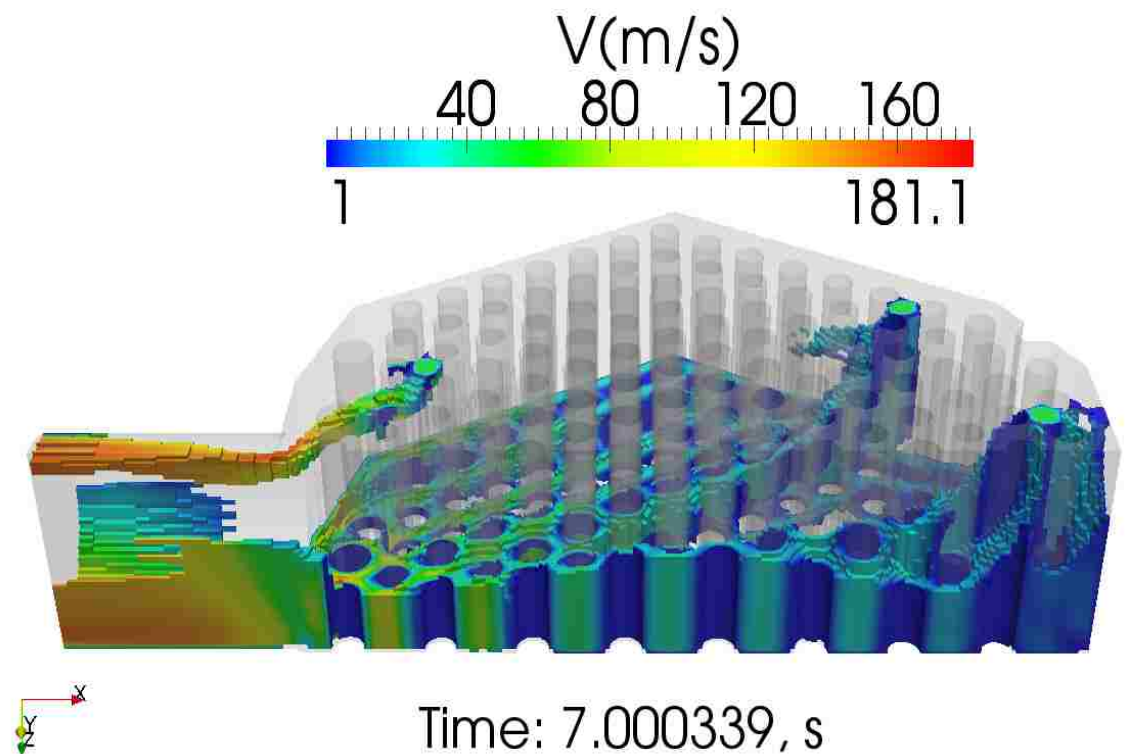
Figure 153. Velocity Threshold for the Three Hot Channels.
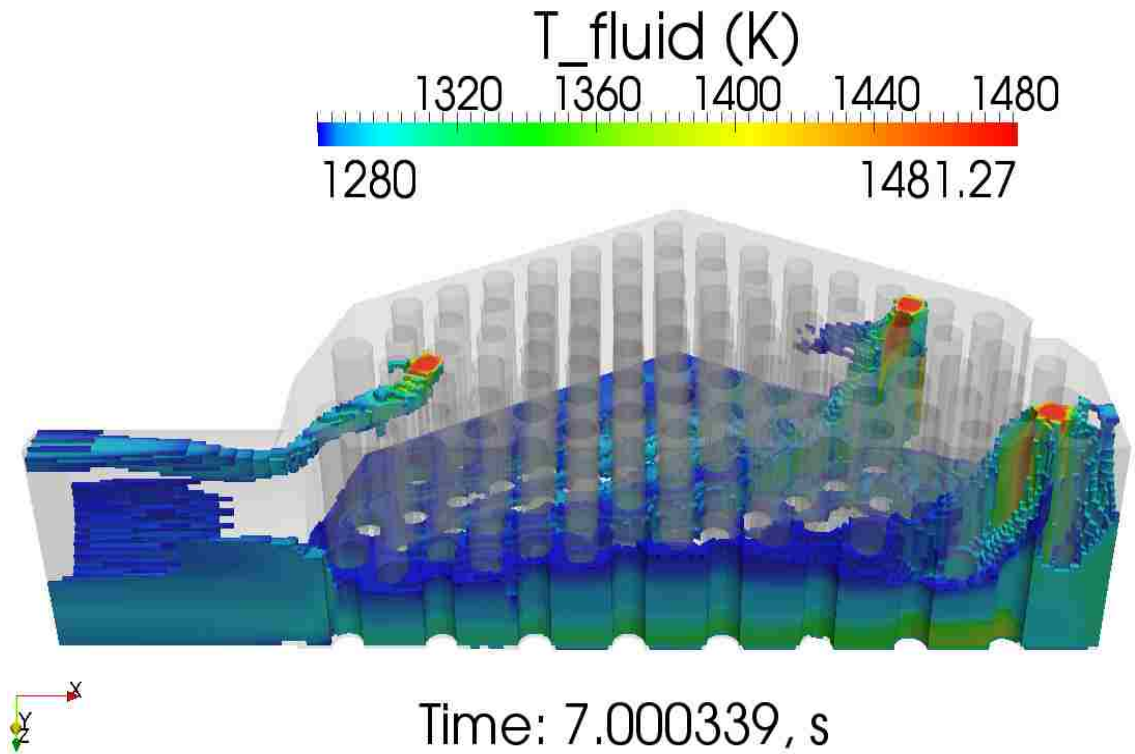
Figure 154. Temperature Threshold for the Three Hot Channels.
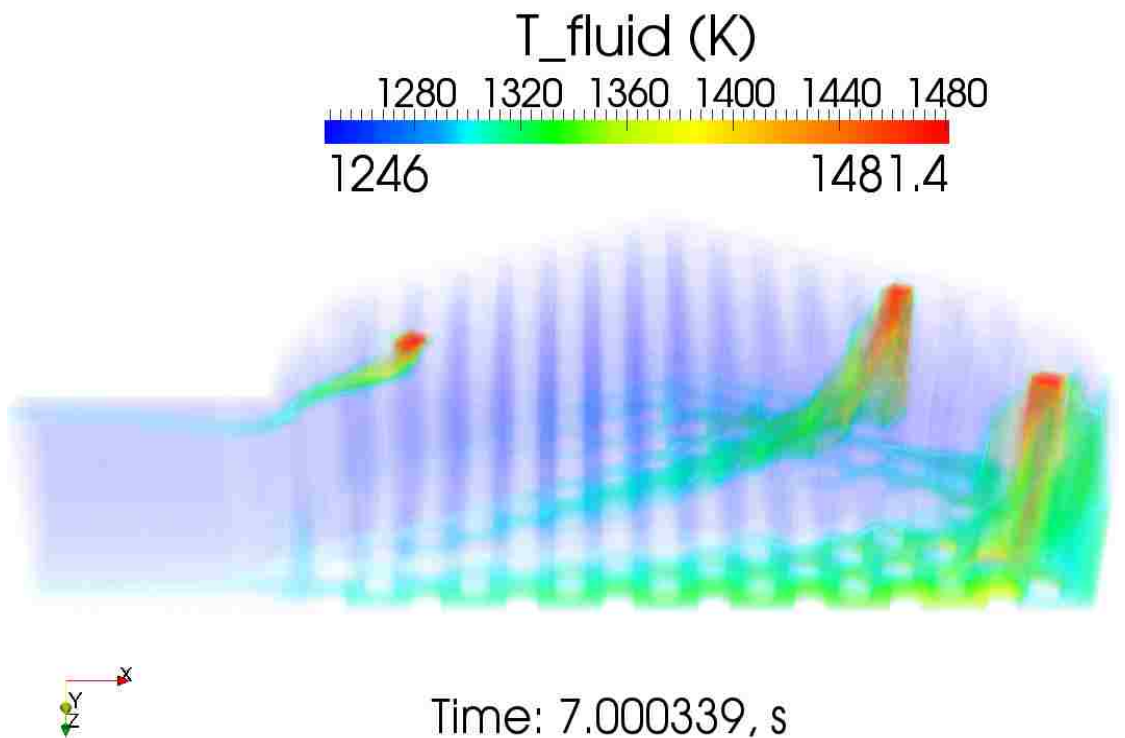
Figure 155. Volume Rendering of Fluid Temperature for the Three Hot Channels.

245

Figure 156 shows the bottom plate temperature. Notice that the higher temperatures occur in areas of the LP where the jets are able to reach the bottom. Thus, the peak temperature corresponded to the jet that impinged onto the region with the lowest Re (opposite end of the LP outlet). Figure 157 shows the fluid temperature adjacent to the bottom plate, while the convective heat transfer coefficient, h, is shown in Figure 158. Notice that its magnitude was small, comparable to that of forced airflow at 2 m/s over a plate [Holman, 1990]. Because the jet velocity was small in the calculations, values for h ~ 2 to 12 W/m^{2}K are reasonable. Notice, too, that h was zero (of course) in the region occupied by the support posts (shown as the large, dark blue circles).

Figure 156. Bottom Plate Temperature.

246

Figure 157. Fluid Temperature Adjacent to the Bottom Plate.
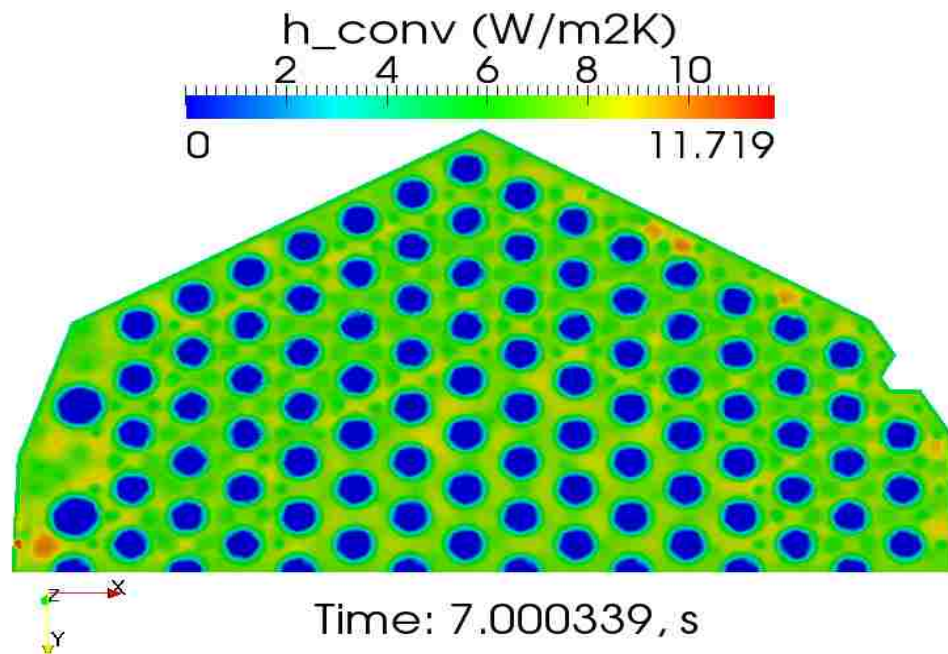
Figure 158. Bottom Plate Heat Transfer Coefficient.

The above figures confirm that swirling jets can mitigate thermal stratification and hot spots. The mitigation of those two issues was obtained at the cost of adding swirling jets that increase the pressure drop across the LP. Whether the benefits are outweighed by the pressure drop liability remains to be shown next.

An inspection of the pressure drop caused by the static helicoid device on a single, standalone helicoid showed that there was a relatively small drop of approximately 1,000 Pa (or 0.15 psi), as shown in Figure 159. This result is consistent with those found in the literature for hubless swirlers [Mathur and MacCallum, 1967]. Given the benefits related to enhanced mixing and turbulence gained as a result of the swirling device, its pressure drop is clearly justified.
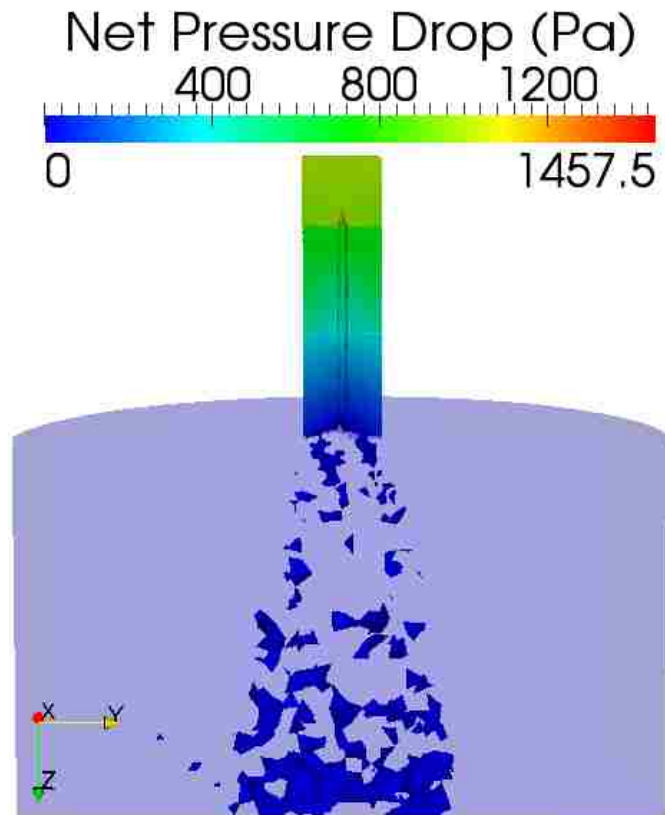
Figure 159. Net Pressure Drop Across Helicoid Geometry.

6. SUMMARY AND NEW CONTRIBUTIONS

In summary, the primary goals of the research found herein were to extend the current knowledge level regarding the heat transfer and mixing enhancement of swirling jets, to extend swirling jet theory modeling, and to apply those advancements to enhance mixing and heat transfer in the LP of a prismatic-core VHTR.

The key original contributions from this research can be summarized into seven distinct areas as follows:

1. Extend the applicability of a CFD code in the safety analysis and design of nuclear reactors undergoing turbulent anisotropic swirl flow conditions. In particular, a systematic process of V&V was conducted for the Fuego CFD code on a set of seven key single-effect thermalhydraulic phenomena that are expected to occur in the LP. This crucial set consists of phenomena that must be modeled correctly before the complex flow in the VHTR LP can be modeled adequately.

2. Formulate the helicoid vortex swirl model. This allowed a comprehensive and analytic research approach to investigate the impact of S on LP mixing and heat transfer. Developing analytical azimuthal and axial velocities that are solely functions of S allowed a deeper analysis of CRZ formation and optimization of S in the LP flow field.

3. Extend vortex theory to find common characteristics of axisymmetric, Newtonian, incompressible vortices. Knowing at a more fundamental level how vortices behave and what traits they have in common allows for insights that lead to vortex engineering for the purpose of maximizing heat transfer and

mixing. Because the CRZ is a strong function of the azimuthal and axial velocities, shaping those velocity profiles has a substantial effect on the flow field.

4.   Demonstrate that the vortices may be expressed as alternating series that expand geometrically with odd exponents. This discovery further substantiates the idea that the 15 axisymmetric vortices discussed in this research are part of a vortex family that has at least seven characteristics in common. Knowing this provides a more fundamental understanding that any given axisymmetric vortex, via parameter modification, behaves as the others. This implies that the insights gained for the helicoid vortex can be applied to the other 14 vortices, and vice versa.

5.   The ideas from Items 2 through 4 above were used to develop new vortices based on one or two series terms that satisfy NS and conserve mass. Eventually, these vortices may be used to further research mixing and heat transfer within the LP. These ideas may be used to obtain other vortices that also satisfy NS, and that can be designed to approximate a desired flow field.

6.   Determine the impact of Re, S, swirl decay, and CRZ formation upon mixing and heat transfer characteristics of swirling jets. This effort helped quantify how the above key parameters impact the flow field, thus allowing for a more optimized approach to solve the thermal stratification and hot spot issues.

7.   Apply the above research towards the final LP calculations to demonstrate that hot spots and thermal stratification in the LP of a VHTR can be mitigated with swirling jets. For Item 7, advantage was taken of the lessons learned from the

V&V effort, optimized helicoid vortex model, vortex behavior, and the impact

of Re, S, swirl decay, and the CRZ. As shown in Figures 141 through 143 and

153 through 155, complete mitigation of hot spots and thermal stratification

can be achieved in the LP.

7. RECOMMENDATIONS FOR FUTURE WORK

As this research winds down, many issues were resolved: the Fuego CFD code underwent a series of V&V applications, vortex theory was extended, and those advancements were applied towards solving the thermal stratification and hot spots in the LP. However, other questions arose, which merit future work. The following are listed below, in no particular order:

1. A substantial advantage of the RANS methods is that they require about 5% of the computing time required by LES methods [Sodja, 2007]. If so, this would strongly compel future investigation of the k-ω model for swirling flows, given its potential ability to model strong swirl at high Re.

2. It is not clear which LES turbulence model may be most suitable for strong swirling jets at high Re. There are various in the literature, including Smagorinsky, dynamic Smagorinsky, KSGS, wall-adapting local eddy-viscosity (WALE), RNG-LES, etc. These should be examined and compared.

3. By the time of the closure of this dissertation (April 2011), it has not been possible to extend the vortex unification theory further. Various questions remain unanswered. For example, what is the fundamental reason that the azimuthal velocity for axisymmetric vortices is in the form of alternating series expansions with odd exponents? Yes, the 15 azimuthal velocities that were investigated in this research were all odd, but what is the fundamental reason?

4. The practical applications of dynamic S, with alternating CW and CCW rotations ought to be examined in order to optimize mixing, turbulence, and heat

transfer.

5. Explicit guidelines for reaching adequate spatial and temporal discretizations should be advanced for LES methods. At what point is sufficient space filtering provided? Generally, from this research and unofficial lore, it would appear that CFL ≤ 2 is reasonable. What time step limit is appropriate and based on what criteria?

6. Since jets within the LP experience various degrees of crossflow, an optimization study can determine an S distribution for the jets such that thermal stratification and hot spot behavior is more uniformly optimized.

7. The experimental field for swirling jets in crossflow is quite limited (*see* Section 5.2.4).

.

REFERENCES

Abbasian, F., S. D. Yu, and J. Cao, "Large Eddy Simulation of Turbulent Axial Flow Along an Array of Rods", *J. of Fluids Engineering*, ASME, Vol. 132, 2010.

Aboelkassem, Y. and G. H. Vatistas, "New Model for Compressible Vortices", *J. of Fluids Engineering*, Vol. 129, 1073 – 1079, 2007.

Aboelkassem, Y., G. H. Vatistas, and N. Esmail, "Viscous Dissipation of Rankine Vortex Profile in Zero Meridional Flow", *Acta Mech. Sinica*, Vol. 21, 550 – 556, 2005.

Abujelala, M. T., T. W. Jackson, and D. G. Lilley, "Swirl Flow Turbulence Modeling", AIAA/SAE/ASME 20th Joint Propulsion Conference, AIAA-84-1376, Cincinnati, Ohio, June 11-13, 1985.

Abujelala, M. T. and D. G. Lilley, "Confined Turbulent Swirling Recirculating Flow Predictions", NASA Contractor Report 174917, 1985.

Afgan, I., "Large Eddy Simulation of Flow over Cylindrical Bodies using Unstructured Finite Volume Meshes", Ph.D. Diss., University of Manchester, July 2007.

Aggarwal, S. K. and T. W. Park, "Dispersion of Evaporating Droplets in a Swirling Axisymmetric Jet", *AIAA Journal*, Vol. 37, No. 12, 1578 – 1587, 1999.

Ahuja, V., M. Deshpande, and C. L. Merle, "The Effect of Swirl on Mixing Characteristics of Turbulent Shear Layers", American Institute of Aeronautics and Astronautics, 1997.

Alekseenko, S. V. *et al*., "Helical Vortices in Swirl Flow", *J. Fluid Mech*., Vol. 382, 195 – 243, 1999.

Alfonsi, G., "Reynolds-Averaged Navier-Stokes Equations for Turbulence Modeling", *Applied Mechanics Reviews*, Vol. 62, 2009.

Allen, T., "Generation IV Systems and Materials", Advanced Computational Materials Science: Application to Fusion and Generation-IV Fission Reactors, University of Wisconsin, 2004.

Al'tshul', A. D. and M. Sh. Margolin, "A Generalized Equation for the Distribution of Circumferential Velocities in Vortices", *Inzhenerno-Fizicheskii Zurnal*, Vol. 18, No. 4, 731 – 733, 1970.

Apte, S. V. *et al*., "Large-Eddy Simulation of Swirling Particle-Laden Flows in a Coaxial-Jet Combustor", *International Journal of Multiphase Flow*, Vol. 29, 1311 – 1331, 2003.

Arzutug, M. and S. Yapici, "Electrochemical Mass Transfer in Impinging Swirl Jets", *Ind. Eng. Chem. Res*, Vol. 48, 1593 – 1602, 2009.

Atvars, K., M. Thompson, and K. Hourigan, "Modification of the Flow Structures in a Swirling Jet", *IUTAM Symposium of Unsteady Separated Flows and their Control*, Vol. 14, 243 – 253, 2009.

Bakker, A., "Turbulence Models", Applied Computational Fluid Dynamics, Lecture 10, www.bakker.org, 2005.

Batchelor, G. K., "Axial Flow in Trailing Line Vortices*", J. Fluid Mech*., Vol. 20, Part 4, 645 – 658, 1964.

Bates, S. C., "Luminescent Visualization of Molecular and Turbulent Transport in a Plane Shear Layer", Thoughtventions Unlimited, LLC, Glastonbury, Connecticut, 2007.

Batterson, J. W., B. A. Maicke, and J. Majdalani, "Advancements in Theoretical Models of Confined Vortex Flowfields", University of Tennessee Space Institute, Tullahoma, Tennessee, 2007.

Bazant, M. Z. and H. K. Moffatt, "Exact Solutions of Navier-Stokes Equations Having Steady Vortex Structures", *J. Fluid Mech.*, Vol. 541, 55 – 64, 2005.

Benjamin, T. B., "Theory of the Vortex Breakdown Phenomenon", *Fluid Mech.*, Vol. 14, 593 – 629, 1962.

Bilen, K. *et al.*, "Heat Transfer from a Plate Impinging Swirl Jet", *Int. J. Energy Res.,* Vol. 26, 305 – 320, 2002.

Billant, P., J.-M. Chomaz, and P. Huerre, "Experimental Study of Vortex Breakdown in Swirling Jets", *J. Fluid Mech.*, Vol. 376, 183 – 219, 1998.

Bird, R., W. Stewart, and E. Lightfoot, *Transport Phenomena*, John Wiley & Sons, 2nd Edition, 2007.

Blevins, R., *Applied Fluid Dynamics Handbook*, Krieger Publishing Company, Malabar, Florida, 1992.

Bonaldo, A., "Experimental Characterisation of Swirl Stabilized Annular Stratified Flames", Ph. D. Diss., Cranfield University, 2007.

Bose, S. T., P. Moin, and D. You, "Grid-Independent Large-Eddy Simulation Using Explicit Filtering", Stanford University and Carnegie Mellon University, to be published ~ 2011.

Boutazakhti, M. *et al*., "Flow Downstream of a Cluster of Nine Jets", *Journal of Fluids Engineering*, Transactions of the ASME, Vol. 129, 541 – 550, 2007.

Bova, S. W., K. D. Copps, and C. K. Newman, "Calore", Theory Manual, Vol. 1, SAND2006-6083P, Sandia National Laboratories, 2006.

Brown, G. L. and J. M. Lopez, "Axisymmetric Vortex Breakdown Part 2. Physical Mechanisms", *J. Fluid Mech*., Vol. 221, 553 – 576, 1990.

Buckthorpe, D., "Materials for the Very High Temperature Reactor – Results and Progress within the Fifth and Sixth Framework Programmes", *Advanced Materials Research*, Vol. 59, 243 – 246, 2009.

Burchell, T., R. Bratton, and W. Windes, "NGNP Graphite Selection and Acquisition Strategy", Oak Ridge National Laboratory, ORNL/TM-2007/153, 2007.

Burgers, J. M., *Advances in Applied Mechanics*, Vol. 1, Academic Press, New York, 171, 1948.

Burns, S. P., "Applications of P Spatial and Angular Domain Based Parallelism to a Discrete Ordinates Formulation with Unstructured Spatial Discretization", Proceedings of the Second International Symposium on Radiation Transfer, 173 – 193, 1997.

Busch, H., K. Ryan, and G. J. Sheard, "Strain-Rate Development Between a Co-Rotating Lamb-Oseen Vortex Pair of Unequal Strength", 16th Australasian Fluid Mechanics Conference, Gold Coast, Australia, December 2-7, 1470 – 1474, 2007.

Buxton, O. R. H. and B. Ganapathisubramani, "The Classification and Composition of Fine Scale Eddies in a Turbulent Jet", 47th AIAA Aerospace Sciences Meeting, AIAA 2009-592, Orlando, Florida, January 5-8, 1 – 11, 2009.

Celik, N. and H. Eren, "Flow Dynamics of Impinging Circular Jets and the Effect of the Jet Diameter and Surface Heating Style on Heat Transfer", *Int. J. of Thermal Sciences*, THESCI-D-07-00333, 2007.

Chadwick, E., "The Vortex Line in Steady, Incompressible Oseen Flow", *Proc. R. Soc. A*, Vol. 462, 391 – 401, 2006.

Chassaing, P. *et al.*, "Physical Characteristics of Subsonic Jets in a Cross-Stream", *J. Fluid Mech.*, Vol. 62, Part 1, 41 – 64, 1974.

Chattot, J.-J., "Optimization of Propellers Using Helicoidal Vortex Model", *Computational Fluid Dynamics Journal*, Vol. 9, No. 2, 2000.

Chattot, J.-J., "Helicoidal Vortex Model for Steady and Unsteady Flows", *Computers & Fluids*, Vol. 35, 733 – 741, 2006.

Chenoweth, J. D. *et al.*, "Modeling Swirling Jet Flows Using Hybrid RANS/LES Methodology", 44th AIAA/ASME/SAE/ASEE Joint Propulsion Conference, AIAA 2008-4746, Hartford, Connecticut, July 21-23, 2008.

Chepura, I. B. *et al*., "On the Tangential Component of the Velocity Field in a Smooth-Wall Vessel Equipped with a Radial-Blade Mixer", *Teoreticheskie Osnovy Khimichesko i Tekhnologii*, Vol. 3, No. 3, 404 – 411, 1969.

Chepura, I. B., "Certain Principles of Varying Circumferential Velocity in Smooth-Walled Vessels with Radial Blade Agitators", *Teoreticheskie Osnovy Khimichesko i Tekhnologii*, Vol. 5, No. 5, 764 – 767, 1971.

Chigier, N. A. and A. Chervinsky, "Experimental Investigation of Swirling Vortex Motion in Jets", *ASME J. Applied Mechanics*, Series E, Vol. 3, 443 – 451, 1967.

Chuah, K. H. and G. Kushida, "The Prediction of Flame Heights and Flame Shapes of Small Fire Whirls", *Proceedings of the Combustion Institute,* Vol. 32, 2599 – 2606, 2007.

Chung, Y., K. Luo, and N. Sandham, "Numerical Study of Momentum and Heat Transfer in Unsteady Impinging Jets", *Int. J. Heat and Fluid Flow,* Vol. 23, 592 – 600, 2002.

Cooper, A. J. and N. Peake, "The Stability of a Slowly Diverging Swirling Jet", *J. Fluid Mech.,* Vol. 473, 389 – 411, 2002.

Crimaldi, J. P. and D. W. Knight, "A Laser-Based Flow Visualization System for Fluid Mechanics Instruction", Proceedings of the 2005 American Society for Engineering Education Annual Conference & Exposition, Session 1526, 2005.

CUBIT, http://www.cs.sandia.gov/capabilities/CubitMeshingProgram/index.html, 2009. Accessed on May 15, 2009.

Cziesla, T. *et al.,* "Large-Eddy Simulation of Flow and Heat Transfer in an Impinging Slot Jet", *Int. J. Heat and Fluid Flow*, Vol. 22, No. 5, 500 – 508, 2001.

Danitz, D. J., "Experimental Investigation of the Mixing of an Axial Jet within a Swirling Flow, Utilizing Laser Doppler Velocimetry and Particle Image Velocimetry", Massachusetts Institute of Technology, M.S. Thesis, 1995.

Darmofal, D. L., "The Role of Vorticity Dynamics in Vortex Breakdown", AIAA 24th Fluid Dynamics Conference, Orlando, Florida*,* Paper No. AIAA-93-3036, 1993.

Davidson, L., "An Introduction to Turbulence Models", Chalmers University of Technology, Sweden, 2003.

DeChant, L., "Modification to the k-ω Turbulence Model for Vortically Dominated Flows", American Institute of Aeronautics and Astronautics, 2010.

Delbende, I. *et al*., "Various Aspects of Fluid Vortices", C. R. Acad. Sci. Paris, France, 2002.

Denev, J. A., J. Frohlich, and H. Bockhorn, "Large Eddy Simulation of a Swirling Transverse Jet into a Crossflow with Investigation of Scalar Transport", *Physics of Fluids*, Vol. 21, 015101, 2009.

Dinesh, K. K. J. R. and M. P. Kirkpatrick, "Study of Jet Precession, Recirculation and Vortex Breakdown in Turbulent Swirling Jets Using LES", *Computers & Fluids*, Vol. 38, Issue 6, 1232 – 1242, 2009.

DOE, "Next-Generation Nuclear Energy", US Department of Energy's Office of Nuclear Energy, 2008.

Domino, S. P., "Sandia National Laboratories Abnormal Fire Environment Simulation Approach Overview", ASC SIERRA/Fuego/Calore/Syrinx, Sandia National Laboratories, 2006.

Domino, S. P. *et al*., "Verification for Multi-Mechanics Applications", presented at the 48th AIAA/ASME/AHS/ASC Structures, Structural Dynamics, and Materials Conference, Honolulu, HI, 2007.

Domino, S. P. and S. Gianoulakis, "Fuego Training", FM Global, Sandia National Laboratories, 2007.

Donaldson, C. duP. and R. D. Sullivan, "Behaviour of Solutions of the Navier-Stokes Equations for a Complete Class of Three-Dimensional Viscous Vortices", Proceedings of the 1960 Heat Transfer and Fluid Mechanics Institute, 16 – 30, 1960.

Dong, M. and D. G. Lilley, "Inlet Velocity Profile Effects on Turbulent Swirling Flow Predictions", 31st Aerospace Sciences Meeting & Exhibit, AIAA-93-0133, Reno, Nevada, January 11-14, 1993.

Doolan, C. J., "Large Eddy Simulation of the Near Wake of a Circular Cylinder at Sub-Critical Reynolds Number", *Engineering Applications of Computational Fluid Mechanics*, Vol. 4, No. 4, 496 – 510, 2010.

Duck, P. W. and M. R. Foster, "The Inviscid Stability of a Trailing Line Vortex", *J. of Applied Mathematics and Physics*, Vol. 31, 524 – 532, 1980.

Duraisamy, K. and S. K. Lele, "DNS of Temporal Evolution of Isolated Vortices", Center for Turbulence Research, Proceedings of the Summer Program, 35 – 47, 2006.

Duwig, C. *et al*., "Large Eddy Simulation of a Swirling Flame Response to Swirl Modulation with Impact on Combustion Stability", 43rd AIAA Aerospace Sciences Meeting and Exhibit, AIAA 2005-1275, Reno, Nevada, January 10-13, 2005.

Ecke, R., "The Turbulence Problem An Experimentalist's Perspective", Los Alamos Science, No. 29, 124 – 141, 2005.

Elavarasan, R. and H. Meng, "Flow Visualization Study of Role of Coherent Structures in a Tab Wake", *Fluid Dynamics Research*, Vol. 27, 183 – 197, 2000.

El-Behery, S. M. and M. H. Hamed, "A Comparative Study of Turbulence Model Performance for Turbulent Flow in a Planar Asymmetric Diffuser", World Academy of Science, *Engineering and Technology*, Vol. 53, 769 – 780, 2009.

Eldrainy, Y. A., M. F. b. Ahmad, and M. N. M. Jaafar, "Investigation of Radial Swirler Effect on Flow Pattern Inside a Gas Turbine Combustor", *Modern Applied Science*, Vol. 3, No. 5, 21 – 30, 2009.

El-Genk, M. and L. Huang, "Effect of Impinging Air Jet Diameter on Local and Average Heat Transfer", Proc. 30th National Heat Transfer Conference, HTD-303, August 5-9, 35 – 42, 1995.

El-Genk, M. S. and L. Huang, "An Experimental Investigation of the Effect of the Diameter of Impinging Air Jets on the Local and Average Heat Transfer", *J. Heat and Technology,* Vol. 17, No. 1, 3 – 12, 1999.

Elle, B. J., "On the Breakdown at High Incidences of the Leading-Edge Vortices on Delta Wings", *J. Roy. Aero. Soc*., Vol. 64, 1960.

Escudier, M. P. and J. J. Keller, "Recirculation in Swirling Flow: A Manifestation of

Vortex Breakdown," *AIAA Journal*, Vol. 23, 111 – 116, 1985.

Facciolo, L., "A Study on Axially Rotating Pipe and Swirling Jet Flows", Royal Institute

of Technology, Department of Mechanics, S-100 44 Stockholm, Sweden, Ph.D.

Diss., 2006.

Falcone, A. M. and J. C. Cataldo, "Entrainment Velocity in an Axisymmetric Turbulent

Jet", *J. of Fluids Engineering*, Transactions of the ASME, Vol. 125, 620 – 627,

2003.

Farokhi, S., R. Taghavi, and E. J. Rice, "Effect of Initial Tangential Velocity Distribution

on the Mean Evolution of a Swirling Turbulent Free Jet", American Institute of

Aeronautics and Astronautics, Inc., 88-3592-CP, 1988.

Felli, M., M. Falchi, and P. Fornari, "Impinging Swirling Jet against a Wall:

Experimental Investigation by PIV and High Speed Visualizations", Propulsion

and Cavitation Laboratory, INSEAN, Italy, 2008.

Fernandes, E. C., M. V. Heitor, and S. I. Shtork, "An Analysis of Unsteady Highly

Turbulent Swirling Flow in a Model Vortex Combustor", *Experiments in Fluids*,

Vol. 40, 177 – 197, 2006.

Feyedelem, M. S. and T. Sarpkaya, "Free and Near-Free-Surface Swirling Turbulent

Jets", AIAA 97-0438, 35th Aerospace Sciences Meeting & Exhibit, Reno, Nevada,

January 6-9, 1997.

FLUENT, "The Reynolds Stress Model (RSM)", Chapter 10.2.11, http://jullio.pe.kr/fluent6.1/help/html/ug/node413.htm, 2011. Accessed on January 11, 2011.

Freitag, M. and M. Klein, "Direct Numerical Simulation of a Recirculating Swirling Flow", *Flow, Turbulence and Combustion*, Vol. 75, 51 – 66, 2005.

Frohlich, J., M. Garcia-Villalba, and W. Rodi, "Scalar Mixing and Large-Scale Coherent Structures in Turbulent Swirling Jet", *Flow Turbulence Combust.*, Vol. 80, 47 – 59, 2008.

Fu, Q.-f., L.-j., and X-d. Wang, "Theoretical and Experimental Study of the Dynamics of a Liquid Swirl Injector", *J. of Propulsion and Power*, Vol. 26, No. 1, 94 – 101, 2010.

Fuchimoto, T. *et al*., "Dynamics of Vortex Rings in the Spray from a Swirl Injector", *Fluid Dyn. Res.,* Vol. 41, 1 – 22, 2009.

Fuego, "SIERRA/Fuego 2.7 Users Manual", Sandia National Laboratories, SAND 2006-6084P, 2008.

Fuego, "SIERRA/Fuego Theory Manual – 4.11", Sandia National Laboratories, 2009.

Fujimoto, Y., Y. Inokuchi, and N. Yamasaki, "Large Eddy Simulation of Swirling Jet in Bluff-Body Burner," *J. Thermal Science,* Vol. 14, No. 1, 28 – 33, 2005.

Fujimoto, Y. and N. Yamasaki, "Large Eddy Simulation of Swirling Jet in a Bluff-Body*", JSME International Journal*, Series B, Vol. 49, No. 4, 1125 – 1132, 2006.

Fukumoto, Y. and V. L. Okulov, "The Velocity Field Induced by a Helical Vortex Tube", *Physics of Fluids*, Vol. 17, 107101, 2005.

Gallaire, F. and J.-M. Chomaz, "Mode Selection in Swirling Jet Experiments: A Linear Stability Analysis", *J. Fluid Mech.*, Vol. 294, 223 – 253, 2003.

Gallaire, F., S. Rott, and J.-M. Chomaz, "Experimental Study of a Free and Forced Swirling Jet", *Physics of Fluids*, Vol. 16, No. 8, 2907 – 2917, 2004.

Gallerano, F. and E. Napoli, "A Dynamic Subgrid-Scale Tensorial Eddy Viscosity Model", *Continuum Mech. Thermodyn.*, Vol. 11, 1 – 14, 1999.

Garcia-Villalba, M., "Large Eddy Simulation of Turbulent Swirling Jets", Ph.D. Diss., Universitat Karlsruhe, 2006.

Garcia-Villalba, M. and J. Frohlich, "LES of a Free Annular Swirling Jet – Dependence of Coherent Structures on a Pilot Jet and the Level of Swirl," *Int. J. Heat and Fluid Flow*, Vol. 27, No. 5, 911 – 923, 2006.

Garcia-Villalba, M., J. Frohlich, and W. Rodi, "Unsteady Phenomena in an Unconfined Annular Swirling Jet," *Advances in Turbulence X,* Proceedings of the Tenth European Turbulence Conference, Barcelona, Spain, 2004.

Garcia-Villalba, M., J. Frohlich, and W. Rodi, "Large Eddy Simulation of Turbulent Confined Coaxial Swirling Jets," *Proc. Appl. Math. Mech.*, Vol. 5, 463 – 464, 2005.

Gardon, R. and J. C. Akfirat, "The Role of Turbulence in Determining the Heat-Transfer Characteristics of Impinging Jets", *Int. J. Heat Mass Transfer*, Vol. 8, 1261 – 1272, 1965.

Germano, M., "Turbulence: The Filtering Approach", *J. Fluid Mech.*, Vol. 238, 325 – 336, 1992.

Germano, M. *et al*., "A Dynamic Subgrid-Scale Eddy Viscosity Model", *Physics of Fluids A*, Vol. 3, No. 7, 1760–1765, 1991.

Ghosal, S. *et al*., "A Dynamic Localization Model for Large-Eddy Simulation of Turbulent Flows*", J. Fluid Mech*., Vol. 286, 229 – 255, 1995.

Giannadakis, A. *et al*., "Characteristics of Recirculating Swirl Flows", Proceedings of the Third European Combustion Meeting ECM, 2007.

Gibson, M. M. and B. A. Younis, "Calculation of Swirling Jets with a Reynolds Stress Closure", *Phys. Fluids*, Vol. 29, No. 1, 38 – 48, 1986.

Gilchrist, R. T. and J. W. Naughton, "Experimental Study of Incompressible Jets with Different Initial Swirl Distributions: Mean Results," *AIAA Journal*, Vol. 43, 741 – 751, 2005.

Gol'Dshtik, M. A. and N. I. Yavorskii, "On Submerged Jets", *Prikl. Matem. Mekhan*. USSR, Vol. 50, No. 4, 438 – 445, 1986.

Goldstein, R. J. and A. I. Behbahani, "Impingement of a Circular Jet with and without Cross Flow", *Int. J. Heat Mass Transfer*, Vol. 25, No. 9, 1377 – 1382, 1982.

Goldstein, R. J. and W. S. Seol, "Heat Transfer to a Row of Impinging Circular Air Jets Including the Effect of Entrainment", *Int. J. Heat Mass Transfer*, Vol. 34, No. 8, 2133 – 2147, 1991.

Gopalan, H. *et al*., "Investigation of Non-Swirling and Swirling Turbulent Jet Flows Using Unified LES-RANS Models", 48th AIAA Aerospace Sciences Meeting, AIAA 2010-1289, Orlando, Florida, January 4-7, 2010.

Gortler, H., "Decay of Swirl in an Axially Symmetrical Jet, Far from the Orifice", *Revista Matematica Hispano-Americana*, Vol. 14, 143 – 178, 1954.

Grimison, E. D., "Correlation and Utilization of New Data on Flow Resistance and Heat Transfer for Cross Flow of Gases Over Tube Banks", *Trans. ASME*, Vol. 59, 583 –594, 1937.

Guillen, D. P. and H. M. McIlroy, "Preliminary Study of Turbulent Flow in the Lower Plenum of a Gas-Cooled Reactor", INL/CON-07-12793, Proc. NURETH-12, Pittsburg, PA, 2007.

Gupta, A. K., D. G. Lilley, and N. Syred, *Swirl Flows*, Energy and Engineering Sciences Series, Abacus Press, 1984.

Gyllenram, W., H. Nilsson, and L. Davidson, "Large Eddy Simulation of Turbulent Swirling Flow Through a Sudden Expansion", 23rd IAHR Symposium, Yokohama, Japan, October 2006.

Hall, M. G., "The Structure of Concentrated Vortex Cores", Royal Aircraft Establishment, Farnborough, Hampshire, 53 – 110, c. 1966.

Herrada, M. A., C. Del Pino, and J. Ortega-Casanova, "Confined Swirling Jet Impingement on a Flat Plate at Moderate Reynolds Numbers", *Physics of Fluids*, Vol. 21, 2009.

Hinze, J., *Turbulence*, 2nd Edition, McGraw-Hill, Inc., 1975.

Hogg, S. and M. A. Leschziner, "Computation of Highly Swirling Confined Flow with a Reynolds Stress Turbulence Model", *AIAA Journal*, Vol. 27, No. 1, 57 – 63, 1989.

Holman, J., *Heat Transfer*, 7th Edition, McGraw-Hill, Inc., 1990.

Huang, L., "Heat Transfer and Flow Visualization of Conventional and Swirling Impinging Jets", Ph.D. Diss., University of New Mexico, 1996.

Huang, L. and M. S. El-Genk, "Heat Transfer of an Impinging Air Jet on a Flat Surface", *Int. J. Heat and Mass Transfer,* Vol. 37, No. 13, 1915 – 1923, 1994.

Huang, L. and M. El-Genk, "Heat Transfer and Flow Visualization Experiments of Swirling, Multi-Channel, and Conventional Impinging Jets", *Int. J. Heat Mass Transfer*, Vol. 41, No. 3, 583 – 600, 1998.

Huang, S.-L. *et al*., "On the Transition Process of a Swirling Vortex Generated in a Rotating Tank", *Exp. Fluids*, Vol. 45, 267 – 282, 2008.

Hwang, W.-S. and A. T. Chwang, "The Swirling Round Laminar Jet", *J. of Engineering Mathematics*, Vol. 26, 339 – 348, 1992.

Iaccarino, G. and P. Constantine, "Large Eddy Simulations of Flow Around a Cylinder with Uncertain Wall Heating", 47th AIAA Aerospace Sciences Meeting, AIAA 2009-975, Orlando, Florida, January 5-8, 2009.

INL, "Next Generation Nuclear Plant Pre-Conceptual Design Report", INL/EXT-07-12967, Rev. 1., Idaho National Laboratory, 2007.

INL, "NGNP Licensing Plan", Idaho National Laboratory, PLN-3202, 2009.

Itoh, K. *et al*., "On Flow Reversal in Turbulent Swirling Flow", *J. of the Physical Society of Japan*, Vol. 72, No. 11, 2781 – 2785, 2003.

Jagus, K. *et al*., "Annular Fuel Jet in a Swirling/Non-Swirling Diesel Environment", 5th European Thermal-Sciences Conference, The Netherlands, 2006.

Jambunathan, K. *et al.,* "A Review of Heat Transfer Data for Circular Jet Impingement", *Int. J. Heat and Fluid Flow,* Vol. 13, No. 2, 106 – 115, 1992.

Jiang, X., G. A. Siamas, and L. C. Wrobel, "Analytical Equilibrium Swirling Inflow Conditions for Computational Fluid Dynamics", *AIAA Journal*, Technical Notes, Vol. 46, No. 4, 1015 – 1018, 2008.

Johnson, G. A., "Power Conversion System Evaluation for the Next Generation Nuclear Plant (NGNP)", Proc. International Congress on Advances in Nuclear Power Plants (ICAPP 08), American Nuclear Society, Paper 8253, Anaheim, CA, 2008.

Johnson, R. W., "Modeling Strategies for Unsteady Turbulent Flows in the Lower Plenum of the VHTR", *Nuclear Engineering and Design*, Vol. 238, 482 – 491, 2007.

Johnson, R. W., "CFD Investigation of Experimental Data Proposed to be a Validation Data Set", INL/CON-09-15331, Proceedings of the 17th International Conference on Nuclear Engineering, ICONE 17-75604, Brussels, Belgium, July 12-16, 2009a.

Johnson, R. W., "Examination of a Proposed Validation Data Set Using CFD Calculations", Proceedings of FEDSM2009, ASME 2009 Fluids Engineering Summer Meeting, Vail, Colorado, August 2-5, 2009b.

Johnson, R. W. and R. R. Schultz, "Computational Fluid Dynamic Analysis of the VHTR Lower Plenum Standard Problem", INL/EXT-09-16325, Idaho National Laboratory, July 2009.

Jorgensen, F. E., "How to Measure Turbulence with Hot-Wire Anemometers—A Practical Guide", DANTEC Dynamics, Skovlunde, Denmark, 2002.

Jung, D., S. Gamard, and W. K. George, "Downstream Evolution of the Most Energetic Modes in a Turbulent Axisymmetric Jet at High Reynolds Number. Part 1. The Near-Field Region", *J. Fluid Mech*., 173 – 204, 2004.

Kamal, M. M., "Combustion in a Cross Flow with Air Jet Nozzles", *Combust. Sci. and Tech*., Vol. 181, 78 – 96, 2009.

Kamotani, Y. and I. Greber, "Experiments on Confined Turbulent Jets in Cross Flow", NASA CR-2392, 1974.

Kannepalli, C. *et al*., "A Hybrid RANS/LES Approach to Modeling of Swirling Jet Flows", *AIAA* 2008-3853, 38th Fluid Dynamics Conference and Exhibit, Seattle, Washington, June 23-26, 2008.

Kavsaoglu, M. S. and J. A. Schetz, "Effects of Swirl and High Turbulence on a Jet in a Crossflow", *J. Aircraft*, Vol. 26, No. 6, 539 – 546, 1989.

Kawai, S. and S. K. Lele, "Mechanisms of Jet Mixing in a Supersonic Crossflow: A Study Using Large-Eddy Simulation", Center for Turbulence Research, Annual Research Briefs, 353 – 365, 2007.

Keffer, J. F. and W. D. Baines, "The Round Turbulent Jet in a Cross-Wind", *J. Fluid Mechanics*, Vol. 8, 481 – 496, 1963.

Kenny, R. J. *et al*., "Effect of Chamber Backpressure on Swirl Injector Fluid Mechanics", *J. of Propulsion and Power*, Vol. 25, No. 4, 902 – 913, 2009.

Kerr, N. M. and D. Fraser, "Swirl. Part I: Effect on Axisymmetrical Turbulent Jets", *J. of the Institute of Fuel*, Vol. 39**,** 519 – 526, 1965.

Khalil, E. E., D. B. Spalding, and J. H. Whitelaw, "The Calculation of Local Flow Properties in Two-Dimensional Furnaces", *Int. J. Heat Mass Transfer*, Vol. 18, 775 – 791, 1975.

Khorrami, R. M., "Stability of a Compressible Axisymmetric Swirling Jet", *AIAA Journal*, Vol. 33, No. 4, 650 – 658, 1995.

Kiel, B. *et al*., "Experimental Investigation of Vortex Shedding of a Jet in Crossflow", 41st Aerospace Sciences Meeting and Exhibit, AIAA 2003-182, Reno, Nevada, January 6-9, 2003.

Kihm, K. D., N. Chigier, and F. Sun, "Laser Doppler Velocimetry Investigation of Swirler Flowfields", *J. Propulsion*, Vol. 6, No. 4, 364 – 374, 1990.

Kilik, E. and R. Finstad, "A Numerical Study of Co- and Counter-Swirling Confined Coaxial Jets", AIAA/ASME/SAE/ASEE 22nd Joint Propulsion Conference, Huntsville, Alabama, June 16-18, 1986.

Kim, K. Y. and M. K. Chung, "Calculation of a Strongly Swirling Turbulent Round Jet with Recirculation by an Algebraic Stress Model", *Int. J. Heat and Fluid Flow*, Vol. 9, No. 1, 62 – 68, 1988.

Kim, M.-H., H.-S Lim, and W.-J. Lee, "A CFD Analysis of a Preliminary Cooled-Vessel Concept for a VHTR", Korea Atomic Energy Research Institute, 2007.

Kim, W. W. and S. Menon, "LES of Turbulent Fuel/Air Mixing in a Swirling Combustor", 37th AIAA Aerospace Sciences Meeting and Exhibit, AIAA 98-0200, Reno, Nevada, January 11-14, 1999.

King, A., "Heat Transfer Enhancement and Fluid Flow Characteristics Associated with Jet Impingement Cooling", Ph.D. Diss., Curtin University of Technology, c. 2005.

Kinsey, J., "Identification of Priority Licensing Issues for NGNP", Next Generation Nuclear Plant Project Regulatory Affairs, Regulatory Information Conference, March 10, 2010.

Knowles, K. and P. W. Carpenter, "The Use of Swirl for Flow Control in Propulsion Nozzles", *J. Propulsion*, Vol. 6, No. 2, 158 – 164, 1990.

Kollmann, W., "Critical Points and Manifolds of the Lamb Vector Field in Swirling Jets", *Computers and Fluids*, Vol. 35, 746 – 754, 2006.

Kollmann, W. and G. Umont, "Lamb Vector Properties of Swirling Jets", The University of Sydney, Sydney, Australia, 2004.

Kravchenko, A. G. and P. Moin, "Numerical Studies of Flow Over a Circular Cylinder at Re_D=3900", *Physics of Fluids*, Vol. 12, No. 2, 403 – 417, 2000.

Kreyszig, E., *Advanced Engineering Mathematics*, John Wiley & Sons, New York, 4th Edition, 1979.

Krishna, S. B. and V. Ganesan, "CFD Analysis of Flow through Vane Swirlers", Vol. 86, *IE(I) Journal-MC*, 2005.

Kullen, A., Hair Dryer with Axial Blower, United States Patent 759424, 1987.

Kurosaka, M., "Vortex Whistle: An Unsteady Phenomenon in Swirling Flow and its Effects on Steady Flow Field", AIAA 19th Aerospace Sciences Meeting, St. Louis, Missouri, January 12-15, 1981.

Labus, T. and E. P. Symons, "Experimental Investigation of an Axisymmetric Free Jet with an Initially Uniform Velocity Profile", NASA Technical Note, NASA TN D-6783, 1972.

Lai, Y. G., "Predictive Capabilities of Turbulence Models for a Confined Swirling Flow", *AIAA Journal*, Vol. 34, No. 8, Technical Notes, 1743 – 1745, 1995.

Lamb, H., *Hydrodynamics*, 6th Ed., Cambridge Univ. Press, 1932.

Laskowski, G. M. *et al.*, "Mixed Convection Heat Transfer to and from a Horizontal Cylinder in Cross-Flow with Heating from Below", *International Journal of Heat and Fluid Flow*, 2006.

Larocque, J., "Heat Transfer Simulation in Swirling Impinging Jet", Institut National Polytechnique de Grenoble, Division of Heat Transfer, September 2004.

Launder, B. E. and D. B. Spalding, "The Numerical Computation of Turbulent Flows", *Comput. Methods Appl. Mech. Engr.*, Vol. 3, 269 – 289, 1974.

Launder, B. E., G. J. Reece, and W. Rodi, "Progress in the Development of a Reynolds-Stress Turbulence Closure", *J. Fluid Mech.*, Vol. 68, Part 3, 537 – 566, 1975.

Laurien, E., D. v. Lavante, and H. Wang, "Hot-Gas Mixing in the Annular Channel Below the Core of High-Power HTR's", Proceedings of the 5th International Topical Meeting on High Temperature Reactor Technology, HTR 2010-138, Prague, Czech Republic, October 18-20, 2010.

Lavante, D. v. and E. Laurien, "3-D Simulation of Hot Gas Mixing in the Lower Plenum of High-Temperature Reactors", *Int. J. for Nuclear Power*, Vol. 52, 648 – 649, 2007.

Leclaire, B., D. Sipp, and L. Jacquin, "The Influence of Upstream Boundary Conditions on the Onset of Axisymmetric Vortex Breakdown in a Duct", 5th AIAA Theoretical Fluid Mechanics Conference, AIAA 2008-3798, Seattle, Washington, June 23-26, 2008.

Lee, J. H. and Z. Rusak, "Bifurcation and Stability of Near-Critical Compressible Swirling Flows", 42nd AIAA Aerospace Sciences Meeting and Exhibit, Reno, Nevada, AIAA 2004-0102, January 5-8, 2004.

Lee, J. W. *et al*., "Generation of High-Level Thermo-Fluid PIRTS for the VHTR High and Low Pressure Conduction Cooling Events", ANS Meeting Embedded ST-NH$_2$, 2007.

Lee, R. S., "Axisymmetrical Turbulent Swirling Natural Convection Plume Part I – Theoretical Investigation", State University of New York at Stony Brook, Report 57, 1965.

Leibovich, S., "The Structure of Vortex Breakdown", *Ann. Rev. Fluid Mech.*, Vol. 10, 221 – 246, 1978.

Leschziner, M. A. and W. Rodi, "Computation of Strongly Swirling Axisymmetric Free Jets", *AIAA Journal*, Vol. 22, No. 12, 1742 – 1747, 1984.

Lesieur, M., *Turbulence in Fluids*, 3rd Edition, Fluid Mechanics and its Applications, Vol. 40, Kluwer Academic Publishers, 1997.

Li, G., "Emissions, Combustion Dynamics, and Control of a Multiple Swirl Combustor", Ph.D. Diss., U. of Cincinnati, 2004.

Li, G. and E. J. Gutmark, "Boundary Condition Effects on Nonreacting and Reacting Flows in a Multiswirl Combustor", *AIAA Journal*, Vol. 44, No. 3, 444 – 456, 2006.

Liang, C. and G. Papadakis, "Large Eddy Simulation of Cross-Flow through a Staggered Tube Bundle at Subcritical Reynolds Number", *J. of Fluids and Structures*, Vol. 23, 1215 – 1230, 2007.

Liang, H. and T. Maxworthy, "An Experimental Investigation of Swirling Jets", *J. Fluid Mech.*, Vol. 525, 115 – 159, 2005.

Liang, H. and T. Maxworthy, "Experimental Investigation of a Swirling Jet in Both Stationary and Rotating Surroundings", *Exp. Fluids*, Vol. 45, 283 – 293, 2008.

Ligrani, P. M. and M. M. Oliveira, "Comparison of Heat Transfer Augmentation Techniques", *AIAA Journal*, Vol. 41, No. 3, 337 – 362, 2003.

Lilley, D. G., "Prediction of Inert Swirl Flows," *AIAA Journal*, Vol. 11, 955 – 960, 1973.

Lilley, D. G., "Swirl Flows in Combustion: A Review", *AIAA Journal*, Vol. 15, No. 8, 1063 – 1078, 1977.

Lilly, D. K., "A Proposed Modification of the Germano Subgrid-Scale Closure Method", *Phys. Fluids A*, Vol. 4, No. 3, 633 – 635, 1992.

Lim, T. T., T. H. New, and S. C. Luo, "On the Development of Large-Scale Structures of a Jet Normal to a Cross Flow", *Physics of Fluids*, Vol. 13, No. 3, 770 – 775, 2001.

Loiseleux, T., J. M. Chomaz, and P. Huerre, "The Effect on Swirl on Jets and Wakes: Linear Instability of the Rankine Vortex with Axial Flow", *Physics of Fluids*, Vol. 10, No. 5, 1120 – 1134, 1998.

Loitsyanskiy, L. G., "The Propagation of a Twisted Jet in an Unbounded Space Filled with the Same Fluid", *Prikladnaya Matematika i Mekhanika*, Vol. 17, No. 1, 3 – 16, 1953.

Lopez, J. M., "Axisymmetric Vortex Breakdown Part 3. Onset of Periodic Flow and Chaotic Advection", *J. Fluid Mech.*, Vol. 221, 533 – 552, 1990.

Lopez, J. M. and A. D. Perry, "Axisymmetric Vortex Breakdown Part 1. Confined Swirling Flow", *J. Fluid Mech.*, Vol. 234, 449 – 471, 1990.

Lu, G. and S. K. Lele, "Inviscid Instability of Compressible Swirling Mixing Layers", *Physics of Fluids*, Vol. 11, No. 2, 450 – 461, 1999.

Lu, X. *et al.*, "Large-Eddy Simulations of Turbulent Swirling Flows Injected into a Dump Chamber", *J. Fluid Mech.*, Vol. 527, 171 – 195, 2005.

Lucca-Negro, O. and T. O'Doherty, "Vortex Breakdown: A Review", *Prog. Energy Combust. Sci.*, Vol. 27, No. 4, 431 – 481, 2001.

MacDonald, P. E., "Next Generation Nuclear Plant (NGNP) A Very High Temperature Gas-Cooled Reactor (VHTR)", Advanced Reactor, Fuel Cycle, and Energy Products, Workshop for Universities, Gaithersburg, MD, March 4-5, 2004.

MacDonald, P. E. *et al.*, "NGNP Preliminary Point Design – Results of the Initial Neutronics and Thermal-Hydraulic Assessments", Idaho National Laboratory, INEEL/EXT-03-00870 Rev. 1, 2003.

Magnussen B. F. *et al*., "Effects of Turbulent Structure and Local Concentrations on Soot

    Formation and Combustion in C2H2 Diffusion Flames", 17th International

    Symposium on Combustion, The Combustion Institute, Pittsburgh, 1383 – 1393,

    1979.

Mao, X. and S. J. Sherwin, "Spectra of Swirling Flow", under consideration for

    publication in *J. Fluid Mech*., received November 15, 2009.

Maple, Waterloo Maple Inc., Version 7.00, 2001.

Marcu, B., E. Meiburg, and P. K. Newton, "Dynamics of Heavy Particles in a Burgers

    Vortex", *Phys. Fluids*, Vol. 7, No. 2, 400 – 410, American Institute of Physics,

    1995.

Mardani, A. S., "Development of Intake System for Improvement of Performance of

    Compressed Natural Gas Spark Ignition Engine", Ph.D. Diss., Universiti

    Teknologi, Malaysia, 2004.

Martin, J. E. and E. Meiburg, "Nonlinear Axisymmetric and Three-Dimensional Vorticity

    Dynamics in a Swirling Jet Model", *Phys. Fluids*, Vol. 8, No. 7, 1917 – 1928,

    1996.

Martynenko, O. G., V. N. Korovkin, and Yu. A. Sokovishin, "A Laminar Swirled Free-

    Convection Jet", *Int. J. Heat Mass Transfer*, Vol. 28, No. 2, 371 – 382, 1985.

Martynenko, O. G., V. N. Korovkin, and Yu. A. Sokovishin, "A Swirled Jet Problem",

    Int. J. Heat Mass Transfer, Vol. 32, No. 12, 2309 – 2317, 1989.

Mathur, M. L. and N. R. L. MacCallum, "Swirling Air Jets Issuing from Vane Swirlers.

    Part 1: Free Jets", *Journal of the Institute of Fuel*, Vol. 40, 214 – 225, 1967.

Matlab, The MathWorks, Inc., Version R11, 1999.

Matsuda, T. and J. Sakakibara, "On the Vortical Structure in a Round Jet", *Physics of Fluids*, Vol. 17, 2005.

Matzner, D., "PBMR Project Status and the Way Ahead", 2nd International Topical Meeting on the High Temperature Reactor Technology, Paper A04, Beijing, China, September 22-24, 2004.

Maxworthy, T., E. J. Hopfinger, and L. G. Redekopp, "Wave Motions on Vortex Cores", *J. Fluid Mech.*, Vol. 151, 141 – 164, 1985.

Mayer, E. W. and K. G. Powell, "Viscous and Inviscid Instabilities of a Trailing Vortex", *J. Fluid Mech.*, Vol. 245, 91 – 114, 1992.

McCreery, G. E. and K. G. Condie, "Experimental Modeling of VHTR Plenum Flows During Normal Operation and Pressurized Conduction Cooldown", INL/EXT-06-11760, 2006.

McEligot, D. M. and G. E. McCreery, "Scaling Studies and Conceptual Experiment Designs for NGNP CFD Assessment", Idaho National Engineering and Environment Laboratory, INEEL/EXT-04-02502, November 30, 2004.

McEligot, D. M. *et al.,* "Key Thermal Fluid Phenomena in Prismatic Gas-Cooled Reactors", INEEL/CON-05-02591, 2005.

McIlroy, H. M. *et al.*, "PIV Experiments to Measure Flow Phenomena in a Scaled Model of a VHTR Lower Plenum", Idaho National Laboratory, INL/EXT-08-15161, 2006a.

McIlroy, H. M. *et al*., "Experimental Measurement of Flow Phenomena in a VHTR Lower Plenum Model", ANS 2006 Annual Meeting, INL/CON-06-01089, 2006b.

McIlroy, H. M., D. M. McEligot, and R. J. Pink, "Measurement of Turbulent Flow Phenomena for the Lower Plenum of a Prismatic Gas-Cooled Reactor", The 12th International Topical Meeting on Nuclear Reactor Thermal Hydraulics (NURETH-12), September 30-October 4, 2007.

McIlroy, H. M., D. M. McEligot, and R. J. Pink, "Measurement of Flow Phenomena in a Lower Plenum Model of a Prismatic Gas-Cooled Reactor", INL/CON-08-13708, Proceedings of the 16th International Conference on Nuclear Engineering (ICONE-16), Orlando, May 11-15, 2008a.

McIlroy, H. M., D. M. McEligot, and R. J. Pink, "Experiments and CFD Code Applications to Nuclear Reactor Safety (XCFD4NRS)", INL/CON-08-14081, 2008b.

McIlroy, H. M., D. M. McEligot, and R. J. Pink, "Measurement of Turbulent Flow Phenomena for the Lower Plenum of a Prismatic Gas-Cooled Reactor", *J. of Engineering for Gas Turbines and Power*, Vol. 132, 2010a.

McIlroy, H. M., D. M. McEligot, and R. J. Pink, "Measurement of Flow Phenomena in a Lower Plenum Model of a Prismatic Gas-Cooled Reactor", INL/CON-08-13708, Proceedings of the 16th International Conference on Nuclear Engineering (ICONE-16), Orlando, May 11-15, 2010b.

McMahon, H. M., D. D. Hester, and J. G. Palfery, "Vortex Shedding from a Turbulent Jet in a Cross-Wind", *J. Fluid Mech*., Vol. 48, Part 1, 73 – 80, 1971.

Menke, M. and I. Gursul, "Unsteady Nature of Leading Edge Vortices", *Phys. Fluids*, Vol. 9, No. 10, 2960 – 2966, 1997.

Merci, B. and E. Dick, "Heat Transfer Predictions with a Cubic k-ɛ Model for Axisymmetric Turbulent Jets Impinging onto a Flat Bed", *Int. J. Heat Mass Transfer,* Vol. 46, 569 – 480, 2003.

Merker, G. P. *et al.*, *Simulating Combustion*, 324, Springer, 2006.

Meyyapan, M., M. P. Schwarz, and J. H. Perry, "Modeling of Swirl Jet Flows", Inter. Conf. on CFD in Mineral & Metal Processing and Power Generation, 177 – 188, 1997.

Moet, H. *et al.*, "Wave Propagation in Vortices and Vortex Bursting", *Phys. Fluids*, 1 – 55, 2004.

Moin, P. K. *et al.*, "A Dynamic Subgrid-Scale Model for Compressible Turbulence and Scalar Transport", *Phys. Fluids A*, Vol. 3, No. 11, 2746 – 2757, 1991.

Moon, S., E. Abo-Serie, and C. Bae, "Air Flow and Pressure Inside a Pressure-Swirl Spray and their Effect on Spray Development", *Experimental Thermal and Fluid Science*, Vol. 33, 222 – 231, 2009.

Muller, S. B. and L. Kleiser, "Large-Eddy Simulation of Vortex Breakdown in Compressible Swirling Jet Flow", *Computers and Fluids*, Vol. 37, 844 – 856, 2008.

Munekata, M., H. Ohba, and K. Matsuzaki, "A Study on Reynolds Shear Stress Measurement by LDV", *J. of Thermal Science*, Vol. 10, No. 1, 20 – 25, 2001.

Najim, S. E., A. C. Styles, and N. Syred, "Flame Movement Mechanisms and Characteristics of Gas Fired Cyclone Combustors," 18th Symposium (International) on Combustion, The Combustion Institute, 1949 — 1957, 1981.

Naughton, J. *et al*., "Integrated Computational/Experimental Study of Turbulence Modification and Mixing Enhancement in Swirling Jets", Report UWAA-2009-01, 2009.

Naughton, J. W. *et al*., "Measurements in the Near Field of a Swirling Jet Using CTA, LDA, and PLS", 45th AIAA Aerospace Sciences and Meeting Exhibit, AIAA 2007-52, Reno, Nevada, January 8-11, 2007.

Nelson, R. C., "The Trailing Vortex Wake Hazard: Beyond the Takeoff and Landing Corridors", Atmospheric Flight Mechanics Conference and Exhibit, AIAA 2004-5171, Providence, Rhode Island, August 16-19, 2004.

Nematollahi, M. R. and M. Nazifi, "Enhancement of Heat Transfer in a Typical Pressurized Water Reactor by New Mixing Vanes on Spacer Grids", ICENES, 2007.

Newman, B. G., "Flow in a Viscous Trailing Vortex", *The Aeronautical Quarterly*, 149 – 162, May 1959.

Nirmolo, A., "Optimization of Radial Jets Mixing in Cross-Flow of Combustion Chambers Using Computational Fluid Dynamics", Ph.D. Diss., Otto-von-Guericke U. of Magdeburg, Germany, 2007.

Nishino, K. *et al*., "Turbulence Statistics in the Stagnation Region of an Axisymmetric Impinging Jet Flow", *Int. J. Heat and Fluid Flow*, Vol. 17, No. 3, 193 – 201, June 1996.

Nozaki, A., Y. Igarashi, and K. Hishida, "Heat Transfer Mechanism of a Swirling Impinging Jet in a Stagnation Region", *Heat Transfer—Asian Research*, Vol. 32, No. 8, 663 – 673, 2003.

NRC, "Next Generation Nuclear Plant Licensing Strategy A Report to Congress", US Nuclear Regulatory Commission, 2008.

O'Doherty, T. *et al*., "Experimental Analysis of Rotating Instabilities in Swirling and Cyclonic Flows", *Dev. Chem. Eng. Mineral Process*., Vol. 7, No. ¾, 245 – 267, 1999.

Ogawa, A., *Vortex Flow*, CRC Press, 1993.

Okulov, V. L. and J. N. Sorensen, "Applications of 2D Helical Vortex Dynamics", *Theor. Comput. Fluid Dyn*., Vol. 24, 395 – 401, 2010.

Olendraru, C. and A. Sellier, "Inviscid Instability of the Batchelor Vortex: Absolute-Convective Transition and Spatial Branches", *Physics of Fluids*, Vol. 11, No. 7, 1805 – 1820, 1999.

Olivier, T. J. and S. P. Nowlen, "A Phenomena Identification and Ranking Table (PIRT) Exercise for Nuclear Power Plant Fire Modeling Applications", Sandia National Laboratories, NUREG/CR-6978, SAND2008-3997P, 2008.

ORNL, "Can the Next Generation Take the Heat?",
http://www.ornl.gov/info/ornlreview/v37_1_04/article_02.shtml. Accessed on
March 25, 2010.

Ortega-Casanova, J. and R. Fernandez-Feria, "Three-Dimensional Transitions in a
Swirling Jet Impinging Against a Solid Wall at Moderate Reynolds Numbers",
Physics of Fluids, Vol. 21, 2009.

Ovadia, D. Z., "Impingement Oven Airflow Devices and Methods", US Patent 6320165,
http://www.patentstorm.us/patents/6320165/fulltext.html, 2001. Accessed on
March 25, 2010.

Pandya, S. A., S. M. Murman, and V. Sankaran, "Unsteady Computations of a Jet in
Crossflow with Ground Effect", 33rd AIAA Fluid Dynamics Conference and
Exhibit, Orlando, Florida, AIAA 2003-3890, June 23-26, 2003.

Paraview, www.paraview.org. Accessed on March 5, 2010.

Park, B. H. and Y. O. Han, "Evolution of Tip Vortices Generated by Two Bladed Rotor
in Hover at Early Wake Ages", *Int. J. of Aeronautical & Space Sciences*, Vol. 10,
No. 2, 106 – 116, 2009.

Paschereit, C. O., E. Gutmark, and W. Weisenstein, "Coherent Structures in Swirling
Flows and their Role in Acoustic Combustion Control", *Physics of Fluids*, Vol.
11, No. 9, 2667 – 2678, 1999.

Paschereit, C. O., P. Flohr, and E. J. Gutmark, "Combustion Control by Vortex
Breakdown Stabilization", *J. of Turbomachinery*, Transactions of ASME, Vol.
128, 679 – 688, 2006.

Patankar, S. V., D. K. Basu, and S. A. Alpay, "Prediction of the Three-Dimensional Velocity Field of a Deflected Turbulent Jet", *J. of Fluids Engineering*, 758 – 762, 1977.

Petti, D., "NGNP Technology Development Status", FY 2009 Office of Nuclear Energy, University Program Workshop, Bethesda, MD, August 19-20, 2008.

Prandtl, L., "Uber die Ausgebildete Turbulenz", *Zeits. f. angew. Math. u. Mech.*, Vol. 5, 136 – 139, 1925.

Prandtl, L., "Bemerkungen zur Theorie der Freien Turbulenz", *Zeits. f. angew. Math. u. Mech.*, Vol. 22, 241 – 243, 1942.

Pratte, B. D. and W. D. Baines, "Profiles of Round Turbulent Jets in a Cross Flow", Proceedings of the American Society of Civil Engineers, *J. Hydraulics Div.*, Vol. 92, 53 – 64, 1967.

Price, J. F., "Lagrangian and Eulerian Representations of Fluid Flow: Kinematics and the Equations of Motion", Woods Hole Oceanographic Institution, Woods Hole, Maine, 2006.

PRO/ENGINEER, http://www.ptc.com/products/proengineer, 2009. Accessed on April 12, 2011.

Qi, S., A. K. Gupta, and M. J. Lewis, "Effect of Swirl on Temperature Distribution in Premixed Flames", *AIAA*, Aerospace Sciences Meeting & Exhibit, 35th, AIAA-97-0373, Reno, Nevada, January 6-9, 1997.

Rajaratnam, N., "Turbulent Jets", Developments in Water Science, Vol. 5, Elsevier Scientific Publishing Co., Amsterdam, 1976.

Rankine, W. J., *A Manual of Applied Mechanics*, 9th Ed., C. Griffin and Co., London, UK, 1858.

Reichardt, H., "Gesetzmassigkeiten der Freien Turbulenz", *VDI-Forschungsheft*, Vol. 414, 1942.

Richardson, L. F., *Weather Prediction by Numerical Process*, Cambridge University Press, London, England, 1922.

Richter, W. M., "Swirling Oscillation Coffee Maker", US Patent 5957035, 1999.

Rivero, A., J. A. Ferre, and F. Giralt, "Organized Motions in a Jet in Crossflow", *J. Fluid Mech.*, Vol. 444, 117 – 149, 2001.

Rodriguez, S. B. *et al.*, "Transient Analysis of Sulfur-Iodine Cycle Experiments and Very High Temperature Reactor Simulations Using MELCOR-H2", *Nuclear Technology Journal*, NT 4-08027, Vol. 166, 2009.

Rodriguez, S. B. and M. S. El-Genk, "Using Helicoids to Eliminate 'Hot Streaking' and Stratification in the Very High Temperature Reactor Lower Plenum", *Proceedings of ICAPP '08*, American Nuclear Society, Paper 8079, Anaheim, CA, 2008a.

Rodriguez, S. B. and M. S. El-Genk, "On Eliminating 'Hot Streaking' and Stratification in the VHTR Lower Plenum Using Helicoid Inserts", *HTR-08*, American Society of Mechanical Engineers, Paper 58292, Washington, DC, 2008b.

Rodriguez, S. B. and M. S. El-Genk, "Numerical Investigation of Potential Elimination of 'Hot Streaking' and Stratification in the VHTR Lower Plenum using Helicoid Inserts", *Nuclear Engineering and Design Journal*, Vol. 240, 995 – 1004, 2010a.

Rodriguez, S. B. and M. S. El-Genk, "Cooling of an Isothermal Plate Using a Triangular Array of Swirling Air Jets", 14th International Heat Transfer Conference, Washington DC, 2010b.

Rodriguez, S. B. and M. S. El-Genk, "On Enhancing VHTR Lower Plenum Heat Transfer and Mixing via Swirling Jets", *Proceedings of ICAPP '10,* Paper 10160, San Diego, CA, 2010c.

Rodriguez, S. B. and M. S. El-Genk, "Heat Transfer and Flow Field Characterization of a Triangular Array of Swirling Jets Impinging on an Adiabatic Plate," *Proc. 14th Int. Heat Transfer Conference*, Washington DC, 2010d.

Rodriguez, S. B., S. Domino, and M. S. El-Genk, "Safety Analysis of the NGNP Lower Plenum Using the Fuego CFD Code", CFD4NRS-3 Workshop, Experimental Validation and Application of CFD and CMFD Codes to Nuclear Reactor Safety Issues, Washington D.C., September 14-16, 2010.

Rodriguez, S. B. and M. S. El-Genk, "Recent Advances in Modeling Axisymmetric Swirl and Applications for the Enhancement of Heat Transfer and Flow Mixing", *Heat Transfer*, ISBN: 978-953-307-317-0, 2011a.

Rodriguez, S. B. and M. S. El-Genk, "Coupled Computational Fluid Dynamics and Heat Transfer Analysis of the VHTR Lower Plenum", Proceedings of ICAPP-11, Paper 11247, Nice, France, May 2-5, 2011b.

Rogallo, R. S. and P. Moin, "Numerical Simulation of Turbulent Flows", *Ann. Rev. Fluid Mech.*, Vol. 16, 99 – 137, 1984.

Rose, W. G., "A Swirling Round Turbulent Jet—Mean-Flow Measurements", *ASME J. Applied Mechanics*, Vol. 84, No. 3, 615 – 625, 1962.

Roshko, A., "Experiments of the Flow Past a Circular Cylinder at Very High Reynolds Number", Guggenheim Aeronautical Laboratory, California Institute of Technology, Pasadena, California, 345 – 356, 1960.

Rossi, M., "Of Vortices and Vortical Layers: An Overview", Laboratoire de Modelisation en Mecanique, Paris, France, 2006.

Rott, N., "On the Viscous Core of a Line Vortex", *Zeitschrift fur Angewandte Mathematik und Physik*, Vol. 9b, 543 – 553, 1958.

Rott, N., "On the Viscous Core of a Line Vortex II", *Zeitschrift fur Angewandte Mathematik und Physik*, Vol. 10, 73 – 81, 1959.

Rusak, Z. and D. Lamb, "Prediction of Vortex Breakdown in Leading-Edge Vortices Above Slender Delta Wings", *J. of Aircraft*, Vol. 36, No. 4, 659 – 667, 1999.

Rusak, Z. and J. H. Lee, "The Critical Swirl of Compressible Vortex Flows", 40th AIAA Aerospace Science Meeting & Exhibit, Reno, Nevada, AIAA 2002-0159, January 14-17, 2002.

Rusak, Z. and S. Wang, "Review of Theoretical Approaches to the Vortex Breakdown Phenomenon", 1st AIAA Theoretical Fluid Mechanics Meeting, New Orleans, Louisiana, June 17-20, 1996.

Saghbini, J.-C. J. and A. F. Ghoniem, "Numerical Simulation of the Dynamics and Mixing in a Swirling Flow", 35th Aerospace Sciences Meeting & Exhibit, AIAA 97-0507, Reno, Nevada, January 6-9, 1997.

Salewski, M. and L. Fuchs, "Dispersion of Circular, Non-Circular, and Swirling Spray
Jets in Crossflow", Lund University, Division of Fluid Dynamics, 2005.

Schlichting, H., *Zeits. f. angew. Math. u. Mech.*, Vol. 13, 260 – 263, 1933.

Schlichting, H., *Boundary Layer Theory*, McGraw-Hill Book Company, 7th Edition, New
York, 1979.

Schluter, J. U., "Large-Eddy Simulations of Combustion Instability Suppression by Static
Turbulence Control", Center for Turbulence Research, Annual Research Briefs,
119 – 120, 2001.

Schultz, R. R. *et al.*, "Next Generation Nuclear Plant—Design Methods Development
and Validation Research and Development Program Plan", INEEL/EXT-04-
02293, Idaho National Engineering and Environmental Laboratory, 2004.

Semaan, R. and J. Naughton, "Evaluation of Similarity Theory for Weakly Swirling Jets
using LDA Measurements", Abstract submitted for the DFD09 Meeting of the
American Physical Society, 2009.

Semaan, R. and J. W. Naughton, "Three Component LDA Measurements in the Near and
Far Field of Swirling Jets", 46th AIAA Aerospace Sciences Meeting and Exhibit,
Reno, Nevada, January 7-10, 2010.

Semaan, R., J. Naughton, and F. D. Ewing, "Approach Toward Similar Behavior of a
Swirling Jet Flow," 47th AIAA Aerospace Sciences Meeting, Orlando, Florida,
Paper No. 2009-1114, 2009.

Senda M. *et al.*, "Heat Transfer and Fluid Flow Characteristics in Swirling Impinging
Jet", *Heat Transfer—Asian Research*, Vol. 34, Vol. 5, 324 – 335, 2005.

Sereno, J. L., J. M. C. Pereira, and J. C. F. Pereira, "A Stochastic Lamb-Oseen Vortex Solution of the 2D Navier-Stokes Equation", *Commun. Numer. Meth. Engng.*, 2009.

Serre, E. and P. Bontoux, "Vortex Breakdown in a Three-Dimensional Swirling Flow", *J. Fluid Mech.*, Vol. 459, 347 – 370, 2002.

Shah, P. N., D. D. Mobed, and Z. S. Spakovszky, "Engine Air-Brakes for Quiet Air Transport", 45th AIAA Aerospace Sciences Meeting and Exhibit, AIAA 2007-1033, Reno, Nevada, January 8-11, 2007.

Sheen, H. J., W. J. Chen, and S. Y. Jeng, "Recirculation Zones of Unconfined and Confined Annular Swirling Jets", *AIAA Journal*, Vol. 34, No. 3, 572 – 579, 1996.

Shiri, A. F., W. K. George, and J. W. Naughton, "An Experimental Study of the Far-Field of Incompressible Swirling Jets," *AIAA Journal,* Vol. 46, No. 8, 2002 – 2009, 2008.

Shiri, A. F., W. K. George, and S. Toutiaei, "Evaluation of Closure Hypotheses Using Recent Experimental Data on the Similarity Region of Swirling Jet Flows," Ankara Int. Aerospace Conference, Ankara, Turkey, Paper AIAC-2007-051, 2007.

Shtern V. and F. Hussain, "Collapse, Symmetry Breaking, and Hysteresis in Swirling Flows", *Annu. Rev. Fluid Mech.,* Vol. 31, 537 – 566, 1999.

Shtern, V. and P. G. Drazin, "Instability of a Free Swirling Jet Driven by a Half-Line Vortex", *Proc. R. Soc. Lond. A*, Vol. 456, No. 1997, 1139 – 1161, 2000.

Singh, G., T. Sundararajan, and K. A. Bhaskaran, "Mixing and Entrainment Characteristics of Circular and Noncircular Confined Jets", *J. of Fluids Engineering*, Transactions of the ASME, Vol. 125, 835 – 842, 2003.

Sipp, D., F. Coppens, and L. Jacquin, "Theoretical and Numerical Analysis of Wake Vortices", Third International Workshop on Vortex Flows and Related Numerical Methods, ESAIM: Proceedings, Vol.7, 397 – 407, 1999.

Sivakumar, D. and B. N. Raghunandan, "Converging Swirling Liquid Jets from Pressure Swirl Atomizers: Effect of Inner Air Pressure", *Physics of Fluids*, Vol. 14, No. 12, 4389 – 4398, 2002.

Smagorinsky, J., "General Circulation Experiments with the Primitive Equations I. The Basic Experiment", Dept. of Commerce, *Monthly Weather Report*, Vol. 91, No. 3, 99 – 164, 1963.

Sodja, J., "Turbulence Models in CFD", University of Ljubljana, 2007.

Som, S. K., "Theoretical and Experimental Studies on the Formation of an Air Core in a Swirl Spray Pressure Nozzle Using a Power Law Non-Newtonian Liquid", *Applied Scientific Research*, Vol. 40, 71 – 91, 1983.

Southworth, F. H. *et al*., "Next Generation Nuclear Plant (NGNP) Project – Preliminary Assessment of Two Possible Designs", 14th Pacific Basin Nuclear Conference, INEEL/CON-03-01014, Paper 91915, March 21-25, 2004.

Squire, H. B., "The Growth of a Vortex in a Turbulent Flow", *The Aeronautical Quarterly*, Vol. 16, Part 1, 302 – 306, 1965.

Stein, O., "Large Eddy Simulation of Combustion in Swirling and Opposed Jet Flows", Ph.D. Diss., Imperial College London, March 2009.

Stoellinger, M. K. and C. P. Zemtsop, "A RANS-LES Study of Swirling and Non-Swirling Jets", 45th AIAA Aerospace Sciences Meeting and Exhibit, AIAA 2007-925, Reno, Nevada, January 8-11, 2007.

Sucec, J. and W. W. Bowley, "Prediction of the Trajectory of a Turbulent Jet Injected into a Crossflowing Stream", *J. of Fluids Engineering*, 667 – 673, 1976.

Sullivan, R. D., "A Two-Cell Vortex Solution of the Navier-Stokes Equations", *J. of the Aerospace Sciences*, Vol. 26, No. 11, 767 – 768, 1959.

Syred, N. and J. M. Beer, "Combustion in Swirling Flows: A Review", *Combustion and Flame*, Vol. 23, 143 – 201, 1974.

Taglia, C. D. *et al.*, "Numerical and Experimental Investigation of an Annular Jet Flow with Large Blockage", *J. of Fluids Engineering*, Vol. 126, No. 375, 2004.

Takahashi, N. and T. Miyazaki, "Interaction between a Columnar Vortex and External Turbulence", IUTAM Symposium on Elementary Vortices and Coherent Structures: Significance in Turbulence Dynamics, 31 – 38, 2006.

Tam, K. K., "A Note on the Flow in a Trailing Vortex", *J. of Engineering Mathematics*, Vol. 7, No. 1, 1 – 6, 1973.

Taub, G. *et al.*, "A Numerical Investigation of Swirling Turbulent Buoyant Jets at Transient Reynolds Numbers", 48th AIAA Aerospace Sciences Meeting, AIAA 2010-1362, Orlando, Florida, January 4-7, 1 – 12, 2010.

Taylor, G. I., "The Boundary Layer in the Converging Nozzle of a Swirl Atomizer", *The Quarterly Journal of Mechanics and Applied Mathematics*, Vol. 3, No. 2, 129 – 139, 1950.

Taylor, G. I. and A. E. Green, "Mechanism of the Production of Small Eddies from Large Ones", *Proceedings of the Royal Society of London, Series A, Mathematical and Physical Sciences*, Vol. 158, No. 895, 499 – 521, 1937.

Todreas, N. E. and M. S. Kazimi, *Nuclear Systems I Thermal Hydraulic Fundamentals*, Hemisphere Publishing Corporation, 1990.

Toh, I. K., D. Honnery, and J. Soria, "Axial Plus Tangential Entry Swirling Jet", *Exp. Fluids*, Vol. 48, 309 – 325, 2010.

Tollmein, W., "Berechnung Turbulenter Ausbreitungsvorgange", *Zeits. f. angew. Math. u. Mech.*, Vol. 6, 468 – 478, 1926.

Tong, A. Y., "A Numerical Study on the Hydrodynamics and Heat Transfer of a Circular Liquid Jet Impinging onto a Substrate", *Numerical Heat Transfer*, Part A, Vol. 44, 1 – 19, 2003.

Toutiaei, S., R. C. Semaan, and J. W. Naughton, "Reynolds Stress and Turbulence Kinetic Energy Balances in Incompressible Swirling Jets", 48th AIAA Aerospace Sciences Meeting, AIAA 2010-105, Orlando, Florida, January 4-7, 2010.

Tsukker, M. S., "A Swirled Jet Propagating in the Space Filled with the Same Fluid", *Prikladnaja Matematika i Mehanika*, Vol. 19, No. 4, 500 – 503, 1955.

Tutar, M. and A. E. Holdo, "Computational Modeling of Flow around a Circular Cylinder in Sub-Critical Flow Regime with Various Turbulence Models", *Int. J. for Numerical Methods in Fluids*, Vol. 35, 763 – 784, 2001.

Uddin, N. *et al.*, "Thermal & Flow Field Analysis of Turbulent Swirling Jet Impingement Using Large Eddy Simulation", Universitat Stuttgart, Germany, 302 – 313, 2009.

Umeh, C. O. *et al.*, "Experimental and Computational Study of Non-Reacting Vortex Breakdown in a Swirl-Stabilized Combustor", 47th AIAA Aerospace Sciences Meeting, AIAA 2009-643, Orlando, Florida, January 5-8, 2009.

Valera-Medina, A., N. Syred, and A. Griffiths, "Large Coherent Structures Visualization in a Swirl Burner", 14th Int. Symp. on Applications of Laser Techniques to Fluid Mechanics, Lisbon, Portugal, July 7-10, 2008.

Valera-Medina, A., N. Syred, and A. Griffiths, "Characterization of Large Coherent Structures in a Swirl Burner under Combustion Conditions", 47th AIAA Aerospace Sciences Meeting Including the New Horizons Forum and Aerospace Exposition, AIAA 2009-646, 1-19, Orlando, Florida, January 5-8, 2009.

Valera-Medina *et al.*, "Studies of Large Coherent Structures and Their Effects on Swirl Combustion", 48th AIAA Aerospace Sciences Meeting, Orlando, AIAA 2010-1168, Florida, January 4-7, 2010.

Vanierschot, M. and E. Van den Bulck, "Influence of Swirl on the Initial Merging Zone of a Turbulent Annular Jet", *Physics of Fluids*, Vol. 20, No. 10, 105104, 2008.

Vanoverberghe, K., "Flow, Turbulence and Combustion of Premixed Swirling Jet Flames", Ph.D. Diss., Katholieke Universiteit Leuven, January 2004.

Vatistas, G. H., V. Kozel, and W. C. Mih, "A Simpler Model for Concentrated Vortices", *Experiments in Fluids*, Vol. 11, 73 – 76, 1991.

Vilim, R. B., W. D. Pointer, and T. Y. C. Wei, "Prioritization of VHTR System Modeling Needs Phenomena Identification, Ranking and Sensitivity Studies", Argonne National Laboratory, ANL-GenIV-071, 2006.

Voke, P. and S. Gao, "Numerical Study of Heat Transfer from an Impinging Jet", *Int. J. Heat Mass Transfer,* Vol. 41, 671 – 680, 1997.

Walther, J. H. *et al.*, "A Numerical Study of the Stability of Helical Vortices Using Vortex Methods", *J. of Physics*, Conference Series, Vol. 75, 1 – 17, 2007.

Wang, P. and X. S. Bai, "Large Eddy Simulation and Experimental Studies of a Confined Turbulent Swirling Flow", *Physics of Fluids*, Vol. 16, No. 9, 3306 – 3324, September 2004.

Watson, E. A. and J. S. Clarke, "Combustion and Combustion Equipment for Aero Gas Engines", *J. Inst. Fuel*, Vol. 21, 572 – 579, 1947.

Wen, M.-Y., "Flow Structures and Heat Transfer of Swirling Jet Impinging on a Flat Surface with Micro-Vibrations", *Int. J. and Mass Transfer*, Vol. 48, 545 – 560, 2005.

Werle, H., "Sur l'eclatement des Tourbillons d'apex d'une Aile Delta aux Faibles Vitesses", *Res. Aero.*, Vol. 23, No. 74, Paris, France, 1960.

White, F., *Viscous Fluid Flow*, 2nd Edition, McGraw-Hill, Inc., 1991.

Whitehead, E. J., "The Stability of Multiple Wing-Tip Vortices", The University of Adelaide, Ph.D. Diss., 2009.

Wigeland, R. A., M. Ahmed, and H. M. Nagib, "Management of Swirling Flows with an

  Application to Wind Tunnel Design", *AIAA Journal*, Vol. 16, No. 11, 1125 –

  1131, 1978.

Wikipedia, "Next Generation Nuclear Plant",

  http://en.wikipedia.org/wiki/Next_Generation_Nuclear_Plant. Accessed on

  March 22, 2010a.

Wikipedia, "Karman Vortex Street",

  http://en.wikipedia.org/wiki/K%C3%A1rm%C3%A1n_vortex_street. Accessed

  on February 2010b.

Wikipedia, "Jonathan Swift", http://en.wikipedia.org/wiki/Jonathan_Swift#Poems.

  (Jonathan Swift poem, "On Poetry: A Rhapsody", 1733.) Accessed on January 6,

  2011a.

Wikipedia, "Direct Numerical Simulation",

  http://en.wikipedia.org/wiki/Direct_numerical_simulation. Accessed on January

  10, 2011b.

Wilcox, D. C., "Turbulence Modeling for CFD", DCW Industries, 2nd edition, 1998.

Williamson, C. H. K., "Oblique and Parallel Modes of Vortex Shedding in the Wake of a

  Circular Cylinder at Low Reynolds Numbers", *J. Fluid Mech.*, Vol. 206, 579 –

  627, 1989.

Witze P. O. and H. A. Dwyer, "The Turbulent Radial Jet", *J. Fluid Mech.*, Vol. 75, Part

  3, 401 – 417, 1976.

Won-Wook, K. and S. Menon, "LES of Turbulent Fuel/Air Mixing in a Swirling Combustor", 37th AIAA Aerospace Sciences Meeting and Exhibit, A99-16124, Reno, Nevada, January 11-14, 1999.

World Nuclear News, "Teams Compete for NGNP Design", http://www.world-nuclear-news.org/NN_Teams_compete_for_NGNP_design_0903101.html. Accessed on March 22, 2010.

Yang, S.-C. and L.-C. Chen, "Swirl Generator with Axial Vanes", United States Patent No. 5,186,607, 1993.

Yongqiang, F., "Aerodynamics and Combustion of Axial Swirlers", Ph.D. Diss., University of Cincinnati, January 2008.

Young, D. L., C. B. Liao, and H. J. Sheen, "Computations of Recirculation Zones of a Confined Annular Swirling Flow", *Int. J. Numer. Mech. Fluids*, Vol. 29, 791 – 810, 1999.

Zemtsop, C. P. *et al*., "Large-Eddy Simulation of Swirling Turbulent Jet Flows in Absence of Vortex Breakdown", *AIAA Journal*, Vol. 47, No. 12, 2009.

Zioutis, C. K. *et al*., "Influence of Helicopter Rotor Wake Modeling on Blade Airload Predictions", *Int. J. of Engineering*, Vol. 3, Is. 6, 521 – 537, 2010.

APPENDICES

Appendix A: Research Publications

The following publications are direct spin-offs of the current research:

Rodriguez, S. B. and M. S. El-Genk, "Using Helicoids to Eliminate 'Hot Streaking' and Stratification in the Very High Temperature Reactor Lower Plenum", *Proceedings of ICAPP '08*, American Nuclear Society, Paper 8079, Anaheim, CA, 2008a.

Rodriguez, S. B. and M. S. El-Genk, "On Eliminating 'Hot Streaking' and Stratification in the VHTR Lower Plenum Using Helicoid Inserts", *HTR-08*, American Society of Mechanical Engineers, Paper 58292, Washington, DC, 2008b.

Rodriguez, S. B. and M. S. El-Genk, "Numerical Investigation of Potential Elimination of 'Hot Streaking' and Stratification in the VHTR Lower Plenum using Helicoid Inserts", *Nuclear Engineering and Design Journal*, Vol. 240, 995 – 1004, 2010a.

Rodriguez, S. B. and M. S. El-Genk, "Cooling of an Isothermal Plate Using a Triangular Array of Swirling Air Jets", 14th International Heat Transfer Conference, Washington DC, 2010b.

Rodriguez, S. B. and M. S. El-Genk, "On Enhancing VHTR Lower Plenum Heat Transfer and Mixing via Swirling Jets", *Proceedings of ICAPP '10,* Paper 10160, San Diego, CA, 2010c.

Rodriguez, S. B. and M. S. El-Genk, "Heat Transfer and Flow Field Characterization of a Triangular Array of Swirling Jets Impinging on an Adiabatic Plate," *Proc. 14th Int. Heat Transfer Conference*, Washington DC, 2010d.

Rodriguez, S. B., S. Domino, and M. S. El-Genk, "Safety Analysis of the NGNP Lower Plenum Using the Fuego CFD Code", CFD4NRS-3 Workshop, Experimental Validation and Application of CFD and CMFD Codes to Nuclear Reactor Safety Issues, Washington D.C., September 14-16, 2010.

Rodriguez, S. B. and M. S. El-Genk, "Recent Advances in Modeling Axisymmetric Swirl and Applications for the Enhancement of Heat Transfer and Flow Mixing", *Heat Transfer*, ISBN: 978-953-307-317-0, 2011a.

Rodriguez, S. B. and M. S. El-Genk, "Coupled Computational Fluid Dynamics and Heat Transfer Analysis of the VHTR Lower Plenum", Proceedings of ICAPP-11, Paper 11247, Nice, France, May 2-5, 2011b.

Appendix B: Fuego LP Input Deck

The Fuego LP input deck is listed below.

BEGIN SIERRA FUEGO

User Subroutine file = u_bc.F

User Subroutine file = v_bc.F

User Subroutine file = w_bc.F

TITLE VHTR LP Model with lower plate

$ Includes LP chrome-moly-SS lower plate and four hot channels...

$===

$

$ Assign material properties to element blocks here.

$

$===

BEGIN FINITE ELEMENT MODEL LPchamber

Database Name = VHTR_LP_Fluid.g

Database Type = EXODUSII

BEGIN PARAMETERS FOR BLOCK block_1

MATERIAL cantera_fuego_material

END   PARAMETERS FOR BLOCK block_1

END   FINITE ELEMENT MODEL LPchamber

BEGIN FINITE ELEMENT MODEL LPplate

Database Name = VHTR_LP_plate.g

Database Type = EXODUSII

Use Material LPplate for block_2

$$$begin parameters for block block_2

$$$material LPplate

$$$end parameters for block block_2

END   FINITE ELEMENT MODEL LPplate

$===

$

$ Define a material property set here.

$

$===

BEGIN PROPERTY SPECIFICATION FOR FUEGO MATERIAL

cantera_fuego_material

CANTERA XML FILE = HeliumAir.xml

REFERENCE PRESSURE = 1.0 # reference pressure is in ATM

REFERENCE TEMPERATURE = 298.0

REFERENCE MASS_FRACTION O2 = 0.00022

REFERENCE MASS_FRACTION N2 = 0.00078

REFERENCE MASS_FRACTION He = 0.999

SCHMIDT_NUMBER = 0.9

PRANDTL_NUMBER = 0.9

END   PROPERTY SPECIFICATION FOR FUEGO MATERIAL

cantera_fuego_material

BEGIN PROPERTY SPECIFICATION FOR MATERIAL LPplate

$$$ Model plate as chrome-moly steel.

DENSITY   = 7560. # kg/m3

SPECIFIC_HEAT   = 460. # J/kg-K

THERMAL_CONDUCTIVITY function = k_LPplate # W/m-K

END   PROPERTY SPECIFICATION FOR MATERIAL LPplate

$===

$ Define the functions here.

$===

BEGIN DEFINITION FOR FUNCTION k_LPplate

TYPE IS PIECEWISE LINEAR

ABSCISSA = temperature

  BEGIN VALUES

   293.1 26.0

   473.1 27.0

   673.1 28.5

  END VALUES

END DEFINITION FOR FUNCTION k_LPplate

$ RESTART TIME = 38.

RESTART = automatic

$==

$

$ Define the global constants here, no gravity

$

$==

BEGIN GLOBAL CONSTANTS turb

 K-E TURBULENCE MODEL PARAMETER CMU = 0.09

 K-E TURBULENCE MODEL PARAMETER SIGMA_K = 1.0

 K-E TURBULENCE MODEL PARAMETER SIGMA_E = 1.3

 K-E TURBULENCE MODEL PARAMETER CEPS_1 = 1.44

 K-E TURBULENCE MODEL PARAMETER CEPS_2 = 1.92

TURBULENCE MODEL SCHMIDT NUMBER = 0.9

TURBULENCE MODEL PRANDTL NUMBER = 0.9

END   GLOBAL CONSTANTS turb


```
$===============================================================

$

$  Define the linear solver parameteres here.

$

$===============================================================
```


BEGIN trilinos EQUATION SOLVER continuity

  SOLUTION METHOD   = gmres

  PRECONDITIONING METHOD = multilevel

  PRECONDITIONING STEPS   = 1

  RESTART ITERATIONS   = 200 #sbr100

  MAXIMUM ITERATIONS   = 200

  RESIDUAL NORM TOLERANCE = 1.0e-07 #sbr1.e-5

  RESIDUAL NORM SCALING   = R0

  PARAM-BOOL "ML validate parameter list" VALUE false

END   trilinos EQUATION SOLVER continuity

BEGIN trilinos EQUATION SOLVER scalar

  SOLUTION METHOD   = gmres

```
    PRECONDITIONING METHOD  = DD-ILUT   #sbr symmetric-gauss-seidel

    PRECONDITIONING STEPS   = 1

    RESTART ITERATIONS      = 200 #sbr50

    MAXIMUM ITERATIONS      = 200 #sbr100

    RESIDUAL NORM TOLERANCE = 1.0e-07  #sbr1.e-4

    RESIDUAL NORM SCALING   = R0

    BC ENFORCEMENT = exact
  END   trilinos EQUATION SOLVER scalar


  BEGIN trilinos EQUATION SOLVER conduction

    SOLUTION METHOD        = cg

    PRECONDITIONING METHOD  = jacobi

    PRECONDITIONING STEPS   = 1

    RESTART ITERATIONS      = 200

    MAXIMUM ITERATIONS      = 200

    RESIDUAL NORM TOLERANCE = 1.0e-07

    RESIDUAL NORM SCALING  = R0

  END   trilinos EQUATION SOLVER conduction



$===============================================================

$

$  Begin the Fuego procedure (integration of equations).

$
```

```
$=============================================================

  BEGIN FUEGO PROCEDURE fuego_procedure

   DEBUG LEVEL = 0


$=============================================================

$

$  Define the parameters for time integration over an interval here.

$

$=============================================================


  Begin Solution Control Description

   Use System Main

   begin initialize mytransient_init
     advance fluid_region
     transfer solid_fluid
     advance solid_region
     transfer solid_fluid
   end initialize mytransient_init
```

```
Begin System Main

  use initialize mytransient_init

  Begin Transient startup

    advance fluid_region

    transfer fluid_solid

    advance solid_region

    transfer solid_fluid

  end Transient startup

end System Main


Begin Parameters For Transient startup

  start time = 0.0

  initial deltat = 0.00065 ###5.0e-03

  termination time = 15.0

  time step style nosnap noclip

  Begin Parameters For Fuego Region fluid_region

    transient step type is automatic

    CFL LIMIT = 4.0 ###2.0 ####10.

    TIME STEP CHANGE FACTOR = 1.2

  END   Parameters For Fuego Region fluid_region


  Begin Parameters For Calore Region solid_region

    transient step type   = automatic
```

time integration rule = trapezoid

predictor rule   = adams bashforth

mass matrix   = lumped

time step   = 5.0e-03

min time step   = 1.0e-04

max time step   = 0.1

max time trunc error = 1.0e-04

End Parameters For Calore Region solid_region

end Parameters For Transient startup

end Solution Control Description

$sbr08062010

$sbr10212010

$==

$ Set up a transfer for conjugate heat transfer

$==

begin TRANSFER Fluid_Solid

interpolate surface nodes from fluid_region to solid_region

send block surface_6 to surface_7

send field convection_coefficient state none to hvar state none

send field convection_temperature state none to tvar state none

```
        SEARCH SURFACE GAP TOLERANCE = 1.0e-02

    end


    begin TRANSFER Solid_Fluid

        interpolate surface nodes from solid_region to fluid_region

        send block surface_7 to surface_6

        send field temperature state new to wall_temperature state none

        SEARCH SURFACE GAP TOLERANCE = 1.0e-02

    end



$===============================================================

$

$  Begin the Fuego region (evauation of equations within a time step).

$

$===============================================================



    BEGIN FUEGO REGION fluid_region



$===============================================================

$ Provide the following conversion factors so that FUEGO is in CGS.

    SET MASS   UNIT CONVERSION FACTOR = 1000.0  # kg to g

    SET LENGTH UNIT CONVERSION FACTOR =  100.0  # m to cm

$===============================================================
```

```
$===============================================================

$  Use Steering file

$===============================================================


$sbr10212010     USE SOLUTION STEERING WITH INTERVAL = 10


$===============================================================

$

$ Select the math model configuration for this run.

$

$===============================================================


   BEGIN SOLUTION OPTIONS


      # turn on equations as needed

      ACTIVATE EQUATION Continuity

      ACTIVATE EQUATION X_Momentum

      ACTIVATE EQUATION Y_Momentum

      ACTIVATE EQUATION Z_Momentum

      ACTIVATE EQUATION Enthalpy

$sbr 08202007   ACTIVATE EQUATION Turbulent Kinetic Energy

$sbr 08202007   ACTIVATE EQUATION Turbulence Dissipation
```

PROJECTION METHOD = fourth_order smoothing with timestep SCALING

specify the nonlinear iterations for the system

MINIMUM NUMBER OF NONLINEAR ITERATIONS = 1

MAXIMUM NUMBER OF NONLINEAR ITERATIONS = 2 $$$$sbr02162010   2

$sbr12012009 Increase max nonlinear iter to 2 per Stefan Domino. $old value=1.

MAXIMUM NUMBER OF CONTINUITY_MOMENTUM NONLINEAR

ITERATIONS = 3

attach solvers to the equations

USE EQUATION SOLVER continuity FOR EQUATION Continuity

USE EQUATION SOLVER scalar FOR EQUATION X_Momentum

USE EQUATION SOLVER scalar FOR EQUATION Y_Momentum

USE EQUATION SOLVER scalar FOR EQUATION Z_Momentum

USE EQUATION SOLVER scalar FOR EQUATION Enthalpy

$sbr08202007 USE EQUATION SOLVER scalar FOR EQUATION Turbulent Kinetic

Energy

$sbr08202007 USE EQUATION SOLVER scalar FOR EQUATION Turbulence

Dissipation

 # set upwinding

 FIRST ORDER UPWIND FACTOR = 0.2 ####sbr0.15

$sbr 11042009 UPWIND METHOD = UPW

upwind method = muscl

upwind limiter = van_leer $$$$ minmod $$$$$superbee

$sbr04162010   FIRST ORDER UPWIND FACTOR = 0.0 FOR EQUATION

X_Momentum

$sbr04162010   FIRST ORDER UPWIND FACTOR = 0.0 FOR EQUATION

Y_Momentum

$sbr04162010   FIRST ORDER UPWIND FACTOR = 0.0 FOR EQUATION

Z_Momentum

$sbr 11042009

$sbr04162010   HYBRID UPWIND FACTOR = 0.0 FOR EQUATION

X_Momentum

$sbr04162010   HYBRID UPWIND FACTOR = 0.0 FOR EQUATION

Y_Momentum

$sbr04162010   HYBRID UPWIND FACTOR = 0.0 FOR EQUATION

Z_Momentum

set under-relaxation

$sbr 08202007   UNDER RELAX Turbulence Dissipation   by 0.75

$sbr 08202007   UNDER RELAX Turbulent Kinetic Energy by 0.75

UNDER RELAX Momentum   by 0.8

UNDER RELAX Pressure   by 0.8

UNDER RELAX Enthalpy   by 0.8

        # set number of species for the material model

$sbr   NUMBER OF SPECIES IS 3

BEGIN TURBULENCE MODEL SPECIFICATION

TURBULENCE MODEL = KE

LIMIT TURBULENT KE PRODUCTION TO 200. TIMES DISSIPATION

TIME FILTER = 0.008

INCLUDE MOLECULAR VISCOSITY IN K-E DIFFUSION COEFFICIENT

UNDER RELAX Turbulent_Viscosity by 0.80

END TURBULENCE MODEL SPECIFICATION

     BEGIN TURBULENCE MODEL SPECIFICATION

       TURBULENCE MODEL = DSMAG

      END   TURBULENCE MODEL SPECIFICATION

     END SOLUTION OPTIONS

$===

$

$ Select the mesh, defined at the Domain level.

$

```
$================================================================

      USE FINITE ELEMENT MODEL LPchamber


$================================================================

$

$  Begin the definition of the contents of the plot file

$  for this region.

$

$================================================================


    Begin Results Output Label output

       DATABASE Name = LPchamber.e

$sbr    At Step 0, Increment = 10 $10   plot frequency

#      at time 0, increment = 0.02 $plot frequency

#      ---------------------------#

    At time 0, increment = 0.50

#      ---------------------------#

    TITLE Turbulent jet with swirl device

    NODAL Variables = pressure       AS Pnd

    NODAL Variables = temperature    AS T_fluid

#     Nodal Variables = turb_visc_nd   AS Tvisc

    NODAL Variables = x_velocity     AS U $Und
```

NODAL Variables = y_velocity   AS V $Vnd

NODAL Variables = z_velocity   AS W $Wnd

NODAL Variables = enthalpy   AS Hnd

$sbr 08202007   NODAL Variables = turbulent_ke   AS K $Knd

$sbr 08202007   NODAL Variables = turbulent_diss AS E $End

NODAL Variables = convection_coefficient   AS htc

NODAL Variables = convection_temperature   AS Tcv

End   Results Output Label output

$==

$ Set up u, v, and w to get u', v', and w' with Paraview

   begin averaging

     reynolds average field x_velocity as u_ave

     reynolds average field y_velocity as v_ave

     reynolds average field z_velocity as w_ave

     starting time = 0.0

     time interval length = 0.0001

   end averaging

$==

$==

$

$ Begin the definition of the restart file

$ for this region.

$

$==

$sbr   Begin Restart Data restart

$sbr#   Input Database Name   = open_jetWall.rsout1

$sbr   Input Database Name   = swirljet.rsout1

$sbr   Output Database Name   = swirljet.rsout1

$sbr   At Step 1 Increment   = 200

$sbr   End Restart Data restart

$==

$

$ Set the initial condition for this region.

$

$==

    Begin Initial Condition Block fluid

      volume is block_1

      pressure = 0.0

      x_velocity = 0.0

      y_velocity = 0.0

z_velocity = 0.0

temperature = 1273.0

End Initial Condition Block fluid

Begin Initial Condition Block blah2

volume is block_2

pressure = 0.0

x_velocity = 0.0

y_velocity = 0.0

z_velocity = 0.0

temperature = 1273.0

End Initial Condition Block blah2

$==

$

$ Define the boundary conditions for this region.

$

$==

$sbr10212010 Add conjugate heat transfer boundary....

begin wall boundary condition on surface surface_6

interface boundary

end   wall boundary condition on surface surface_6

```
$ Manifold exit -- open boundary

begin open boundary condition on surface surface_2

  pressure = 0.0

  temperature = 1273.0

end   open boundary condition on surface surface_2


$ Symmetry boundary -- approximate 1/2 LP

begin symmetry boundary condition on surface surface_3

 pressure = 0.0

 temperature = 1273.0

end   symmetry boundary condition on surface surface_3


$    $ Support tube outer surfaces -- act as wall surface

begin  wall boundary condition on surface surface_4

end    wall boundary condition on surface surface_4


#####    $ All other exterior LP surfaces except the LPplate -- act as wall surface

#####     begin  wall boundary condition on surface surface_5

#####     end    wall boundary condition on surface surface_5


$ LP plate -- acts as wall surface  !!!!!sbr later make convective/radiative BC...

begin  wall boundary condition on surface surface_5
```

end   wall boundary condition on surface surface_5

$ Begin swirling jet entries, sidesets 103 through 1519, not inclusive.

$ All the swirling jet inlet sidesets are three or four digit numbers. The three digit

numbers

$ are those in which the column is less than 10, i.e. "710" is row 7 column 10.

$ # Surface 1 represents the 1/2 circle helicoids that were cut by the 1/2 symmetry.

$ begin inflow boundary condition on surface surface_1

$#   subroutine for x_velocity = u_bc

$#   subroutine for y_velocity = v_bc

$ subroutine for z_velocity = w_bc

$ temperature = 1273.0

$ end   inflow boundary condition on surface surface_1

$$$!!!!sbr: set these pesky 1/2 BCs as zero inflow for now!!!

    begin inflow boundary condition on surface surface_103

      x_velocity = 0.0

      y_velocity = 0.0

      z_velocity = 0.0

      temperature = 1273.0

    end   inflow boundary condition on surface surface_103

begin inflow boundary condition on surface surface_106

  x_velocity = 0.0

  y_velocity = 0.0

  z_velocity = 0.0

  temperature = 1273.0

end   inflow boundary condition on surface surface_106

begin inflow boundary condition on surface surface_127

  x_velocity = 0.0

  y_velocity = 0.0

  z_velocity = 0.0

  temperature = 1273.0

end   inflow boundary condition on surface surface_127

begin inflow boundary condition on surface surface_130

  x_velocity = 0.0

  y_velocity = 0.0

  z_velocity = 0.0

  temperature = 1273.0

end   inflow boundary condition on surface surface_130

$$$!!!!sbr: set these pesky 1/2 BCs as zero inflow for now!!!

begin inflow boundary condition on surface surface_201

real data for subroutine u_bc = 9.77798221996 9.86301778004

subroutine for x_velocity = u_bc

real data for subroutine v_bc = 12.688313 12.774223

subroutine for y_velocity = v_bc

subroutine for z_velocity = w_bc

   temperature = 1273.0

end   inflow boundary condition on surface surface_201

begin inflow boundary condition on surface surface_204

real data for subroutine u_bc = 9.7471 9.8939

subroutine for x_velocity = u_bc

real data for subroutine v_bc = 12.2433344 12.3901344

subroutine for y_velocity = v_bc

subroutine for z_velocity = w_bc

   temperature = 1273.0

end   inflow boundary condition on surface surface_204

begin inflow boundary condition on surface surface_205

real data for subroutine u_bc = 9.7471 9.8939

subroutine for x_velocity = u_bc

real data for subroutine v_bc = 12.0360676 12.1828676

subroutine for y_velocity = v_bc

subroutine for z_velocity = w_bc

temperature = 1273.0

end   inflow boundary condition on surface surface_205

begin inflow boundary condition on surface surface_208

  real data for subroutine u_bc = 9.77798221996 9.86301778004

  subroutine for x_velocity = u_bc

  real data for subroutine v_bc = 11.651973 11.737883

  subroutine for y_velocity = v_bc

  subroutine for z_velocity = w_bc

    temperature = 1273.0

end   inflow boundary condition on surface surface_208

begin inflow boundary condition on surface surface_225

  real data for subroutine u_bc = 9.77798221996 9.86301778004

  subroutine for x_velocity = u_bc

  real data for subroutine v_bc = 8.957489 9.043399

  subroutine for y_velocity = v_bc

  subroutine for z_velocity = w_bc

    temperature = 1273.0

end   inflow boundary condition on surface surface_225

begin inflow boundary condition on surface surface_228

  real data for subroutine u_bc = 9.7471 9.8939

subroutine for x_velocity = u_bc

  real data for subroutine v_bc = 8.512532 8.659332

  subroutine for y_velocity = v_bc

  subroutine for z_velocity = w_bc

    temperature = 1273.0

end   inflow boundary condition on surface surface_228

begin inflow boundary condition on surface surface_229

  real data for subroutine u_bc = 9.7471 9.8939

  subroutine for x_velocity = u_bc

  real data for subroutine v_bc = 8.3052652 8.4520652

  subroutine for y_velocity = v_bc

  subroutine for z_velocity = w_bc

    temperature = 1273.0

end   inflow boundary condition on surface surface_229

begin inflow boundary condition on surface surface_232

  real data for subroutine u_bc = 9.77798221996 9.86301778004

  subroutine for x_velocity = u_bc

  real data for subroutine v_bc = 7.921149 8.007059

  subroutine for y_velocity = v_bc

  subroutine for z_velocity = w_bc

    temperature = 1273.0

end   inflow boundary condition on surface surface_232

begin inflow boundary condition on surface surface_302

  real data for subroutine u_bc = 9.581493429 9.70050786422

  subroutine for x_velocity = u_bc

  real data for subroutine v_bc = 12.567799 12.687469

  subroutine for y_velocity = v_bc

  subroutine for z_velocity = w_bc

    temperature = 1273.0

end   inflow boundary condition on surface surface_302

Lower RHS hot channel BC

begin inflow boundary condition on surface surface_303

  real data for subroutine u_bc = 9.56760168584 9.71440168584

  subroutine for x_velocity = u_bc

  real data for subroutine v_bc = 12.3469678 12.4937678

  subroutine for y_velocity = v_bc

  subroutine for z_velocity = w_bc

    temperature = 1473.0

end   inflow boundary condition on surface surface_303

begin inflow boundary condition on surface surface_306

  real data for subroutine u_bc = 9.56760168584 9.71440168584

subroutine for x_velocity = u_bc

   real data for subroutine v_bc = 11.9324342 12.0792342

   subroutine for y_velocity = v_bc

   subroutine for z_velocity = w_bc

      temperature = 1273.0

end   inflow boundary condition on surface surface_306

begin inflow boundary condition on surface surface_307

   real data for subroutine u_bc = 9.581493429 9.70050786422

   subroutine for x_velocity = u_bc

   real data for subroutine v_bc = 11.738727 11.858397

   subroutine for y_velocity = v_bc

   subroutine for z_velocity = w_bc

      temperature = 1273.0

end   inflow boundary condition on surface surface_307

begin inflow boundary condition on surface surface_326

   real data for subroutine u_bc = 9.581493429 9.70050786422

   subroutine for x_velocity = u_bc

   real data for subroutine v_bc = 8.836975 8.956645

   subroutine for y_velocity = v_bc

   subroutine for z_velocity = w_bc

      temperature = 1273.0

end   inflow boundary condition on surface surface_326

begin inflow boundary condition on surface surface_327

  real data for subroutine u_bc = 9.56760168584 9.71440168584

  subroutine for x_velocity = u_bc

  real data for subroutine v_bc = 8.6161654 8.7629654

  subroutine for y_velocity = v_bc

  subroutine for z_velocity = w_bc

    temperature = 1273.0

end   inflow boundary condition on surface surface_327

begin inflow boundary condition on surface surface_330

  real data for subroutine u_bc = 9.56760168584 9.71440168584

  subroutine for x_velocity = u_bc

  real data for subroutine v_bc = 8.2016318 8.3484318

  subroutine for y_velocity = v_bc

  subroutine for z_velocity = w_bc

    temperature = 1273.0

end   inflow boundary condition on surface surface_330

begin inflow boundary condition on surface surface_331

  real data for subroutine u_bc = 9.581493429 9.70050786422

  subroutine for x_velocity = u_bc

real data for subroutine v_bc = 8.007903 8.127573

  subroutine for y_velocity = v_bc

  subroutine for z_velocity = w_bc

    temperature = 1273.0

end   inflow boundary condition on surface surface_331

begin inflow boundary condition on surface surface_401

  real data for subroutine u_bc = 9.41898351318 9.5040190732

  subroutine for x_velocity = u_bc

  real data for subroutine v_bc = 12.688313 12.774223

  subroutine for y_velocity = v_bc

  subroutine for z_velocity = w_bc

    temperature = 1273.0

end   inflow boundary condition on surface surface_401

begin inflow boundary condition on surface surface_404

  real data for subroutine u_bc = 9.38810337168 9.53490337168

  subroutine for x_velocity = u_bc

  real data for subroutine v_bc = 12.2433344 12.3901344

  subroutine for y_velocity = v_bc

  subroutine for z_velocity = w_bc

    temperature = 1273.0

end   inflow boundary condition on surface surface_404

begin inflow boundary condition on surface surface_405

  real data for subroutine u_bc = 9.38810337168 9.53490337168

  subroutine for x_velocity = u_bc

  real data for subroutine v_bc = 12.0360676 12.1828676

  subroutine for y_velocity = v_bc

  subroutine for z_velocity = w_bc

    temperature = 1273.0

end   inflow boundary condition on surface surface_405

begin inflow boundary condition on surface surface_408

  real data for subroutine u_bc = 9.41898351318 9.50401907325

  subroutine for x_velocity = u_bc

  real data for subroutine v_bc = 11.651973 11.737883

  subroutine for y_velocity = v_bc

  subroutine for z_velocity = w_bc

    temperature = 1273.0

end   inflow boundary condition on surface surface_408

begin inflow boundary condition on surface surface_425

  real data for subroutine u_bc = 9.41898351318 9.50401907325

  subroutine for x_velocity = u_bc

  real data for subroutine v_bc = 8.957489 9.043399

subroutine for y_velocity = v_bc

subroutine for z_velocity = w_bc

temperature = 1273.0

end   inflow boundary condition on surface surface_425

begin inflow boundary condition on surface surface_428

real data for subroutine u_bc = 9.38810337168 9.53490337168

subroutine for x_velocity = u_bc

real data for subroutine v_bc = 8.512532 8.659332

subroutine for y_velocity = v_bc

subroutine for z_velocity = w_bc

temperature = 1273.0

end   inflow boundary condition on surface surface_428

begin inflow boundary condition on surface surface_429

real data for subroutine u_bc = 9.38810337168 9.53490337168

subroutine for x_velocity = u_bc

real data for subroutine v_bc = 8.3052652 8.4520652

subroutine for y_velocity = v_bc

subroutine for z_velocity = w_bc

temperature = 1273.0

end   inflow boundary condition on surface surface_429

begin inflow boundary condition on surface surface_432

  real data for subroutine u_bc = 9.41898351318 9.50401907325

  subroutine for x_velocity = u_bc

  real data for subroutine v_bc = 7.921149 8.007059

  subroutine for y_velocity = v_bc

  subroutine for z_velocity = w_bc

    temperature = 1273.0

end   inflow boundary condition on surface surface_432

begin inflow boundary condition on surface surface_502

  real data for subroutine u_bc = 9.22249472222 9.34150915743

  subroutine for x_velocity = u_bc

  real data for subroutine v_bc = 12.567799 12.687469

  subroutine for y_velocity = v_bc

  subroutine for z_velocity = w_bc

    temperature = 1273.0

end   inflow boundary condition on surface surface_502

begin inflow boundary condition on surface surface_503

  real data for subroutine u_bc = 9.20860505752 9.35540505752

  subroutine for x_velocity = u_bc

  real data for subroutine v_bc = 12.3469678 12.4937678

  subroutine for y_velocity = v_bc

subroutine for z_velocity = w_bc

  temperature = 1273.0

end   inflow boundary condition on surface surface_503

begin inflow boundary condition on surface surface_506

  real data for subroutine u_bc = 9.20860505752 9.35540505752

  subroutine for x_velocity = u_bc

  real data for subroutine v_bc = 11.9324342 12.0792342

  subroutine for y_velocity = v_bc

  subroutine for z_velocity = w_bc

  temperature = 1273.0

end   inflow boundary condition on surface surface_506

begin inflow boundary condition on surface surface_507

  real data for subroutine u_bc = 9.22249472222 9.34150915743

  subroutine for x_velocity = u_bc

  real data for subroutine v_bc = 11.738727 11.858397

  subroutine for y_velocity = v_bc

  subroutine for z_velocity = w_bc

    temperature = 1273.0

end   inflow boundary condition on surface surface_507

begin inflow boundary condition on surface surface_526

real data for subroutine u_bc = 9.22249472222 9.34150915743

  subroutine for x_velocity = u_bc

  real data for subroutine v_bc = 8.836975 8.956645

  subroutine for y_velocity = v_bc

  subroutine for z_velocity = w_bc

    temperature = 1273.0

end   inflow boundary condition on surface surface_526

begin inflow boundary condition on surface surface_527

  real data for subroutine u_bc = 9.20860505752 9.35540505752

  subroutine for x_velocity = u_bc

  real data for subroutine v_bc = 8.6161654 8.7629654

  subroutine for y_velocity = v_bc

  subroutine for z_velocity = w_bc

    temperature = 1273.0

end   inflow boundary condition on surface surface_527

begin inflow boundary condition on surface surface_530

  real data for subroutine u_bc = 9.20860505752 9.35540505752

  subroutine for x_velocity = u_bc

  real data for subroutine v_bc = 8.2016318 8.3484318

  subroutine for y_velocity = v_bc

  subroutine for z_velocity = w_bc

temperature = 1273.0

end   inflow boundary condition on surface surface_530

begin inflow boundary condition on surface surface_531

  real data for subroutine u_bc = 9.22249472222 9.34150915743

  subroutine for x_velocity = u_bc

  real data for subroutine v_bc = 8.007903 8.127573

  subroutine for y_velocity = v_bc

  subroutine for z_velocity = w_bc

    temperature = 1273.0

end   inflow boundary condition on surface surface_531

begin inflow boundary condition on surface surface_601

  real data for subroutine u_bc = 9.0599848064 9.14502036647

  subroutine for x_velocity = u_bc

  real data for subroutine v_bc = 12.688313 12.774223

  subroutine for y_velocity = v_bc

  subroutine for z_velocity = w_bc

    temperature = 1273.0

end   inflow boundary condition on surface surface_601

begin inflow boundary condition on surface surface_604

  real data for subroutine u_bc = 9.02910674336 9.17590674336

subroutine for x_velocity = u_bc

  real data for subroutine v_bc = 12.2433344 12.3901344

  subroutine for y_velocity = v_bc

  subroutine for z_velocity = w_bc

    temperature = 1273.0

end   inflow boundary condition on surface surface_604

begin inflow boundary condition on surface surface_605

  real data for subroutine u_bc = 9.02910674336 9.17590674336

  subroutine for x_velocity = u_bc

  real data for subroutine v_bc = 12.0360676 12.1828676

  subroutine for y_velocity = v_bc

  subroutine for z_velocity = w_bc

    temperature = 1273.0

end   inflow boundary condition on surface surface_605

begin inflow boundary condition on surface surface_608

  real data for subroutine u_bc = 9.04299536882 9.16200980404

  subroutine for x_velocity = u_bc

  real data for subroutine v_bc = 11.635093 11.754763

  subroutine for y_velocity = v_bc

  subroutine for z_velocity = w_bc

    temperature = 1273.0

end   inflow boundary condition on surface surface_608

begin inflow boundary condition on surface surface_609

  real data for subroutine u_bc = 9.0599848064 9.14502036647

  subroutine for x_velocity = u_bc

  real data for subroutine v_bc = 11.444705 11.530615

  subroutine for y_velocity = v_bc

  subroutine for z_velocity = w_bc

     temperature = 1273.0

end   inflow boundary condition on surface surface_609

begin inflow boundary condition on surface surface_624

  real data for subroutine u_bc = 9.0599848064 9.14502036647

  subroutine for x_velocity = u_bc

  real data for subroutine v_bc = 9.164757 9.250667

  subroutine for y_velocity = v_bc

  subroutine for z_velocity = w_bc

     temperature = 1273.0

end   inflow boundary condition on surface surface_624

begin inflow boundary condition on surface surface_625

  real data for subroutine u_bc = 9.04299536882 9.16200980404

  subroutine for x_velocity = u_bc

real data for subroutine v_bc = 8.940609 9.060279

subroutine for y_velocity = v_bc

subroutine for z_velocity = w_bc

temperature = 1273.0

end   inflow boundary condition on surface surface_625

begin inflow boundary condition on surface surface_628

real data for subroutine u_bc = 9.02910674336 9.17590674336

subroutine for x_velocity = u_bc

real data for subroutine v_bc = 8.512532 8.659332

subroutine for y_velocity = v_bc

subroutine for z_velocity = w_bc

temperature = 1273.0

end   inflow boundary condition on surface surface_628

LHS by exit hot channel BC

begin inflow boundary condition on surface surface_629

real data for subroutine u_bc = 9.02910674336 9.17590674336

subroutine for x_velocity = u_bc

real data for subroutine v_bc = 8.3052652 8.4520652

subroutine for y_velocity = v_bc

subroutine for z_velocity = w_bc

temperature = 1473.0

end   inflow boundary condition on surface surface_629

begin inflow boundary condition on surface surface_632

  real data for subroutine u_bc = 9.0599848064 9.14502036647

  subroutine for x_velocity = u_bc

  real data for subroutine v_bc = 7.921149 8.007059

  subroutine for y_velocity = v_bc

  subroutine for z_velocity = w_bc

    temperature = 1273.0

end   inflow boundary condition on surface surface_632

begin inflow boundary condition on surface surface_702

  real data for subroutine u_bc = 8.88048545301 8.96552101308

  subroutine for x_velocity = u_bc

  real data for subroutine v_bc = 12.584679 12.670589

  subroutine for y_velocity = v_bc

  subroutine for z_velocity = w_bc

    temperature = 1273.0

end   inflow boundary condition on surface surface_702

begin inflow boundary condition on surface surface_703

  real data for subroutine u_bc = 8.86349601543 8.98251045065

  subroutine for x_velocity = u_bc

real data for subroutine v_bc = 12.360531 12.480201

  subroutine for y_velocity = v_bc

  subroutine for z_velocity = w_bc

    temperature = 1273.0

end   inflow boundary condition on surface surface_703

begin inflow boundary condition on surface surface_706

  real data for subroutine u_bc = 8.84960842919 8.99640842919

  subroutine for x_velocity = u_bc

  real data for subroutine v_bc = 11.9324342 12.0792342

  subroutine for y_velocity = v_bc

  subroutine for z_velocity = w_bc

    temperature = 1273.0

end   inflow boundary condition on surface surface_706

begin inflow boundary condition on surface surface_707

  real data for subroutine u_bc = 8.84960842919 8.99640842919

  subroutine for x_velocity = u_bc

  real data for subroutine v_bc = 11.7251674 11.8719674

  subroutine for y_velocity = v_bc

  subroutine for z_velocity = w_bc

    temperature = 1273.0

end   inflow boundary condition on surface surface_707

begin inflow boundary condition on surface surface_710

  real data for subroutine u_bc = 8.86349601543 8.98251045065

  subroutine for x_velocity = u_bc

  real data for subroutine v_bc = 11.324191 11.443861

  subroutine for y_velocity = v_bc

  subroutine for z_velocity = w_bc

    temperature = 1273.0

end   inflow boundary condition on surface surface_710

begin inflow boundary condition on surface surface_711

  real data for subroutine u_bc = 8.88048545301 8.96552101308

  subroutine for x_velocity = u_bc

  real data for subroutine v_bc = 11.133803 11.219713

  subroutine for y_velocity = v_bc

  subroutine for z_velocity = w_bc

    temperature = 1273.0

end   inflow boundary condition on surface surface_711

begin inflow boundary condition on surface surface_722

  real data for subroutine u_bc = 8.88048545301 8.96552101308

  subroutine for x_velocity = u_bc

  real data for subroutine v_bc = 9.475659 9.561569

subroutine for y_velocity = v_bc

subroutine for z_velocity = w_bc

temperature = 1273.0

end   inflow boundary condition on surface surface_722

begin inflow boundary condition on surface surface_723

real data for subroutine u_bc = 8.86349601543 8.98251045065

subroutine for x_velocity = u_bc

real data for subroutine v_bc = 9.251511 9.371181

subroutine for y_velocity = v_bc

subroutine for z_velocity = w_bc

temperature = 1273.0

end   inflow boundary condition on surface surface_723

begin inflow boundary condition on surface surface_726

real data for subroutine u_bc = 8.84960842919 8.99640842919

subroutine for x_velocity = u_bc

real data for subroutine v_bc = 8.8234322 8.9702322

subroutine for y_velocity = v_bc

subroutine for z_velocity = w_bc

temperature = 1273.0

end   inflow boundary condition on surface surface_726

begin inflow boundary condition on surface surface_727

  real data for subroutine u_bc = 8.84960842919 8.99640842919

  subroutine for x_velocity = u_bc

  real data for subroutine v_bc = 8.6161654 8.7629654

  subroutine for y_velocity = v_bc

  subroutine for z_velocity = w_bc

  temperature = 1273.0

end   inflow boundary condition on surface surface_727

begin inflow boundary condition on surface surface_730

  real data for subroutine u_bc = 8.86349601543 8.98251045065

  subroutine for x_velocity = u_bc

  real data for subroutine v_bc = 8.215171 8.334841

  subroutine for y_velocity = v_bc

  subroutine for z_velocity = w_bc

    temperature = 1273.0

end   inflow boundary condition on surface surface_730

begin inflow boundary condition on surface surface_731

  real data for subroutine u_bc = 8.88048545301 8.96552101308

  subroutine for x_velocity = u_bc

  real data for subroutine v_bc = 8.024783 8.110693

  subroutine for y_velocity = v_bc

subroutine for z_velocity = w_bc

   temperature = 1273.0

end   inflow boundary condition on surface surface_731

begin inflow boundary condition on surface surface_804

  real data for subroutine u_bc = 8.68399666204 8.80301109726

  subroutine for x_velocity = u_bc

  real data for subroutine v_bc = 12.256897 12.376567

  subroutine for y_velocity = v_bc

  subroutine for z_velocity = w_bc

   temperature = 1273.0

end   inflow boundary condition on surface surface_804

begin inflow boundary condition on surface surface_805

  real data for subroutine u_bc = 8.67011011503 8.81691011503

  subroutine for x_velocity = u_bc

  real data for subroutine v_bc = 12.0360676 12.1828676

  subroutine for y_velocity = v_bc

  subroutine for z_velocity = w_bc

   temperature = 1273.0

end   inflow boundary condition on surface surface_805

begin inflow boundary condition on surface surface_808

real data for subroutine u_bc = 8.67011011503 8.81691011503

  subroutine for x_velocity = u_bc

  real data for subroutine v_bc = 11.621534 11.768334

  subroutine for y_velocity = v_bc

  subroutine for z_velocity = w_bc

    temperature = 1273.0

end   inflow boundary condition on surface surface_808

begin inflow boundary condition on surface surface_809

  real data for subroutine u_bc = 8.67011011503 8.81691011503

  subroutine for x_velocity = u_bc

  real data for subroutine v_bc = 11.4142672 11.5610672

  subroutine for y_velocity = v_bc

  subroutine for z_velocity = w_bc

    temperature = 1273.0

end   inflow boundary condition on surface surface_809

begin inflow boundary condition on surface surface_812

  real data for subroutine u_bc = 8.68399666204 8.80301109726

  subroutine for x_velocity = u_bc

  real data for subroutine v_bc = 11.013289 11.132959

  subroutine for y_velocity = v_bc

  subroutine for z_velocity = w_bc

temperature = 1273.0

end   inflow boundary condition on surface surface_812

begin inflow boundary condition on surface surface_813

  real data for subroutine u_bc = 8.70098609961 8.78602165969

  subroutine for x_velocity = u_bc

  real data for subroutine v_bc = 10.822901 10.908811

  subroutine for y_velocity = v_bc

  subroutine for z_velocity = w_bc

    temperature = 1273.0

end   inflow boundary condition on surface surface_813

begin inflow boundary condition on surface surface_820

  real data for subroutine u_bc = 8.70098609961 8.78602165969

  subroutine for x_velocity = u_bc

  real data for subroutine v_bc = 9.786561 9.872471

  subroutine for y_velocity = v_bc

  subroutine for z_velocity = w_bc

    temperature = 1273.0

end   inflow boundary condition on surface surface_820

begin inflow boundary condition on surface surface_821

  real data for subroutine u_bc = 8.68399666204 8.80301109726

subroutine for x_velocity = u_bc

real data for subroutine v_bc = 9.562413 9.682083

subroutine for y_velocity = v_bc

subroutine for z_velocity = w_bc

temperature = 1273.0

end   inflow boundary condition on surface surface_821

begin inflow boundary condition on surface surface_824

real data for subroutine u_bc = 8.67011011503 8.81691011503

subroutine for x_velocity = u_bc

real data for subroutine v_bc = 9.1343324 9.2811324

subroutine for y_velocity = v_bc

subroutine for z_velocity = w_bc

temperature = 1273.0

end   inflow boundary condition on surface surface_824

begin inflow boundary condition on surface surface_825

real data for subroutine u_bc = 8.67011011503 8.81691011503

subroutine for x_velocity = u_bc

real data for subroutine v_bc = 8.9270656 9.0738656

subroutine for y_velocity = v_bc

subroutine for z_velocity = w_bc

temperature = 1273.0

end   inflow boundary condition on surface surface_825

begin inflow boundary condition on surface surface_828

  real data for subroutine u_bc = 8.67011011503 8.81691011503

  subroutine for x_velocity = u_bc

  real data for subroutine v_bc = 8.512532 8.659332

  subroutine for y_velocity = v_bc

  subroutine for z_velocity = w_bc

     temperature = 1273.0

end   inflow boundary condition on surface surface_828

begin inflow boundary condition on surface surface_829

  real data for subroutine u_bc = 8.68399666204 8.80301109726

  subroutine for x_velocity = u_bc

  real data for subroutine v_bc = 8.318805 8.438475

  subroutine for y_velocity = v_bc

  subroutine for z_velocity = w_bc

     temperature = 1273.0

end   inflow boundary condition on surface surface_829

begin inflow boundary condition on surface surface_903

  real data for subroutine u_bc = 8.52148674622 8.60652230629

  subroutine for x_velocity = u_bc

real data for subroutine v_bc = 12.377411 12.463321

  subroutine for y_velocity = v_bc

  subroutine for z_velocity = w_bc

    temperature = 1273.0

end   inflow boundary condition on surface surface_903

begin inflow boundary condition on surface surface_906

  real data for subroutine u_bc = 8.49061180087 8.63741180087

  subroutine for x_velocity = u_bc

  real data for subroutine v_bc = 11.9324342 12.0792342

  subroutine for y_velocity = v_bc

  subroutine for z_velocity = w_bc

    temperature = 1273.0

end   inflow boundary condition on surface surface_906

begin inflow boundary condition on surface surface_907

  real data for subroutine u_bc = 8.49061180087 8.63741180087

  subroutine for x_velocity = u_bc

  real data for subroutine v_bc = 11.7251674 11.8719674

  subroutine for y_velocity = v_bc

  subroutine for z_velocity = w_bc

    temperature = 1273.0

end   inflow boundary condition on surface surface_907

begin inflow boundary condition on surface surface_910

  real data for subroutine u_bc = 8.49061180087 8.63741180087

  subroutine for x_velocity = u_bc

  real data for subroutine v_bc = 11.3106338 11.4574338

  subroutine for y_velocity = v_bc

  subroutine for z_velocity = w_bc

    temperature = 1273.0

end   inflow boundary condition on surface surface_910

begin inflow boundary condition on surface surface_911

  real data for subroutine u_bc = 8.49061180087 8.63741180087

  subroutine for x_velocity = u_bc

  real data for subroutine v_bc = 11.103367 11.250167

  subroutine for y_velocity = v_bc

  subroutine for z_velocity = w_bc

    temperature = 1273.0

end   inflow boundary condition on surface surface_911

begin inflow boundary condition on surface surface_914

  real data for subroutine u_bc = 8.50449730865 8.62351174387

  subroutine for x_velocity = u_bc

  real data for subroutine v_bc = 10.702387 10.822057

subroutine for y_velocity = v_bc

subroutine for z_velocity = w_bc

temperature = 1273.0

end   inflow boundary condition on surface surface_914

begin inflow boundary condition on surface surface_915

real data for subroutine u_bc = 8.52148674622 8.60652230629

subroutine for x_velocity = u_bc

real data for subroutine v_bc = 10.511999 10.597909

subroutine for y_velocity = v_bc

subroutine for z_velocity = w_bc

temperature = 1273.0

end   inflow boundary condition on surface surface_915

begin inflow boundary condition on surface surface_918

real data for subroutine u_bc = 8.52148674622 8.60652230629

subroutine for x_velocity = u_bc

real data for subroutine v_bc = 10.097463 10.183373

subroutine for y_velocity = v_bc

subroutine for z_velocity = w_bc

temperature = 1273.0

end   inflow boundary condition on surface surface_918

begin inflow boundary condition on surface surface_919

  real data for subroutine u_bc = 8.50449730865 8.62351174387

  subroutine for x_velocity = u_bc

  real data for subroutine v_bc = 9.873315 9.992985

  subroutine for y_velocity = v_bc

  subroutine for z_velocity = w_bc

    temperature = 1273.0

end   inflow boundary condition on surface surface_919

begin inflow boundary condition on surface surface_922

  real data for subroutine u_bc = 8.49061180087 8.63741180087

  subroutine for x_velocity = u_bc

  real data for subroutine v_bc = 9.4452326 9.5920326

  subroutine for y_velocity = v_bc

  subroutine for z_velocity = w_bc

    temperature = 1273.0

end   inflow boundary condition on surface surface_922

begin inflow boundary condition on surface surface_923

  real data for subroutine u_bc = 8.49061180087 8.63741180087

  subroutine for x_velocity = u_bc

  real data for subroutine v_bc = 9.2379658 9.3847658

  subroutine for y_velocity = v_bc

subroutine for z_velocity = w_bc

    temperature = 1273.0

end   inflow boundary condition on surface surface_923

begin inflow boundary condition on surface surface_926

  real data for subroutine u_bc = 8.49061180087 8.63741180087

  subroutine for x_velocity = u_bc

  real data for subroutine v_bc = 8.8234322 8.9702322

  subroutine for y_velocity = v_bc

  subroutine for z_velocity = w_bc

    temperature = 1273.0

end   inflow boundary condition on surface surface_926

begin inflow boundary condition on surface surface_927

  real data for subroutine u_bc = 8.49061180087 8.63741180087

  subroutine for x_velocity = u_bc

  real data for subroutine v_bc = 8.6161654 8.7629654

  subroutine for y_velocity = v_bc

  subroutine for z_velocity = w_bc

    temperature = 1273.0

end   inflow boundary condition on surface surface_927

begin inflow boundary condition on surface surface_930

real data for subroutine u_bc = 8.50449730865 8.62351174387

subroutine for x_velocity = u_bc

real data for subroutine v_bc = 8.215171 8.334841

subroutine for y_velocity = v_bc

subroutine for z_velocity = w_bc

   temperature = 1273.0

end   inflow boundary condition on surface surface_930

begin inflow boundary condition on surface surface_1004

real data for subroutine u_bc = 8.34198739283 8.4270229529

subroutine for x_velocity = u_bc

real data for subroutine v_bc = 12.273777 12.359687

subroutine for y_velocity = v_bc

subroutine for z_velocity = w_bc

   temperature = 1273.0

end   inflow boundary condition on surface surface_1004

begin inflow boundary condition on surface surface_1005

real data for subroutine u_bc = 8.32499795526 8.44401239048

subroutine for x_velocity = u_bc

real data for subroutine v_bc = 12.049629 12.169299

subroutine for y_velocity = v_bc

subroutine for z_velocity = w_bc

temperature = 1273.0

end   inflow boundary condition on surface surface_1005

Upper RHS hot channel BC

begin inflow boundary condition on surface surface_1008

  real data for subroutine u_bc = 8.31111348671 8.45791348671

  subroutine for x_velocity = u_bc

  real data for subroutine v_bc = 11.621534 11.768334

  subroutine for y_velocity = v_bc

  subroutine for z_velocity = w_bc

    temperature = 1473.0

end   inflow boundary condition on surface surface_1008

begin inflow boundary condition on surface surface_1009

  real data for subroutine u_bc = 8.31111348671 8.45791348671

  subroutine for x_velocity = u_bc

  real data for subroutine v_bc = 11.4142672 11.5610672

  subroutine for y_velocity = v_bc

  subroutine for z_velocity = w_bc

    temperature = 1273.0

end   inflow boundary condition on surface surface_1009

begin inflow boundary condition on surface surface_1012

real data for subroutine u_bc = 8.31111348671 8.45791348671

  subroutine for x_velocity = u_bc

  real data for subroutine v_bc = 10.9997336 11.1465336

  subroutine for y_velocity = v_bc

  subroutine for z_velocity = w_bc

    temperature = 1273.0

end   inflow boundary condition on surface surface_1012

begin inflow boundary condition on surface surface_1013

  real data for subroutine u_bc = 8.31111348671 8.45791348671

  subroutine for x_velocity = u_bc

  real data for subroutine v_bc = 10.7924668 10.9392668

  subroutine for y_velocity = v_bc

  subroutine for z_velocity = w_bc

    temperature = 1273.0

end   inflow boundary condition on surface surface_1013

begin inflow boundary condition on surface surface_1016

  real data for subroutine u_bc = 8.32499795526 8.44401239048

  subroutine for x_velocity = u_bc

  real data for subroutine v_bc = 10.391485 10.511155

  subroutine for y_velocity = v_bc

  subroutine for z_velocity = w_bc

temperature = 1273.0

end   inflow boundary condition on surface surface_1016

begin inflow boundary condition on surface surface_1017

  real data for subroutine u_bc = 8.32499795526 8.44401239048

  subroutine for x_velocity = u_bc

  real data for subroutine v_bc = 10.184217 10.303887

  subroutine for y_velocity = v_bc

  subroutine for z_velocity = w_bc

     temperature = 1273.0

end   inflow boundary condition on surface surface_1017

begin inflow boundary condition on surface surface_1020

  real data for subroutine u_bc = 8.31111348671 8.45791348671

  subroutine for x_velocity = u_bc

  real data for subroutine v_bc = 9.7561328 9.9029328

  subroutine for y_velocity = v_bc

  subroutine for z_velocity = w_bc

     temperature = 1273.0

end   inflow boundary condition on surface surface_1020

begin inflow boundary condition on surface surface_1021

  real data for subroutine u_bc = 8.31111348671 8.45791348671

subroutine for x_velocity = u_bc

  real data for subroutine v_bc = 9.548866 9.695666

  subroutine for y_velocity = v_bc

  subroutine for z_velocity = w_bc

    temperature = 1273.0

end   inflow boundary condition on surface surface_1021

begin inflow boundary condition on surface surface_1024

  real data for subroutine u_bc = 8.31111348671 8.45791348671

  subroutine for x_velocity = u_bc

  real data for subroutine v_bc = 9.1343324 9.2811324

  subroutine for y_velocity = v_bc

  subroutine for z_velocity = w_bc

    temperature = 1273.0

end   inflow boundary condition on surface surface_1024

begin inflow boundary condition on surface surface_1025

  real data for subroutine u_bc = 8.31111348671 8.45791348671

  subroutine for x_velocity = u_bc

  real data for subroutine v_bc = 8.9270656 9.0738656

  subroutine for y_velocity = v_bc

  subroutine for z_velocity = w_bc

    temperature = 1273.0

end   inflow boundary condition on surface surface_1025

begin inflow boundary condition on surface surface_1028

  real data for subroutine u_bc = 8.32499795526 8.44401239048

  subroutine for x_velocity = u_bc

  real data for subroutine v_bc = 8.526073 8.645743

  subroutine for y_velocity = v_bc

  subroutine for z_velocity = w_bc

    temperature = 1273.0

end   inflow boundary condition on surface surface_1028

begin inflow boundary condition on surface surface_1029

  real data for subroutine u_bc = 8.34198739283 8.4270229529

  subroutine for x_velocity = u_bc

  real data for subroutine v_bc = 8.335685 8.421595

  subroutine for y_velocity = v_bc

  subroutine for z_velocity = w_bc

    temperature = 1273.0

end   inflow boundary condition on surface surface_1029

begin inflow boundary condition on surface surface_1106

  real data for subroutine u_bc = 8.16248803944 8.24752359951

  subroutine for x_velocity = u_bc

real data for subroutine v_bc = 11.962875 12.048785

 subroutine for y_velocity = v_bc

 subroutine for z_velocity = w_bc

    temperature = 1273.0

end   inflow boundary condition on surface surface_1106

begin inflow boundary condition on surface surface_1107

 real data for subroutine u_bc = 8.14549860187 8.26451303709

 subroutine for x_velocity = u_bc

 real data for subroutine v_bc = 11.738727 11.858397

 subroutine for y_velocity = v_bc

 subroutine for z_velocity = w_bc

    temperature = 1273.0

end   inflow boundary condition on surface surface_1107

begin inflow boundary condition on surface surface_1110

 real data for subroutine u_bc = 8.13161517255 8.27841517255

 subroutine for x_velocity = u_bc

 real data for subroutine v_bc = 11.3106338 11.4574338

 subroutine for y_velocity = v_bc

 subroutine for z_velocity = w_bc

    temperature = 1273.0

end   inflow boundary condition on surface surface_1110

begin inflow boundary condition on surface surface_1111

  real data for subroutine u_bc = 8.13161517255 8.27841517255

  subroutine for x_velocity = u_bc

  real data for subroutine v_bc = 11.103367 11.250167

  subroutine for y_velocity = v_bc

  subroutine for z_velocity = w_bc

    temperature = 1273.0

end inflow boundary condition on surface surface_1111

begin inflow boundary condition on surface surface_1114

  real data for subroutine u_bc = 8.13161517255 8.27841517255

  subroutine for x_velocity = u_bc

  real data for subroutine v_bc = 10.6888334 10.8356334

  subroutine for y_velocity = v_bc

  subroutine for z_velocity = w_bc

    temperature = 1273.0

end inflow boundary condition on surface surface_1114

begin inflow boundary condition on surface surface_1115

  real data for subroutine u_bc = 8.13161517255 8.27841517255

  subroutine for x_velocity = u_bc

  real data for subroutine v_bc = 10.4815666 10.6283666

subroutine for y_velocity = v_bc

subroutine for z_velocity = w_bc

temperature = 1273.0

end   inflow boundary condition on surface surface_1115

begin inflow boundary condition on surface surface_1118

real data for subroutine u_bc = 8.13161517255 8.27841517255

subroutine for x_velocity = u_bc

real data for subroutine v_bc = 10.067033 10.213833

subroutine for y_velocity = v_bc

subroutine for z_velocity = w_bc

temperature = 1273.0

end   inflow boundary condition on surface surface_1118

begin inflow boundary condition on surface surface_1119

real data for subroutine u_bc = 8.13161517255 8.27841517255

subroutine for x_velocity = u_bc

real data for subroutine v_bc = 9.8597662 10.0065662

subroutine for y_velocity = v_bc

subroutine for z_velocity = w_bc

temperature = 1273.0

end   inflow boundary condition on surface surface_1119

begin inflow boundary condition on surface surface_1122

  real data for subroutine u_bc = 8.13161517255 8.27841517255

  subroutine for x_velocity = u_bc

  real data for subroutine v_bc = 9.4452326 9.5920326

  subroutine for y_velocity = v_bc

  subroutine for z_velocity = w_bc

    temperature = 1273.0

end   inflow boundary condition on surface surface_1122

begin inflow boundary condition on surface surface_1123

  real data for subroutine u_bc = 8.13161517255 8.27841517255

  subroutine for x_velocity = u_bc

  real data for subroutine v_bc = 9.2379658 9.3847658

  subroutine for y_velocity = v_bc

  subroutine for z_velocity = w_bc

    temperature = 1273.0

end   inflow boundary condition on surface surface_1123

begin inflow boundary condition on surface surface_1126

  real data for subroutine u_bc = 8.14549860187 8.26451303709

  subroutine for x_velocity = u_bc

  real data for subroutine v_bc = 8.836975 8.956645

  subroutine for y_velocity = v_bc

subroutine for z_velocity = w_bc

    temperature = 1273.0

end   inflow boundary condition on surface surface_1126

begin inflow boundary condition on surface surface_1127

  real data for subroutine u_bc = 8.16248803944 8.24752359951

  subroutine for x_velocity = u_bc

  real data for subroutine v_bc = 8.646587 8.732497

  subroutine for y_velocity = v_bc

  subroutine for z_velocity = w_bc

    temperature = 1273.0

end   inflow boundary condition on surface surface_1127

begin inflow boundary condition on surface surface_1208

  real data for subroutine u_bc = 7.98298868605 8.06802424612

  subroutine for x_velocity = u_bc

  real data for subroutine v_bc = 11.651973 11.737883

  subroutine for y_velocity = v_bc

  subroutine for z_velocity = w_bc

    temperature = 1273.0

end   inflow boundary condition on surface surface_1208

begin inflow boundary condition on surface surface_1209

real data for subroutine u_bc = 7.96599924847 8.08501368369

subroutine for x_velocity = u_bc

real data for subroutine v_bc = 11.427825 11.547495

subroutine for y_velocity = v_bc

subroutine for z_velocity = w_bc

temperature = 1273.0

end   inflow boundary condition on surface surface_1209

begin inflow boundary condition on surface surface_1212

real data for subroutine u_bc = 7.95211685839 8.09891685839

subroutine for x_velocity = u_bc

real data for subroutine v_bc = 10.9997336 11.1465336

subroutine for y_velocity = v_bc

subroutine for z_velocity = w_bc

temperature = 1273.0

end   inflow boundary condition on surface surface_1212

begin inflow boundary condition on surface surface_1213

real data for subroutine u_bc = 7.95211685839 8.09891685839

subroutine for x_velocity = u_bc

real data for subroutine v_bc = 10.7924668 10.9392668

subroutine for y_velocity = v_bc

subroutine for z_velocity = w_bc

temperature = 1273.0

end   inflow boundary condition on surface surface_1213

begin inflow boundary condition on surface surface_1216

  real data for subroutine u_bc = 7.95211685839 8.09891685839

  subroutine for x_velocity = u_bc

  real data for subroutine v_bc = 10.3779332 10.5247332

  subroutine for y_velocity = v_bc

  subroutine for z_velocity = w_bc

    temperature = 1273.0

end   inflow boundary condition on surface surface_1216

begin inflow boundary condition on surface surface_1217

  real data for subroutine u_bc = 7.95211685839 8.09891685839

  subroutine for x_velocity = u_bc

  real data for subroutine v_bc = 10.1706664 10.3174664

  subroutine for y_velocity = v_bc

  subroutine for z_velocity = w_bc

    temperature = 1273.0

end   inflow boundary condition on surface surface_1217

begin inflow boundary condition on surface surface_1220

  real data for subroutine u_bc = 7.95211685839 8.09891685839

subroutine for x_velocity = u_bc

  real data for subroutine v_bc = 9.7561328 9.9029328

  subroutine for y_velocity = v_bc

  subroutine for z_velocity = w_bc

    temperature = 1273.0

end   inflow boundary condition on surface surface_1220

begin inflow boundary condition on surface surface_1221

  real data for subroutine u_bc = 7.95211685839 8.09891685839

  subroutine for x_velocity = u_bc

  real data for subroutine v_bc = 9.548866 9.695666

  subroutine for y_velocity = v_bc

  subroutine for z_velocity = w_bc

    temperature = 1273.0

end   inflow boundary condition on surface surface_1221

begin inflow boundary condition on surface surface_1224

  real data for subroutine u_bc = 7.96599924847 8.08501368369

  subroutine for x_velocity = u_bc

  real data for subroutine v_bc = 9.147877 9.267547

  subroutine for y_velocity = v_bc

  subroutine for z_velocity = w_bc

    temperature = 1273.0

end   inflow boundary condition on surface surface_1224

begin inflow boundary condition on surface surface_1225

  real data for subroutine u_bc = 7.98298868605 8.06802424612

  subroutine for x_velocity = u_bc

  real data for subroutine v_bc = 8.957489 9.043399

  subroutine for y_velocity = v_bc

  subroutine for z_velocity = w_bc

     temperature = 1273.0

end   inflow boundary condition on surface surface_1225

begin inflow boundary condition on surface surface_1310

  real data for subroutine u_bc = 7.80348933266 7.88852489273

  subroutine for x_velocity = u_bc

  real data for subroutine v_bc = 11.341071 11.426981

  subroutine for y_velocity = v_bc

  subroutine for z_velocity = w_bc

     temperature = 1273.0

end   inflow boundary condition on surface surface_1310

begin inflow boundary condition on surface surface_1311

  real data for subroutine u_bc = 7.78649989508 7.9055143303

  subroutine for x_velocity = u_bc

real data for subroutine v_bc = 11.116923 11.236593

subroutine for y_velocity = v_bc

subroutine for z_velocity = w_bc

temperature = 1273.0

end   inflow boundary condition on surface surface_1311

begin inflow boundary condition on surface surface_1314

real data for subroutine u_bc = 7.77261854423 7.91941854423

subroutine for x_velocity = u_bc

real data for subroutine v_bc = 10.6888334 10.8356334

subroutine for y_velocity = v_bc

subroutine for z_velocity = w_bc

temperature = 1273.0

end   inflow boundary condition on surface surface_1314

begin inflow boundary condition on surface surface_1315

real data for subroutine u_bc = 7.77261854423 7.91941854423

subroutine for x_velocity = u_bc

real data for subroutine v_bc = 10.4815666 10.6283666

subroutine for y_velocity = v_bc

subroutine for z_velocity = w_bc

temperature = 1273.0

end   inflow boundary condition on surface surface_1315

begin inflow boundary condition on surface surface_1318

  real data for subroutine u_bc = 7.77261854423 7.91941854423

  subroutine for x_velocity = u_bc

  real data for subroutine v_bc = 10.067033 10.213833

  subroutine for y_velocity = v_bc

  subroutine for z_velocity = w_bc

    temperature = 1273.0

end   inflow boundary condition on surface surface_1318

begin inflow boundary condition on surface surface_1319

  real data for subroutine u_bc = 7.77261854423 7.91941854423

  subroutine for x_velocity = u_bc

  real data for subroutine v_bc = 9.8597662 10.0065662

  subroutine for y_velocity = v_bc

  subroutine for z_velocity = w_bc

    temperature = 1273.0

end   inflow boundary condition on surface surface_1319

begin inflow boundary condition on surface surface_1322

  real data for subroutine u_bc = 7.78649989508 7.9055143303

  subroutine for x_velocity = u_bc

  real data for subroutine v_bc = 9.458779 9.578449

subroutine for y_velocity = v_bc

subroutine for z_velocity = w_bc

temperature = 1273.0

end   inflow boundary condition on surface surface_1322

begin inflow boundary condition on surface surface_1323

real data for subroutine u_bc = 7.80348933266 7.88852489273

subroutine for x_velocity = u_bc

real data for subroutine v_bc = 9.268391 9.354301

subroutine for y_velocity = v_bc

subroutine for z_velocity = w_bc

temperature = 1273.0

end   inflow boundary condition on surface surface_1323

begin inflow boundary condition on surface surface_1412

real data for subroutine u_bc = 7.62398997926 7.70902553934

subroutine for x_velocity = u_bc

real data for subroutine v_bc = 11.030169 11.116079

subroutine for y_velocity = v_bc

subroutine for z_velocity = w_bc

temperature = 1273.0

end   inflow boundary condition on surface surface_1412

begin inflow boundary condition on surface surface_1413

  real data for subroutine u_bc = 7.60700054169 7.72601497691

  subroutine for x_velocity = u_bc

  real data for subroutine v_bc = 10.806021 10.925691

  subroutine for y_velocity = v_bc

  subroutine for z_velocity = w_bc

    temperature = 1273.0

end   inflow boundary condition on surface surface_1413

begin inflow boundary condition on surface surface_1416

  real data for subroutine u_bc = 7.60700054169 7.72601497691

  subroutine for x_velocity = u_bc

  real data for subroutine v_bc = 10.391485 10.511155

  subroutine for y_velocity = v_bc

  subroutine for z_velocity = w_bc

    temperature = 1273.0

end   inflow boundary condition on surface surface_1416

begin inflow boundary condition on surface surface_1417

  real data for subroutine u_bc = 7.60700054169 7.72601497691

  subroutine for x_velocity = u_bc

  real data for subroutine v_bc = 10.184217 10.303887

  subroutine for y_velocity = v_bc

subroutine for z_velocity = w_bc

   temperature = 1273.0

end   inflow boundary condition on surface surface_1417

begin inflow boundary condition on surface surface_1420

  real data for subroutine u_bc = 7.60700054169 7.72601497691

  subroutine for x_velocity = u_bc

  real data for subroutine v_bc = 9.769681 9.889351

  subroutine for y_velocity = v_bc

  subroutine for z_velocity = w_bc

   temperature = 1273.0

end   inflow boundary condition on surface surface_1420

begin inflow boundary condition on surface surface_1421

  real data for subroutine u_bc = 7.62398997926 7.70902553934

  subroutine for x_velocity = u_bc

  real data for subroutine v_bc = 9.579293 9.665203

  subroutine for y_velocity = v_bc

  subroutine for z_velocity = w_bc

   temperature = 1273.0

end   inflow boundary condition on surface surface_1421

begin inflow boundary condition on surface surface_1514

real data for subroutine u_bc = 7.44449062587 7.52952618595

subroutine for x_velocity = u_bc

real data for subroutine v_bc = 10.719267 10.805177

subroutine for y_velocity = v_bc

subroutine for z_velocity = w_bc

  temperature = 1273.0

end   inflow boundary condition on surface surface_1514

begin inflow boundary condition on surface surface_1515

real data for subroutine u_bc = 7.4275011883 7.54651562352

subroutine for x_velocity = u_bc

real data for subroutine v_bc = 10.495119 10.614789

subroutine for y_velocity = v_bc

subroutine for z_velocity = w_bc

  temperature = 1273.0

end   inflow boundary condition on surface surface_1515

TOP central hot channel BC

begin inflow boundary condition on surface surface_1518

real data for subroutine u_bc = 7.4275011883 7.54651562352

subroutine for x_velocity = u_bc

real data for subroutine v_bc = 10.080583 10.200253

subroutine for y_velocity = v_bc

subroutine for z_velocity = w_bc

temperature = 1473.0

$real data for subroutine u_bc = 7.4275011883 7.54651562352

$subroutine for x_velocity = u_bc

$real data for subroutine v_bc = 10.080583 10.200253

$subroutine for y_velocity = v_bc

$subroutine for z_velocity = w_bc

$temperature = 1273.0

end   inflow boundary condition on surface surface_1518

begin inflow boundary condition on surface surface_1519

real data for subroutine u_bc = 7.44449062587 7.52952618595

subroutine for x_velocity = u_bc

real data for subroutine v_bc = 9.890195 9.976105

subroutine for y_velocity = v_bc

subroutine for z_velocity = w_bc

temperature = 1273.0

end   inflow boundary condition on surface surface_1519

END   FUEGO REGION fluid_region

BEGIN CALORE REGION solid_region

$==

$ Select the mesh, defined at the Domain level.

$==

USE FINITE ELEMENT MODEL LPplate

USE LINEAR SOLVER conduction

NUMBER OF NONLINEAR STEPS = 30

NONLINEAR CONVERGENCE TOLERANCE = 1.0e-06

$==

$ Set the initial condition for this region.

$==

Begin Initial Condition Block solid

  add volume block_2

  temperature = 1273.0

End Initial Condition Block solid

$==

$ Define the boundary conditions for this region.

$==

  $--

$ First create/define variables for transfer of BCs

```
$---------------------------------------------------------


begin user variable hvar

  type = node real length = 1

  initial value = 0

end


begin user variable tvar

  type = node real length = 1

  initial value = 1273.

end



$-------------------------------------------------------------

$  this is the boundary where conjugate heat transfer occurs

$  (top surface of LP plate block).

$-------------------------------------------------------------


begin convective flux boundary condition bc1

  add surface surface_7

  reference temperature node variable  = tvar

  convective coefficient node variable = hvar

  Integrated Power Output Qhx

end   convective flux boundary condition bc1
```

Begin History Output Power

  Title Integrated Power Output and Surface Power

  Database Name = Qhx.e

  At Time 0, Increment = 0.2

  variable is global Qhx

  End

$===

  $ Begin the definition of the contents of the plot file

$===

  Begin Results Output Label output

  Database Name = LPplate.e

At Step 0, Increment = 1

---------------------------#

  At Time 0, Increment = 0.5

---------------------------#

  TITLE Temperature in the LP Plate

  NODAL Variables = temperature AS T_solid

  NODAL Variables = hvar AS hconv

  NODAL Variables = tvar AS tconv

  End   Results Output Label output

```
  END   CALORE REGION solid_region


  END   FUEGO PROCEDURE fuego_procedure


END   SIERRA FUEGO
```

Appendix C: Maple Input Files

The following Maple input files are listed below:

C.1. Maple Script for Modified Newman.

C.2. Maple Script for Two Field Solution for NS.

C.3. Maple Script for Three Field Solution for NS.

C.4. Maple Script for Series and Plots for Loitsyanskiy Vortex.

C.5. Maple Script for Series and Plots for Vatistas Vortex.

C.6. Maple Script to Show that v(r) and w(r) Satisfy Euler and Conservation of Mass.

C.7. Maple Script to Investigate AVE Vortex, Bessel Function, and Sin-Like Attributes.

C.1. Maple Script for Modified Newman.

> **### Program for axisymmetric, ss NS for r, theta, and z velocities:**

> **### Modified Newman Vortex--the solution is ideal for Domain 2 (away from 0).**

> **### 11/10/2010.**

> **### Programmed by Sal Rodriguez.**

>

>

> **ur_exp := 0;**

$$ur\_exp := 0$$

> **utheta_exp := (A/r)*exp(-Wo*r*r/(4*nu*z));**

$$utheta\_exp \ := \frac{A\,\mathbf{e}^{\left(-1/4\,\frac{Wo\,r^2}{\nu\,z}\right)}}{r}$$

> **uz_exp := Wo;**

$$uz\_exp := Wo$$

> **NS_EXP_R := ur_exp*diff(ur_exp,r) - 0*(1/r)*(utheta_exp)^2 +**

uz_exp*diff(ur_exp,z) - nu*(diff(diff(ur_exp,r),r) + (1/r)*diff(ur_exp,r) -

(1/r^2)*(ur_exp) + diff(diff(ur_exp,z),z));

$$NS\_EXP\_R := 0$$

> **simplify(NS_EXP_R);**

$$0$$

>

> **# Do theta.**

> **NS_EXP_THETA := 0*ur_exp*diff(utheta_exp,r) + 0*(1/r)*utheta_exp*ur_exp +**

uz_exp*diff(utheta_exp,z) - nu*(diff(diff(utheta_exp,r),r) + (1/r)*diff(utheta_exp,r)

- utheta_exp/(r*r) + 0*diff(diff(utheta_exp,z),z));

$$NS\_EXP\_THETA := \frac{1}{4}\frac{Wo^2\,A\,r\,\mathbf{e}^{\left(-1/4\,\frac{Wo\,r^2}{\nu\,z}\right)}}{\nu\,z^2} - \nu\left(\frac{A\,\mathbf{e}^{\left(-1/4\,\frac{Wo\,r^2}{\nu\,z}\right)}}{r^3} + \frac{\frac{1}{2}A\,Wo\,\mathbf{e}^{\left(-1/4\,\frac{Wo\,r^2}{\nu\,z}\right)}}{r\,\nu\,z}\right.$$
$$\left.+ \frac{\frac{1}{4}A\,Wo^2\,r\,\mathbf{e}^{\left(-1/4\,\frac{Wo\,r^2}{\nu\,z}\right)}}{\nu^2\,z^2} + \frac{-\frac{A\,\mathbf{e}^{\left(-1/4\,\frac{Wo\,r^2}{\nu\,z}\right)}}{r^2} - \frac{1}{2}\frac{A\,Wo\,\mathbf{e}^{\left(-1/4\,\frac{Wo\,r^2}{\nu\,z}\right)}}{\nu\,z}}{r}\right)$$

> **simplify(NS_EXP_THETA);**

$$0$$

>

> **NS_EXP_Z := ur_exp*diff(uz_exp,r) + uz_exp*diff(uz_exp,z) - nu*(**

diff(diff(uz_exp,r),r) + (1/r)*diff(uz_exp,r) + diff(diff(uz_exp,z),z));

$$NS\_EXP\_Z := 0$$

> **simplify(NS_EXP_Z);**

>

> **##**

> **# Conservation of Mass in cylindrical coordinates, SS, axisymmetric.**

##

> **diff(ur_exp,r) + ur_exp/r + diff(uz_exp,z);**

$$0$$

> **term1_comass := diff(ur_exp,r);**

$$term1\_comass := 0$$

> **term2_comass := ur_exp/r;**

$$term2\_comass := 0$$

> **term3_comass := diff(uz_exp,z);**

$$term3\_comass := 0$$

>

> **### Do series expansion for Newman:**

> **series((Gamma/(2*Pi*r))*(1 - exp(-Wo*r*r/(4*nu*z))), r, 11);**

$$\frac{1}{8}\frac{\Gamma\,Wo}{\pi\,\nu\,z}\,r - \frac{1}{64}\frac{\Gamma\,Wo^2}{\pi\,\nu^2\,z^2}\,r^3 + \frac{1}{768}\frac{\Gamma\,Wo^3}{\pi\,\nu^3\,z^3}\,r^5 - \frac{1}{12288}\frac{\Gamma\,Wo^4}{\pi\,\nu^4\,z^4}\,r^7 + \frac{1}{245760}\frac{\Gamma\,Wo^5}{\pi\,\nu^5\,z^5}\,r^9 + O(r^{10})$$

>

> **### Now do series expansion for Mod-Newman:**

> **series(-(Gamma/(2*Pi*r))*exp(-Wo*r*r/(4*nu*z)), r, 11);**

$$-\frac{1}{2}\frac{\Gamma}{\pi}\,r^{-1}+\frac{1}{8}\frac{\Gamma\,Wo}{\pi\,\nu\,z}\,r-\frac{1}{64}\frac{\Gamma\,Wo^2}{\pi\,\nu^2\,z^2}\,r^3+\frac{1}{768}\frac{\Gamma\,Wo^3}{\pi\,\nu^3\,z^3}\,r^5-\frac{1}{12288}\frac{\Gamma\,Wo^4}{\pi\,\nu^4\,z^4}\,r^7+$$

$$\frac{1}{245760}\frac{\Gamma\,Wo^5}{\pi\,\nu^5\,z^5}\,r^9+\mathrm{O}(r^{10})$$

C.2. Maple Script for Two Field Solution for NS.

> ### Program for axisymmetric, ss NS for radial and azimuthal velocities not equal

0; axial velocity=0.

> ### 01/02/2010.

> ### Programmed by Sal Rodriguez.

> ### Referred as file "Full_blown_NS_solver_Sine_Series_Fit__2Dg__works for

any Bo(z)_div_r+B2(z)r2n+1, ur 2nnu_div_r.mws"

>

>

>##

> # Conservation of momentum in cylindrical coordinates, SS, axisymmetric.

> # Note, per weak swirl assumption, p(r,z) = po = const.

##

> ###n := 1;

>

> **ur := 2*n*nu/r; ##4*nu/r + 0*A2*r; ##A1/r; ##2*nu/r; ##4*nu/r; ##A1(z)/r;**

$$ur := 2\,\frac{n\,\nu}{r}$$

> **utheta := B0(z)/r + B4(z)*r^(2*n+1);**

$$utheta \; := \frac{B0(z)}{r} + B4(z)\,r^{(2\,n+1)}$$

> **uz := 0;**

$$uz := 0$$

>

> **# Do r first. Multiply (1/r)*(utheta(r,z))^2 with 0 to get NS_r to work for series.**

> **NS_R := 0*ur*diff(ur,r) - 0*(1/r)*(utheta)^2 + uz*diff(ur,z) - nu*(diff(diff(ur,r),r)**

> **+ (1/r)*diff(ur,r) - (1/r^2)*(ur) + diff(diff(ur,z),z));**

$$NS\_R := 0$$

> **simplify(NS_R);**

$$0$$

> **uz*diff(ur,z);**

$$0$$

> **-diff(diff(ur,r),r);**

$$-4\,\frac{n\,\nu}{r^3}$$

> **-(1/r)*diff(ur,r);**

$$2\,\frac{n\,\nu}{r^3}$$

> **(1/r^2)*(ur);**

$$2\,\frac{n\,\nu}{r^3}$$

>

> **# Now do theta next.**

> **### NOTE: need 0*diff(diff(utheta,z),z) to get conservation of momentum ==>**

utheta does not vary much wrt to z.

> **NS_THETA := ur*diff(utheta,r) + (1/r)*utheta*ur + uz*diff(utheta,z) - nu*(**

diff(diff(utheta,r),r) + (1/r)*diff(utheta,r) - utheta/(r*r) + 0*diff(diff(utheta,z),z));

$$
\begin{aligned}
\mathit{NS\_THETA} := {}& 2\,\frac{n\,\nu\left(-\dfrac{B0(z)}{r^2}+\dfrac{B4(z)\,r^{(2\,n+1)}\,(2\,n+1)}{r}\right)}{r} \\[2mm]
&+\frac{2\left(\dfrac{B0(z)}{r}+B4(z)\,r^{(2\,n+1)}\right)n\,\nu}{r^2}-\nu\left(2\,\frac{B0(z)}{r^3}+\frac{B4(z)\,r^{(2\,n+1)}\,(2\,n+1)^2}{r^2}\right. \\[2mm]
&-\frac{B4(z)\,r^{(2\,n+1)}\,(2\,n+1)}{r^2}+\frac{-\dfrac{B0(z)}{r^2}+\dfrac{B4(z)\,r^{(2\,n+1)}\,(2\,n+1)}{r}}{r} \\[2mm]
&\left.-\frac{\dfrac{B0(z)}{r}+B4(z)\,r^{(2\,n+1)}}{r^2}\right)
\end{aligned}
$$

> **simplify(NS_THETA);**

$$0$$

> **ur*diff(utheta,r);**

$$2\,\frac{n\,\nu\left(-\dfrac{B0(z)}{r^2}+\dfrac{B4(z)\,r^{(2\,n+1)}\,(2\,n+1)}{r}\right)}{r}$$

> **(1/r)*utheta*ur;**

$$2\,\frac{\left(\dfrac{B0(z)}{r}+B4(z)\,r^{(2\,n+1)}\right)n\,\nu}{r^2}$$

> **uz*diff(utheta,z);**

$$0$$

> **-nu*diff(diff(utheta,r),r);**

$$-\nu\left(2\,\frac{B0(z)}{r^3}+\frac{B4(z)\,r^{(2\,n+1)}\,(2\,n+1)^2}{r^2}-\frac{B4(z)\,r^{(2\,n+1)}\,(2\,n+1)}{r^2}\right)$$

> **-nu*(1/r)*diff(utheta,r);**

$$-\frac{\nu\left(-\dfrac{B0(z)}{r^2}+\dfrac{B4(z)\,r^{(2\,n+1)}\,(2\,n+1)}{r}\right)}{r}$$

> **nu*utheta/(r*r);**

$$\frac{\nu\left(\dfrac{B0(z)}{r}+B4(z)\,r^{(2\,n+1)}\right)}{r^2}$$

>

> ###

> # Conservation of Mass in cylindrical coordinates, SS, axisymmetric.

> ###

> **diff(ur,r) + ur/r + diff(uz,z);**

$$0$$

> **term1_comass := diff(ur,r);**

$$term1\_comass := -2\,\frac{n\,\nu}{r^2}$$

> **term2_comass := ur/r;**

$$term2\_comass := 2\frac{n\,\nu}{r^2}$$

> **term3_comass := diff(uz,z);**

$$term3\_comass := 0$$

C.3. Maple Script for Three Field Solution for NS.

> **### Program for axisymmetric, ss NS for radial, azimuthal, and axial velocities not equal 0.**

> **### 12/24/2010.**

> **### Programmed by Sal Rodriguez.**

> **### Referred as file "Full_blown_NS_solver_Sine_Series_Fit__3Dk__NS_comass__works for u(r,n),v(r,n),w(r,n),B=const.mws"**

>

>

>

###

> **# Conservation of momentum in cylindrical coordinates, SS, axisymmetric.**

> **# Note, per weak swirl assumption, p(r,z) = po = const.**

```
>
```

###

```
>

> ur := 2*n*nu/r;
```

$$ur := 2\,\frac{n\,\nu}{r}$$

```
> utheta := B1*r^(2*n+1);
```

$$utheta := B1\,r^{(2\,n+1)}$$

```
> uz := -C1*r^(2*n);
```

$$uz := -C1\,r^{(2\,n)}$$

```
>

> # Do r first.  Multiply (1/r)*(utheta(r,z))^2 with 0 to get NS_r to work for series.

> NS_R := 0*ur*diff(ur,r) - 0*(1/r)*(utheta)^2 + uz*diff(ur,z) - nu*( diff(diff(ur,r),r)

+ (1/r)*diff(ur,r) - (1/r^2)*(ur) + diff(diff(ur,z),z) );
```

$$NS\_R := 0$$

```
> simplify(NS_R);
```

$$0$$

```
> term1r := uz*diff(ur,z);
```

$$term1r := 0$$

```
> term2r := -nu*diff(diff(ur,r),r);
```

$$term2r := -4\,\frac{\nu^2\,n}{r^3}$$

```
> term3r := -nu*(1/r)*diff(ur,r);
```

$$term3r := 2\,\frac{\nu^2\,n}{r^3}$$

> **term4r := nu*(1/r^2)*(ur);**

$$term4r := 2\,\frac{\nu^2\,n}{r^3}$$

> **term5r := -nu*diff(diff(ur,z),z);**

$$term5r := 0$$

>

> **# Now do theta next.**

> **### NOTE: need 0*diff(diff(utheta,z),z) to get cons. of momentum...**

> **NS_THETA := ur*diff(utheta,r) + (1/r)*utheta*ur + uz*diff(utheta,z) - nu*(**

> **diff(diff(utheta,r),r) + (1/r)*diff(utheta,r) - utheta/(r*r) + 0*diff(diff(utheta,z),z));**

$$NS\_THETA := 2\,\frac{n\,\nu\,B1\,r^{(2\,n+1)}\,(2\,n+1)}{r^2} + \frac{2\,B1\,r^{(2\,n+1)}\,n\,\nu}{r^2}$$
$$- \nu\left(\frac{B1\,r^{(2\,n+1)}\,(2\,n+1)^2}{r^2} - \frac{B1\,r^{(2\,n+1)}}{r^2}\right)$$

> **simplify(NS_THETA);**

$$0$$

> **term1t := ur*diff(utheta,r);**

$$term1t := 2\,\frac{n\,\nu\,B1\,r^{(2\,n+1)}\,(2\,n+1)}{r^2}$$

> **term2t := (1/r)*utheta*ur;**

$$term2t := 2\,\frac{B1\,r^{(2\,n+1)}\,n\,\nu}{r^2}$$

> **term3t := uz*diff(utheta,z);**

386

$$term3t := 0$$

> **term4t := -nu*diff(diff(utheta,r),r);**

$$term4t := -\nu \left(\frac{B1\ r^{(2n+1)}\ (2n+1)^2}{r^2} - \frac{B1\ r^{(2n+1)}\ (2n+1)}{r^2} \right)$$

> **term5t := -nu*(1/r)*diff(utheta,r);**

$$term5t := -\frac{\nu\ B1\ r^{(2n+1)}\ (2n+1)}{r^2}$$

> **term6t := nu*utheta/(r*r);**

$$term6t := \frac{\nu\ B1\ r^{(2n+1)}}{r^2}$$

>

> **# Finish by doing z direction.**

> **NS_Z := ur*diff(uz,r) + uz*diff(uz,z) - nu*(diff(diff(uz,r),r) + (1/r)*diff(uz,r) + diff(diff(uz,z),z));**

$$NS\_Z := 0$$

> **simplify(NS_Z);**

$$0$$

> **term1z := ur*diff(uz,r);**

$$term1z := -4\frac{n^2\ \nu\ C1\ r^{(2n)}}{r^2}$$

> **term2z := uz*diff(uz,z);**

$$term2z := 0$$

> **term3z := -nu*diff(diff(uz,r),r);**

$$term3z := -\nu \left(-4\frac{C1\ r^{(2n)}\ n^2}{r^2} + \frac{2\ C1\ r^{(2n)}\ n}{r^2} \right)$$

387

> **term4z := -nu*(1/r)*diff(uz,r);**

$$term4z := 2\,\frac{\nu\,C1\,r^{(2\,n)}\,n}{r^2}$$

> **term5z := -nu*diff(diff(uz,z),z);**

$$term5z := 0$$

>

>

##

> **# Conservation of Mass in cylindrical coordinates, SS, axisymmetric.**

>

##

> **diff(ur,r) + ur/r + diff(uz,z);**

$$0$$

> **term1_comass := diff(ur,r);**

$$term1\_comass := -2\,\frac{n\,\nu}{r^2}$$

> **term2_comass := ur/r;**

$$term2\_comass := 2\,\frac{n\,\nu}{r^2}$$

> **term3_comass := diff(uz,z);**

$$term3\_comass := 0$$

C.4. Maple Script for Series and Plots for Loitsyanskiy Vortex.

> ### Additional tinkering with Loitsyanskiy to get sin(pi*r) expansion....

> ### 10/13/2010.

> ### Programmed by Sal Rodriguez.

> ###NOTE: sin approximation is best for small r.

>

> alpha := sqrt(3*Ko/(16*pi*mu));

$$\alpha := \frac{1}{4}\sqrt{3}\,\sqrt{\frac{Ko}{\pi\,\mu}}$$

> gamma1 := 3*alpha*Lo/(16*pi*sqrt(mu/rho));

$$\gamma 1 := \frac{3}{64}\frac{\sqrt{3}\,\sqrt{\dfrac{Ko}{\pi\,\mu}}\,Lo}{\pi\,\sqrt{\dfrac{\mu}{\rho}}}$$

> eta := r/(z*sqrt(mu/rho));

$$\eta := \frac{r}{z\,\sqrt{\dfrac{\mu}{\rho}}}$$

> ###NOTE: the constants in Loitsyanskii can be lumped into C1 and C2, to make the series expansion easier to figure out:

> ###C1 := (9/256)*(Ko*Lo*rho)/(Pi*Pi*mu*mu*z*z*z);

> ###C2 := (3/64)*Ko*rho/(Pi*mu*mu*z*z);

> ###loi := gamma1*(1/z^2)*alpha*eta/((1 + (1/4)*alpha*alpha*eta*eta)^2);

> loi := C1*r/(1 + C2*r^2)^2;

$$loi := \frac{C1\,r}{\left(1 + C2\,r^2\right)^2}$$

> ### NOTE: for C2-->0, get Rankine...

> **### NOTE: for C1=3.5 and C2=1.3, get closest approximation to sin(pi*r)....**

> **C1 := 3.5; C2 := 1.3;**

$$C1 := 3.5$$

$$C2 := 1.3$$

> **plot([3.5*r/(1+1.1*r^2)^2, 3.5*r/(1+1.3*r^2)^2, 3.5*r/(1+1.5*r^2)^2,**

3.5*r/(1+1.7*r^2)^2, sin(Pi*r)], r=-1..1, color=[red,blue,green,cyan,black],

legend=["C2=1.1", "C2=1.3","C2=1.5","C2=1.7","sin(pi*r)"],

linestyle=[SOLID,SOLID,SOLID,SOLID,DASH], thickness=[5,5,5,5,5],

font=[COURIER,BOLD,20], view=[-1..1, -1.1..1.1], labels=["r","U_theta(r)"],

labeldirections=[HORIZONTAL,VERTICAL], scaling=CONSTRAINED);

###labelfont=[SYMBOL]
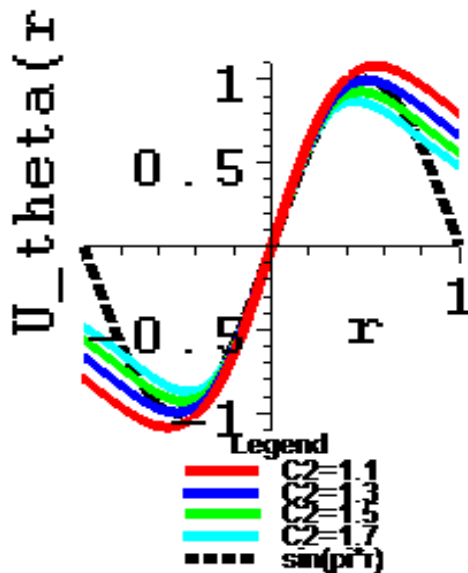
> **plot([loi, sin(Pi*r)], r=-1..1, color=[red,blue], linestyle=[SOLID,DASH],**

legend=["Loistyanskii with C2=1.3", "sin(pi*r)"], font=[COURIER,BOLD,20],

thickness=[5,5], labels=["r","U_theta(r)"],
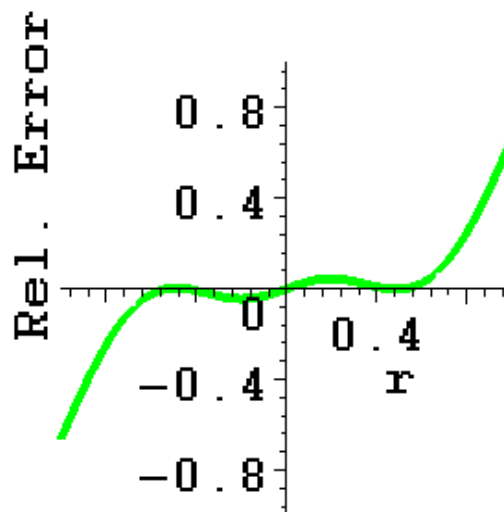
$$3.5\, r - 9.10\, r^3 + 17.745\, r^5 - 30.7580\, r^7 + 49.98175\, r^9 + O(r^{11})$$

391

> **series(sin(Pi*r),r,10);**

$$\pi\,r - \frac{1}{6}\,\pi^3\,r^3 + \frac{1}{120}\,\pi^5\,r^5 - \frac{1}{5040}\,\pi^7\,r^7 + \frac{1}{362880}\,\pi^9\,r^9 + O(r^{10})$$

> **plot([3.5*r-9.10*r^3+17.745*r^5-30.7580*r^7+49.98175*r^9, Pi*r+(-**

1/6*Pi^3)*r^3+1/120*Pi^5*r^5+(-1/5040*Pi^7)*r^7+1/362880*Pi^9*r^9], r=-1..1,

color=[red,blue], linestyle=[SOLID,DASH], thickness=[5,5],

font=[COURIER,BOLD,20], view=[-1..1, -2..2], legend=["Loitsyanskii Series",

"Sine Series"], labels=["r","U_theta(r)"],

labeldirections=[HORIZONTAL,VERTICAL], scaling=CONSTRAINED);
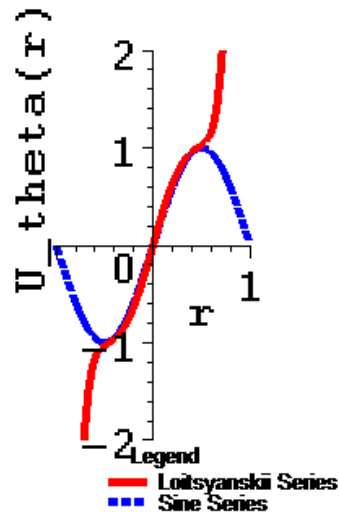
C.5. Maple Script for Series and Plots for Vatistas Vortex.

> **### Vatistas Vortex.**

> **### 01/01/2011.**

> **### Programmed by Sal Rodriguez.**

>

392

\>

\> **series(r/(1+r^(2*1))^(1/1),r, 20); ###n=1.**

$$r - r^3 + r^5 - r^7 + r^9 - r^{11} + r^{13} - r^{15} + r^{17} - r^{19} + O(r^{21})$$

\> **series(r/(1+r^(2*2))^(1/2),r, 20); ###n=2.**

$$r - \frac{1}{2}r^5 + \frac{3}{8}r^9 - \frac{5}{16}r^{13} + \frac{35}{128}r^{17} + O(r^{21})$$

\> **series(r/(1+r^(2*3))^(1/3),r, 20); ###n=3.**

$$r - \frac{1}{3}r^7 + \frac{2}{9}r^{13} - \frac{14}{81}r^{19} + O(r^{25})$$

\> **series(r/(1+r^(2*4))^(1/4),r, 20); ###n=4.**

$$r - \frac{1}{4}r^9 + \frac{5}{32}r^{17} + O(r^{25})$$

\> **series(r/(1+r^(2*5))^(1/5),r, 20); ###n=5.**

$$r - \frac{1}{5}r^{11} + O(r^{21})$$

\> **series(r/(1+r^(2*6))^(1/6),r, 20); ###n=6.**

$$r - \frac{1}{6}r^{13} + O(r^{25})$$

\> **series(r/(1+r^(2*7))^(1/7),r, 20); ###n=7.**

$$r - \frac{1}{7}r^{15} + O(r^{29})$$

\>

\> **series(r/(1+r^(2*8))^(1/8),r, 20); ###n=8.**

$$r - \frac{1}{8}r^{17} + O(r^{33})$$

\>

> plot([Pi*r/(1+r^(2*1))^(1/1), sin(Pi*r)], r=-1..1, color=[red, blue],

linestyle=[SOLID,SOLID], thickness=[5,5], font=[COURIER,BOLD,20],

labels=["r","U_theta(r)"], legend=["Vatistas", "sin(pi*r)"],

labeldirections=[HORIZONTAL,VERTICAL], scaling=CONSTRAINED);

###view=[-1..1, -1..1],
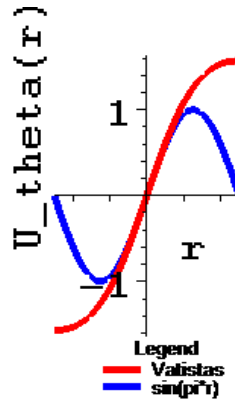
> plot([Pi*r/(1+r^(2*1))^(1/1), Pi*r/(1+r^(2*2))^(1/2), Pi*r/(1+r^(2*3))^(1/3),

Pi*r/(1+r^(2*4))^(1/4), Pi*r/(1+r^(2*20))^(1/20)], r=-7..7, color=[red, blue, cyan,

black,brown], linestyle=[SOLID,SOLID,SOLID,SOLID, SOLID], thickness=[5,5],

font=[COURIER,BOLD,20], labels=["r","U_theta(r)"], legend=["n=1", "n=2",

"n=3", "n=4", "n=20"], labeldirections=[HORIZONTAL,VERTICAL],

scaling=CONSTRAINED);
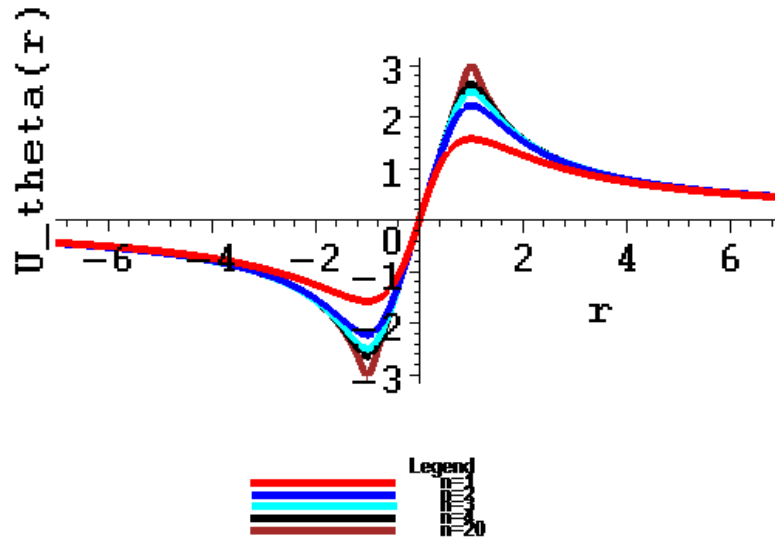
> **### Vatistas vortex pressure drop.**

> **series((2/Pi)*arctan(r*r),r,25);**

$$2\frac{1}{\pi}r^2 - \frac{2}{3}\frac{1}{\pi}r^6 + \frac{2}{5}\frac{1}{\pi}r^{10} - \frac{2}{7}\frac{1}{\pi}r^{14} + \frac{2}{9}\frac{1}{\pi}r^{18} - \frac{2}{11}\frac{1}{\pi}r^{22} + \mathrm{O}(r^{25})$$

C.6. Maple Script to Show that v(r) and w(r) Satisfy Euler and Conservation of Mass.

> **### Program FULL-BLOWN axisymmetric, ss NS for r, theta, and z velocities.**

> **### 01/03/2011.**

> **### Programmed by Sal Rodriguez.**

###Rossi, 2006, claims on page 70 that any utheta(r), uz(r) satisfies the Euler equations. Show that this is true. Pretty cool!

>

>

> ur := 0;

$$ur := 0$$

> utheta := r^n;

$$utheta := r^n$$

> uz := r^m;

$$uz := r^m$$

>

> # Do r first. Multiply (1/r)*(utheta(r,z))^2 with 0 to get NS_r to work for series.

> NS_R := 0*ur*diff(ur,r) - 0*(1/r)*(utheta)^2 + uz*diff(ur,z) - nu*(diff(diff(ur,r),r) + (1/r)*diff(ur,r) - (1/r^2)*(ur) + diff(diff(ur,z),z));

$$NS\_R := 0$$

>

> # Now do theta next.

> ### NOTE: need 0*diff(diff(utheta,z),z) to get cons. of momentum...

> NS_THETA := ur*diff(utheta,r) + (1/r)*utheta*ur + uz*diff(utheta,z) - 0*(diff(diff(utheta,r),r) + (1/r)*diff(utheta,r) - utheta/(r*r) + diff(diff(utheta,z),z));

$$NS\_THETA := 0$$

> simplify(NS_THETA);

$$0$$

> **term1t := ur*diff(utheta,r);**

$$term1t := 0$$

> **term2t := (1/r)*utheta*ur;**

$$term2t := 0$$

> **term3t := uz*diff(utheta,z);**

$$term3t := 0$$

> **term4t := -nu*diff(diff(utheta,r),r);**

$$term4t := -\nu \left(\frac{r^n\, n^2}{r^2} - \frac{r^n\, n}{r^2} \right)$$

> **term5t := -nu*(1/r)*diff(utheta,r);**

$$term5t := -\frac{\nu\, r^n\, n}{r^2}$$

> **term6t := nu*utheta/(r*r);**

$$term6t := \frac{\nu\, r^n}{r^2}$$

>

> **# Finish by doing z direction.**

> **NS_Z := ur*diff(uz,r) + uz*diff(uz,z) - 0*(diff(diff(uz,r),r) + (1/r)*diff(uz,r) +**

diff(diff(uz,z),z));

$$NS\_Z := 0$$

> **simplify(NS_Z);**

$$0$$

> **term1z := ur*diff(uz,r);**

$$term1z := 0$$

> **term2z := uz*diff(uz,z);**

$$term2z := 0$$

> **term3z := -nu*diff(diff(uz,r),r);**

$$term3z := -\nu \left(\frac{r^m m^2}{r^2} - \frac{r^m m}{r^2} \right)$$

> **term4z := -nu*(1/r)*diff(uz,r);**

$$term4z := -\frac{\nu \, r^m \, m}{r^2}$$

> **term5z := -nu*diff(diff(uz,z),z);**

$$term5z := 0$$

>

> **###**

> **# Conservation of Mass in cylindrical coordinates, SS, axisymmetric.**

###

> **diff(ur,r) + ur/r + diff(uz,z);**

$$0$$

> **term1_comass := diff(ur,r);**

$$term1\_comass := 0$$

> **term2_comass := ur/r;**

$$term2\_comass := 0$$

> **term3_comass := diff(uz,z);**

$$term3\_comass := 0$$

C.7. **Maple** **Script** **to** **Investigate** **AVE** **Vortex,** **Bessel** **Function,** **and** **Sin-Like** **Attributes.**

> **### Program to investigae AVE and Bessel first order, sine-like series attributes.**

> **### 12/26/2010.**

>

>

> **### Plot most sine-like bessel of order 1:**

> **plot(['1.72*BesselJ(1,0.9812861499*3.831705970*r)', 'sin(Pi*r)'], r=-1.1..1.1, color=[green,blue], linestyle=[SOLID,DASH], legend=["Bessel", "Sin(pi*r)"], font=[COURIER,BOLD,20], thickness=[5,5], labels=["r","U_theta(r)"], labeldirections=[HORIZONTAL,VERTICAL], scaling=CONSTRAINED);**
####view=[0..1.1, 0..1],
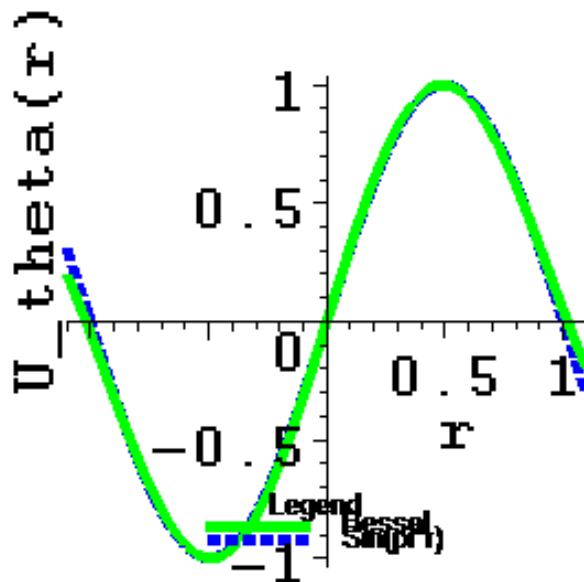
> **plot(['1.88*BesselJ(1,3.831705970*r)', 'sin(Pi*r)'], r=0..1);**
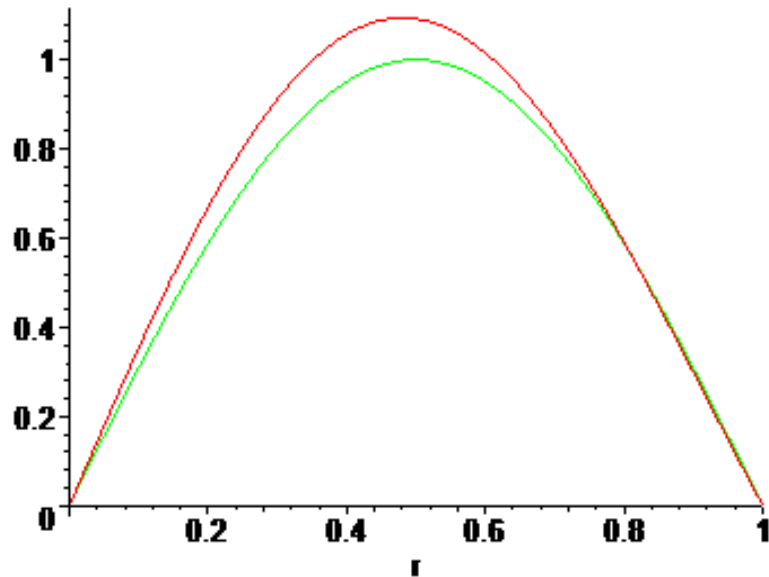
> **series(1.72*BesselJ(1,0.9812861499*3.76*r),r,11); #### Bessel order n=1...use**

3.76...

$$3.173086895\,r - 5.399567895\,r^3 + 3.062772882\,r^5 - .8686415191\,r^7 + .1478146995\,r^9 + O(r^{11})$$

> **BesselJZeros(1.,0..6);**

$$0, 3.831705970, 7.015586670, 10.17346814, 13.32369194, 16.47063005, 19.61585851$$

>

> **###'0.4*r + 1.4*BesselJ(1,4.2*r)'**

>

> **### Plot most sine-like C1*r - J(1,C2*r)....0.1*r + 1.63*BesselJ(1,3.831705970*r)**

> **plot(['0.1*r + 1.63*BesselJ(1,3.831705970*r)', 'sin(Pi*r)'], r=-1.1..1.1,**

color=[green,blue], linestyle=[SOLID,DASH], legend=["Bessel", "Sin(pi*r)"],

font=[COURIER,BOLD,20], thickness=[5,5], labels=["r","U_theta(r)"],

labeldirections=[HORIZONTAL,VERTICAL], scaling=CONSTRAINED);

###view=[-3..3, -3..3],

>
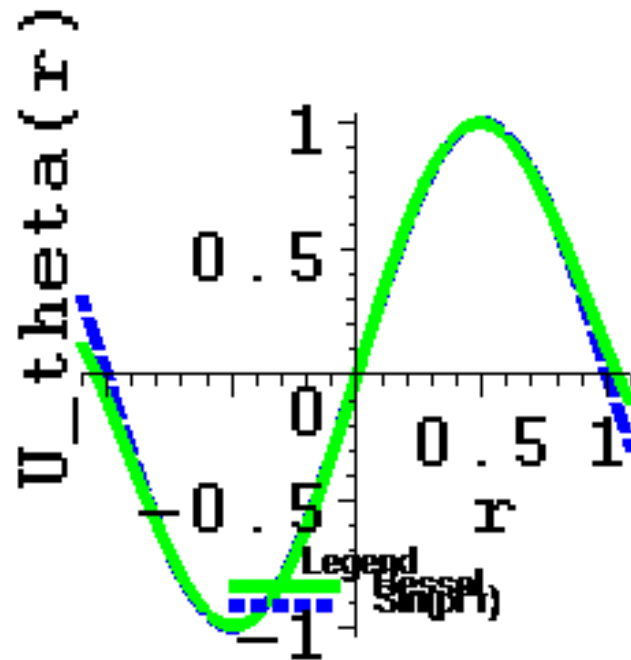
> **series(0.1*r + 1.63*BesselJ(1,3.831705970*r), r,8);**

$$3.222840366\,r - 5.731181321\,r^3 + 3.506043160\,r^5 - 1.072408807\,r^7 + \mathrm{O}(r^8)$$

>

>

> **###Solve PDE presented by Aboelkassem, Vatistas, and Esmail:**

> **pde1 := diff(vtheta(r,t),t) - diff(vtheta(r,t),r,r) - (1/r)*diff(vtheta(r,t),r) +**

vtheta(r,t)/(r*r);

$$pde1 := \left(\frac{\partial}{\partial t}\,\mathrm{vtheta}(r,t)\right) - \left(\frac{\partial^2}{\partial r^2}\,\mathrm{vtheta}(r,t)\right) - \frac{\frac{\partial}{\partial r}\,\mathrm{vtheta}(r,t)}{r} + \frac{\mathrm{vtheta}(r,t)}{r^2}$$

> **sol := pdsolve({pde1}) ; ###This will result in a splittable pair of odes...**

$sol := (\text{vtheta}(r, t) = \_F1(r) \_F2(t)) \ \&\text{where}$

$$\left[\left\{\frac{\partial}{\partial t} \_F2(t) = \_F2(t) \_c_1, \frac{\partial^2}{\partial r^2} \_F1(r) = \_F1(r) \_c_1 - \frac{\left(\frac{\partial}{\partial r} \_F1(r)\right) r - \_F1(r)}{r^2}\right\}\right]$$

>

> **ode1 := diff(F2(t),t) = -F2(t)*c1*c1;**

> **dsolve({ode1});**

$$ode1 := \frac{\partial}{\partial t} F2(t) = -F2(t) \, c1^2$$

$$\{ F2(t) = \_C1 \, \mathrm{e}^{(-c1^2 t)} \}$$

> **ode2 := diff(F1(r),r,r) + F1(r)*c1*c1 - (-diff(F1(r),r)*r + F1(r))/r^2;**

$$ode2 := \left(\frac{\partial^2}{\partial r^2} F1(r)\right) + F1(r) \, c1^2 - \frac{-\left(\frac{\partial}{\partial r} F1(r)\right) r + F1(r)}{r^2}$$

> **dsolve({ode2});**

$$\{ F1(r) = \_C1 \, \text{BesselJ}(1, c1 \, r) + \_C2 \, \text{BesselY}(1, c1 \, r) \}$$

> ###Final sol = F1(r)*F2(t).

Appendix D: Matlab Input Files

The following Matlab input files are listed below:

D.1. Matlab Script to Compute S, u, v, w, and V.

D.2. Matlab Script for Chepura Vortex Overhaul.

D.3. Matlab Script for Plotting Modified Newman Vortex.

D.4. Matlab Script to Plot Various Axisymmetric Vortices.

D.1. Matlab Script to Compute S, u, v, w, and V.

clear all

theta_deg = 75; %%%0; %%%15;

theta = theta_deg*pi/180;

%Vvec = 4.515; % Re=5,000

%Vvec = 9.03; % Re=10,000

%Vvec = 18.06; % Re=20,000

Vvec = 45.15; % Re=50,000

Vvec = 67.0; %%% This is for the LP case only!!!

S=(2./3.)*tan(theta)

```
uo = Vvec/( sqrt(2)*(sqrt( 1 + 4./(9*S*S) ) ) )

vo = -uo

wo = sqrt( Vvec*Vvec - 2*uo*uo )

utheta = sqrt(2)*uo


%check:

theta_check = (180/pi)*atan(utheta/wo)

Vvec_check = sqrt(uo*uo + vo*vo + wo*wo)
```

D.2. Matlab Script for Chepura Vortex Overhaul.

```
%%% Do overhaul of Chepura vortex using sinusoid vortex theory....

% Programmed by Sal B. Rodriguez

% 01/11/2011


clear;


Chedata1 = [

0.015  0.263

0.030  0.527

0.034  0.597

0.044  0.773

0.054  0.950
```

0.064 0.800

0.074 0.692

0.084 0.610

0.094 0.545

0.104 0.493

0.115 0.446

];

Chedata2 = [

0.06   0.515

0.075 0.650

0.08   0.696

0.09   0.78

0.10   0.87

0.12   1.04

0.14   0.885

0.15   0.825

0.175 0.71

0.20   0.62

0.22   0.562

0.24   0.516

0.26   0.476

];

% Matrix X of arbitrary row size m and 2 columns (x-y data pairs).

Chevalues1 = [

0.015 0.271

0.030 0.509

0.034 0.561

0.044 0.670

0.054 0.739

0.064 0.749

0.074 0.695

0.084 0.615

0.094 0.550

0.104 0.500

0.115 0.450

];

Chevalues2 = [

0.06   0.546

0.075 0.648

0.08   0.676

0.09   0.730

0.10   0.765

0.12   0.805

0.14 0.775

0.15 0.740

0.175 0.636

0.20 0.556

0.22 0.507

0.24 0.465

0.26 0.43

];

% get number of rows, which = number of data pairs.

n1 = length(Chedata1);

n2 = length(Chedata2);

% store col 1 in vector xcol1 and col 2 in vector xcol2

for i=1:n1

  xcol1(i) = Chedata1(i,1);

  xcol2(i) = Chedata1(i,2);

end

for i=1:n2

  xcol3(i) = Chedata2(i,1);

  xcol4(i) = Chedata2(i,2);

end

```
%%%%%%%%%%%%%%%%%%%%%%%%%%%%%%%%%%%%%%
axes('fontsize', 16);
%%%%%%%%%%%%%%%%%%%%%%%%%%%%%%%%%%%%%%


% plot x-y pairs.
%axis([0 6 0 550]);
%%%fplot('(k*r_t/2)*(2 - (r/r_t)^2)', [0,0.115]);
k = 18.6;
r_t = 0.075;
fplot('(18.6*r/2)*(2 - (r/0.075)^2)', [0,0.06], 'LineSpec', 'rx:');  %%% Chepura, domain 1
%%%%[0,0.08]
hold on;
fplot('(18.6*0.075^2)/(2*r)', [0.05,0.115], 'LineSpec', 'rd-'); %%% Chepura, domain 2
hold on;
%%%% k_sal=1.36; great value.
%%%% Third order version.
fplot('1.36*(r/0.075) - 1.36*(1/6)*(r/0.075)^3', [0,0.06], 'LineSpec', 'cp:'); %%% heli,
third order
hold on;
%%%% Fifth order version.
fplot('1.36*(r/0.075) - 1.36*(1/6)*(r/0.075)^3 + 1.36*(1/120)*(r/0.075)^5', [0,0.06],
'LineSpec', 'g>:'); %%% heli, fifth order
```

```
hold on;

%%%SLOW DECAY...Sal-Modified Newman Vortex Azimuthal Velocity.

% Sal-Modified Newman Vortex Azimuthal Velocity. (0.5<r<1)

fplot('[ (0.32/(2*pi*r))*exp(-0.1*r*r/(4*0.05*1.0)) ]', [0.05 0.115], 'LineSpec', 'gs-');

hold on;

fplot('1.36*(r/0.075)', [0,0.06], 'LineSpec', 'bh:'); %%%Rankine, domain 1

hold on;

fplot('0.0515/r', [0.05,0.115], 'LineSpec', 'b<-'); %%%Rankine, domain 2

hold on;

plot(xcol1,xcol2,'ko');

xlabel('r, m');

ylabel('Azimuthal Velocity, m/s');

hold off;

legend('Chepura, Domain 1', 'Chepura, Domain 2', 'REG: 3rd Order Heli', 'REG: 5th

Order Heli', 'REG: Mod. Newman', 'Rankine, Domain 1', 'Rankine, Domain 2', 'Data in

Chepura', 0);

grid on, box on;


pause


%%%%%%%%%%%%%%%%%%%%%%%%%%%%%%%%%%%%%%

axes('fontsize', 16);

%%%%%%%%%%%%%%%%%%%%%%%%%%%%%%%%%%%%%%
```

%axis([0 6 0 550]);

%%%fplot('(k*r_t/2)*(2 - (r/r_t)^2)', [0,0.26]);

k = 9.9;

r_t = 0.158 %%%%%0.155; %%% 01/03/2011...0.15;

fplot('(9.9*r/2)*(2 - (r/0.158)^2)', [0,0.12], 'LineSpec', 'rx:'); %%% Chepura, domain 1

hold on;

fplot('(9.9*0.158^2)/(2*r)', [0.1,0.26], 'LineSpec', 'rd-'); %%% Chepura, domain 2

hold on;

%%%% k_sal=1.38; great value.

%%%% Third order version.

fplot('1.38*(r/0.158) - 1.38*(1/6)*(r/0.158)^3', [0,0.12], 'LineSpec', 'cp:'); %%% heli,

third order

hold on;

%%%% Fifth order version.

fplot('1.38*(r/0.158) - 1.38*(1/6)*(r/0.158)^3 + 1.38*(1/120)*(r/0.158)^5', [0,0.12],

'LineSpec', 'g>:'); %%% heli, fifth order

hold on;

%%%SLOW DECAY...Sal-Modified Newman Vortex Azimuthal Velocity.

% Sal-Modified Newman Vortex Azimuthal Velocity. (0.5<r<1)

fplot('[(0.8/(2*pi*r))*exp(-0.1*r*r/(4*0.05*1.0))]', [0.1,0.26], 'LineSpec', 'gs-');

hold on;

fplot('1.38*(r/0.158)', [0,0.12], 'LineSpec', 'bh:'); %%% Rankine, domain 1

hold on;

fplot('0.125/r', [0.1,0.26], 'LineSpec', 'b<-'); %%%Rankine, domain 2

hold on;

plot(xcol3,xcol4,'ko');

xlabel('r, m');

ylabel('Azimuthal Velocity, m/s');

hold on;

legend('Chepura, Domain 1', 'Chepura, Domain 2', 'REG: 3rd Order Heli', 'REG: 5th

Order Heli', 'REG: Mod. Newman', 'Rankine, Domain 1', 'Rankine, Domain 2', 'Data in

Chepura', 0);

grid on, box on;

D.3. Matlab Script for Plotting Modified Newman Vortex.

%%% Plot various forms of the Modified Newman Vortex

% Programmed by Sal B. Rodriguez

% 12/26/2010

clear;

%%%%%%%%%%%%%%%%%%%%%%%%%%%%%%%%%%%%

%   AZIMUTHAL

%%%%%%%%%%%%%%%%%%%%%%%%%%%%%%%%%%%%%

axes('fontsize', 16);

% Rankine Vortex Azimuthal Velocity (-1<r<-0.5)

fplot('[0.5/r]', [-1 -0.5], 'LineSpec', 'k^-');

hold on;

% Rankine Vortex Azimuthal Velocity (-0.5<r<-0.5), a=2

fplot('[2*r]', [-0.5 0.5], 'LineSpec', 'k^-');

hold on;

% Rankine Vortex Azimuthal Velocity (0.5<r<1)

fplot('[0.5/r]', [0.5 1], 'LineSpec', 'k^-');

hold on;

%%%SLOW DECAY....

% Sal-Modified Newman Vortex Azimuthal Velocity. (-1<r<-0.5)

fplot('[(3.13/(2*pi*r))*exp(-0.001*r*r/(4*0.05*1.0))]', [-1 -0.5], 'LineSpec', 'bo-');

hold on;

% Sal-Modified Newman Vortex Azimuthal Velocity. (-0.5<r<-0.5)

fplot('[2*r]', [-0.5 0.5], 'LineSpec', 'bo-');

hold on;

% Sal-Modified Newman Vortex Azimuthal Velocity. (0.5<r<1)

fplot('[(3.13/(2*pi*r))*exp(-0.001*r*r/(4*0.05*1.0))]', [0.5 1], 'LineSpec', 'bo-');

hold on;

%%%INTERMEDIATE DECAY....

% Sal-Modified Newman Vortex Azimuthal Velocity. (-1<r<-0.5)

fplot('[(4.05/(2*pi*r))*exp(-0.2*r*r/(4*0.05*1.0))]', [-1 -0.5], 'LineSpec', 'cp-');

hold on;

% Sal-Modified Newman Vortex Azimuthal Velocity. (-0.5<r<-0.5)

fplot('[2*r]', [-0.5 0.5], 'LineSpec', 'cp-');

hold on;

% Sal-Modified Newman Vortex Azimuthal Velocity. (0.5<r<1)

fplot('[(4.05/(2*pi*r))*exp(-0.2*r*r/(4*0.05*1.0))]', [0.5 1], 'LineSpec', 'cp-');

hold on;

%%%FAST DECAY....

% Sal-Modified Newman Vortex Azimuthal Velocity. (-1<r<-0.5)

fplot('[(10.9/(2*pi*r))*exp(-1*r*r/(4*0.05*1.0))]', [-1 -0.5], 'LineSpec', 'gd-');

hold on;

% Sal-Modified Newman Vortex Azimuthal Velocity. (-0.5<r<-0.5)

fplot('[2*r]', [-0.5 0.5], 'LineSpec', 'gd-');

hold on;

% Sal-Modified Newman Vortex Azimuthal Velocity. (0.5<r<1)

fplot('[(10.9/(2*pi*r))*exp(-1*r*r/(4*0.05*1.0))]', [0.5 1], 'LineSpec', 'gd-');

hold on;

%%%ULTA FAST DECAY....

% Sal-Modified Newman Vortex Azimuthal Velocity. (-1<r<-0.5)

fplot('[(133/(2*pi*r))*exp(-3*r*r/(4*0.05*1.0))]', [-1 -0.5], 'LineSpec', 'rs-');

hold on;

% Sal-Modified Newman Vortex Azimuthal Velocity. (-0.5<r<-0.5)

fplot('[2*r]', [-0.5 0.5], 'LineSpec', 'rs-');

hold on;

% Sal-Modified Newman Vortex Azimuthal Velocity. (0.5<r<1)

fplot('[(133/(2*pi*r))*exp(-3*r*r/(4*0.05*1.0))]', [0.5 1], 'LineSpec', 'rs-');

hold off;

legend('Rankine', 'Rodriguez/El-Genk: Mod Newman, Slow Decay', 'Rodriguez/El-Genk:

Mod Newman, Medium Decay', 'Rodriguez/El-Genk: Mod Newman, Fast Decay',

'Rodriguez/El-Genk: Mod Newman, Ultra Fast Decay');

grid on;

xlabel('Normalized r');

ylabel('Normalized Azimuthal Velocity')

D.4. Matlab Script to Plot Various Axisymmetric Vortices.

%%% Script to plot azimuthal velocities of various axisymmetric vortices.

% Programmed by Sal B. Rodriguez

% 10/25/2010

%%%THIS IS THE FINAL FORM FOR THE 10 AZIMUTHAL VELOCITY PLOTS!!!

12/28/2010.

%%%%%%%% Azimuthal Velocity %%%%%%%%%%%%%%%

axes('fontsize', 16);

% Batchelor Vortex Azimuthal Velocity.

fplot('[0.625*(1/r)*(1 - exp(-2*pi*r*r))]', [-1 1], 'LineSpec', 'b.--');

hold on;

% Gortler Vortex Azimuthal Velocity.

fplot('[3.08*(r/(1 + r^2)^2)]', [-1 1], 'LineSpec', 'gd:');

hold on;

% Helicoid (Sine Azimuthal Velocity).

fplot('[sin(pi*r)]', [-1 1], 'LineSpec', 'bp-.');

hold on;

%%%!!!! NOTE: Loitsyanskii is V(r,z); here,have set z=1 to do plot V(r,z=1).

% Loitsyanskii Vortex Azimuthal Velocity.

fplot('[1.537*5*(r/1.0)*(1/(1 + 0.25*5*5*1.0*(r/1)^2)^2)]', [-1 1], 'LineSpec', 'rh--');

hold on;

% Newman Vortex Azimuthal Velocity.

%%%!!!! NOTE: Newman is V(r,z); here,have set z=1 to do plot V(r,z=1).

```
fplot('[ (4.4/(2*pi*r))*(1 - exp(-1*r*r/(4*0.05*1.0)) ) ]', [-1 1], 'LineSpec', 'c.--');
%%%NOTE: nu=0.001 or very tiny -->Rankine... fplot('[ (7*pi/(2*pi*r))*(1 - exp(-
1*r*r/(4*0.001*1.0)) ) ]', [-1 1], 'LineSpec', 'c^--');
hold on;
```

```
% Burgers Vortex Azimuthal Velocity.
fplot('(1/r)*(1 - exp(-(1/2)*2.8*r*r))*(1/( (1 - exp(-(1/2)*2.8)) ))', [-1 1], 'LineSpec', 'm.--
');
hold on;
```

```
% Sullivan Vortex Azimuthal Velocity.
fplot('[ 2.22*(1/r)*(1 - exp(-r^2/1^2)) ]', [-0.5, 0.5], 'LineSpec', 'cs-');
hold on;
fplot('[0.44*( (1 - 1/2)*1*1 + 1*1*(1 - exp(-1)) )/r]', [0.5, 1], 'LineSpec', 'cs-');
hold on;
fplot('[0.44*( (1 - 1/2)*1*1 + 1*1*(1 - exp(-1)) )/r]', [-1, -0.5], 'LineSpec', 'cs-');
hold on;
```

```
% Chepura Vortex Azimuthal Velocity (-1<r<-0.6)
fplot('[ 3.75/(2*pi*r) ]', [-1 -0.6], 'LineSpec', 'r.-');
hold on;
% Chepura Vortex Azimuthal Velocity (-0.6<r<0.6)
fplot('[ (2.44*r/2.0)*(2 - (r/0.75)^2) ]', [-0.6 0.6], 'LineSpec', 'r.-');
```

hold on;

% Chepura Vortex Azimuthal Velocity (0.6<r<1)

fplot('[3.75/(2*pi*r)]', [0.6 1], 'LineSpec', 'r.-');

hold on;

% Rankine Vortex Azimuthal Velocity (-1<r<-0.5)

fplot('[0.5/r]', [-1 -0.5], 'LineSpec', 'k.-');

hold on;

% Rankine Vortex Azimuthal Velocity (-0.5<r<-0.5), a=2

fplot('[2*r]', [-0.5 0.5], 'LineSpec', 'k.-');

hold on;

% Rankine Vortex Azimuthal Velocity (0.5<r<1)

fplot('[0.5/r]', [0.5 1], 'LineSpec', 'k.-');

hold on;

% AVE Azimuthal Velocity

fplot('[0.1*r + 1.63*BesselJ(1,3.831705970*r)]', [-1 1], 'LineSpec', 'g.-');

hold off;

legend('Batchelor', 'Gortler', 'REG Heli', 'Loitsyanskii', 'Newman', 'Burgers', 'Sullivan',

'Chepura', 'Rankine', 'AVE');

grid on;

xlabel('Normalized r');

ylabel('Normalized Azimuthal Velocity');

Appendix E: FORTRAN Subroutines

The following FORTRAN input files are listed below:

E.1. FORTRAN Subroutine for Computing u in the LP.

E.2. FORTRAN Subroutine for Computing v in the LP.

E.3. FORTRAN Subroutine for Computing w in the LP.

E.4. FORTRAN Subroutine for Computing u for S(t).

E.5. FORTRAN Subroutine for Computing v for S(t).

E.6. FORTRAN Subroutine for Computing w for S(t).

E.7. FORTRAN Subroutine for Calling the Fuego User Functions.

E.1. FORTRAN Subroutine for Computing u in the LP.

```
      SUBROUTINE u_BC (NPTS, TIME, COORDS, VALUES,

     $              ICONST, ILEN, RCONST, RLEN)

C*********************************************************************

C

#include <Afgo_numbers.h>

C

      INTEGER        NPTS, ICONST, ILEN, RLEN

C

      DOUBLE PRECISION TIME, COORDS, VALUES, RCONST

      double precision ymin, ymax
```

```fortran
C

      DIMENSION      COORDS(3,NPTS), VALUES(NPTS), ICONST(ILEN)

      DIMENSION      RCONST(RLEN)

C

C---------------------------------------------------------------------

C

      DOUBLE PRECISION X, Y, Z, T, PI

      DOUBLE PRECISION MMS

C

      INTEGER J

C

      PI = FOUR*ATAN(ONE)

      ymin = RCONST(1)

      ymax = RCONST(2)

C

      DO 200 J=1, NPTS

C

        Y = COORDS(2,J)

C

      mms = 30.0*sin( 2*pi*( ((y-ymin)/(ymax-ymin)) ) )

        VALUES(J) = MMS

C

  200 CONTINUE
```

C

    RETURN

C

    END

E.2. FORTRAN Subroutine for Computing v in the LP.

    SUBROUTINE v_BC (NPTS, TIME, COORDS, VALUES,

   $ ICONST, ILEN, RCONST, RLEN)

C***

C

#include <Afgo_numbers.h>

C

    INTEGER   NPTS, ICONST, ILEN, RLEN

C

    DOUBLE PRECISION TIME, COORDS, VALUES, RCONST

    double precision xmin, xmax

C

    DIMENSION   COORDS(3,NPTS), VALUES(NPTS), ICONST(ILEN)

    DIMENSION   RCONST(RLEN)

C

C---

C

```fortran
      DOUBLE PRECISION X, Y, Z, T, PI

      DOUBLE PRECISION MMS

C

      INTEGER J

C

      PI = FOUR*ATAN(ONE)

      xmin = RCONST(1)

      xmax = RCONST(2)

C


      DO 200 J=1, NPTS

C

        X = COORDS(1,J)

C

        mms = -30.0*sin( 2*pi*( ((x-xmin)/(xmax-xmin)) ) )

        VALUES(J) = MMS

C

  200 CONTINUE

C

      RETURN

C

      END
```

E.3. FORTRAN Subroutine for Computing w in the LP.

```
      SUBROUTINE w_BC (NPTS, TIME, COORDS, VALUES,
     $              ICONST, ILEN, RCONST, RLEN)
C*************************************************************************
C
#include <Afgo_numbers.h>
C
      INTEGER      NPTS, ICONST, ILEN, RLEN
C
      DOUBLE PRECISION TIME, COORDS, VALUES, RCONST
C
      DIMENSION      COORDS(3,NPTS), VALUES(NPTS), ICONST(ILEN)
      DIMENSION      RCONST(RLEN)
C
C------------------------------------------------------------------
C
      DOUBLE PRECISION X, Y, Z, T, PI
      DOUBLE PRECISION MMS
C
      INTEGER J
C
C************* FIRST EXECUTABLE STATEMENT OF MMS_2bw_BC
*******************
```

```fortran
C
      PI = FOUR*ATAN(ONE)
C
      DO 200 J=1, NPTS
C
c       X = COORDS(1,J)
c       Y = COORDS(2,J)
c       Z = COORDS(3,J)
c       T = TIME
C
ccccccc       MMS = 63.7*(1 -abs(X))**0.14286
      mms = 42.4
      VALUES(J) = MMS
C
  200 CONTINUE
C
      RETURN
C
C
      END
```

E.4. FORTRAN Subroutine for Computing u for S(t).

```fortran
      SUBROUTINE u_BC (NPTS, TIME, COORDS, VALUES,
     $              ICONST, ILEN, RCONST, RLEN)
C*********************************************************************
C
#include <Afgo_numbers.h>
C
      INTEGER       NPTS, ICONST, ILEN, RLEN
C
      DOUBLE PRECISION TIME, COORDS, VALUES, RCONST
C
      DIMENSION     COORDS(3,NPTS), VALUES(NPTS), ICONST(ILEN)
      DIMENSION     RCONST(RLEN)
C
C----------------------------------------------------------------------
C
      DOUBLE PRECISION X, Y, Z, T, PI
      DOUBLE PRECISION MMS
      double precision ymin, ymax, Vtot, uo, S, theta
      double precision t1, t2, t3, t4, thetam
C
      INTEGER J
```

```fortran
C
      PI = FOUR*ATAN(ONE)

      Vtot = 100.0

      t1 = 1.0

      t2 = 11.0

      t3 = 21.0

      t4 = 23.0

      thetam = 89.0


      ymin=9.989667

      ymax=10.010333


      DO 200 J=1, NPTS
C

        X = COORDS(1,J)

        Y = COORDS(2,J)

        Z = COORDS(3,J)

        T = TIME
C

        if (t .le. t1) then

          theta = 0.0

        elseif (t .le. t2) then

          theta = (thetam/(t2-t1))*(t-t1)
```

```fortran
      elseif (t .le. t3) then

         theta = -(thetam/(t3-t2))*(t-t3)

      else

         theta = 0.0

      end if


      S = (2./3.)*tan(pi*theta/180.)

      if (S .eq. 0.0) then

         uo = 0.0

      else

         uo = Vtot/sqrt(2*(1 + 4/(9*S*S)))

      end if

      mms = uo*sin( 2.0d0*pi*( ((y-ymin)/(ymax-ymin)) ) )

      VALUES(J) = MMS
C
 200  CONTINUE
C

      RETURN
C
C

      END
```

E.5. FORTRAN Subroutine for Computing v for S(t).

```
C

#include <Afgo_numbers.h>

C

      INTEGER       NPTS, ICONST, ILEN, RLEN

C

      DOUBLE PRECISION TIME, COORDS, VALUES, RCONST

C

      DIMENSION     COORDS(3,NPTS), VALUES(NPTS), ICONST(ILEN)

      DIMENSION     RCONST(RLEN)

C

C-----------------------------------------------------------------------

C

      DOUBLE PRECISION X, Y, Z, T, PI

      DOUBLE PRECISION MMS

      double precision xmin, xmax, Vtot, vo, S, theta

      double precision t1, t2, t3, t4, thetam

C

      INTEGER J

      Vtot = 100.0

      t1 = 1.0

      t2 = 11.0

      t3 = 21.0
```

```fortran
      t4 = 23.0

      thetam = 89.0


C

      PI = FOUR*ATAN(ONE)


      xmin=9.989667

      xmax=10.010333


      DO 200 J=1, NPTS
C

        X = COORDS(1,J)

        Y = COORDS(2,J)

        Z = COORDS(3,J)

        T = TIME
C

        if (t .le. t1) then

          theta = 0.0

        elseif (t .le. t2) then

          theta = (thetam/(t2-t1))*(t-t1)

        elseif (t .le. t3) then

          theta = -(thetam/(t3-t2))*(t-t3)

        else
```

```fortran
         theta = 0.0

      end if


      S = (2./3.)*tan(pi*theta/180.)

      if (S .eq. 0.0) then

         vo = 0.0

      else

         vo = Vtot/sqrt(2*(1 + 4/(9*S*S)))

      end if

      mms = -vo*sin( 2.0*pi*( ((x-xmin)/(xmax-xmin)) ) )

      VALUES(J) = MMS
C

 200 CONTINUE
C

      RETURN
C

C

      END
```

E.6. FORTRAN Subroutine for Computing w for S(t).

```fortran
      SUBROUTINE w_BC (NPTS, TIME, COORDS, VALUES,

     $           ICONST, ILEN, RCONST, RLEN)
```

```
C*****************************************************************

C

#include <Afgo_numbers.h>

C

      INTEGER      NPTS, ICONST, ILEN, RLEN

C

      DOUBLE PRECISION TIME, COORDS, VALUES, RCONST

C

      DIMENSION      COORDS(3,NPTS), VALUES(NPTS), ICONST(ILEN)

      DIMENSION      RCONST(RLEN)

C

C----------------------------------------------------------------------

C

      DOUBLE PRECISION X, Y, Z, T, PI

      DOUBLE PRECISION MMS

      double precision Vtot, wo, S, theta

      double precision t1, t2, t3, t4, thetam

C

      INTEGER J

C

      PI = FOUR*ATAN(ONE)

      Vtot = 100.0

      t1 = 1.0
```

```fortran
      t2 = 11.0

      t3 = 21.0

      t4 = 23.0

      thetam = 89.0


C

      DO 200 J=1, NPTS

C

        X = COORDS(1,J)

        Y = COORDS(2,J)

        Z = COORDS(3,J)

        T = TIME

C

        if (t .le. t1) then

          theta = 0.0

        elseif (t .le. t2) then

          theta = (thetam/(t2-t1))*(t-t1)

        elseif (t .le. t3) then

          theta = -(thetam/(t3-t2))*(t-t3)

        else

          theta = 0.0

        end if
```

```fortran
      S = (2./3.)*tan(pi*theta/180.)

      if (S .eq. 0.0) then

        wo = Vtot

      else

        wo = Vtot*(2./(3.*S))/sqrt(1 + 4/(9*S*S))

      end if

      mms = wo

ccc      MMS = 63.7*(1 -abs(X))**0.14286

ccc      mms=46.88d0

      VALUES(J) = MMS

C

 200 CONTINUE

C

      RETURN

C

C

      END
```

E.7. FORTRAN Subroutine for Calling the Fuego User Functions.

```
subroutine Fmwk_reg_user_subs()



    implicit none


    external apub_ftx3_sub


    external u_bc

    external v_bc

    external w_bc


    call fmwkusersub(apub_ftx3_sub,u_bc,'u_bc')

    call fmwkusersub(apub_ftx3_sub,v_bc,'v_bc')

    call fmwkusersub(apub_ftx3_sub,w_bc,'w_bc')


end
```

Appendix F: Cubit Input Files

The following Cubit input files are listed below:

F.1. Swirling Jet.

F.2. Cylinder in Crossflow.

F.3. LP Model, No Insulation.

F.1. Swirling Jet.

#sbr 12/11/2008

Generate mesh for jet (FUEGO BCs will then determine if jet is conventional or

swirling).

#sbr 10/30/2009

Units are for input deck in meters. Final domain is 0.248 m height and 0.1 m radius.

Start with height=0.248+0.01=0.258. Cubit will place 1/2 of cylinder on positive side

of

z axis, and other half on negative axis (i.e. gets centered on z=0 plane). Then do

webcut to

remove 0.01 length (which is needed to help imprint circular BC boundary): most

negative part

# of height is now at z=-0.129. Add 0.01 to it: z=-0.129 + 0.01=-0.119. This means that

height

# of cylinder is 0.129 + 0.119 = 0.248.

create cylinder height 0.258 radius 0.1

webcut vol 1 with plane zplane offset -0.119 ### z=-0.129 + 0.01=-0.119.

webcut volume 2 with cylinder radius 0.010333 axis z # L/D = 0.248/(2*0.01033)=12 :-)

delete vol 2

imprint body all

merge vol all

delete vol 3

#Note: sur 12 size 0.001 and vol all size 0.0016 yields 2.75e6 el.

Set the cylinders as tetmesh

surf 12 scheme map ###sbrtriadvance

surf 12 size 0.0006 ###0.0005 ###0.0007

mesh surf 12

vol all scheme sweep ###sbrtetmesh

Set Mesh Interval Size

vol all size 0.0017 ###0.002 ###0.0025

mesh vol all

sideset 100 surf 12 # top surface of small cylinder ("heli jet inflow")

sideset 101 surf 14 # top of large cylinder

sideset 102 surf 5 # annular surface of large cylinder

sideset 103 surf 3 # bottom surface of large cylinder

block 1 volume all

Setup Element Block Type

###sbrblock 1 element type tetra

#Place mesh squarely on a positive quadrant

transform mesh output translate 10 10 10

quality volume all aspect ratio #####allmetrics ###aspect ratio

export genesis "L:\NUCLEAR ENGINEERING PHD\INPUT MODEL FILES\JET

WITH BC SWIRL__NEW METHOD\jetless_01302011.g" overwrite

F.2. Cylinder in Crossflow.

Units are for FUEGO input deck that uses meters.

03/11/2009

Generate mesh for flow around cylinder.

################################NOTES: Change brick height and mesh size!

###sbr 05122010

L/D=3.048/0.2032=15; W/D=2.032/0.2032=10; cyl shift=(0.6096/0.2032)+1=4.

height=body 1 size=0.08   -->   978 el

height=body 1 size=0.04   -->   3,878 el

height=body 1 size=0.02   -->   15,558 el

height=body 1 size=0.01   -->   62,106 el

height=body 1 size=0.005 --> 241,315 el

height=body 1 size=0.0025 --> 914,364 el

create brick width 3.048 depth 2.032 height 0.08

webcut body 1 with cylinder radius 0.1016 axis z center 0.6096 0.0 0.0

###delete vol 2

delete body 2

#imprint body all

#merge body all

Set the cylinders as tetmesh

volume 1 scheme auto #####sweep ######tetmesh

Set Mesh Interval Size

body 1 size 0.08 ###

####mesh vol 1

mesh body 1

sideset 101 surf 6 # X-dir, RHS of cube, inflow BC

sideset 102 surf 4 # X-dir, LHS of cube, open BC

sideset 103 surf 5 # Y-dir, Front of cube, open BC

sideset 104 surf 3 # Y-dir, Back of cube, open BC

sideset 105 surf 9 # Z-dir, Top of cube, symmetry BC

sideset 106 surf 8 # Z-dir, Bottom of cube, symmetry BC

sideset 107 surf 7 # Cylinder surface, wall BC

####block 1 volume 1

block 1 body 1

Setup Element Block Type

block 1 element type hex ####tetra

quality volume all allmetrics ###aspect ratio

###quality volume 1 aspect ratio

export genesis "L:\NUCLEAR ENGINEERING PHD\FUEGO\INPUT

FILES\CYLINDER WITH CROSS FLOW\cylinder_1el_1kel_15D_by10D.g" overwrite

###export genesis "cylinder_1el_1kel_15D_by10D.g" overwrite

F.3. LP Model, No Insulation.

VHTR LP (Very High Temperature Reactor Lower Plenum) Finite Element Mesh

Ryan Jamison

rdjamis@sandia.gov

Last Updated: May 6, 2009

CUBIT 11.1 Build 4

#---

This files builds the mesh of the lower plenum only

#---

reset

import acis "C:\Documents and

Settings\sbrodri\Desktop\trashit\VHTR_LP_FLUID.1.sat" attributes_on separate_bodies

import acis "C:\Documents and

Settings\sbrodri\Desktop\trashit\HELICOID_FLUID.1.sat" attributes_on separate_bodies

import acis "C:\Documents and

Settings\sbrodri\Desktop\trashit\HELICOID_FLUID.2.sat" attributes_on separate_bodies

#import acis "./VHTR_LP_FLUID.1.sat" attributes_on separate_bodies

#import acis "./HELICOID_FLUID.1.sat" attributes_on separate_bodies

#import acis "./HELICOID_FLUID.2.sat" attributes_on separate_bodies

vol 1 vis off

subtract volume 7 13 19 25 31 37 43 49 55 61 67 73 79 85 91 97 103 109 115 121 127 133 139 145 151 157 163 169 175 181 187 193 199 205 and \

211 217 223 229 235 241 247 253 259 265 271 277 283 289 295 301 307 313 319 325 331 337 343 349 355 361 367 373 379 385 391 397 and \

403 to 405 from volume 406

subtract volume 412 418 424 430 436 442 448 454 460 466 472 478 484 490 496 502 508 514 520 526 532 538 544 550 556 562 568 574 580 and \

586 592 598 604 610 616 622 628 634 640 646 652 658 664 670 676 682 688 694 700 706 712 718 724 730 736 742 748 754 760 766 and \

772 778 784 790 796 802 808 to 810 from volume 811

split body 406 811

webcut vol 812 with sheet extended from surf 10108
webcut vol 880 with sheet extended from surf 10524

del vol 812 880 948 951

del vol 2 to 6, 8 to 12, 14 to 18, 20 to 24, 26 to 30, 32 to 36, 38 to 42, 44 to 48, 50 to 54, 56 to 60, 62 to 66, 68 to 72, 74 to 78, and \

80 to 84, 86 to 90, 92 to 96, 98 to 102, 104 to 108, 110 to 114, 116 to 120, 122 to 126, 128 to 132, 134 to 138, 140 to 144, and \

146 to 150, 152 to 156, 158 to 162, 164 to 168, 170 to 174, 176 to 180, 182 to 186, 188 to 192, 194 to 198, 200 to 204, 206 to 210, and \

212 to 216, 218 to 222, 224 to 228, 230 to 234, 236 to 240, 242 to 246, 248 to 252, 254 to 258, 260 to 264, 266 to 270, 272 to 276, and \

278 to 282, 284 to 288, 290 to 294, 296 to 300, 302 to 306, 308 to 312, 314 to 318, 320 to 324, 326 to 330, 332 to 336, 338 to 342, and \

344 to 348, 350 to 354, 356 to 360, 362 to 366, 368 to 372, 374 to 378, 380 to 384, 386 to 390, 392 to 396, 398 to 402, 407 to 411, and \

413 to 417, 419 to 423, 425 to 429, 431 to 435, 437 to 441, 443 to 447, 449 to 453, 455 to 459, 461 to 465, 467 to 471, 473 to 477, and \

479 to 483, 485 to 489, 491 to 495, 497 to 501, 503 to 507, 509 to 513, 515 to 519, 521 to 525, 527 to 531, 533 to 537, 539 to 543, and \

545 to 549, 551 to 555, 557 to 561, 563 to 567, 569 to 573, 575 to 579, 581 to 585, 587 to 591, 593 to 597, 599 to 603, 605 to 609, and \

611 to 615, 617 to 621, 623 to 627, 629 to 633, 635 to 639, 641 to 645, 647 to 651, 653 to 657, 659 to 663, 665 to 669, 671 to 675, and \

677 to 681, 683 to 687, 689 to 693, 695 to 699, 701 to 705, 707 to 711, 713 to 717, 719 to 723, 725 to 729, 731 to 735, 737 to 741, and \

743 to 747, 749 to 753, 755 to 759, 761 to 765, 767 to 771, 773 to 777, 779 to 783, 785 to 789, 791 to 795, 797 to 801, 803 to 807

tweak surface 5382 offset -1.0

webcut vol 1 with sheet extended from surf 5379

```
#--------------------------------------------------------------------------------

# CREATE MESH


imprint vol all

merge vol all


del volume 813 to 879, 881 to 947, 949 to 950, 952 to 953


#sbr06252009

body all rotate 270 about x


vol all scheme tetmesh ##########auto ######!!!!!tetmesh

vol all size 2.0

###0.25, fails in tetmesh

###0.5, fails in tetmesh

###1.0, fails in tetmesh

###2.0 OK in tetmesh (857351 el)

###3.0 OK in tetmesh (318962 el), but fails when thex is done

###4.0 fails in tetmesh

mesh vol all


###sbr07192010
```

###sbr07192010# Set the Volume as a tetmesh

###sbr07192010vol all scheme tetmesh #######sweep # pave #auto # submap #map

###sweep ###sbr 12072009 Set to hex mesh ####tetmesh

###sbr07192010vol all size 0.5 ########0.75 ####2.0

###sbr07192010surf 10962 10961 10946 10943 10927 10783 10771 10911 10504 10320

10292 10476 10859   \

###sbr07192010 10787 10759 10847 10428 10324 10268 10400 10923 10775 10763

10907 10496 10296 10272 \

###sbr07192010 10468 10855 10779 10751 10839 10416 10300   \

###sbr07192010 10252 10384 10919 10767 10755 10835 10895 10500 10420 10276

10256 10456 10915 10851 \

###sbr07192010 10743 10735 10823 10883 10508 10432 10304 10280 10388 10460

10843 10747 10727 10719 \

###sbr07192010 10815 10875 10512 10440 10328 10308 10260 10392 10903 10739

10731 10711 10703 10807 \

###sbr07192010 10867 10516 10448 10344 10332 10284 10264 10380 10899 10831

10723 10715 10695 10687 \

###sbr07192010 10799 10452 10360 10348 10312 10288 10396 10464 10891 10827

10707 10699 10679 10671 \

###sbr07192010 10372 10364 10336 10316 10404 10472 10887 10819 10691 10683

10663 10376 10352 10340 \

###sbr07192010 10408 10480 10879 10811 10675 10667 10368 10356 10412 10484

10871 10803 10791 10444 \

###sbr07192010 10424 10488 10863 10795 10436 10492 size 0.5

###sbr07192010mesh vol all

Start by setting the volume as a tetmesh, and then convert it to hexes--but the conversion must be

done after the sidesets have been declared, otherwise they get renamed!!!

#vol all scheme tetmesh

#vol all size 1.0 #####2 (sbr12082009 setting size to 1.0 for vol and surfs below yields 5.2e6 tet elements.)

#surf 10962 10961 10946 10943 10927 10783 10771 10911 10504 10320 10292 10476 10859   \

10787 10759 10847 10428 10324 10268 10400 10923 10775 10763 10907 10496 10296 10272 \

10468 10855 10779 10751 10839 10416 10300   \

10252 10384 10919 10767 10755 10835 10895 10500 10420 10276 10256 10456 10915 10851 \

10743 10735 10823 10883 10508 10432 10304 10280 10388 10460 10843 10747 10727 10719 \

10815 10875 10512 10440 10328 10308 10260 10392 10903 10739 10731 10711 10703 10807 \

10867 10516 10448 10344 10332 10284 10264 10380 10899 10831 10723 10715 10695 10687 \

10799 10452 10360 10348 10312 10288 10396 10464 10891 10827 10707 10699 10679 10671 \

10372 10364 10336 10316 10404 10472 10887 10819 10691 10683 10663 10376 10352 10340 \

10408 10480 10879 10811 10675 10667 10368 10356 10412 10484 10871 10803 10791 10444 \

10424 10488 10863 10795 10436 10492 size 1.0 ####0.5

#mesh vol all

Set the Volume as a tetmesh

#vol all scheme sweep # pave #auto # submap #map ###sweep ###sbr 12072009 Set to hex mesh ####tetmesh

#vol all size 2.0

#surf 10962 10961 10946 10943 10927 10783 10771 10911 10504 10320 10292 10476 10859   \

10787 10759 10847 10428 10324 10268 10400 10923 10775 10763 10907 10496 10296 10272 \

10468 10855 10779 10751 10839 10416 10300   \

10252 10384 10919 10767 10755 10835 10895 10500 10420 10276 10256 10456 10915 10851 \

10743 10735 10823 10883 10508 10432 10304 10280 10388 10460 10843 10747 10727 10719 \

\# 10815 10875 10512 10440 10328 10308 10260 10392 10903 10739 10731 10711 10703 10807 \

\# 10867 10516 10448 10344 10332 10284 10264 10380 10899 10831 10723 10715 10695 10687 \

\# 10799 10452 10360 10348 10312 10288 10396 10464 10891 10827 10707 10699 10679 10671 \

\# 10372 10364 10336 10316 10404 10472 10887 10819 10691 10683 10663 10376 10352 10340 \

\# 10408 10480 10879 10811 10675 10667 10368 10356 10412 10484 10871 10803 10791 10444 \

\# 10424 10488 10863 10795 10436 10492 size 0.5

\#mesh vol all

\#--

\# Create blocks and sidesets

\#block 1 vol all \#\#\#\#\#\#\#block 1 vol 1 954

\# Row 2

sideset 0201 surf 10927

sideset 0204 surf 10783

sideset 0205 surf 10771

sideset 0208 surf 10911

sideset 0225 surf 10504

sideset 0228 surf 10320

sideset 0229 surf 10292

sideset 0232 surf 10476

Row 3

sideset 0302 surf 10859

sideset 0303 surf 10787 # Lower RHS

sideset 0306 surf 10759

sideset 0307 surf 10847

sideset 0326 surf 10428

sideset 0327 surf 10324

sideset 0330 surf 10268

sideset 0331 surf 10400

Row 4

sideset 0401 surf 10923

sideset 0404 surf 10775

sideset 0405 surf 10763

sideset 0408 surf 10907

sideset 0425 surf 10496

sideset 0428 surf 10296

sideset 0429 surf 10272

sideset 0432 surf 10468

Row 5

sideset 0502 surf 10855

sideset 0503 surf 10779

sideset 0506 surf 10751

sideset 0507 surf 10839

sideset 0526 surf 10416

sideset 0527 surf 10300

sideset 0530 surf 10252

sideset 0531 surf 10384

Row 6

sideset 0601 surf 10919

sideset 0604 surf 10767

sideset 0605 surf 10755

sideset 0608 surf 10835

sideset 0609 surf 10895

sideset 0624 surf 10500

sideset 0625 surf 10420

sideset 0628 surf 10276

sideset 0629 surf 10256 ### LHS by exit

sideset 0632 surf 10456

Row 7

sideset 0702 surf 10915

sideset 0703 surf 10851

sideset 0706 surf 10743

sideset 0707 surf 10735

sideset 0710 surf 10823

sideset 0711 surf 10883

sideset 0722 surf 10508

sideset 0723 surf 10432

sideset 0726 surf 10304

sideset 0727 surf 10280

sideset 0730 surf 10388

sideset 0731 surf 10460

Row 8

sideset 0804 surf 10843

sideset 0805 surf 10747

sideset 0808 surf 10727

sideset 0809 surf 10719

sideset 0812 surf 10815

sideset 0813 surf 10875

sideset 0820 surf 10512

sideset 0821 surf 10440

sideset 0824 surf 10328

sideset 0825 surf 10308

sideset 0828 surf 10260

sideset 0829 surf 10392

Row 9

sideset 0903 surf 10903

sideset 0906 surf 10739

sideset 0907 surf 10731

sideset 0910 surf 10711

sideset 0911 surf 10703

sideset 0914 surf 10807

sideset 0915 surf 10867

sideset 0918 surf 10516

sideset 0919 surf 10448

sideset 0922 surf 10344

sideset 0923 surf 10332

sideset 0926 surf 10284

sideset 0927 surf 10264

sideset 0930 surf 10380

Row 10

sideset 1004 surf 10899

sideset 1005 surf 10831

sideset 1008 surf 10723 ### Upper RHS

sideset 1009 surf 10715

sideset 1012 surf 10695

sideset 1013 surf 10687

sideset 1016 surf 10799

sideset 1017 surf 10452

sideset 1020 surf 10360

sideset 1021 surf 10348

sideset 1024 surf 10312

sideset 1025 surf 10288

sideset 1028 surf 10396

sideset 1029 surf 10464

Row 11

sideset 1106 surf 10891

sideset 1107 surf 10827

sideset 1110 surf 10707

sideset 1111 surf 10699

sideset 1114 surf 10679

sideset 1115 surf 10671

sideset 1118 surf 10372

sideset 1119 surf 10364

sideset 1122 surf 10336

sideset 1123 surf 10316

sideset 1126 surf 10404

sideset 1127 surf 10472

Row 12

sideset 1208 surf 10887

sideset 1209 surf 10819

sideset 1212 surf 10691

sideset 1213 surf 10683

sideset 1216 surf 10663

sideset 1217 surf 10376

sideset 1220 surf 10352

sideset 1221 surf 10340

sideset 1224 surf 10408

sideset 1225 surf 10480

Row 13

sideset 1310 surf 10879

sideset 1311 surf 10811

sideset 1314 surf 10675

sideset 1315 surf 10667

sideset 1318 surf 10368

sideset 1319 surf 10356

sideset 1322 surf 10412

sideset 1323 surf 10484

Row 14

sideset 1412 surf 10871

sideset 1413 surf 10803

sideset 1416 surf 10791

sideset 1417 surf 10444

sideset 1420 surf 10424

sideset 1421 surf 10488

Row 15

sideset 1514 surf 10863

sideset 1515 surf 10795

sideset 1518 surf 10436

sideset 1519 surf 10492

######sbr Split sideset 1 into 4.

######sideset 1 surf 10962 10961 10946 10943

######sbr

Inlet Flow Channels Sideset

Half Inlets

sideset 0103 surf 10962

sideset 0106 surf 10961

sideset 0127 surf 10946

sideset 0130 surf 10943

LP manifold outlet sideset -- open boundary

sideset 2 surface 1

Symmetry Sideset

####sideset 3 surface 5171 5176 5178 5180 5182 5184 to 5185 5188 10966 to 10967

5170 5174 5177 5179 5181 5183 5186 5187

sideset 3 surface 5171 5176 5178 5180 5182 5184 to 5185 5188 10966 10967

Support Post Surfaces -- wall boundary

sideset 4 surface 5189 to 5366 5170 5186 5174 5177 5179 5181 5183 5187

All outer walls

sideset 5 surface 5175 5371 to 5378 5381 to 5382 10969 11106

vol all scale 0.0254

#sbr Place mesh squarely on a positive quadrant

transform mesh output translate 10 10 10

#!!thex volume all

block 1 vol all #sbr12082009 Do block after thex command so that hexes appear in

block!!!

export genesis "C:\Documents and

Settings\sbrodri\Desktop\trashit\VHTR_Lower_Plenum_07202010.g" block all overwrite

    #export genesis "./VHTR_Lower_Plenum_12082009.g" block all overwrite

qual vol all aspect ratio #####allme ###

Appendix G: CANTERA Thermo-Physical Properties

The helium and air physical properties used herein were used in an XML file, and are listed below.

```xml
<?xml version="1.0" ?>
- <ctml>
  <validate reactions="yes" species="yes" />
- <!--
  phase gas
  -->
- <phase dim="3" id="gas">
  <elementArray datasrc="elements.xml">He O N</elementArray>
  <speciesArray datasrc="#species_data">HE O2 N2</speciesArray>
  <reactionArray datasrc="#reaction_data" />
- <state>
  <temperature units="K">300.0</temperature>
  <pressure units="Pa">101325.0</pressure>
  </state>
  <thermo model="IdealGas" />
  <kinetics model="GasKinetics" />
  <transport model="Mix" />
  </phase>
```

- <!--

 species definitions

 -->

- <speciesData id="**species_data**">

- <!--

 species HE

 -->

- <species name="**HE**">

 <atomArray>**He:1**</atomArray>

 <note>**120186**</note>

- <thermo>

- <NASA Tmax="**1000.0**" Tmin="**300.0**" P0="**100000.0**">

 <floatArray name="**coeffs**" size="**7**">**2.500000000E+00, 0.000000000E+00,**

0.000000000E+00, 0.000000000E+00, 0.000000000E+00, -7.453750000E+02,

9.153488000E-01</floatArray>

 </NASA>

- <NASA Tmax="**5000.0**" Tmin="**1000.0**" P0="**100000.0**">

 <floatArray name="**coeffs**" size="**7**">**2.500000000E+00, 0.000000000E+00,**

0.000000000E+00, 0.000000000E+00, 0.000000000E+00, -7.453750000E+02,

9.153489000E-01</floatArray>

 </NASA>

 </thermo>

- <transport model="**gas_transport**">

<string title="**geometry**">**atom**</string>

<LJ_welldepth units="**K**">**10.200**</LJ_welldepth>

<LJ_diameter units="**A**">**2.580**</LJ_diameter>

<dipoleMoment units="**Debye**">**0.000**</dipoleMoment>

<polarizability units="**A3**">**0.000**</polarizability>

<rotRelax>**0.000**</rotRelax>

</transport>

</species>

- <!--

species O2

-->

- <species name="**O2**">

<atomArray>**O:2**</atomArray>

<note>**121386**</note>

- <thermo>

- <NASA Tmax="**1000.0**" Tmin="**300.0**" P0="**100000.0**">

<floatArray name="**coeffs**" size="**7**">**3.212936000E+00, 1.127486400E-03, -5.756150000E-07, 1.313877300E-09, -8.768554000E-13, -1.005249000E+03, 6.034737000E+00**</floatArray>

</NASA>

- <NASA Tmax="**5000.0**" Tmin="**1000.0**" P0="**100000.0**">

```xml
<floatArray name="coeffs" size="7">3.697578000E+00, 6.135197000E-04, -
1.258842000E-07, 1.775281000E-11, -1.136435400E-15, -1.233930100E+03,
3.189165000E+00</floatArray>
  </NASA>
  </thermo>
- <transport model="gas_transport">
  <string title="geometry">linear</string>
  <LJ_welldepth units="K">107.400</LJ_welldepth>
  <LJ_diameter units="A">3.460</LJ_diameter>
  <dipoleMoment units="Debye">0.000</dipoleMoment>
  <polarizability units="A3">1.600</polarizability>
  <rotRelax>3.800</rotRelax>
  </transport>
  </species>
- <!--
 species N2
  -->
- <species name="N2">
  <atomArray>N:2</atomArray>
  <note>121286</note>
- <thermo>
- <NASA Tmax="1000.0" Tmin="300.0" P0="100000.0">
```

```
<floatArray name="coeffs" size="7">3.298677000E+00, 1.408240400E-03, -
3.963222000E-06, 5.641515000E-09, -2.444854000E-12, -1.020899900E+03,
3.950372000E+00</floatArray>
</NASA>
- <NASA Tmax="5000.0" Tmin="1000.0" P0="100000.0">
<floatArray name="coeffs" size="7">2.926640000E+00, 1.487976800E-03, -
5.684760000E-07, 1.009703800E-10, -6.753351000E-15, -9.227977000E+02,
5.980528000E+00</floatArray>
</NASA>
</thermo>
- <transport model="gas_transport">
<string title="geometry">linear</string>
<LJ_welldepth units="K">97.530</LJ_welldepth>
<LJ_diameter units="A">3.620</LJ_diameter>
<dipoleMoment units="Debye">0.000</dipoleMoment>
<polarizability units="A3">1.760</polarizability>
<rotRelax>4.000</rotRelax>
</transport>
</species>
</speciesData>
<reactionData id="reaction_data" />
</ctml>
```